分类号：TP391　　　　　　　　　　　　　　单位代码：10422
密　级：　　　　　　　　　　　　　　　　　学　　号：201420401

SHANDONG UNIVERSITY

博士学位论文

Dissertation for Doctoral Degree

论文题目：**面向增减材制造的几何研究与应用**

GEOMETRIC RESEARCH AND APPLICATION ON ADDITIVE AND SUBTRACTIVE MANUFACTURING

作　者　姓　名　**赵海森**

培　养　单　位　**计算机科学与技术学院**

专　业　名　称　**计算机科学与技术**

指　导　教　师　**陈宝权 教授**

合　作　导　师

2018 年 10 月 20 日

原创性声明和关于论文使用授权的说明

原 创 性 声 明

本人郑重声明：所呈交的学位论文，是本人在导师的指导下，独立进行研究所取得的成果。除文中已经注明引用的内容外，本论文不包含任何其他个人或集体已经发表或撰写过的科研成果。对本文的研究作出重要贡献的个人和集体，均已在文中以明确方式标明。本声明的法律责任由本人承担。

论文作者签名：赵海勃　　日　期：2018.10.20

关于学位论文使用授权的声明

本人完全了解山东大学有关保留、使用学位论文的规定，同意学校保留或向国家有关部门或机构送交论文的复印件和电子版，允许论文被查阅和借阅；本人授权山东大学可以将本学位论文的全部或部分内容编入有关数据库进行检索，可以采用影印、缩印或其他复制手段保存论文和汇编本学位论文。

(保密论文在解密后应遵守此规定)

论文作者签名：赵海勃 导师签名：　　日　期：2018.10.20

目 录

目 录

摘 要

制造业是一个国家的支柱产业，能够直接体现一个国家的生产力水平。按工艺来分类，可分为“等材制造”，“减材制造”和“增材制造”。工业制造是一个典型的多学科交叉的领域，涉及到材料，机械，控制，通讯等众多方面。从前期的工件模型的设计（CAD），力学模拟分析（CAE），及最终的加工过程规划（CAM），都涉及到大量的几何问题。本学位论文面向增减材制造领域，对其中的部分过程规划和应用相关的几何问题进行研究。

本学位论文面向智能制造中的几何问题及其应用，具体研究了增减材制造路径规划相关的空间填充曲线生成问题，自由曲面模型装夹规划相关的区域分割问题；在应用方面研究了一种基于三维打印可定制化制造的创意投影灯罩几何模型生成方法。本文创新点和贡献主要包括以下几个方面：

（1）提出一种全局连续且平滑的增材制造路径规划方法

本文将费马螺旋线引入到空间填充曲线的生成中，提出了一种新的空间填充曲线——连通费马螺旋线，并详细阐述了其作为增材制造路径规划方法的优良特性。与传统的空间填充曲线不同，连通费马螺旋线对任意拓扑连通的区域都可以生成一条全局连续且平滑的空间填充曲线。将连通费马螺旋线应用到三维打印的截面填充路径规划中，并与现有的三维打印路径进行比较，证明应用连通费马螺旋线路径规划算法，能够显著提升打印质量并降低打印时间。

（2）提出一种残留分布均匀的减材制造路径规划方法

本文探索了连通费马螺旋线的三维形式，提出了一种同时满足全局连续，平滑和等残留三种特性的减材制造路径规划方法，该路径的跟随区域边界生成，能够显著提升铣削加工的表面质量和加工效率。为了使得残留均匀分布，基于曲面方向曲率本文提出了一种控制费马螺旋线路径间距的方法生成等残留连通费马螺旋线。通过实际的加工实验与已有的路径规划方法的对比，表明本文方法对加工效率和质量的提升作用。

（3）提出一种封闭自由曲面数控加工的装夹规划方法

已有的装夹规划方法主要处理基本几何图元组成的 CAD 模型，本文提出了一个针对封闭自由曲面模型数控加工的自动装夹规划方法。基于可达性分析，将装夹

规划问题定义为一个带方向标签的区域分割问题。考虑定轴加工的约束，应用图割理论将输入模型预分割为高度场子区域。之后通过求解一个可达性分析相关的最小覆盖问题，生成装夹规划的工件方向及其对应的加工范围划分。

（4）提出了一种投影半色调图像的多孔结构灯罩模型生成方法

本文提出了一种基于光线投影的新的半色调成像技术，根据用户给定的灰度图像和灯罩三维模型，通过在灯罩模型表面上设置微小孔洞调制投影图像。对于模型上的微孔优化其大小、位置和相对光源朝向角度，同时保证可打印性的结构约束，使光源透过这些孔洞在投影面上形成一幅与给定图像最相近的连续灰度图像。

关键词：增材制造，减材制造，路径规划，装夹规划，空间填充曲线，半色调图像

ABSTRACT

Manufacturing industry is the mainstay industry of a country, which can directly reflect a country's productivity level, including “additive manufacturing”, “subtractive manufacturing” and molding manufacturing distinguished by different fabricating technologies. Manufacturing industry is a typical interdisciplinary field involving materials, machinery, control, communication and many other aspects. A large number of geometric problems are involved in the model designing process (CAD), the mechanical simulation analysis (CAE), the final process planning (CAM).

This dissertation focuses on the geometry and application problems in the intelligent manufacturing. We pay attention to the space filling curves used in additive and subtractive manufacturing, domain decomposition problems during the setup planning for fully closed freeform surfaces. Regarding to the application problems, we propose a creative modeling method of perforated lampshades for continuous projective images. Main contributions of this dissertation are presented as follows:

1. A globally continuous and low-curvature tool path for additive manufacturing

We introduce Fermat spirals to “space-filling” curves and develop a new kind of “space-filling” curves, connected Fermat spirals, and show their compelling properties as a tool path fill pattern for layered fabrication. Unlike classical space-filling curves such as the Peano or Hilbert curves, which constantly wind and bind to preserve locality, connected Fermat spirals are formed mostly by long, low-curvature paths. This geometric property, along with continuity, influences the quality and efficiency of layered fabrication. We demonstrate that printing 2D layers following tool paths as connected Fermat spirals leads to efficient and quality fabrication, compared to conventional fill patterns.

2. An iso-scallop tool path for subtractive manufacturing

We generate a continuous, space-filling, and iso-scallop tool path which conforms to the machining patch boundary, enabling efficient carving with high-quality surface finishing. The tool path is generated in the form of connected Fermat spirals, which have been generalized from a 2D fill pattern for layered manufacturing to work for curved surfaces. Furthermore, we develop a novel method to control the spacing of Fermat spirals based on directional surface curvature and adapt the heat method to obtain iso-scallop

tool path. We demonstrate iso-scallop Fermat spiral carving paths for freeform 3D patches. Comparisons are made to tool paths generated by commercial software in terms of real machining time and surface quality.

3. Setup planning of fully closed freeform surfaces in CNC

Setup planning methods from the CAD and manufacturing literature have mainly focused on CAD models. We present an automatic setup planning algorithm for subtractive manufacturing of freeform 3D objects. Our method decomposes the input object's surface into a small number of patches each of which is fully accessible and machinable by the CNC machine, in continuous fashion, under a fixed cutter-object setup configuration. This is achieved by covering the input surface with a minimum number of accessible regions and then extracting a set of machinable patches from each accessible region.

4. Fabricated perforated lampshades for continuous projective images

We present a new halftoning technique for designing fabricated perforated lampshades that project continuous grayscale images onto the surrounding walls. Given the geometry of the lampshade and a target grayscale image, our method computes a distribution of tiny holes over the shell, such that the combined footprints of the light emanating through the holes form the target image on a nearby diffuse surface. Our objective is to approximate the continuous tones and the spatial detail of the target image, to the extent possible within the constraints of the fabrication process.

Keywords: additive manufacturing, subtractive manufacturing, tool path planning, setup planning, space filling curve, halftoning image

第1章 绪 论

1.1 研究背景及意义

工业制造（Industry Manufacturing）是指采用手工或机械加工的方式，借助各种加工工具通过一系列化学、物理或生物反应过程，生产制造富于使用或销售价值的产品或货物的过程[1]。工业制造的过程就是将原材料转化为最终工业产品的过程。随着信息技术的发展，工业制造由手工方式为主逐步转化为自动化为主。工业制造业是一个国家的支柱产业，能够直接体现一个国家的生产力水平，是区别一个国家属于发展中国家或发达国家的重要因素。从历史上可以看到，凡是工业发达的国家，其经济水平以及国际地位都处于世界前端[2]。

从制造工艺上分类，工业制造可分为“等材制造”，“减材制造”和“增材制造”：如图 1-1，铸、锻、焊技术没有改变原材料的质量,被称为“等材制造”；车、铣、磨技术则使原材料在制造中减少,被称为“减材制造”（Subtractive Manufacturing）；采用材料逐渐累加的方法制造实体零件的技术，被称为“增材制造”（Additive Manufacturing, AM）技术。

传统铸造技术　　数控机床加工　　金属三维打印

图 1-1 工业制造按工艺不同分为“等材制造”，“减材制造”和“增材制造”[3]

工业制造是一个典型的多学科交叉的领域，涉及到材料，机械，控制，通讯等众多方面。工业制造的过程中涉及到大量的几何问题，从前期的工件模型的设计制造（CAD），考虑力学或材料特性的模拟分析（CAE），以及最终的规划合理的加工过程控制机械设备进行实际加工（CAM）。随着工业制造自动化水平的提高，

如何应用先进的信息技术，解决工业制造中流程规划或应用中蕴含的几何问题变的越来越重要了。

三种主要的工业制造工艺中，以模具注塑，铸造加工为代表的“等材制造”发展时间较长，在生产实践中形成了很多工艺经验，以数控加工为核心的减材制造和以三维打印为代表的增材制造历史较短，其中蕴含了很有待优化解决的几何问题。本学位论文主要面向于增材制造和减材制造，试图对其中包含的部分几何和应用问题进行研究。

1.1.1 增材制造

增材制造，俗称“3D 打印”，或快速原型制造（Rapid Prototyping），实体自由制造（Solid Free-form Fabrication），采用分层加工、迭加成型的方式逐层累加材料的方法制造实体零件，如图 1-2。相对于传统的减材制造，是一种“自下而上”或“自下而上”的制造方法[4]。

图 1-2 增材制造生产的实体零件，广泛应用于建筑，航空，医疗，创意设计等领域

3D 打印技术被认为将会为个性化产品的设计及生产带来革新。《经济学人》杂志在其 2012 年的一期专题报导中称，3D 打印技术的发展与逐渐成熟，是第三次工业革命的重要标志之一[6]。同年，2012 年，美国政府正式宣布建立国家增材制造创新机构，推动 3D 打印技术向国家主流制造技术发展， 也促使各国政府开始重视 3D 打印。3D 打印的技术研究和产业化发展也受到我国政府的充分重视，2015 年 2 月 28 日，国家工信部正式发布了《国家增材制造产业发展推进计划

（2015-2016 年）》[7]。《计划》中明确提出我国增材制造的发展目标为：“到 2016 年，初步建立较为完善的增材制造产业体系，整体技术水平保持与国际同步，在航空航天等制造领域达到国际先进水平，在国际市场上占有较大的市场份额”，这为我国的增材制造产业带来了新一轮的发展契机。

增材制造，一般采用金属、光敏树脂、塑料、陶瓷、石膏等多种材料，相关的工艺技术包括激光选区熔化（SLM）、光固化成型（SLA）、熔融沉积成型（FDM）、激光选区烧结（SLS）、三维立体打印（3DP）等多种类型，但基本原理都是将数字三维模型分解成若干层平面切片，然后将一定厚度的可粘合材料按切片图形逐层叠加，最终堆积生成整个成型件[5]。

三维打印技术是逐层累加的技术（也是加法加工技术），通常包括三维数字模型生成、数据格式转换、切片计算、打印路径规划和实际打印过程[8]，如图 1-3。三维数字模型生成是整个 3D 打印流程的基础，通常利用各种三维建模软件（如 CAD 软件）或三维扫描设备生成 3D 数字模型；之后经过一定的数据格式转换过程传递给后续步骤，当前支持 3D 打印的最常见的数据格式为 STL 格式；切片计算过程为将三维模型通过“切割分片”，形成一片片的薄片；为将切片计算过程生成的薄片实体化，需要对打印喷头的路径进行规划，在喷头移动过程中将 3D 打印材料转化为薄片实体；最终 3D 打印机根据上述切片和喷头路径控制信息进行打印，直到完整的物体成型。显然该过程中包含的几何问题有输入三维模型的特定功能需求下的优化设计，三维模型的切片分层，打印路径的规划。

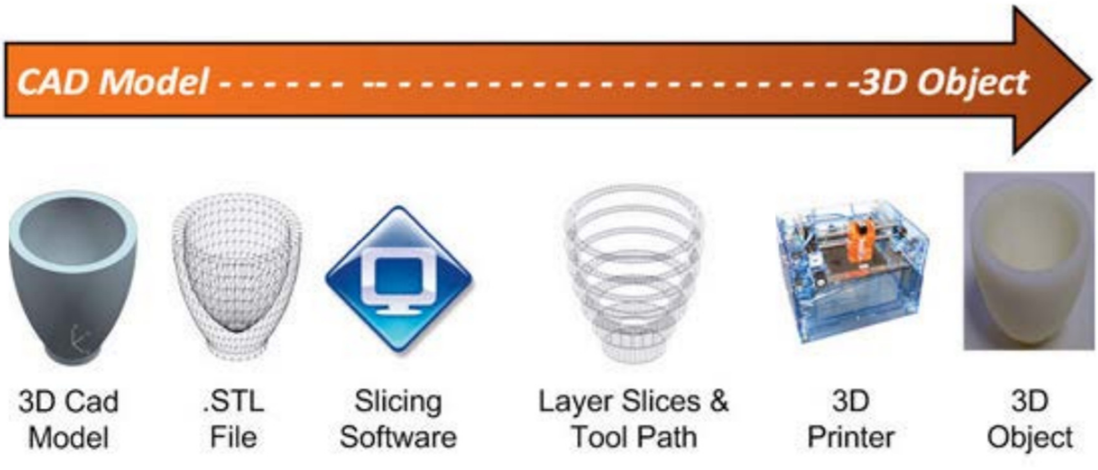

图 1-3 三维打印流程图[5]

作为快速成型领域的新兴技术，3D 打印技术以数字模型文件为基础制造几乎任意形状三维实体，而不像传统的机械加工技术通过切削或钻孔（即减材制造）等工艺或模具等完成制造过程，不但能够缩短产品的研制周期从而提高生产率和降低成本，而且在材料耗费、环境保护等方面也有益处。

增材制造主要优势体现在：产品复杂度、多样化与成本无关；零技能制造；个性化定制的优势三方面有明显的优势[5]，尤其适合对任意复杂结构零件，个性化定制产品和高附加值产品进行加工。然而，增材制造的缺点也很突出，主要在于：产品制造效率还有待提升；耗材价格昂贵；产品尺寸受限，表面质量精度较差；大批量生产率低下。因此，增材制造可被视为对传统制造业的有益补充，在相当长时期内，两者将共存[4]。

三维打印中的路径规划问题是增材制造流程中的一个核心过程，是一个典型的几何优化问题，直接影响到制造产品的成型时间和质量。本学位论文拟对该问题进行重点研究。

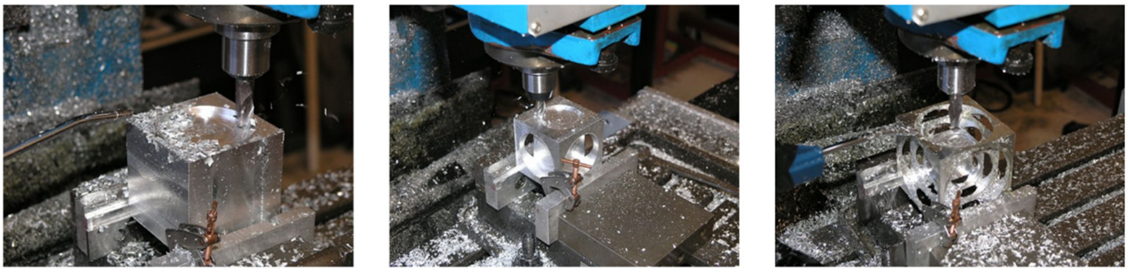

图 1-4 数控机床加工一个镂空工件

1.1.2 减材制造

减材制造通常是指利用切削刀具，从毛坯上切除多余材料，从而获得具有一定形状和精度零件的过程[9]。减材制造主要包括手动加工和数控加工两大类。手动加工是指机械工人通过手工操作车床、铣床、刨床和磨床等机械设备来实现对各种材料加工的方法。手动加工适合进行小批量、简单的零件生产。

数控加工（Computer Numerical Control, CNC），自从 20 世纪 40 年代第一台手动控制机床诞生开始，经历了近 80 年的历史发展，指的是机械工人运用数控设备来进行加工，通过编程，数控机床自动按要求去除材料，从而得到精加工工件[10]，如图 1-4。

从制造工艺上来分，数控加工可以分为最常见的车，铣，刨，磨。近年来，加工中心作为一种能够将多种制造工艺融合为一体的机械设备发展迅速。数控加工以连续的方式来加工工件，适于加工大批量、形状复杂的零件。

在数控加工领域流程规划为连接工件设计阶段和实际加工阶段的中间步骤，可以被定义为以最小化加工花费和最优化加工质量为目标的预先规划的加工指令[14]。流程规划包含许多核心步骤，包括设计描述（Design interpretation），流程选择和机床选择，装夹规划，流程参数选择，周期时间预估和花费估计，及相应的文档管理，如图 1-5。

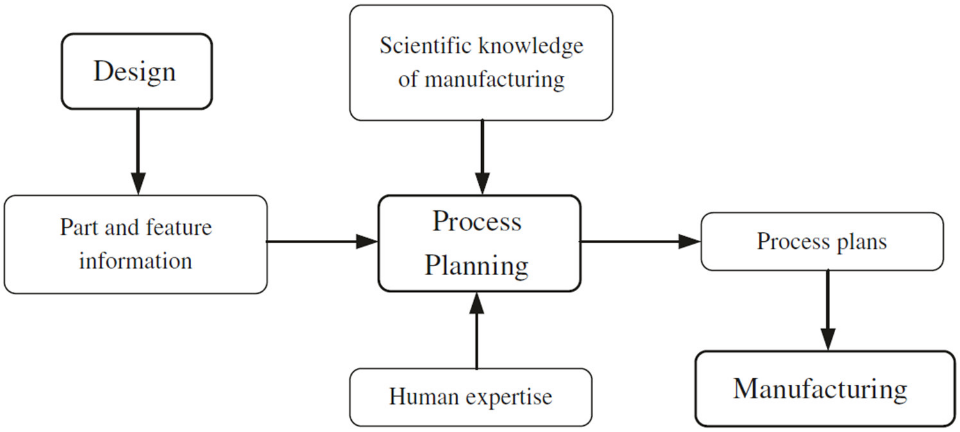

图 1-5 数控机床的流程规划

在不同的数控加工工艺中，铣削加工最常用于复杂自由曲面的加工。当前最常用的铣床分为三轴铣床和五轴铣床。其中，三轴铣床一般用于平面型腔加工[11-12]。五轴铣床一般用于复杂曲面的制造。

数控加工的加工流程，通常包括粗加工，精加工和后清理。如图 1-6，粗加工一般采用大尺寸铣削刀头，快速去除大部分不属于目标部件的工件部分，得到目标部件的近似形状；该近似形状实际上是目标部件的一个等距离偏置面。精加工用小尺寸铣削刀头，去除近似形状上不属于最终部件的额外部分材料。由于精加工刀头尺寸较小及待加工部件本身的复杂结构，精加工后仍可能会遗留部分未清理部分，在后清理阶段进行进一步清理。加工流程的每个阶段都涉及到很多几何问题：粗加工阶段刀具的优化选择，装夹工具的设计，装夹规划设计，粗加工刀具路径的规划，加工过程的模拟；精加工过程中的刀具路径规划，加工区域的划分，加工过程的模拟；清根步骤的待加工区域的快速检测，清根路径的自动规划等。

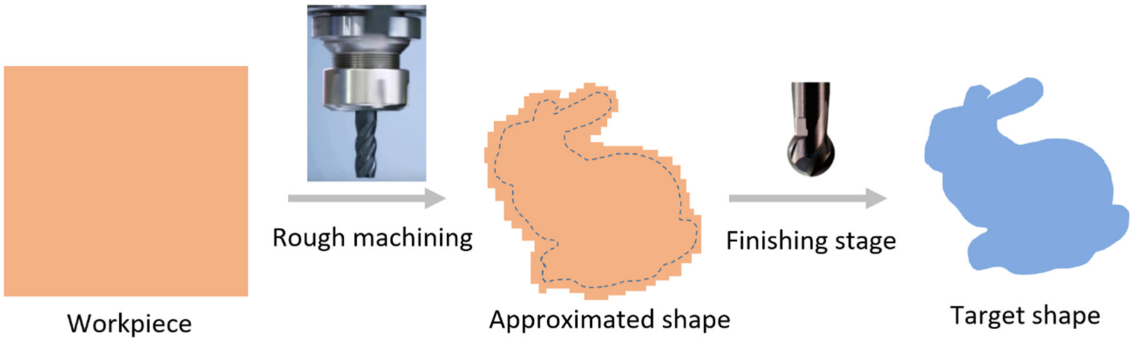

图 1-6 数控机床的一般流程

1.1.3 增减材制造的几何问题

本学位论文面向增减材制造中的路径规划规划，装夹规划以及基于三维打印的创意设计与制造方面，研究其中涉及的几何问题。增减材制造中的路径规划涉及到的是空间填充曲线的生成。空间填充曲线在不同应用语境下，需要考虑不同的目标约束。装夹规划涉及到三维模型的区域分割。本学位论文拟研究三维模型的区域分割在数控加工装夹规划语境下的应用。此外，基于三维打印的创意设计与制造可能涉及的几何问题可能是多方面的，本学位论文聚焦于一种基于光线投影的半色调方法表现任意连续灰度图像。下文将介绍这四个方面的研究现状。

1.2 研究现状

1.2.1 增材制造的路径规划

增材制造技术是逐层累加的技术（也加法加工技术）。首先输入一个三维数字模型；然后将模型进行切片生成打印路径，并且进行路径优化：最后三维打印机逐层地按照打印路径堆积形成物体。其中，路径规划是整个三维模型打印工作流程中的关键步骤。

拓扑上讲，连续性是路径规划中的一个关键因素。不连续的路径会导致频繁的打印头“关闭/开启”操作，影响打印质量和时间[15-16]。从几何特征方面考虑，剧烈的转向会导致在切片边缘形成严重的阶梯状效应，影响打印质量；打印头在剧烈转向时不可避免的要进行“减速再增速”过程，从而影响打印效率[17]。

由于其简易性，目前最常用的路径规划方法为 Zigzag 方法[18]。对于任意拓扑的连通区域，Zigzag 方法一方面可能会使用多条打印路径对其进行填充,打印喷头

频繁的关闭/开启操作会严重影响打印质量[15-16]；另一方面，生成的打印路径会有很多小于或接近 90 度的拐角，打印喷头的骤然转向会严重影响打印时间以及打印质量[17]。下面从机械工艺角度，分别对路径的连续性和平滑性进行进一步阐述。

路径的连续性 熔融沉积成型技术是最为常用的增材制造技术，在熔融沉积过程中，材料被熔化为粘稠流体并通过一个细小的喷头挤出。由于流体的特性所限，材料的挤出量难以精确控制，因此导致喷头在开始挤出与停止挤出时，材料的挤出量会过多或过少；同时，当打印头自某段路经的终止点移动到下一段路径的起始点时，喷头上的多余材料会在截面上产生一条细长直线。因此导致的填充误差如出现在物体表面时，可导致肉眼可见的痕迹，如在物体内部出现，则会降低其结构强度。因此，打印路径规划要求尽量减少单层打印路径的间断。

路径的平滑性 熔融沉积成型技术在打印过程中，通过两轴或三轴电机控制喷头在二维平面上移动，因此当路径上存在尖锐转折时，喷头需要进行减速-加速，这一阶段相对于匀速移动阶段，将会消耗更多的时间，同时，在拐角部分，填充材料的分布是不均匀的，其在拐角内侧过多，外侧过少，这样会导致打印截面的厚度不均匀，因此，尽量保证打印路径上的低曲率将会减少打印时间并且提高打印质量。

因此，生成连续且平滑的路径，将能够显著提升打印质量，降低打印所用时间。

1.2.2 减材制造的路径规划

减材制造中的自动化制造方法主要通过计算机数值控制（computer numerical control, CNC）的方式实施。一台数控机床按照预先设计好的指令操纵一个圆柱形的铣削刀具从一个毛坯件上以减材的方式生产出最终的工件形体。其中预先设计刀具行进轨迹和方向的过程称为减材制造的路径规划。

如前文所述，复杂自由曲面工件一般采用铣削加工技术，在三轴或五轴数控机床上经过粗加工，精加工和清根加工。该加工过程中的每一阶段都需要进行相应的路径规划，路径规划的好坏不仅直接影响最终的加工质量的加工效率，还影响刀具的使用寿命等因素。目前大部分研究工作都围绕这精加工阶段的路径规划问题展开，主要原因在于精加工直接影响成型工件的表面质量，并且在整个加工过程中精加工时间占比往往更大。粗加工关系的核心因素在于完成度，对路径本身的质量要求不是特别高；后清理阶段的核心问题在于待后清理区域的检测。

以五轴铣床为例，路径规划不仅仅包括刀位点和刀触点的指定，还包括刀具姿态的控制，用于消除刀具干涉的影响。路径规划问题作为数控加工的一个核心关键问题，其研究与发展一直伴随在整个数控加工发展历程中。因此设计一个满足各种数控加工因素的路径规划算法就变得尤其重要了。尤其是近年来，随着数控加工领域的发展，高速加工越来越受到工业界和学术界的青睐。对于高速加工，设计负载均衡，最小化撤刀次数等因素的路径规划算法非常重要。

当前数控加工一般用于加工由较简单几何曲面包围成的传统 CAD 模型，一般最常用的路径式样为 Zigzag 路径。对于自由曲面的加工也有很多已有工作，比如参数法，截面法，导动面法等。

本学位论文主要关注自由曲面精加工中的刀具路径规划问题，精加工一般采用球头刀加工，主要原因在于球头刀对加工方向不敏感，也就是说球头刀具相对于自由曲面的方向在一定范围内任意变化，不影响其切削范围。精加工路径规划的主要目标约束有：1）加工路径连续不断；2）加工路径平滑，减少急转弯；3）满足用户指定的最大残留高度的前提下，自由曲面上残留高度均匀分布。其中，加工残留高度是指两条相邻刀路切削后剩余残留部分的高度。自由曲面上的等测地距离分布的路径并不能产生均匀分布的残留高度。为了获得均匀分布的残留高度，自由曲面上的路径间距需要根据相邻路径对应点处的方向曲率进行相应调节。

1.2.3 数控加工的装夹规划

如前文说述，铣削加工最常用于复杂自由曲面的加工，包括一般用于加工平面型腔结构（单独一个方向的自由曲面）的三轴铣床和用于加工复杂自由曲面的五轴铣床[11-12]。五轴数控机床的工作模式包括定轴加工模式和五轴联动工作模式。应用五轴数控机床加工一个完整的零部件，受到机床刀具可达性范围的限制，往往不能在一次装夹下完成所有部件区域的加工，需要多次进行重新装夹定位。应用定轴加工模式五轴数控铣床加工前需要进行装夹规划和定轴加工区域划分。

其中，装夹规划指的是装夹过程工件方向规划及对应加工范围划分，及设计或选择的装夹工具对工件进行加紧定位。定轴加工区域划分指的是将某装夹方向下的加工范围进一步划分为定轴加工模式可加工的子区域并指定其刀具方向。

图 1-7 减材制造加工的模型类型包括 CAD 模型和三维自由曲面模型

学术领域，装夹规划主要采用遗传算法、专家系统、决策树、训练学习等方法[19-20]，主要处理由基本几何元素组成的 CAD 模型。目前学术界还未见到相关能够处理无明显特征线的自由曲面组成的封闭工件，如图 1-7 所示的小猫模型。在当前的实际生产中，装夹规划和定轴加工区域划分还需要依赖于工程师的经验进行手动设计。本学位论文拟开展对于全封闭自由曲面模型的装夹规划的研究。

1.2.4 基于三维打印的创意设计与制造

随着信息技术在制造应用领域的发展，三维打印技术的出现为人类可定制化制造的需求带来了福音。第一次工业革命以来的大规模集约化的生产模式，显然无法满足越来越追求个性的当代人类的普遍需求。三维打印技术可以直接以数字模型文件为输入，能够制造任意复杂形状的三维实体，恰恰满足了这种个性化定制制造的需求。

图 1-8 发条玩具内部机械结构的制动设计[22]

目前三维打印在创意设计与制造方面，已经出现了很多有意思的工作，广泛应用于艺术设计，玩具设计，功能连接件等方面[21]。如图 1-7，Song 等人提出一种根据用户需求自动设计发条玩具内部机械结构的算法[22]。Wang 等人提出一种考虑到浮力平衡的模型内部结构镂空方法，能否生成用户指定的漂浮方向[23]。Li 等人可以在用户指定的三维模型内部计算生成特定的管道结构，演奏出用户指定的声音频率或响度大小的声音[24]。

本学位论文拟在三维打印图像个性化展示方面做出一定的研究工作。图像以色调连续性来划分，可以分为连续调图像和半色调图像，如图 1-9。连续调图像是指在一幅图像上，存在着色调、亮度与饱和度连续变化的真彩色图像，其连续变化是以单位面积成像物质颗粒的密度构成的，如 CRT 显示器。连续调图像的深浅变化是无级的。连续调图像的展示方式主要有图像打印，图像投影（二维幕布投影，三维全息投影），以及各种显示设备（计算机屏幕,VR/AR 显示眼镜等）。

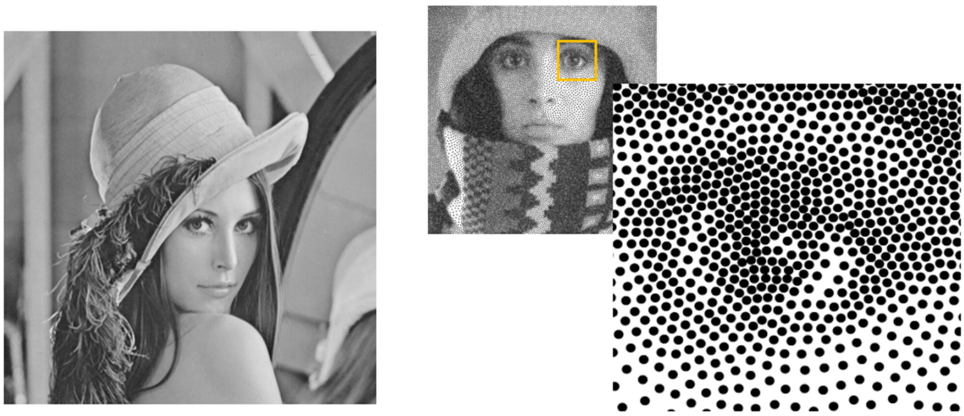

图 1-9 图像按照色调连续性分类，连续调图像（左图），半色调图像（右图）

与之对应的半色调图像，又称为网目图像，表现的色调则相对少一些，通过网点的大小或稀疏表达图像的层次，图像细节的变化不连续，如喷墨类型的打印机。因此从某种程度上来说，半色调图像是连续调图像的一种。由连续调图像生成半色调图像的方法，可称之为半色调图像生成技术，或半色调技术。

半色调技术已经广泛应用于传统的纸面印刷和数字显示术等领域。半色调技术利用人类视觉融合原理，用相互离散分布的单元（基本的几何元素，黑圆点，三角形，方形等其他形状），而人类眼睛又和成像屏幕成一定合适距离时候，人类视觉可以把离散单元融合为连续灰度或彩色变化[25-26]。其核心在于结构保持，色调再

现，点密度和空间解析等问题。经过几十年的探索研究，以保持原始图像的相对色调为目的，国内国外的研究学者们提出了很多相应的半色调技术[27-28]。

然而，已有的半色调图像生成的技术，所面向的是数字半色调图像或者 2D 图像的点刻画表达[27-28]，如图 1-9 左图所示点刻画形式。用其他形式表达半色调图像的研究还比较少见，这方面的研究工作有，Schwartzburg 等人利用近似平行光通过透明玻璃产生的折射光线路径发生转变的原理，在投影接收面上形成特定的高对比度焦散图像[29]，如图 1-10 所示。

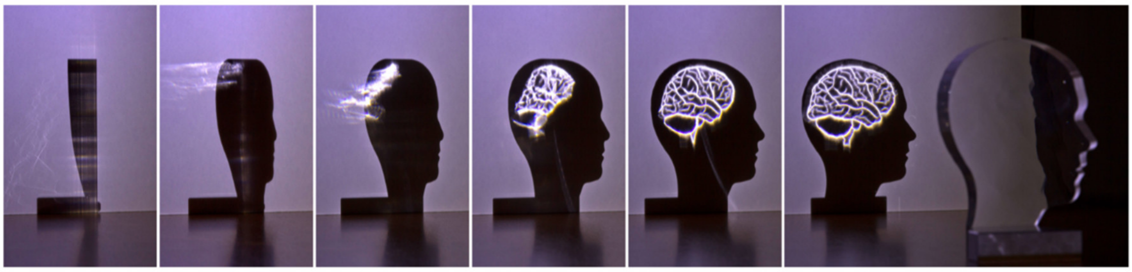

图 1-10 高对比度焦散图像[29]

1.3 研究目标、研究内容及主要创新点

1.3.1 研究目标

本学位论文的研究成果将为增减材制造包括路径规划，装夹规划，以及基于三维打印的创意设计与制造提供新的思路和方法，为解决增减材制造中的其他几何问题提供借鉴。论文成果有望直接应用于指导实际的增减材制造，减少人工成本，提升增减材制造过程的加工效率和成品质量，并在基于三维打印的创意设计与制造方面为提出一种新的投影图像展示技术，应用于室内家具，创意产品展示，艺术形象展示等领域，具体目标如下：

（1）研究实现一种新的增材制造路径规划算法，新的路径规划算法能够提高增材制造的打印效率和打印质量。

（2）研究实现一种新的减材制造路径规划算法，将研究目标一中提出的增材制造的路径规划方法拓展到减材制造中，新的路径规划算法能够提高减材制造的加工效率和表面质量。

（3）研究实现一种用于加工三维全封闭自由曲面模型的装夹规划算法，该算

法针对用户输入的任意封闭自由曲面模型给出合理的装夹规划方案。

（4）研究实现一种面向三维打印的半色调投影与模型生成方法，该方法生成的可打印多孔结构灯罩能够在投影接收面上形成一幅与给定任意灰度图像最接近的半色调投影灰度图像。

1.3.2 研究内容

本学位论文主要研究增减材制造中的几何问题及其应用，具体研究了增减材制造路径规划涉及的空间填充曲线生成问题，以减材制造的方式加工封闭自由曲面模型的装夹规划对应的区域分割问题，以及基于三维打印可定制化制造的投影半色调图像的多孔结构灯罩模型生成问题。针对这些问题，结合特定的增减材制造的约束背景，本学位论文提出了相应的解决方案。本学位论文具体的研究内容有：

（1）截面填充曲线生成方法

将费马螺旋线引入到增材制造的路径规划中，提出一种同时具有全局连续和平滑两种特性的截面填充曲线生成方法——连通费马螺旋线。

（2）自由曲面精加工路径生成方法

面向减材制造的路径规划问题，将上文提出的截面填充曲线生成方法拓展到自由曲面精加工路径生成中，提出了一种同时满足全局连续，平滑且残留均匀分布三种特性的自由曲面填充曲线生成方法。

（3）装夹规划区域分割算法

在五轴数控机床上采用定轴加工（3+2 工作模式）的方式，加工三维封闭自由曲面模型，针对其中的装夹规划步骤，提出一种考虑数控机床刀具可达性和最小化装夹次数的区域分割算法，算法输出装夹过程工件方向规划及对应加工范围划分。

（4）透射光半色调投影与模型生成方法

将传统的半色调技术应用于光线上，将光线透射形成的光斑作为显示介质，根据用户给定的灰度图像和三维模型，通过在模型表面上设置微小孔洞调制投影图像。对于模型上的微孔优化其大小、位置和相对光源朝向角度，同时保证可打印性的结构约束，使光源透过这些孔洞在投影面上形成一幅与给定图像最相近的连续灰度图像。

1.3.3 主要创新点

本文研究了面向增减材制造部分几何问题，包括空间填充曲线，三维曲面区域分割以及透射光半色调图像生成问题，并研究了他们在增减材制造路径规划，装夹规划和基于三维打印的创意设计与制造方面的应用。本文的主要创新点和贡献主要分为以下几个方面：

（1）连通费马螺旋线及其在三维打印路径规划上的应用

本文将费马螺旋线引入到空间填充曲线的生成中。详细阐述了费马螺旋线作为一种新的空间填充曲线基础图案式样的优良特性：跟随区域边界生成；费马螺旋线的两个末端点都位于区域外边界上；并且末端点的位置在区域外边界是任意可变的。针对任意拓扑连通的区域，提出了一种连通费马螺旋线生成算法。采用分而治之的方法，将任意的拓扑连通区域分为多个相互独立的子区域分别填充费马螺旋线，之后将多条独立的费马螺旋线连接起来生成一条连续间断且平滑的空间填充曲线，并应用一种全局优化的方法在保持曲线路径间距一致的约束下对打印路径进行平滑。将连通费马螺旋线应用到三维打印的截面填充路径规划中，并与现有的三维打印路径进行比较，证明应用连通费马螺旋线路径规划算法，能够显著提升打印质量并降低打印时间。

（2）等残留连通费马螺旋线及其在自由曲面精加工上的应用

本文探索了连通费马螺旋线的三维形式，将二维平面的连通费马螺旋线生成算法拓展到三维自由曲面上，提出了一种路径间距可变的连通费马螺旋线生成算法，并将其应用于自由曲面精加工的等残留路径规划中。等残留路径规划，要求在满足用户指定的最大残留高度的前提下，自由曲面上残留高度均匀分布。为了获得均匀分布的残留高度，自由曲面上的路径间距需要根据相邻路径对应点处的方向曲率去调节。针对用户指定的最大残留高度，自由曲面不同采样点处的方向曲率对应不同的路径间距约束。本文将自由曲面各采样点不同的路径间距约束，统一在一个约束相关的距离标量场的迭代求解中。从该约束相关的距离标量场中抽取出残留高度等值线，恰恰满足均匀残留高度的路径分布约束，并将提取的等值线连接为连通费马螺旋线，最后对生成的连通费马尔螺旋线进行平滑处理。面向自由曲面精加工，本文提出的路径规划方法能够同时满足连续不断且平滑、区域边界相关、残

留高度分布均匀的形状，通过实际的加工实验与已有的路径规划方法对比表明，本文方法可以在满足加工质量的前提下显著提升加工效率。

（3）可达性分析驱动的区域分割方法及其在装夹规划上的应用

已有的装夹规划方法主要处理基本几何图元组成的 CAD 模型，本文针对三维封闭自由曲面模型，首次探索了一个自动的装夹规划方法。具体的本文设置的装夹规划的前提背景为，五轴数控机床采用定轴加工的方式对自由曲面模型进行加工。本文对五轴数控机床刀具相对于曲面模型的可达性进行了分析。将该装夹规划问题定义为一个可达性分析驱动的带方向标签的区域分割问题。考虑到定轴加工的约束，基于图割理论将输入模型预分割为高度场子区域。之后通过求解一个可达性分析相关的最小覆盖问题，生成装夹规划的工件方向及其对应的加工范围划分。本文提出的装夹规划技术方案具备很好的开放性，适合在本文提出的统一计算框架内融合其他本文没有考虑到的约束。

（4）透射光半色调投影生成及其在三维打印创意图像表达上的应用

本文将传统的半色调技术应用于光线上，将光线透射形成的光斑作为显示介质，从而提出了一种新的半色调图像表达方式。提出了一种可投影该半色调图像的三维打印多孔结构灯罩的模型生成方法和一种特定的模拟方法。根据用户给定的灰度图像和三维模型，通过在模型表面上设置微小孔洞调制投影图像。对于模型上的微孔优化其大小、位置和相对光源朝向角度，同时保证可打印性的结构约束，使光源透过这些孔洞在投影面上形成一幅与给定图像最相近的连续灰度图像。实际实验表明，本文提出的模型生成方法构建的三维可打印灯罩的投影效果非常接近于原始灰度图像。

1.4 论文组织结构

本文的结构安排如下：

第一章描述了本学位论文的研究背景及意义，回顾了相关研究的发展现状，总结和概括了整个研究的目标、内容以及主要贡献点，并介绍了本学位论文的基本组织结构。

第二章详细描述了本文提出的面向增材制造的路径规划方法——连通费马螺旋线的生成算法；本章对相关工作进行了总结描述，分析展示了相关的实验结果以

及对比实验结果。

第三章介绍了本文提出的面向减材制造的路径规划方法，总结概括了三维曲面铣削加工路径规划的特定约束，详细叙述了等残留连通费马螺旋线的生成算法，并展示了算法实际的铣削实验结果和量化数据对比。

第四章介绍了加工全封闭自由曲面模型的装夹规划方法，总结概括了已有的装夹规划相关的工作，介绍了自由曲面模型装夹规划涉及的机床特性，对装夹规划算法进行了详细的介绍，并给出了相应的实验结果和数据对比。

第五章介绍了透射光半色调投影与模型生成方法，对三维打印创意设计与制造的相关工作进行了总结，详细阐述了多孔结构灯罩的生成算法以及透射光投影的模拟算法，最后展示了算法生成的实际打印灯罩的投影效果，并对其进行了量化对比分析。

第六章对本学位论文进行了总结和归纳，并详尽描述了未来的研究方向及研究价值。

第2章 增材制造的路径规划

2.1 引言

以目前的技术水平来看，影响增材制造（三维打印）进一步向普通用户推广的一个很重要的原因是加工效率低下，一般尺寸的三维模型都需要数个小时的时间。而影响三维打印效率的一个关键因素就是三维打印的路径规划的优劣。

得益于其易于理解与生成的优势，目前在商业软件中最常用的路径规划方法为 Zigzag 方法。对于任意打印截面区域，Zigzag 方法无法保证用最少数量的打印路径生成截面填充曲线，随之产生的打印喷头频繁的开启和关闭以及空行程行进操作，将会对打印效率和成品质量产生双重影响[15-16]。从另外一个角度观察，Zigzag 采用循环往复的路径规划方法，生成的路径中不可避免的会出现许多接近甚至小于 90 度的硬拐角，打印喷头通过这些硬拐角需要花费更多的打印时间，并且对打印质量产生不好的影响[17]。

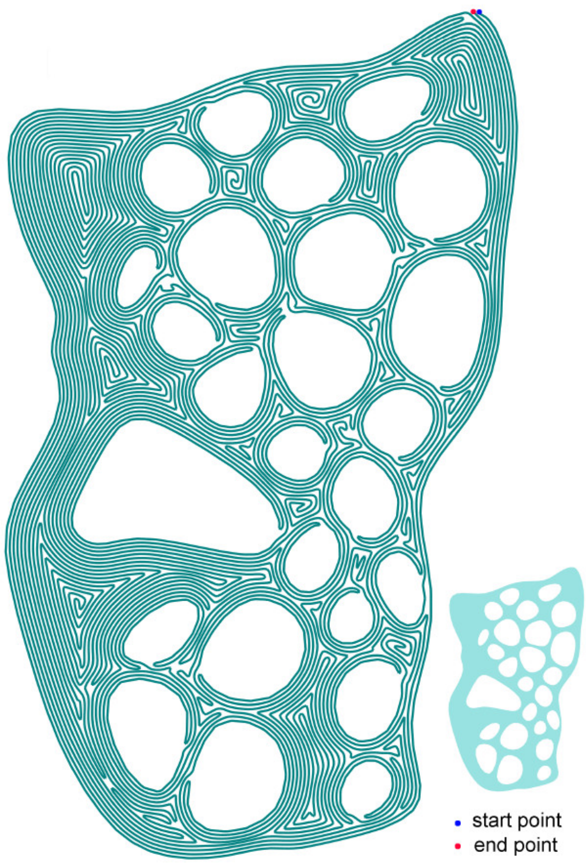

图 2-1 一种新的空间填充曲线“连通费马螺旋线”实例

因此，有必要探索一种能使三维打印喷头在行进过程中尽量平滑匀速运动，且能够连续不间断工作的路径规划方法。以此为目的，本章详细阐述了费马螺旋线作为一种新的基本图案式样的优良特征，提出了一种称为连通费马螺旋线的空间填充曲线，并将其应用于增材制造的路径规划中。如图 2-1，在一个多孔结构小猫模型的截面区域生成连通费马螺旋线的实例，其中蓝点和红点分别指出了路径的起点和终点位置。

本文将费马螺旋线引入到空间填充曲线的生成中，提出了一种连通费马螺旋线的生成算法。首先，采用分而治之的方法，将任意的拓扑连通区域分为多个相互独立的子区域分别填充费马螺旋线，之后将多条独立的费马螺旋线连接起来生成一条连续间断且平滑的空间填充曲线。

传统的基于分形的空间填充曲线为了严格的保证空间填充，以及保持一种局部填充的特性，比如 Hilbert 和 Peano 在内的空间填充曲线，会产生很大程度的弯曲路径。而基于费马螺旋的空间填充曲线，会尽量避免产生高曲率路径，不可避免的一定程度上破坏了局部填充的特性。而且，连通费马螺旋线路径并不能严格的保证绝对的空间填充。然而，对于增材制造语境下的路径规划的应用，连通费马螺旋线仍具备相当的吸引力和实用价值。

2.2 相关工作

近年来，计算机图形学领域中智能制造相关的研究方向发展迅速，出现许多以提高三维打印制造效能为目的研究工作，比如基于特定物理特性的几何优化，考虑到物体平衡性[30]和结构强度[31-33]的几何结构的设计与优化，以改善打印模型外表面质量的打印方向计算[34]，以节省三维打印耗费为目的的优化结构计算[35-36]，通过三维形状的分解和重组来突破打印空间的尺寸限制的工作[37-40]。

针对增材制造的路径规划问题，为了进一步强调路径的连续性和平滑性的重要性，本节首先详细叙述了三维打印设备的电机控制喷头移动的力学机制，以及在喷嘴行进过程中挤出粘弹性材料的机械原理与特点。然后总结增材制造路径规划的相关工作和当前研究热点。本节并不寄希望于能够详尽介绍路径规划所有已有工作，如果读者感兴趣的话，推荐读者阅读相关的综述文章[41-42]，或者 Gibson 等人的专门著述[43]，或者查阅 Dinh 等人 2015 年的 SIGGRAPH 课程[44]。

2.2.1 路径连续性

熔融沉积成型（FDM）是一种应用非常广泛的增材制造技术。在 FDM 制造工艺过程中，加热组件将丝状的热熔性材料加热融化为粘弹性状态并从打印喷嘴的末端开口处挤出。在熔融状态下粘弹性的塑性材料具备一定的可拉伸性，通常难于确保以绝对均匀且连续的形式控制挤出材料的精确用量。因此，当进给电机控制喷嘴开始挤出材料或者停止挤出材料的时候，通常是欠填充或过填充的，导致填充的不均匀性出现。当这种由于喷头频繁的开启或停止挤出材料发生在打印部件表面时，这些由于欠填充或过填充形成的材料分布的非均匀性将影响打印模型的表面观感；当这种不均匀填充发生在部件内部的填充路径之间时，熔融丝状材料相互附着的粘合力可能被削弱，从而降低打印部件的强度。

类似的过程在所有挤出型打印工艺中都会出现，比如对于粉末打印设备喷嘴挤出粘合剂的过程与 FDM 打印工艺挤出熔融材料的过程类似。规划路径的任何不连续性，除了会导致打印喷嘴的频繁开关之外，还会不可避免的引入空走路径。打印喷嘴空走过程中并不参与实际的打印工作，将会影响整体制造过程的效率。

因此，增材制造路径规划的一项核心目标是使得路径的开关切换最少化，或者说使其连续性最大化。

2.2.2 路径平滑性

路径的几何特征，尤其是路径曲率会显著影响加工效率和质量。当打印喷嘴在步进电机的控制下通过曲率变化较大的规划路径时，需要更多的减速和加速时间。对于 FDM 制造工艺，打印喷嘴根据事先设置好的规划路径填充熔融材料时，需要控制两种速度，一种是喷嘴本身的进给速度，一种是喷嘴挤出熔融材料的挤出速度。在喷嘴通过曲率变化较大的硬拐角路径时，进给速度不可避免的要经历先降低再提升的过程，为了保证单位时间内喷嘴挤出的材料量不发生剧烈变化，进给速度变化的同时需要配合挤出速度的相应变化，而这往往将极大的增加控制系统的设计难度和设备运行响应的精准度。若两者无法密切配合，在曲率变化较大的路径部分，将会出现过填充或欠填充的现象[45]。大曲率路径造成的这种影响打印质量和效率的现象，在高速制造条件下的影响会进一步扩大。高速制造意味着初始设置很高的

进给速度，喷嘴在通过硬拐角路径时需要花费更多的时间经历减速和加速过程。

因此，尽量减少急转弯的连续路径可以使打印喷嘴以适宜的速度沿着整个路径移动，从而达到高效和高质量的制造。

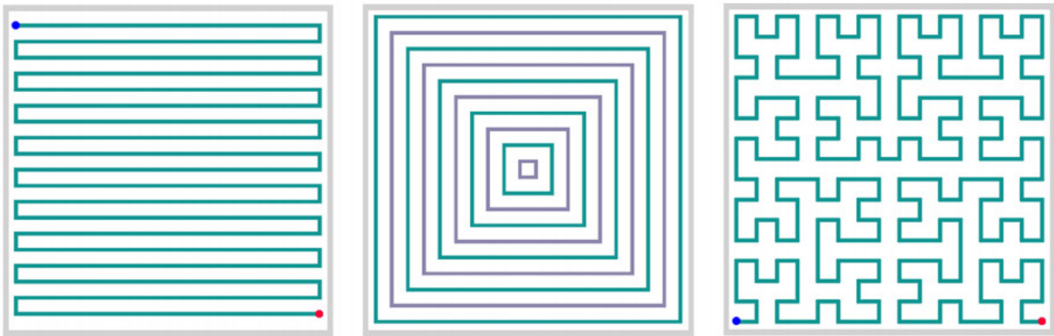

(a)平行扫描路径　　(b)轮廓平行路径　　(c)空间填充曲线

图 2-2 增材制造的常用路径规划方法

2.2.3 平行扫描路径与轮廓平行路径

目前，商用三维打印软件中最常用的增材制造截面填充路径主要是平行扫描路径和轮廓平行路径，如图 2-2。

平行扫描路径，由一组相互平行的直线路径在区域边界内往复扫描形成的，也被称为 Zigzag 路径[42]。平行扫描路径，是一种外轮廓无关的路径生成方法，对于拓扑比较简单的二维区域连续性较好，但是对于拓扑比较复杂的区域连续性并无法保证连续性。平行扫描路径中有很多接近甚至小于九十度的硬拐角，不适合高速制造场景下的加工。

轮廓平行路径，是由区域轮廓边界的一系列等距离偏置线组成的[46]。轮廓平行方法能够保证打印部件的外表面质量较好[47]。对于拓扑简单的二维区域，轮廓平行路径的平滑性更好，曲率变化距离的拐角较少出现，但是路径的连续性很差，不同距离的偏置线之间都是独立不连续的。

一种融合二者优势的杂交方法在商业软件中应用尤为广泛[48]，在内部区域生成平行扫描路径之前，先在区域轮廓的最外部区域生成几条轮廓平行路径。这种杂交方法的缺点在于，两种不同的路径规划方法的连接区域的填充质量无法保证。尤其需要强调的是，待填充的二维截面的外轮廓具有较高的凹度（concavities），两种路径规划方法易于出现不连续的问题。

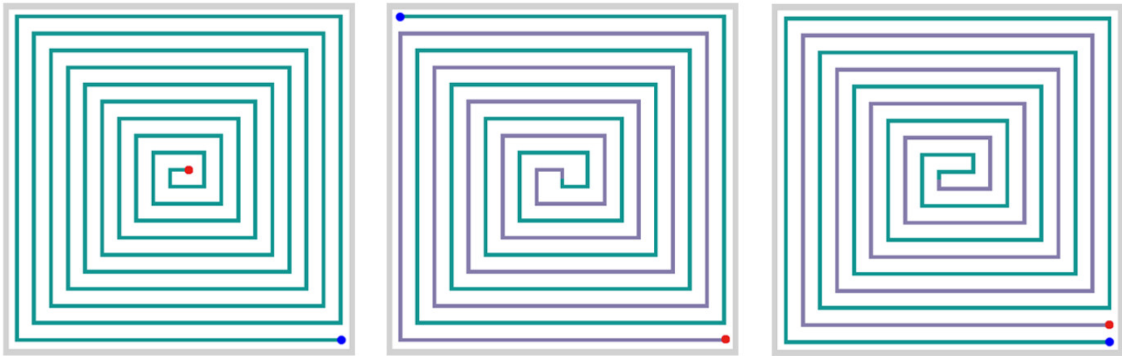

(a)螺旋线　　(b)费马螺旋线 1　　(c)费马螺旋线 2

图 2-3 螺旋线和费马螺旋线实例

2.2.4 螺旋线路径

如图 2.3(a)，螺旋线路径在数控加工型腔类结构中应用非常广泛[48]，Held 和 Spielberger 等人将一个复杂的二维型腔区域分割为相互独立的可用螺旋线填充的子区域[49]。该方法用单条螺旋线路径加工各子区域，路径的整体连续性较差。螺旋线路径在增材制造中应用较少，其主要原因在于螺旋线路径各项异性较差。增材制造对三维模型切片处理之后，如果相邻两层截面都用同样类型的螺旋线路径，会导致相邻层之间路径相互叠加，不利于打印模型横向方向的力学强度[43]。当然，这一问题可以通过在相邻切片层中应用不同的路径规划方法来改善。

2.2.5 空间填充曲线

空间填充曲线 (space-filling curve, SFC)，如图 2-2(c)，是填充二维区域一些短小的分形折线组成[51]，比如 Hilbert 分形曲线，Peano 分形曲线。空间填充曲线应用非常广泛，例如图像信息编码[52]，迷宫路径设计[53]等。空间填充曲线很早就被应用于增材制造的路径规划[54]。然而，空间填充曲线中频繁的方向转换，打印时间会相应的加长，并且打印质量也会降低。因此 SFC 曲线在商用的三维打印路径规划软件中实际应用较少。然而，空间填充曲线在类似的割草机路径规划中应用非常广泛[55]。割草机的路径规划问题主要考虑的是能够以尽量短的路径长度覆盖一个拓扑任意复杂的二维区域。

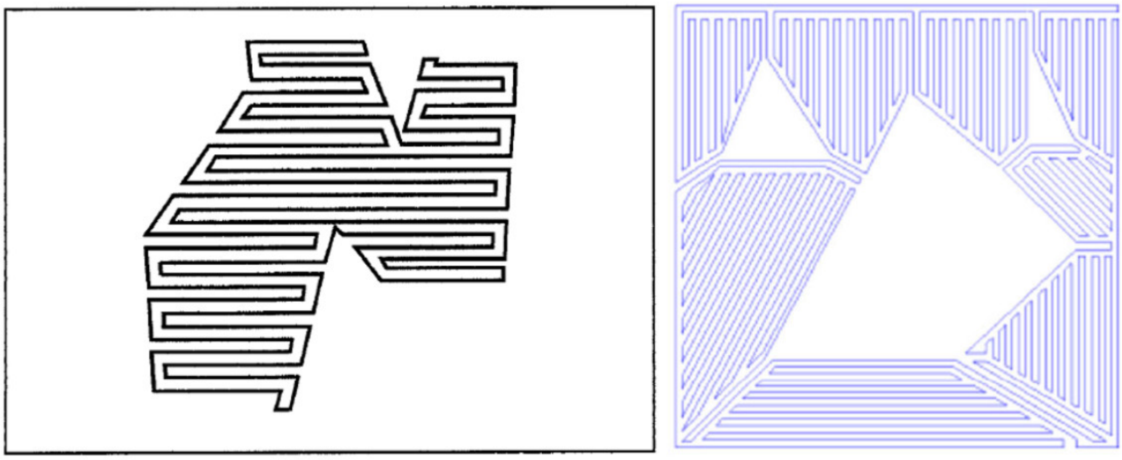

单调多边形子区域[15]　　　　凸多边形子区域[16]

图 2-4 基于区域划分的路径规划方法

2.2.6 基于区域划分的路径规划

为了改善增材制造路径规划的路径连续性，很多研究者提出了基于区域划分的路径规划方法。其基本思想在于将一个二维连通区域分解为多个可使用连续打印路径填充的子区域，将所有子区域连接后即可构成一条连续的打印路径[11]。Dwivedi 和 Kovacevic 等人将二维连通区域分解为独立的单调多边形，在每个单调多边形中生成封闭的平行扫描路径，在将各个相邻的路径连接为一条连续路径[15]，如图 2-4 左图。Ding 等人[16]对二维连通区域进行凸分解，每一个凸多边形区域对应一个最优的平行扫描路径方向，将所有凸多边形区域连接后即可得到一个连续的打印路径，如图 2-4 右图。然而这两种方法均只能够对多边形输入进行路径规划，对于有着平滑边界的图像，这两种算法均无法工作。

上述两种以提升路径连续性为目的的区域分解方法中，实质上分别利用了凸多边形和单调多边形适合连续平行扫描路径生成的特性。对于单调多边形区域，生成连续路径的平行扫描路径的方向是受限的；对于凸多边形区域，则可以在任何方向下生成连续的平行扫描路径。

本学位论文提出的路径规划方法同样采取“分而治之”的区域分割方法，不同之处在于，本学位论文不仅可以处理多边形区域，也可以处理平滑边界区域；拟在子区域中填充螺旋线路径。满足何种几何特性的多边形区域可以被一条螺旋线曲线填充，据本文所知，这个问题还未见前人进行过相关探索。

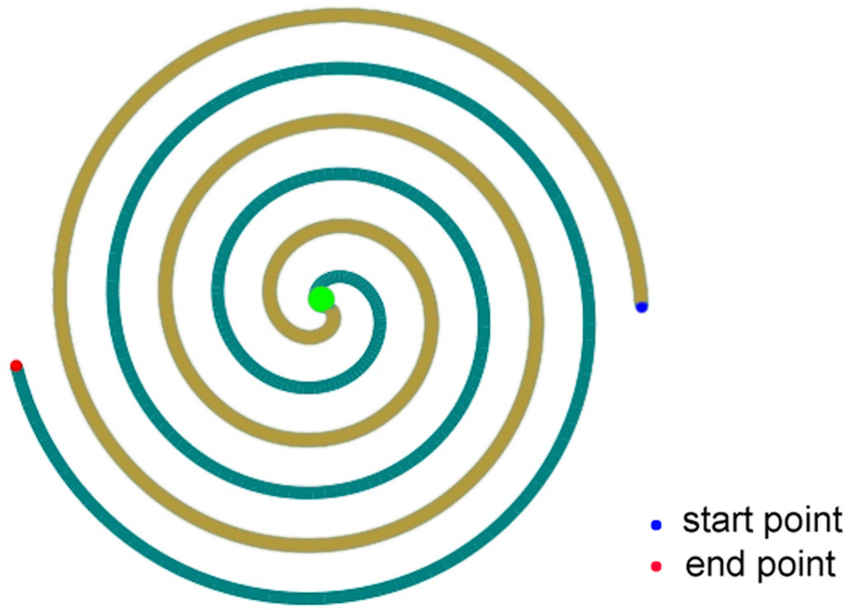

图 2-5 由两条相互间隔的螺旋线组成的费马螺旋线，
蓝色点和红色点分别为螺旋线路径的起始点，绿色点为费马螺旋线的中心点

2.3 费马螺旋线

费马螺旋线（Fermat spiral），由被称为“业余数学家之王”的法国著名数学大师 Pierre de Fermat 提出的一种螺旋线[56]。费马螺旋线是一种非常有趣的空间填充曲线，由两条相互间隔分布的子螺旋线组成，一条由外向内生成的螺旋线和一条由内向外生成的螺旋线，如图 2-5。本文拟将费马螺旋线作为一种新的基本路径式样应用于空间填充区域的生成中，分别介绍了费马螺旋线应用于空间填充曲线的优良特征，以及费马螺旋线的生成方法。

2.3.1 空间填充曲线特征

据我们所知，费马螺旋线还没有作为一种基本的空间填充曲线应用于增材制造的路径规划中。作为一种新的空间填充曲线，费马螺旋的优良特性在于：

1， 与轮廓平行方法类似，满足跟随区域边界生成的特点；

2， 一条费马螺旋线只在曲线中心由一个急转弯的硬拐角；

3， 费马螺旋线的两个末端点都位于区域边界外部，且末端点在区域边界上的位置可以任意变化，如图 2-3(b)和 2-3(c)；

4， 通过在将末端点首尾相连的方法，多条费马螺旋线可以形成一条连续路径；

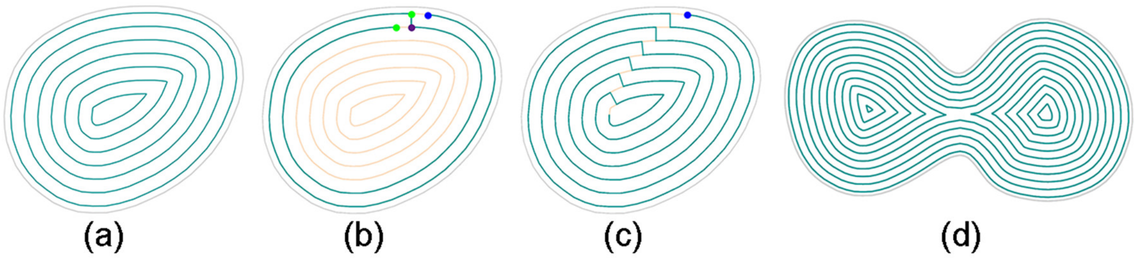

图 2-6 (a)为轮廓平行路径；取图(a)最外面的两层轮廓进行断开与重新连接，得到图(b)；重复这一过程得到图(c)所示的单螺旋曲线；从(a)到(c)展示了算法最常见的运行情况，实际的运行中会碰到图(d)的情况，即一个边界内包含多个中心；图(d)的区域属于非可螺旋的区域

2.3.2 生成方法

费马螺旋线的生成过程主要分为三个步骤，首先对于给定的二维轮廓区域，生成其对应的轮廓扫描路径，并将其与区域的欧氏距离场等值线相对应；然后将包含嵌套关系的等值线转换为螺旋线；最后从得到的螺旋线出发，生成费马螺旋线路径。在生成费马螺旋线的过程中，路径的起始点是可以在区域边界上任意选择。

不妨用符号R表示给定的二维区域，用符号∂R表示区域R的边界。以∂R为边界条件，通过欧几里得距离变换可在在区域R中计算距离标量场ϑ_R。标量场ϑ_R中任意点$p \in R$对应的标量值$\vartheta_R(p)$定义为点p到边界∂R的最短距离值。距离标量场ϑ_R中标量值为d的所有点p组成距离值为d的等值线。区域R的边界∂R可以说是值为 0 的等值线。根据打印喷嘴挤出熔融细丝的宽度w，在距离标量场ϑ_R中提取值为w倍数的等值线，如图 2-6(a)所示，这些等值线呈现相互独立相互嵌套的位置关系。

两条相邻的等值线可以通过先断开再重新连接形成一条连续路径，如图 2-6(b)。继续以这样的断开再连接的方式将所有相邻的等值线依次连接，生成螺旋线路径π，如图 2-6(c)。如果区域R的距离标量场ϑ_R只有一个局部极大值点，则定义该区域R为可生成单条螺旋线路径的区域，如图 2-6(c)。若距离标量场ϑ_R存在多个局部极大值点，则该区域R不能通过以上连接方式生成单条螺旋线路径，如图 2-6(d)。

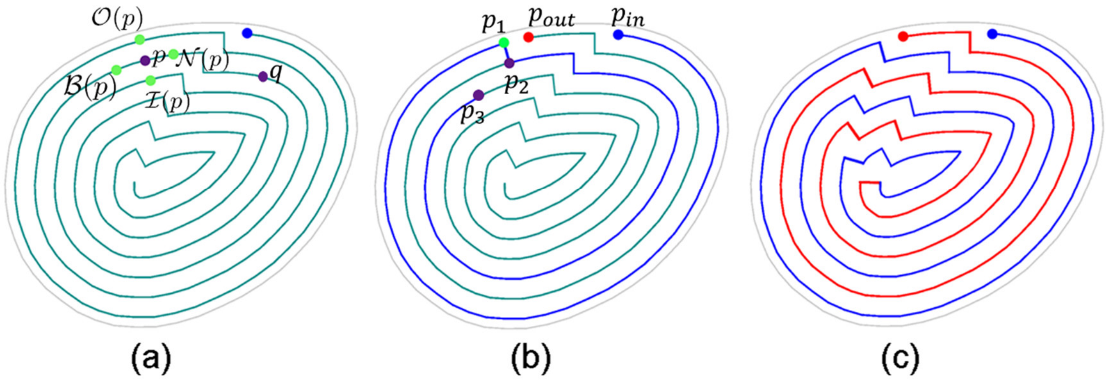

图 2-7 从螺旋线(a)出发生成费马螺旋线(c)，(a)螺旋线π上的任意点p及其相关的梯度前向点$\mathcal{L}(p)$，梯度后向点$\mathcal{O}(p)$，及沿着螺旋线π的前向点 B(p)，后向点 N(p)；(b)从点p_{in}遍历到$p_1 = \mathcal{B}(p_{out})$，跳转到$p_2 = \mathcal{L}(p_1)$继续遍历直到$p_3 = \mathcal{B}(\mathcal{L}(\mathcal{B}(p_1)))$；(c)费马螺旋线

费马螺旋线路径可以在上述步骤生成的单条螺旋线路径π的基础上生成得到。在从单条螺旋线到费马螺旋线的转换过程中，可以任意选择费马螺旋线的两个末端点在区域边界∂R上所处的位置。

为了便于描述这个转换过程，首先需要做一些符号定义。任取螺旋线路径π上一点$p \in \pi$，从点p出发沿着距离标量场ϑ_R正向梯度方向前进，与螺旋线路径π若存在交点，则交点用符号$\mathcal{L}(p)$表示。当点p非常接近距离标量场ϑ_R的中心位置时，该交点可能并不存在。相应的沿着反向梯度方向前进，与螺旋线路径π的交点为$\mathcal{O}(p)$。当点p位于螺旋线路径π最外围位置时，该交点$\mathcal{O}(p)$也可能不存在。新定义的这些交点$\mathcal{L}(p)$和$\mathcal{O}(p)$将作为新的连接点出现在费马螺旋线的生成过程中。

为了便于描述费马螺旋线的生成过程，不妨给螺旋线π上的点$p \in \pi$定义出前后位置关系。沿着距离场梯度变化为正的方向，定义螺旋线π的第一个点为路径π在区域边界处的末端点，最后一个点为接近距离标量场ϑ_R最大值处的另外一个末端点。对于螺旋线π上任意两点$p, q \in \pi$，若从螺旋线π首端点向末端点遍历过程中先遇到点p再遇到点q，则定义点p为点q的前向点，点q为点p的后向点。从螺旋线路径π上任意点$p \in \pi$出发，沿着π分别向前和向后行进w的距离，得到点$\mathcal{B}(p)$和$\mathcal{N}(p)$，如图 2-7(a)所示。

令p_{in}为螺旋线路径π的起点，假定费马螺旋线的终点为路径π区域最外围处的点p_{out}，如图 2-7(b)。从起点p_{in}出发沿着螺旋线路径π行进直到$p_1 = \mathcal{B}(p_{out})$，之后路径从点$p_1 = \mathcal{B}(p_{out})$向正梯度方向跳转到$p_2 = \mathcal{L}(p_1)$，继续沿着螺旋线$\pi$正方向行

进直到遇到点$p_3 = \mathcal{B}(\mathcal{L}(\mathcal{B}(p_1)))$，之后继续正梯度方向跳转，直到到达区域的中心。之后从螺旋线π位于区域中心的末端点出发沿着反梯度的方向将未遍历到的路径连接成为一条路径，最终生成费马螺旋线，如图 2-7(c)。

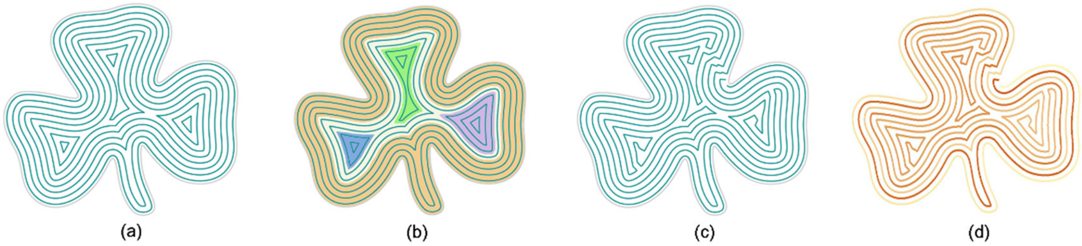

图 2-8 连通费马螺旋线的生成算法，(a)从区域距离标量场提取的等值线；(b)等值线被划分为四个可以生成费马螺旋线的子区域；(c)费马螺旋线连接为一条连续路径；(d)通过颜色平滑过渡渐变对连通费马螺旋线进行可视化展示

2.4 连通费马螺旋线

对于任意二维拓扑连通的区域，都可以生成连通费马螺旋线路径。本章将介绍连通费马螺旋线的具体生成算法。算法需要解决的核心问题在于如何巧妙的连接从区域R距离标量场ϑ_R中提取的等值线。对于距离标量场ϑ_R中只存在一个极大值点的区域R，可以直接应用上文描述的方法生成费马螺旋线。如图 2-8(a)，对于出现多个极大值点的距离标量场ϑ_R对应的区域R，基于对相邻等值线可连通性的分析，将区域R预分解为可生成费马螺旋线的子区域，如图 2-8(b)。在每个子区域内生成子费马螺旋线，并将这些子费马螺旋线连接起来形成一条连续路径，如图 2-8(c)。

打印喷嘴挤出熔融细丝的宽度w，定义了从距离标量场ϑ_R中提取的等值线的路径间距。本文通过调用 Johnson 等人的 Clipper 算法库[57]计算区域R的距离标量场ϑ_R，并从中提取路径间距为w的等值线集合$\mathcal{L}$。每条等值线标号为$C_{i,j}$，其中i表示该等值线到区域边界∂R的距离值：$d\left(\partial R, C_{i,j}\right) = (i - 0.5)w$；j表示该等值线在所有到边界$\partial R$的距离值为$d\left(\partial R, C_{i,j}\right)$的等值线中的索引值。比如，$C_{1,1}$通常代表区域边界$\partial R$本身，等值线$C_{i,j}$和$C_{i,j'}$到边界$\partial R$的距离相等，若$j \neq j'$，等值线$C_{i,j}$和$C_{i,j'}$在距离标量场中包含不同的局部极大值点。

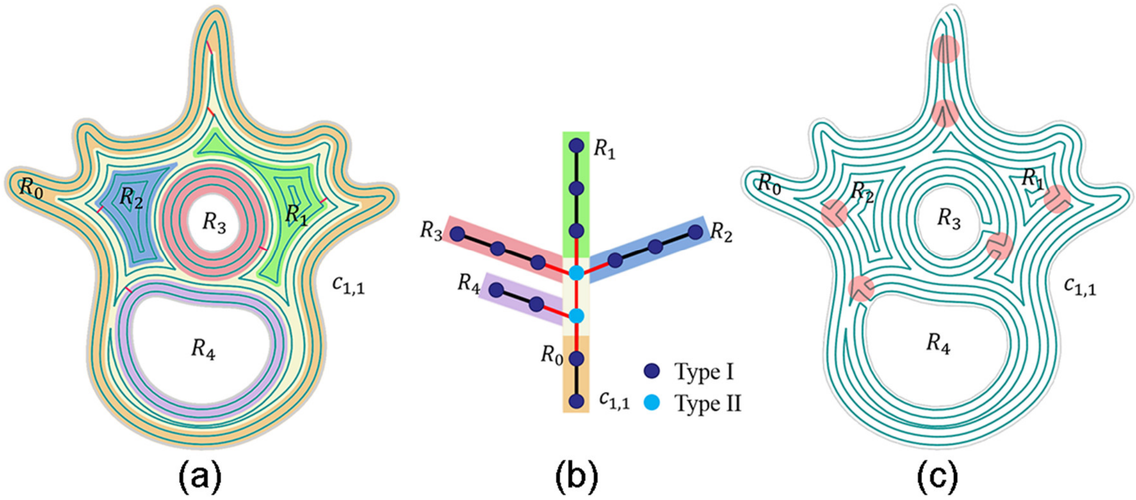

图 2-9 基于螺旋连通树生成连通费马螺旋线，(a)等值线被划分为五个可以生成费马螺旋线的子区域，红色短线段表示相邻两螺旋线的断开和重连接位置；(b)连通费马螺旋线；(d)五条子费马螺旋线连接形成一条连续路径

2.4.1 螺旋连通树

基于距离标量场ϑ_R中提取的等值线集合$\mathcal{L}$，构造一种称为“螺旋连通树”的树形结构$\mathbb{T}$。每条等值线$C_{i,j}$对应螺旋连通树$\mathbb{T}$的一个节点；若两相邻等值线$C_{i,j}$和$C_{k,l}$可以断开再连接的方式连接起来，则其对应螺旋连通树$\mathbb{T}$的两节点直接存在一条边。定义边的权重值为连接对应的两条等值线的花费大小。基于这样一个螺旋连通树$\mathbb{T}$，采用一种从低向上的遍历方式将所有的等值线连接为一条连续路径。

为了构造螺旋连通树$\mathbb{T}$，首先需要将等值线集合$\mathcal{L}$构造成为螺旋连通图$\mathbb{G}$。每条等值线$C_{i,j}$对应螺旋连通图的一个节点。定义两条相邻的等值线$C_{i,j}$和$C_{i+1,j'}$之间的“连通边”为：

$$\mathcal{O}_{i,j,j'} = \{p \in C_{i,j} \,|\, d(p, C_{i+1,j'}) < d(p, C_{i+1,k}), k \neq j'\},$$

其中，$d(p,C)$表示点p到等值线C曲线上的点的最近距离值。$\mathcal{O}_{i,j,j'}$定义了等值线$C_{i,j}$和$C_{i+1,j'}$上可以被断开再连接的路径部分。若$\mathcal{O}_{i,j,j'}$非空，则在螺旋连通图$\mathbb{G}$中$C_{i,j}$和$C_{i+1,j'}$对应节点之间添加一条边，边的权重定义为“连通边”$\mathcal{O}_{i,j,j'}$的长度值。权重值如此设置的原因在于期望可以尽量少的破坏长路径连续性。

带权重的螺旋连通图$\mathbb{G}$构造完成后，计算加权最小生成树（minimum-weight spanning tree, MST）[58]作为螺旋连通树$\mathbb{T}$。等值线$C_{1,1}$对应的节点定义为螺旋连通树的根节点，如图 2-9(b)。螺旋连通树$\mathbb{T}$中，定义所有度小于或等于两度的节点为

I型节点，大于两度的节点为II型节点，将相互邻接的I型节点进行组合。如图2-9(b)中形成五组节点组合，分组内部可生成一条费马螺旋线。II型节点对应的等值线将作为媒介路径，将各子区域费马螺旋线连接形成一条连续路径。

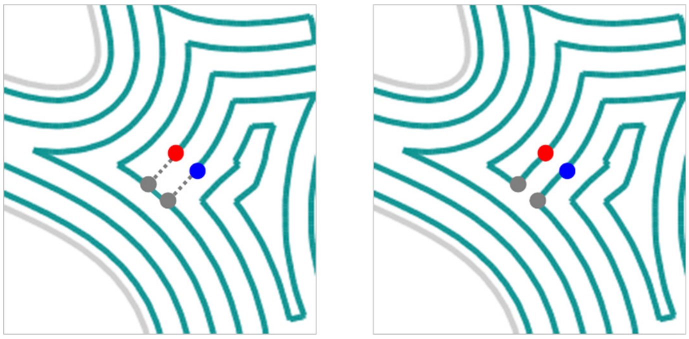

图 2-10 子费马螺旋线的生成

2.4.2 连通路径生成

为了生成一条连续路径，采用一种从低向上的方式从螺旋连通树$\mathbb{T}$的叶节点出发以根节点为结束，遍历螺旋连通树$\mathbb{T}$。在遍历过程中，存在两种断开和重连接操作，其中一种断开和重连接操作作用于I型节点分组对应的等值线区域内部，按照上文所述费马螺旋线的生成算法生成子区域的费马螺旋线，如图2-9的子区域R_0；另一种断开和重连接操作作用于生成的子费马螺旋线和II型节点对应的等值线之间。如图2-10所示，将子费马螺旋线的起始点与相邻的II型节点对应等值线的最近点相连。

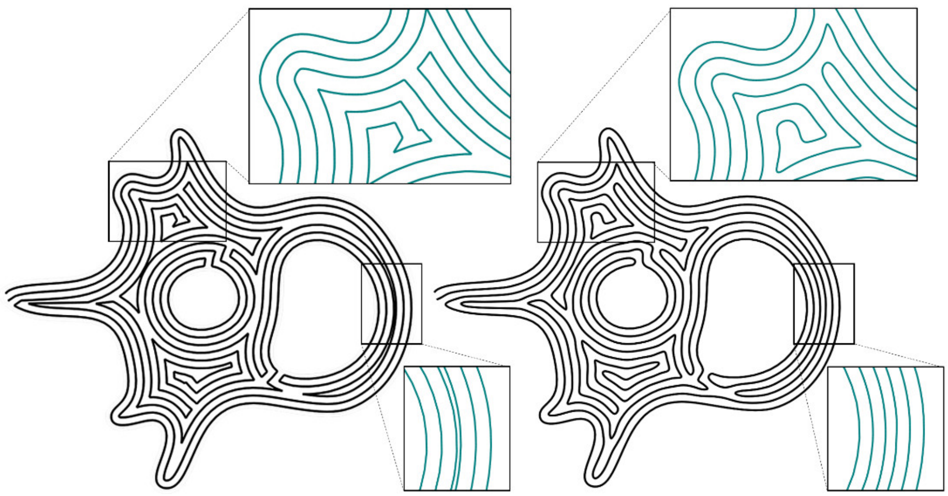

图 2-11 连通费马螺旋线的优化，

左图：优化前连通费马螺旋线路径；右图：优化后连通费马螺旋线路径

2.4.3 路径优化

至此生成的连通费马螺旋线路径已能够覆盖区域R且满足全局连续性。然而，当前的连通费马螺旋线只满足C^0连续，可能存在间距不均匀和路径不平滑的问题，如图 2-11 左图所示。作为一种后处理步骤，在路径间距一致的约束条件下，通过局部优化方法对初始化构造的连通费马尔螺旋线进行平滑化处理。如图 2-11 所示，左图为优化前的路径，右图为优化后的路径。

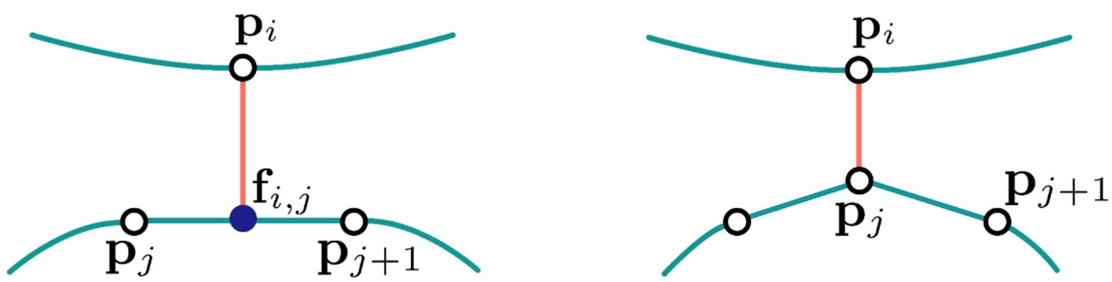

图 2-12 点p_i到邻接路径的最近点的两种情况，

左图：最近点处于邻接边上；右图：最近点为邻接路径顶点

基于连通费马尔螺旋线各处曲率动态选取采样点，目的在于在曲率大的地方多选取采样点，在曲率小的地方较少的选取采样点，选取的采用点为$p_1^0, \dots, p_N^0$。

在保持打印路径宽度一致的约束条件下，对采样点进行局部位置扰动，达到对生成路径进行平滑的目的。构造全局优化函数，包括三个惩罚项：用于对采样点扰动程度，平滑程度和间隔宽度保持程度进行惩罚；$f_{regu} = \sum_{i=1}^{N} \left| p_i p_i^0 \right|^2$为采样点扰动程度惩罚项，其中$p_1, \dots, p_N$为采样点，$\left| p_i p_i^0 \right|$表示边$p_i p_i^0$的长度；平滑程度惩罚项表示为：$f_{smooth} = \sum_{i=1}^{N-2} \| (1 - u_i) p_i + u_i p_{i+2} - p_{i+1} \|^2$，其中$u_i = \left| p_{i+1}^0 p_i^0 \right| / \left(\left| p_{i+1}^0 p_i^0 \right| + \left| p_{i+2}^0 p_{i+1}^0 \right| \right)$；

对于每个点p_i，存在其到邻接路径的最近点共分两种情况，一种为最近点为邻接路径边上一点，如图 2-12 左图；一种为最近点为邻接路径边上的顶点，如图 2-12 右图。如图 2-12 右图所示，若为第二种情况，最近点可表示为：

$f_{i,j} = \left(1 - t_{i,j}\right) p_j + t_{i,j} p_{j+1}$，由此，$t_{i,j} = \frac{\left(p_i - p_j\right)^T \left(p_j - p_{j+1}\right)}{\left| p_j p_{j+1} \right|^2}, 0 \le t_{i,j} \le 1$。

定义$\varepsilon = \left\{ \left(p_i, p_j, p_{j+1}\right) \right\}$。

若为第一种情况求得的最近定点p_j一定满足$0 \le t_{i,j} \le 1$，有$V = \left\{ p_i, p_j \right\}$。

定义间隔宽度保持程度的惩罚项为：

$$f_{space}=\sum_{(p_i,p_j,p_{j+1})\in\varepsilon}(|p_if_{ij}|-d)^2+\sum_{(p_i,p_j)\in V}(|p_ip_j|-d)^2。$$

综上所述，全局优化目标函数为：$\underset{p_1,\dots,p_N}{minimize}\, f_{requ}+\alpha f_{smooth}+\beta f_{space}$。

其中α为控制平滑程度的参数，β为控制间隔宽度保持程度的参数，一般取值为$\alpha=200,\beta=1.0$。

上述全局优化目标函数中同时含有离散成分(ε,V)和连续分量，比如曲顶点位置相关的非线性最小二乘惩罚项f_{requ}。依次分别对其进行迭代优化，当曲线顶点位置固定时，用上文描述的方法计算各顶点到邻接路径的最近点；当离散成分(ε,V)固定时，应用 Gauss-Newton 方法对优化目标函数求解。

在每次迭代过程种，Gauss-Newton 方法为各顶点计算位移量达到优化总体目标函数的目的。f_{requ}和f_{smooth}只依赖于点的坐标，因此维持之前的表达式即可。$|p_if_{ij}|$和$|p_ip_j|$都是非线性的，必须采用某种线性近似予以代替。令$e_j=p_j-p_{j+1}$，则$|p_if_{ij}|$被估计为：$|\overline{p_i}\overline{f_{i,j}}|\approx|p_if_{ij}|+g_{ij1}^Td_i+g_{ij2}^Td_j+g_{ij3}^Td_{j+1}$。其中，$g_{ij1}$，$g_{ij2}$和$g_{ij3}$定义为：$g_{ij1}=\frac{p_i-f_{ij}}{|p_if_{ij}|}$，$g_{ij2}=-(1-t_{ij})g_{ij1}-g_{ij1}^Te_j\frac{\partial t_{ij}}{\partial p_j}$，$g_{ij3}=-t_{ij}g_{ij1}+t_{ij}g_{ij1}^Te_j\frac{\partial t_{ij}}{\partial p_{j+1}}$。$|p_ip_j|$被估计为$|\overline{p_i}\overline{p_j}|\approx|p_ip_j|+g_{ij}^T(d_i-d_j)$，其中$g_{ij}=(p_i-p_j)/|p_ip_j|$。至此，最小二乘问题的优化目标可以写成：

$$\begin{aligned}&\sum_{i=1}^{N}|d_ir_i|^2+\alpha\sum_{i=1}^{N-2}\left||(1-u_i)d_i+u_id_{i+2}-d_{i+1}-r_i'|\right|^2\\&+\beta\sum_{(p_i,p_j,p_{j+1})\in\varepsilon}(g_{ij1}^Td_i+g_{ij2}^Td_j+g_{ij3}^Td_{j+1}-r_{ij})^2\\&+\sum_{(p_i,p_j)\in V}(|p_ip_j|+g_{ij}^T(d_i-d_j)-d)^2\end{aligned}$$

其中$r_i=p_i^0-p_i, r_i'=p_{i+1}-(1-u_i)p_i-u_ip_{i+2}, r_{ij}=d-|p_if_{ij}|, r_{ij}'$=d-$|p_ip_j|$.

通过对线性系统的求解上述最小二乘目标函数。令d_i^*为最优偏移量，下次迭代定点位置更新为$p_i\leftarrow p_i+d_i^*$。当$max_{1\le i\le N}||d_i||<10^{-6}$时，终止 Gauss-Newton 优化。每一次对顶点位置进行了优化，就必须重新计算邻近路径最近点。该过程交替进行，直到曲线位置的最大位移低于10^{-5}。通常只需要 4-8 次迭代即可完成整个优化过程。

2.5 实验结果和分析

为了充分验证算法的有效性，本章针对一系列具备不同凸度和亏格的二维截面区域生成连通费马螺旋线路径，并在路径几何特征，填充制造，实际的打印时间等方面，与经典的平行扫描路径和轮廓平行路径进行对比。

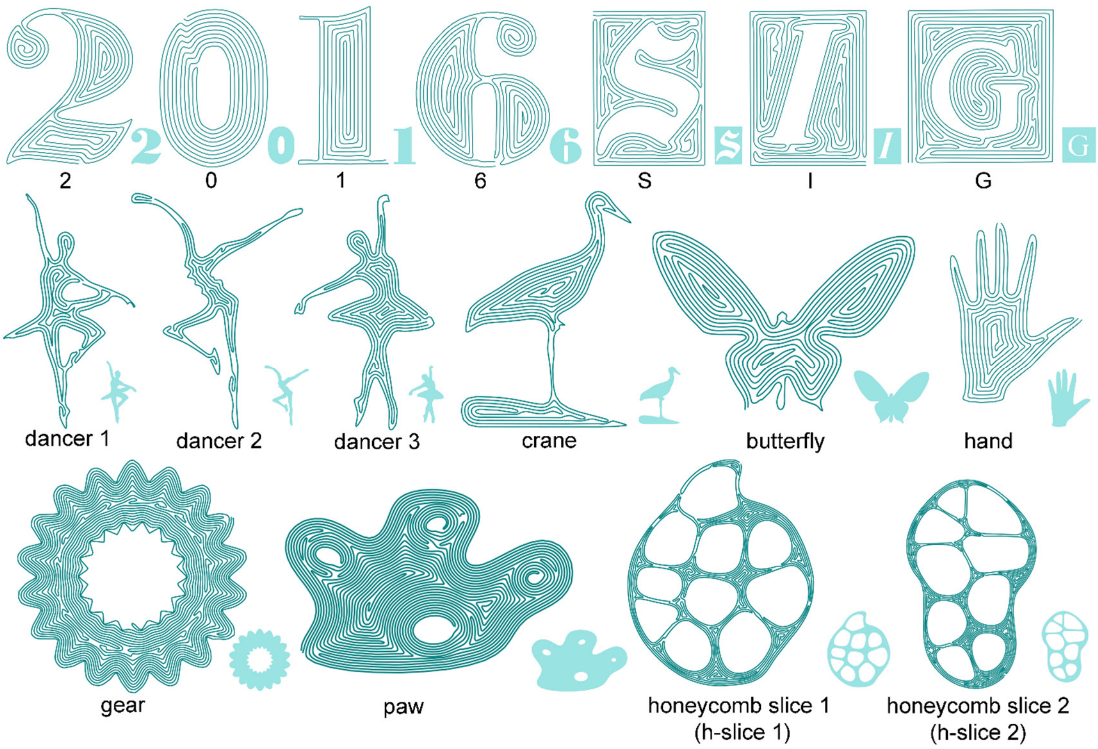

图 2-13 本文生成的连通费马螺旋线，每条路径右下角为打印截面区域

2.5.1 实验环境

实际打印实验在固件为 Marlin 1.1.0RC 的 RepRap Prusa i3 FDM 3D 打印机上进行。打印结果和分析使用默认的参数设置，打印路径宽度为 0.4mm，单层厚度为 0.3mm，喷嘴的最大进给速度为 80mm/s，打印材料为 PLA，打印线材直径为 1.75mm，出料率为 100%。打印路径编写成 Gcode 代码的形式输入打印机。

2.5.2 路径生成

对于体现著差异的内部或外部结构的二维截面区域，图 2-13 展示了本文算法生成的连通费马螺旋线路径。值得一提的是，图 2-13 两个高亏格切片区域和图 2-1 中的“小猫”的打印截面区域，来自 Lu 等人在 ACM SIGGRAPH 2014 大会上发

表的基于蜂窝状多孔结构的三维打印内部支撑结构优化设计的文章[59]。算法生成的所有费马螺旋线路径，遵循统一的参数设置，无需对特定输入区域进行逐一调节。

Input	#segZ	#segC	%stZ	%stC	%stF
dancer 1	22	14	5.87%	1.40%	**1.38%**
dancer 2	19	10	6.58%	1.55%	**1.08%**
dancer 3	21	13	4.11%	1.19%	**0.81%**
crane	8	17	4.86%	**0.46%**	0.93%
butterfly	16	24	1.81%	0.83%	**0.52%**
hand	9	11	4.84%	1.07%	**0.56%**
gear	51	105	1.18%	2.11%	**0.23%**
paw	20	55	1.25%	0.51%	**0.31%**
h-slice1	53	58	4.35%	1.08%	**0.81%**
h-slice2	47	56	5.12%	0.88%	**0.70%**

表 2-1 连通费马螺旋线路径（F），平行扫描路径（Z），

轮廓平行路径（C）在路径段数（#seg），硬拐角点比例（%st）方面的对比结果

本章中展示所有的平行扫描路径和轮廓平行路径，都来自于一款业界非常知名的三维打印路径规划软件 Slic3r[60]。表 2-1 给出了连通费马螺旋线路径，平行扫描路径和轮廓平行路径在路径段数，硬拐角点比例方面的对比结果。表 2-1 中并没有给出连通费马螺旋线路径的路径段数，因为本文提出的连通费马螺旋线具有全局连续的特征，路径段数都为 1。

Input	#P	#R	CFSt (s)	OPt (s)	Total (s)
dancer 1	4	31	0.25	1.676	1.926
dancer 2	6	27	0.297	1.59	1.887
dancer 3	4	33	0.203	7.085	7.288
crane	2	42	0.125	1.917	2.042
butterfly	4	51	0.359	4.479	4.838
hand	1	30	0.125	7.277	7.402
gear	19	143	0.766	8.978	9.744
paw	8	147	0.813	9.429	10.242
h-slice 1	22	148	0.834	7.092	7.926
h-slice 2	22	145	0.95	7.412	8.362

表 2-2 路径统计信息和算法运行时间，包括区域距离标量场极大值点个数（$\#P$），

新连接点的个数（$\#R$），路径初始构造（CFSt(s)）和优化阶段（OPt(s)的运行时间

表 2-1 中报告的硬拐角点比例的计算方法为，首先沿着路径π均匀采样 50000 个点p。对于每个点p，在一个半径为$0.2mm$的圆内计算其积分曲率[61]。本文中定义积分曲率为相关小圆中较小部分的面积小于30%的点为硬拐角点。表 2-1 中给

出了如此定义的硬拐角点在所有 50000 个采样点中的比例。可以看到，本文提出的费马螺旋线路径硬拐角点的比例显著低于平行扫描路径，与轮廓平行路径相比也具有相当的可比性。

对于图 2-13 中的部分路径，表 2-2 给出了算法运行时间，包括路径初始构造的时间和优化阶段所用的时间。与此同时，表 2-2 还报告了路径生成过程中的统计信息，涉及到区域距离标量场极大值点个数，生成过程中新连接点的个数。连通费马螺旋线的生成算法中的初始构造阶段的算法用 C++语言实现，路径优化部分的算法用 MATLAB 程序实现。表 2-2 中程序运行时间数据是在一台 16GB 内存的 Intel® Core™ i7-6700 CPU 4.0GHz 台式机上测试得到的。

2.5.3 填充质量

由于路径间距分布的不均匀性，在打印过程中往往会发生欠填充(under filling)和过填充(over filling)的现象。欠填充和过填充的现象在实际打印的成品中非常难以量化，本文采用一种较为简单的几何估计的方法，展示连通费马螺旋线路径在欠填充和过填充方面的表现。沿着路径曲线在截面区域中拓展出宽度w，将路径相交的部分记为过填充的区域，没有被加宽路径覆盖到的区域记为欠填充的区域。

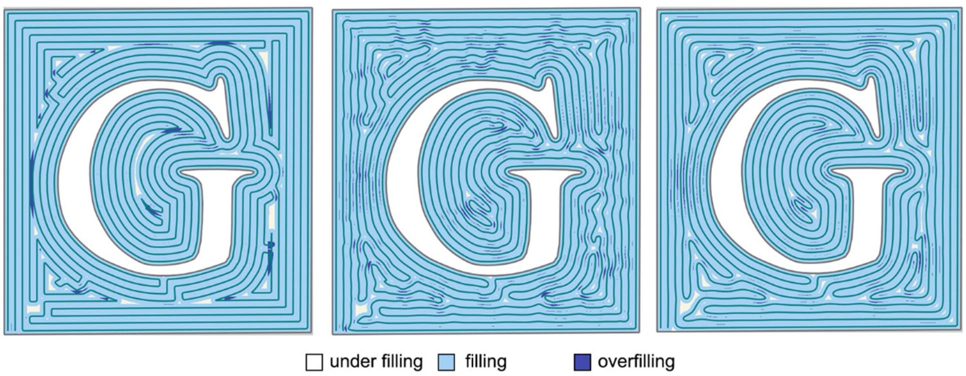

图 2-14 连通费马螺旋线的欠填充（under filling）和过填充（overfilling）区域

左图：路径优化之前；中图：路径优化中只考虑均匀路径间距的约束；

右图：路径优化中同时考虑均匀路径间距和平滑性的约束

如图 2-14 分别展示了路径优化之前，路径优化中只考虑均匀路径间距的约束，以及路径优化中同时考虑均匀路径间距和平滑性的约束，三种情况下对应的欠填充和过填充情况。可以发现，路径优化中的平滑项，会增加欠填充区域的面积，尤其在路径拐角区域。

总的来说，路径优化步骤往往会增加欠填充并减少过填充现象。当前的路径优化方案，由于有限的曲线移动范围设定并不能填充所有的路径间隙。例如，曲线不能被拉长以减轻底部填充。在尖角和转弯附近，在曲线的平滑性和路几个间距之间需要做出权衡。由于欠填充区域往往较少出现并且相互分布距离较远，因此一种允许曲线拉伸的算法，可能会实现更好的效果，这也是本文未来的研究工作之一。

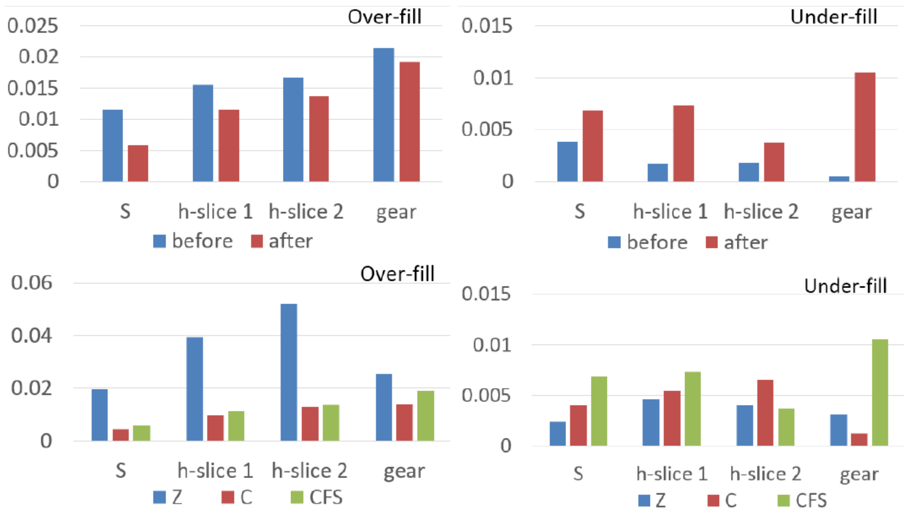

图 2-15 上图：四种连通费马螺旋线曲线优化之前和之后的欠填充和过填充统计信息对比，下图：三种路径的欠填充和过填充统计信息对比

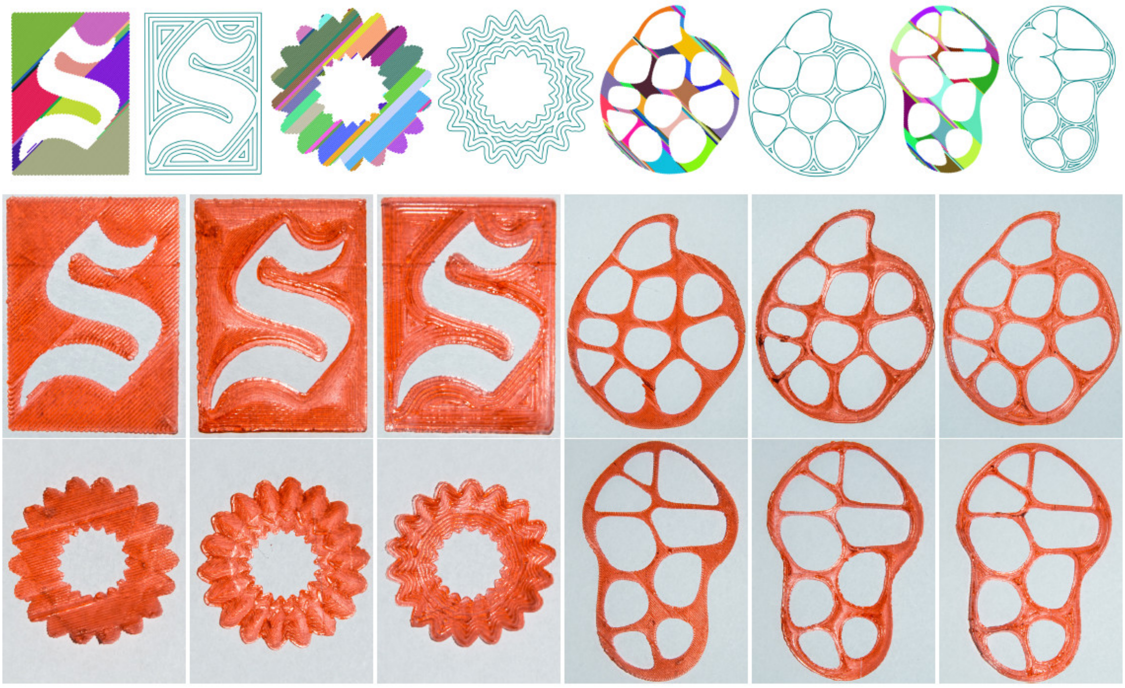

图 2-16 三种路径实际打印切片的照片对比图

2.5.4 外观质量

图 2-13 中四种二维区域（‘S’, gear, 两个蜂窝状支撑结构切片），图 2-16 给出了分别用三种路径进行打印填充的切片照片。图 2-15 左下角和右下角的柱状图，分别绘制了四种二维区域种生成的三种路径的欠填充和过填充质量的统计数据。

在切片的外观上来看，平行扫描路径的切填充质量较好，并且喷嘴挤出的材料填充的也比较均匀。然后，平行扫描路径在区域边界处的填充质量较差，出现很多肉眼可见的锯齿状结构。另外两种路径则在区域边界处的填充质量较好。另一方面，由于平行扫描路径中有很多相互断开的路径段，在切片照片中可以看到在路径连接处的填充质量不是很好。如图 2-15，与另外两种路径相比，平行扫描路径的过填充的过高，一个可能的原因在于 Slicer 生成的平行扫描路径在区域边界处的距离略小于$0.5w$，从而导致较高的过填充率。

对于轮廓平行路径，明显的可以看到在区域距离标量场的极大值处以及轮廓邻接区域附近的填充质量不是很好。相比之下，连通费马螺旋线路径的填充质量整体上来说更好一些，打印切片中肉眼可见的瑕疵更少一些。如上文分析的那样，由于当前路径优化部分的问题，连通费马螺旋的欠填充率会比较高，有机会在未来工作中加以改进。此外，需要额外说明的是三维打印机本身在机械结构控制等方面的缺陷，也会可能反应在打印切片的视觉外观质量上。

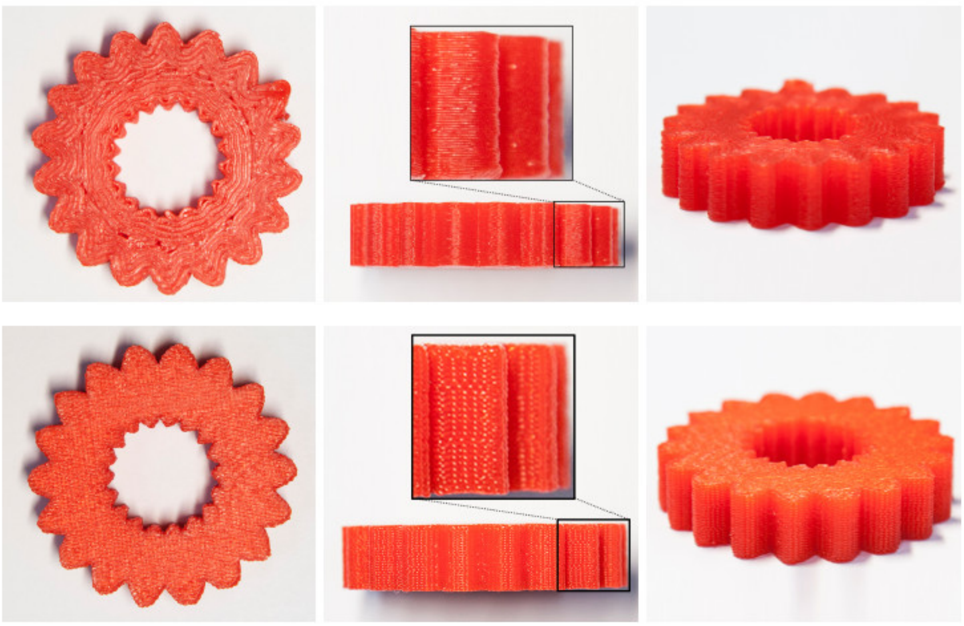

图 2-17 连通费马螺旋线（上）和平行扫描路径（下）的多层打印模型

图 2-17，展示了连通费马螺旋线和平行扫描路径的多层打印切片。该多层打印模型，由 50 层图 2-13 中的“gear”区域中生成的连通费马螺旋线和平行扫描路径打印生成，最终的打印成品高约 10mm。对于连通费马螺旋线，从图中可以明显看到欠填充现象。产生这一现象的原因上文做出了相关分析。对于连通费马螺旋线，如图 2-17 中的下图所示，内部填充质量较为致密，可能的原因在于 Slicer 生成的平行扫描路径在相邻层的方向是交错规划的。从侧视图来看，连通费马螺旋线的表面质量更为平滑。当然，平行扫描路径的外表面打印质量可以通过先在区域轮廓的最外部区域生成几条轮廓平行路径加以改善。

2.5.5 打印时间

应用三种路径规划方法，在 RepRap Prusa i3 FDM 3D 打印机上打印五种 2D 轮廓区域，图 2-18 展示了记录的实际打印时间。可以看到，连通费马螺旋线的打印效率普遍较高。对于简单形状的 2D 轮廓区域，平行扫描路径具备一定的竞争优势。然而随着 2D 轮廓区域复杂性的提高，连通费马螺旋线的优势越来越明显。而轮廓平行路径由于过于频繁的喷嘴开关操作，需要花费很多的打印时间。

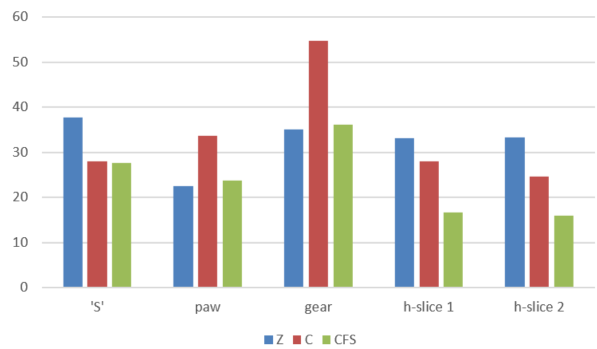

图 2-18 三种路径实际打印时间的比较

2.5.6 迷宫路径

如图 2-19 中，将连通费马螺旋线与一种通过随机演化生成的曲线做了对比[53]。结果变得更加直观如果通过更好的一致性来奖励进化，则可比较具有输入形状边界的曲线。 然而，曲线演化的方法将曲线路径内向侵蚀，因此它不太可能像本文提出的费马螺旋线一样能够同时保持平滑性和具备跟随边界生成的特征。 而且，曲线的局部随机扰动可能会导致更多的硬拐角出现。

图 2-19 迷宫路径对比，左图：本文生成的连通费马螺旋线路径；
右图：Pedersen 和 Singh 等人生成的迷宫路径[53]，需要说明的是右图中的外边界轮廓是迷宫路径的输入并属于文章[53]生成的迷宫路径

2.6 本章小结

本章将费马螺旋线引入到空间填充曲线的生成中。详细阐述了费马螺旋线作为一种新的空间填充曲线基础图案式样的优良特性，并提出了一种从区域距离标量场提取的等值线生成螺旋线的算法，进而描述了一种连通费马螺旋线生成算法。为了进一步优化生成路径的平滑性和路径间距均匀性的特征，提出一种后处理步骤，在路径间距一致的约束条件下，通过局部优化方法对初始化构造的连通费马尔螺旋线进行平滑化处理。在实验结果方面，将连通费马螺旋线应用到三维打印的截面填充路径规划中，并与现有的三维打印路径进行比较，证明应用连通费马螺旋线路径规划算法，能够显著提升打印质量并降低打印时间。

第3章 减材制造的路径规划

3.1 引言

与增材制造相比，减材制造是一种历史非常悠久的制造工艺。数万年前还处于茹毛饮血时期的人类，用敲击的方式将石块多余的部分去除，制作趁手的工具从事各种狩猎或农业生产活动，可以说就是最早期的减材制造过程。上个世纪 40 年代，随着第一台手动控制机床的诞生，“减材制作”进入数控加工的时代。数控加工按照工艺分类可以分为车，铣，刨，磨。

由于具备加工自由度高的优势，其中的铣削加工最常用于复杂自由曲面的加工。数控加工的加工流程，包括粗加工，精加工和后清理。该加工过程中的每一阶段都需要进行相应的路径规划，路径规划的好坏不仅直接影响最终的加工质量的加工效率，还影响刀具的使用寿命等因素。

本学位论文关注复杂自由曲面的精加工阶段的路径规划问题，需要考虑到的核心约束有规划路径的连续性，平滑性以及等残留高度的特性。本章拟将前一章提出的满足全局连续性和平滑性的连通费马螺旋线，应用于数控加工路径规划中，并拓展其满足等残留高度的特征，如图 3-1 所示的等残留连通费马螺旋线。我们将生成等残留路径规划的约束，转化成对一个自适应距离标量场的计算中。最终，通过实际的加工实验与已有的路径规划方法对比表明，本文方法可以在满足加工质量的前提下显著提升加工效率。

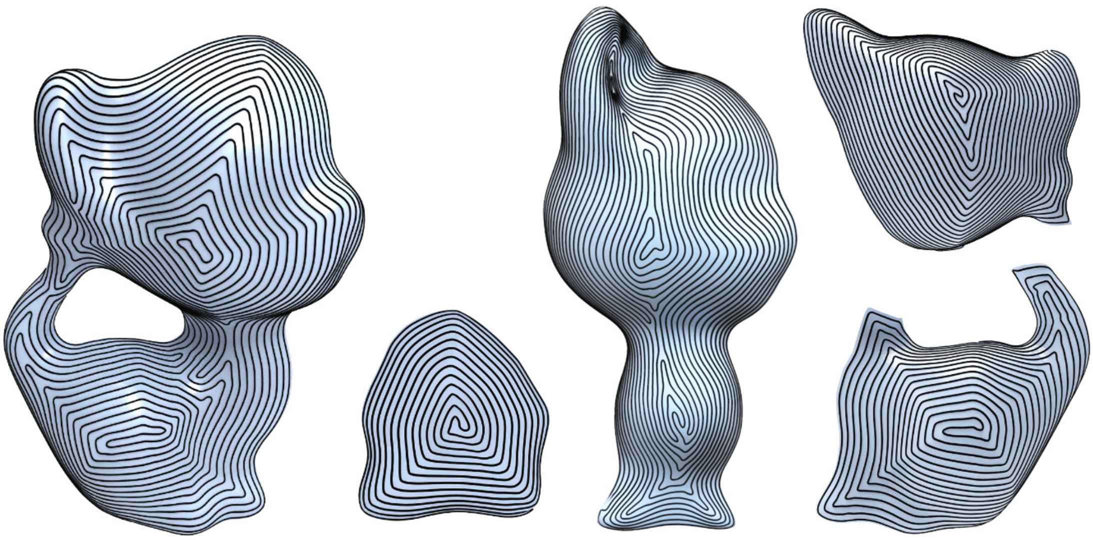

图 3-1 等残留连通费马螺旋线

3.2 相关工作

对于复杂自由曲面的数控加工的路径规划，已经出现了众多面向数控加工的路径规划，相关工作部分只是列举其中最重要的一些代表工作和方法。面向数控加工的路径规划的详细综述文章，参见[13][82-84]。

已有工作可以粗略的分为参数法和导动面法[62]。参数法，通过某种参数化方法将三维自由曲面映射到二维平面区域，先在二维平面区域进行路径，之后将生成的规划路径反向转换到原三维自由曲面[63]。导动面法，借助一系列预先计算的“导动”曲面，通过与原自由曲面投影或相交操作计算刀具路径。在机械加工领域，最常用的导动面法为等截面法，借助一组相互平行的空间截面截取待加工曲面及其偏置面，获得的交线轨迹即为刀触点轨迹，与偏置面的交线为刀位点轨迹[64]。等截面法中的平行截面的朝向的优化计算，与增材制造中切片方向的计算类似[65]，将会影响后续的路径规划。

3.2.1 路径基本式样

图 3-2 数控加工常用路径基本式样

关于路径规划的基本式样，与增材制造对照来看，平行扫描路径[66]，轮廓平行方法[67]和空间填充曲线也比较常见[68-69]。如图 3-2，平行扫描路径根据走刀方向是否存在往复，可分为单方向路径和往复方向路径，广泛应用于工业 CAM 系统中[79-80]。平行扫描路径，一般具有计算便捷和鲁棒性好的优点，缺点在于存在很多小短边和剧烈拐点，影响加工效率和加工质量。轮廓平行方法，由加工曲面边界的偏置生成[67]，优势在于生成的路径光顺性较好，在几何特征上较为平滑；缺点在于计算复杂性比较高且路径不连续，包含大量的进退刀。空间填充曲线，已有方法主要是利用分形理论生成能够遍历整个曲面的曲线，优点在于有很好的连续性和参数区

间上分布的均匀性，能够有效减少抬刀次数，消除切削过程中的空行程；缺点是轨迹频繁换向，在加工过程中影响加工效率和表面质量。如上一章相关工作部分所述，螺旋线路径在增材制造中应该并不广泛。然而，螺旋线路径[70-71]在数控加工中应用则广泛得多，尤其应用于三轴数控机床加工“型腔”结构。

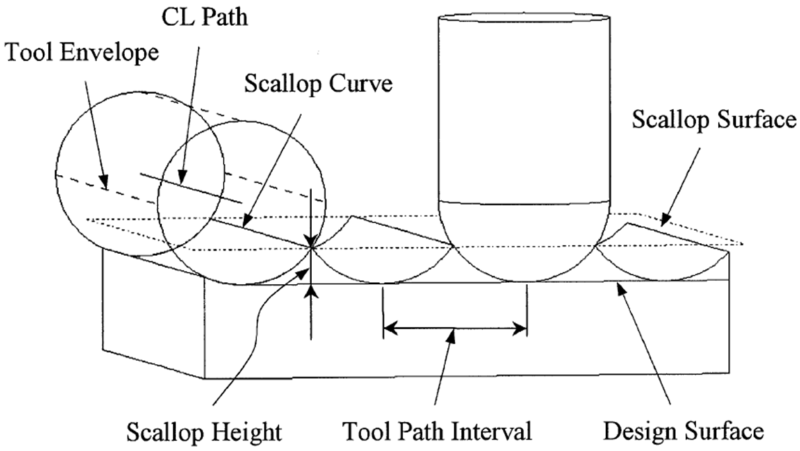

图 3-3 数控加工曲面的几何描述[81]，
相邻球头刀具路径切削行后遗留的未加工部分称为加工残留（scallop curve）

3.2.2 等残留高度

数控加工路径规划需要考虑的主要几何特征有路径的平滑性，连续性，以及均匀残留分布相关的路径间距约束[13]。铣削加工中，通常用最大残留高度来表征用户预期的表面加工质量，即要求加工完成后曲面上剩余残留的高度不能超过设置的最大残留高度[72]，如图 3-3。铣削残留高度与规划路径的路径间距是直接相关的。增材制造路径规划中要求路径间距一致，不均匀的路径分布会导致欠填充或过填充的问题。数控加工中的“欠填充”意味着由于路径间距过大分布过于稀疏，导致刀具切削不到位，遗留过多的残留；而“过填充”在铣削加工中对应着“过加工”，意味着加工路径过于致密而重复，影响加工效率的提升。最理想的情况为，加工完成后曲面上遗留的残留高度恰好等于最大残留高度，这种路径被称为等残留路径[71]。等残留路径可以有效的避免刀具重复走刀过程，加工效率和加工质量都得到很大提高。大部分等参数法和等截面法的方法，都不满足等残留高度的约束，在待加工曲面生生成的路径只有少部分能接近残留高度的约束上限，因此极大的限制的加工效率的提升[13]。

3.2.3 连续性和平滑性

对于高速铣削加工（high-speed machining, HSM），路径的连续性和平滑性相较于增材制造对整个加工效率和质量的影响更大。在 HSM 的高进给速度设置下，任何的“撤刀”，“回刀”操作和刀具通过硬拐角都会不可避免的产生减速过程，严重影响加工质量和效率[71][73]。以优化路径的平滑性和连续性为目标，数控领域出现了很多应用费马螺旋线或双螺旋曲线的工作[70] [71] [74] [75]，但是这些工作都没有考虑等残留高度的约束。已有的等残留高度方法[76-78]大多生成的是平行扫描路径或轮廓平行路径。据我们所知，本文是第一次尝试提出一种应用费马螺旋线的等残留高度路径规划算法。

3.3 等残留连通费马螺旋线

对于增材制造的路径规划，上一章提出了一种满足全局连续性和平滑性的连通费马螺旋线路径。本文探索了连通费马螺旋线的三维形式，将二维平面的连通费马螺旋线生成算法拓展到三维自由曲面上，提出了一种路径间距可变的连通费马螺旋线生成算法——等残留连通费马螺旋线。

为了获得均匀分布的残留高度，自由曲面上的路径间距需要根据相邻路径对应点处的方向曲率去调节[85]。针对用户指定的最大残留高度，自由曲面不同采样点处的方向曲率对应不同的路径间距约束，本文将自由曲面各采样点不同的路径间距约束，统一在一个约束相关的距离标量场的迭代求解中。从该约束相关的距离标量场中抽取出残留高度等值线，恰恰满足均匀残留高度的路径分布约束，并将提取的等值线连接为连通费马螺旋线，最后对生成的连通费马尔螺旋线进行平滑处理。本节将具体描述等残留连通费马螺旋线的生成过程。

等残留连通费马螺旋线路径规划算法，主要分为三个步骤：1) 给定连通的自由曲面，计算距离标量场，所述距离标量场满足均匀残留高度约束；2）提取所述距离标量场中的等值线，生成连通费马螺旋线；3）在最大残留高度约束下，对生成的连通费马尔螺旋线进行平滑处理。其中步骤 2 主要通过将上一章连通费马螺旋线的算法拓展到三维曲线实现的，具体算法细节请参见第二章[74]。下文将主要对步骤 1 和步骤 3 进行详细描述。

对于步骤 2 中费马螺旋线的生成算法，如图 2-7 所展示了算法导致在初始的费

马螺旋线生成阶段就出现很多 90 度的硬拐角，只能通过后续的路径优化步骤进行处理。这些硬拐角主要出现于断开和重新连接相邻的两封闭等值线路径的过程时，用小短线直接连接的方式。在费马螺旋线生成过程中用短斜线代替短直线连接，能够有效的减少费马螺旋线初始构造过程中产生的硬拐角数量，经过路径优化之后的连通费马螺旋线路径明显取得了更好的平滑性效果，如图 3-4 的左图展示了上一章费马螺旋线生成算法生成的路径，右图展示了当前算法生成的路径。

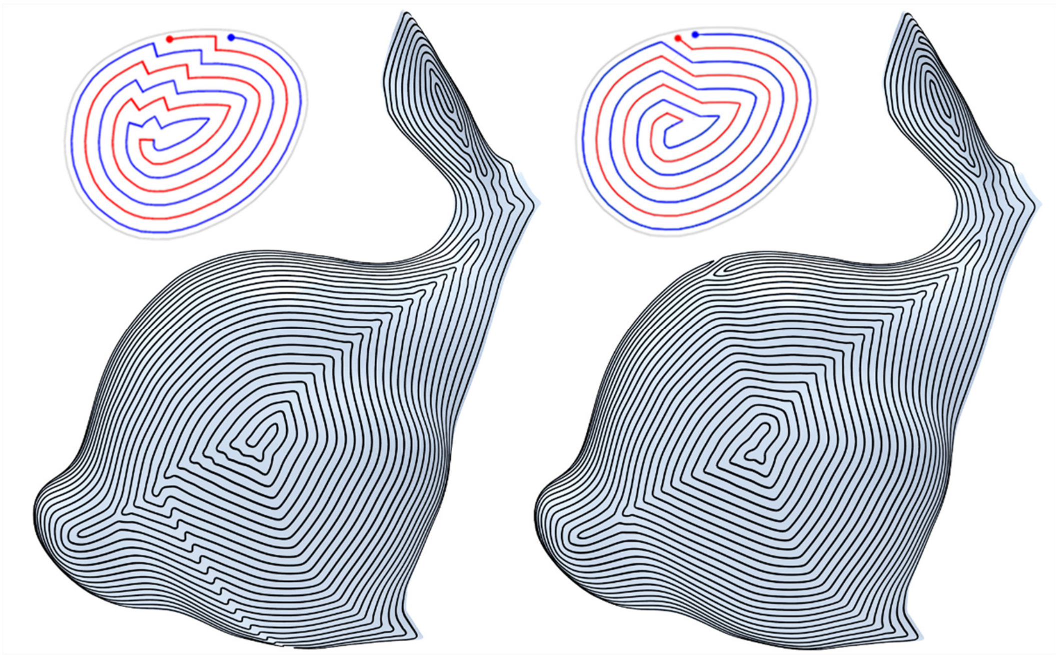

图 3-4 费马螺旋线生成过程中用短斜线代替短直线连接

左图：直角边连接生成的连通费马螺旋线；右图：斜线边生成的连通费马螺旋线

3.3.1 残留距离场

如上文所述，在铣削精加工过程中残留高度与相邻路径对应点处的方向曲率存在一一对应的对应关系[85]。给定自由曲面S，令p为曲面S上铣削路径Π上的某采样点，点p过路径Π切线的垂直方向的方向曲率记为$G(p,\Pi)$。Kim 等人指出[85]，为了满足用户指定的残留高度h，点p处的刀具路径间距$\mathrm{g}(p,\Pi)$为：

$$\mathrm{g}(p,\Pi)=\sqrt{\frac{8hR_{cutter}}{1+R_{cutter}G(p,\Pi)}},R_{cutter}\gg h$$

其中，h为最大残留高度，R_{cutter}为球头刀刀头半径，$G(p,\Pi)$为通过点p垂直于路径Π前向切线的方向曲率，$\mathrm{g}(p,\Pi)$为曲面采样点p在最大残留高度h约束下，通过

刀具路径Π的路径间距。

等残留高度的约束，被转化为对一个自由曲面S的方向张量场G相关的距离标量场的迭代求解中，通过提取该距离标量中的等值线为初始的计算连通费马螺旋线的初始轮廓平行路径。一旦该距离标量计算完成，自由曲面S的区域轮廓∂S即为零等值线，其他等值线通过依次增加与边界的距离值从距离标量场中提取得到。

很容易想到 fast marching 方法看起来也可以用于提取满足等残留高度的等值线路径，由当前的等值线$g|L_i$可以通过逐点向内偏置遍历的方法生成下一条等值线$g|L_{i+1}$。然后这种方法往往并不稳定，由于缺少全局性，直接由上一条等值线生成的下一条等值线$g|L_{i+1}$常需要经过裁剪处理，而且在这一逐步生成的过程中容易产生累计误差。另一方面，在从等值线$g|L_i$生成 $g|L_{i+1}$的过程中，每个采样点向内偏置距离的计算需要依赖于$g|L_{i+1}$，然而$g|L_{i+1}$等值线还未生成。在这种状态下，只能采取某种近似计算方法不可避免的会引入误差。本文采用一种迭代的方式计算一种具有全局性的满足残留高度约束的距离标量场，直接从得到的距离标量场中提取等值线即满足等残留高度的约束。

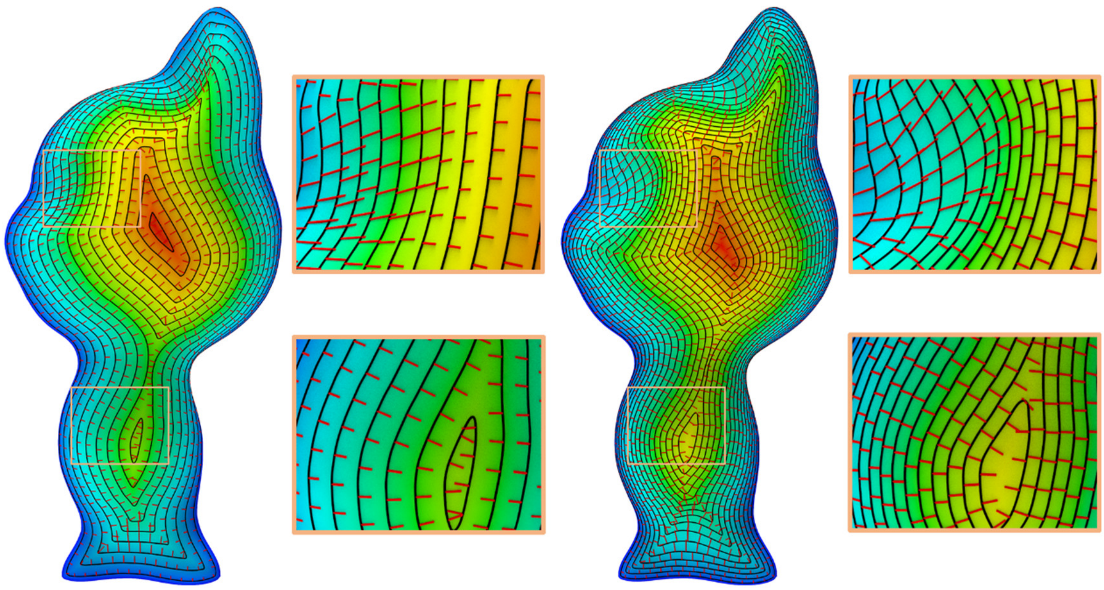

图 3-5 等残留高度约束相关的距离标量场的迭代计算,

左图：测地距离场的等值线；右图：迭代后等残留高度约束相关的距离标量场等值线；

图中红色短线的可视化了曲面上各采样点的理想路径间距

以自由曲面S的区域边界∂S为边界条件，计算得到曲面S内部各采样点到边界∂S的测地距离，由此形成了曲面S的一个测地距离场。从该测地距离场中提取的等

值线两两间的路径间距是一致的，但这并不满足等残留高度的要求。我们的基本思路为将曲面S各采样点p_i的理想路径间距$\mathrm{g}(p,\Pi)$，作为某种约束加入到测地距离场的计算中，生成一种等残留高度约束相关的距离场。距离场中采样点p_i的梯度方向作为计算理想路径间距$\mathrm{g}(p_i,\Pi)$所用的方向曲率的方向。在极短的时间周期内热量传播的梯度场与测地距离场的梯度一致，基于该理论，Crane 等人对于网格曲面S上的测地距离计算，通过求解一个偏微分方程（PDE）能够很好的求解近似测地距离场[86]。受到 Crane 等人工作的启发，本文定义了一个考虑等残留高度约束的偏微分方程：

$$(\mathrm{A}-\mathrm{t}L_c \otimes H)\mu=\delta_\gamma$$

其中，A为描述三角面片面积的对角矩阵，$A^{-1}L_c$定义了拉普拉斯矩阵，L_c描述了三角网格点邻接关系的对角矩阵，δ_γ为初始热量分布的边界条件。H与L_c一样也是三角网格点邻接关系的对角矩阵，H为一个融合了各采样点p_i理想路径间距$\mathrm{g}(p_i,\Pi)$信息的对角矩阵，H矩阵的每一项$H_{i,j}$描述三角网格采样点p_i和p_j的邻接信息。若p_i和p_j不存在邻接关系，$H_{i,j}$设置为无限大；若p_i和p_j存在邻接关系，$H_{i,j}$设置为点p_i和p_j对应路径间距$\mathrm{g}(p_i,\Pi)$和$\mathrm{g}\left(p_j,\Pi\right)$的平均值。$\otimes$表示对角矩阵$L_c$和$H$对应项相乘。

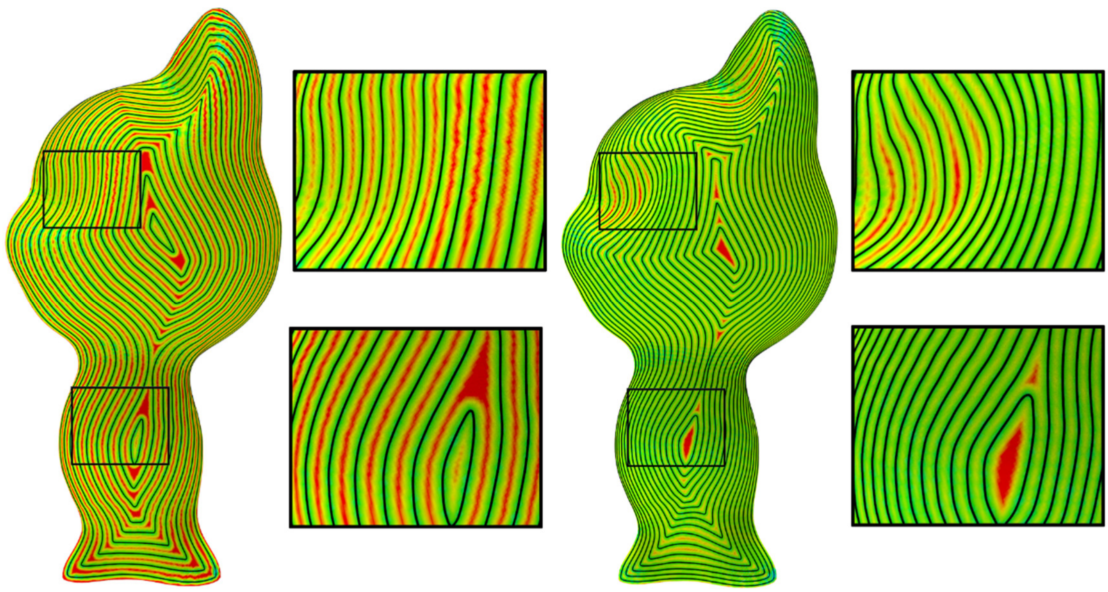

图 3-6 残留高度可视化，左图：测地距离等值线的残留高度；

右图：残留距离场的等值线路径对应的残留高度

为了使得等残留高度约束相关的距离标量场中提取的等值线上各点的路径间

距巧合满足该点理想的路径间距，需要多次迭代的计算等残留高度约束相关的距离标量场。其基本过程为，首先直接应用 Crane 等人的方法计算原始的测地距离场，从距离场中提取曲面S各采样点p_i的梯度方向作为计算方向曲率$G(p_i,\Pi)$的方向，通过点p_i的方向曲率$G(p_i,\Pi)$获得该点的理想路径间距$\mathrm{g}(p_i,\Pi)$，带入上文定义的考虑等残留高度约束的偏微分方程公式中，求得新的等残留高度约束相关的距离标量场。

如图 3-5，左图为从初始的测地距离场中提取的等值线，右图为经过一轮迭代后的等残留高度约束相关的距离标量场中提取的等值线，图中红色短线的可视化了曲面S各采样点p_i的理想路径间距$\mathrm{g}(p_i,\Pi)$。通常，只需要 2-3 次迭代就可以满足收敛要求。如图 3-6 的左右两图，分别对测地距离场和残留距离场中提取的等值线的残留高度进行了可视化，可以看到优化之后的残留分布更加均匀。

需要说明的是，残留距离场的计算采用了一种迭代求解的方法。残留距离场无法在一次计算过程中完成的核心原因是曲面S各采样点p_i的理想路径间距的计算必须依赖于已经存在的等值线，而将当前各点的理想路径间距应用到新的距离场计算中又会直接更改结果距离场中的等值线提取，因此我们采用了一种迭代求解逐步减少误差的方法计算等残留高度的等值线。然而每次迭代过程中距离场的计算，也可以考虑用其他的计算方法，比如 STVD 方法[87]。

3.3.2 路径优化

路径优化的目的是在曲面S各采样点p_i理想路径间距$\mathrm{g}(p_i,\Pi)$的约束下，对生成的等残留连通费马螺旋线Π进行平滑处理。路径间距的约束：

1) 曲面S各采样点p_i当前的路径间距中的极大值不能大于$\mathrm{g}(p_i,\Pi)$，简写为g，即曲面S中最大空圆的半径不大于$\mathrm{g}/2$；

2) 曲面S各采样点p_i当前的路径间距中的极小值越接近$\mathrm{g}(p_i,\Pi)$越好。

不妨假设自由曲面S的采样点为$\{p_i\}_{i=1}^{k}$，基于连通费马尔螺旋线Π各处的曲率动态选取路径采样点为$\{x_i\}_{i=1}^{n}$。路径优化的基本思路为通过优化如下目标函数，通过拉普拉斯平滑的方式对路径采样点$\{x_i\}_{i=1}^{n}$进行迭代更新：

$$\frac{dx_i}{dt} = \lambda_1 \times T_{Smooth} + \lambda_2 \times T_{Attraction} + \lambda_3 \times T_{Repulsion}$$

其中，T_{Smooth}，$T_{Attraction}$，$T_{Repulsion}$分别为拉普拉斯算子的平滑项，引力项和斥力项。λ_1，λ_2，λ_3为各项权重，$\lambda_1+\lambda_2+\lambda_3=1.0$。目标函数中的 t 可以理解为迭代次数。$T_{Smooth}$描述当前点$x_i$与其前后相邻点$x_{i-1}$和$x_{i+1}$的差异，$T_{Smooth}|_{x_i}=\frac{x_{i-1}+x_{i+1}}{2}-x_i$；$T_{Attraction}$描述点$x_i$附近的最大空圆的圆心作为引力中心点$\{q_i\}_{i=1}^m$对路径采样点$\{x_i\}_{i=1}^n$的吸引作用力；$T_{Repulsion}$描述相邻路径上的采样点对路径采样点的排斥作用力。

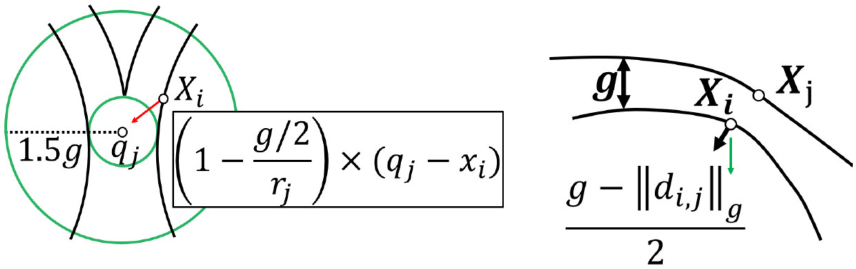

图 3-7 路径优化引力项和斥力项的计算

为了满足路径间距第一条的约束，首先在曲面S采样点$\{p_i\}_{i=1}^k$中计算一组空心圆使得 1)这些空心圆的半径都大于g/2且 2)任意两空心圆圆心的距离都不小于g。将计算得到的这组空心圆的圆心记为$\{q_j\}_{j=1}^k$，称之为锚点。引力项$T_{Attraction}$的作用是对锚点3g/2距离范围内的路径采样点为$\{x_i\}_{i=1}^n$产生吸引力。令$r_j(>\frac{g}{2})$为锚点q_j与路径Π的最近距离，如图 3-7。引力项$T_{Attraction}$的具体定义为：

$$T_{Attraction}|_{x_i}=\frac{\sum_{||x_i-q_j||_{3g/2}}\frac{r_j-g/2}{||x_i-q_j||_g-r_j+\varepsilon}\times\left(1-\frac{g/2}{r_j}\right)\times(q_j-x_i)}{\sum_{||x_i-q_j||_{3g/2}}\frac{r_j-g/2}{||x_i-q_j||_g-r_j+\varepsilon}}$$

其中，$(1-\frac{g/2}{r_j})\times(q_j-x_i)$能够将$x_i$与$q_j$距离收缩为g/2，如果点$x_i$恰好是点$q_j$到路径Π的最近点。权重项$\frac{r_j-g/2}{||x_i-q_j||_g-r_j+\varepsilon}$是为了加强点$q_j$对点$x_i$的吸引力，如果点$x_i$不是点$q_j$到路径Π的最近点。

如图 3-7，对点x_i的斥力项定义为与x_i距离小于g的路径Π上的其他点x_j，$||d_{i,j}||_g<h$。满足该要求的点可能不只一个，斥力项定义为一种加权形式：

$$T_{Repulsion}|_{x_i}=\frac{\sum_{||d_{i,j}||_g<h}\frac{1}{||d_{i,j}||_g+\varepsilon}\times\frac{g-||d_{i,j}||_g}{2}\times\frac{x_i-x_j}{||d_{i,j}||_g}}{\sum_{||d_{i,j}||_g<h}\frac{1}{||d_{i,j}||_g+\varepsilon}}$$

设置$\frac{g-||d_{i,j}||_g}{2}\times\frac{x_i-x_j}{||d_{i,j}||_g}$项是为了考虑当$x_i$和$x_j$同时远离对方时，二者之间的距离能够恰好是$g$。权重项$\frac{1}{||d_{i,j}||_g+\varepsilon}$是为了加强$x_i$和$x_j$之间的排斥力，当二者距离非常接近的时候。

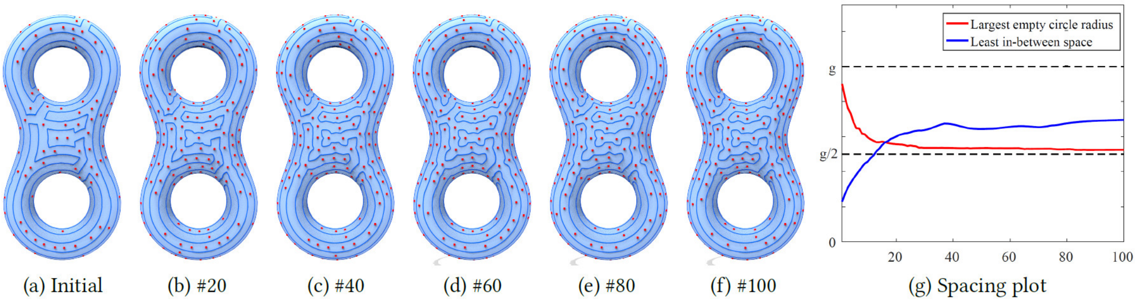

图 3-8 路径优化迭代过程示例，右侧曲线图给出了迭代过程中最大空圆的半径大小变化情况（蓝色曲线），以及路径间距中的极小值的变化情况（红色曲线）

目标函数的各项参数默认取值：$\lambda_1=0.6$，$\lambda_2=0.2$，$\lambda_3=0.2$，$\varepsilon=10^{-4}$，优化过程的终止条件设置为前后两次的最大空圆的半径大小变化小于g 的 5%。在我们当前的实验中，测试的自由曲面的体积都在$50\times60\times70\mathrm{mm}^3$范围内，曲面$S$上的采样点$\{p_i\}_{i=1}^k$个数为$80K$，并通过蓝噪声采样的方式确定采样点的位置。对于更大体积的自由曲面，所用的采样点个数需要相应增加。

如图 3-7 给出了一个路径优化迭代过程的具体实例，图中展示的每次迭代过程的下标为迭代次数。图 3-8 最右侧图片绘制的曲线为迭代过程中最大空圆的半径大小变化情况（蓝色），以及路径间距中的极小值的变化情况（红色）。图 3-9 给出了路径优化前后的等残留连通费马螺旋线路径。

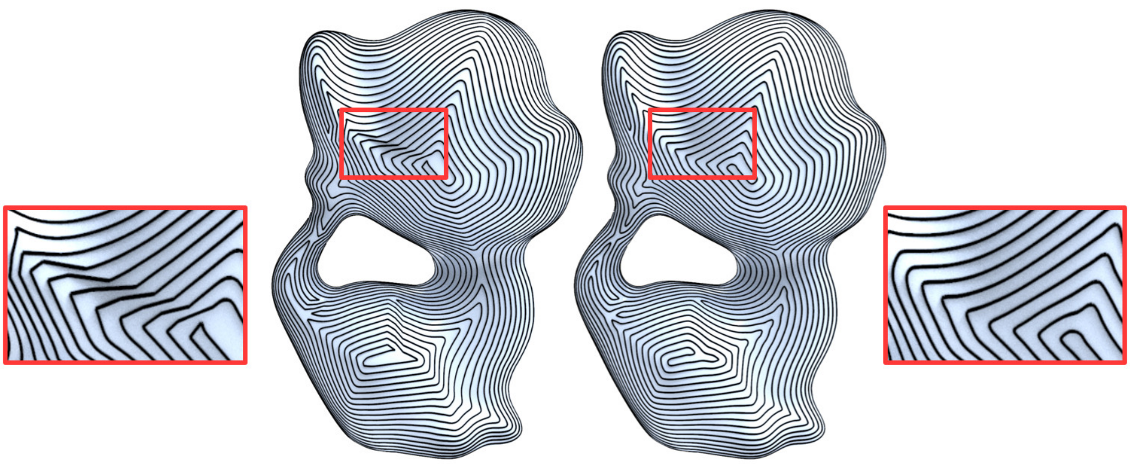

图 3-9 路径优化的效果实例

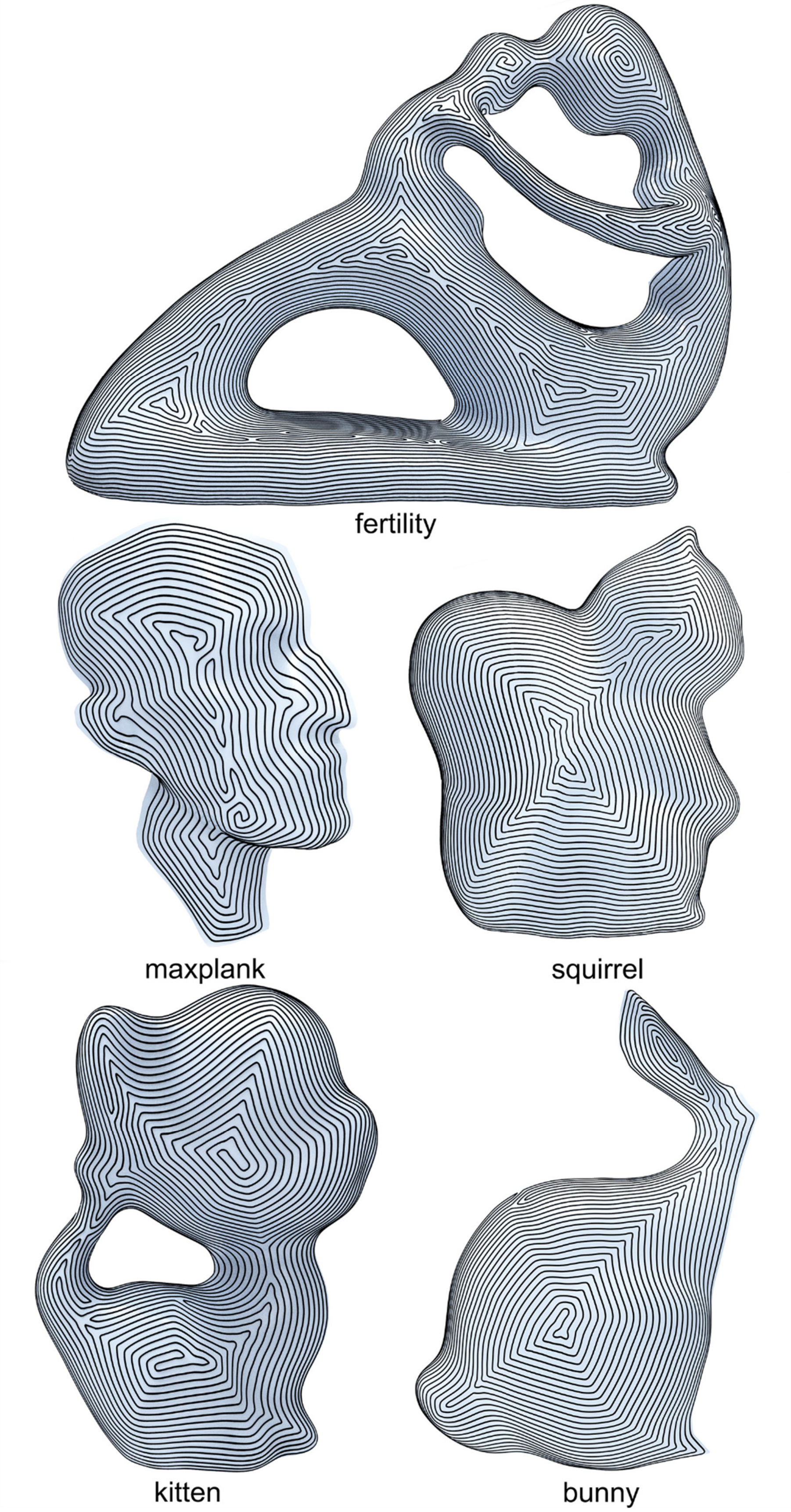

图 3-10 等残留连通费马螺旋线实例

3.4 实验结果与分析

为了充分验证算法的有效性，本章针对一系列具备不同复杂度的自由曲面生成等残留连通费马螺旋线路径，并在路径几何特征，实际的打印时间方面，与经典的平行扫描路径和轮廓平行路径进行对比。

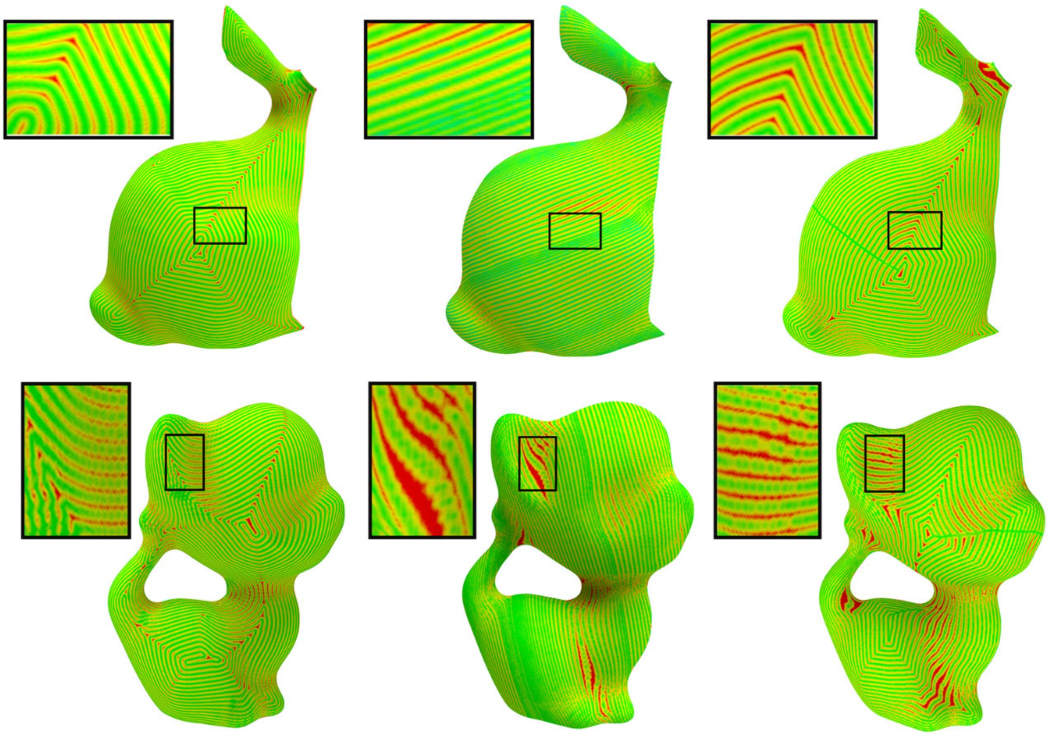

等残留连通费马螺旋线　　平行扫描方法　　轮廓平行路径

图 3-11 残留高度可视化，深红色标记区域为残留区域

3.4.1 路径生成

本章提出的路径生成算法的实现语言为 C++。实际加工实验中相关参数有，精加工球头刀具直径为 4.0mm，最大残留高度设置为 0.02mm。然后，为了更好的展示路径，本章给的路径生成的结果图中设置的最大残留高度为 0.045mm。在路径生成过程中采用统一的参数设置，残留距离场生成步骤采用默认的参数设置，路径优化阶段经过约 40 次迭代。

图 3-10 给出了算法对于不同的自由曲面生成的等残留连通费马螺旋线路径。用于展示路径结果的自由曲面具备不同的轮廓凹度及不同程度复杂的内部结构，展示了算法的一般性和鲁棒性。为了更清楚的可视化生成的螺旋线路径，我们刻意的降低了路径的分辨率。

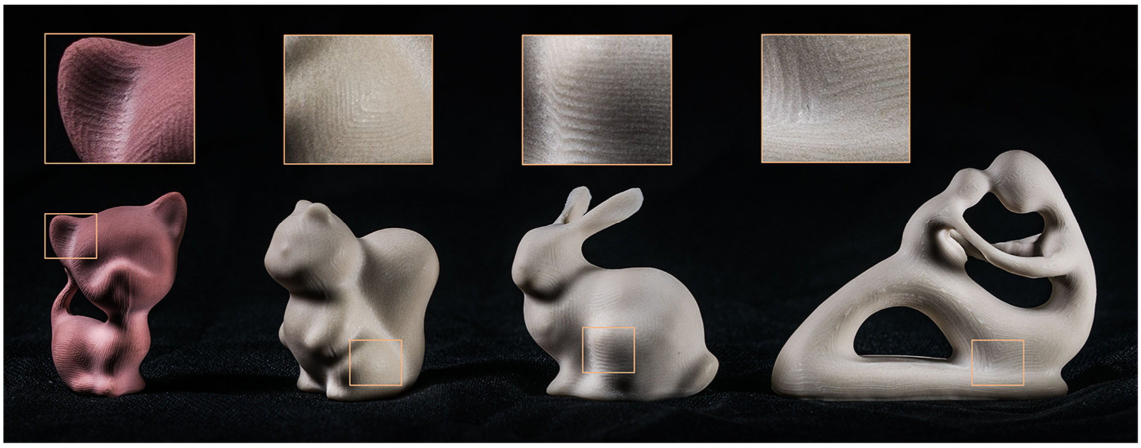

图 3-12 实际加工的自由曲面

3.4.2 实际加工

我们的实际加工实验在五轴数控机床 CNC 6040 2200W 上进行，应用一种可加工的树脂材料（代木）作为实验材料。五轴数控机床的相关参数如下，刀具选取的是直径 4.0mm 的球头刀，最大进给速度为 500mm / min，路径弦差为 0.001mm，机床主轴速度为 15,000 r/min。G 代码用于输入机床进行实际的加工实验。图 3-12 展示了用本文生成等残留连通费马螺旋线加工自由曲面的真实照片，提供特写图片展示了加工残留的细节情况。

3.4.3 路径对比

最常见的两种 CNC 刀具加工路径模是平行扫描路径和轮廓平行路径。用于左对比的平行扫描路径和轮廓平行路径，都取自 Siemens PLM Software 软件包[88]。Siemens PLM Software 软件包，也被称为 NX Unigraphics，是一种机械领域常用的 CAD/CAE/CAM 软件。图 3-11 展示了等残留连通费马螺旋线路径，与平行扫描路径，轮廓平行路径的残留高度的可视化，可以看到本文路径的残留高度更加均匀。

表 3-1 给出了等残留连通费马螺旋线路径，平行扫描路径和轮廓平行路径在路径段数，硬拐角点比例和实际的加工时间方面的对比结果。可以看到，等残留连通费马螺旋线路径具有全局连续的特征，路径段数都为 1，而平行扫描路径和轮廓平行路径完成自由曲面的加工都需要较多的路径段数。随着曲面边界或内部复杂程度的提高，需要到的路径段数越多，比如其中的 Fertility 和 Kitten 曲面。对于加工时间的对比结果，也证明了等残留连通费马螺旋线路径具备更高的加工效率。需

要说明的是，为了计算加工路径的硬拐角的数量，采取了与上一章类似的基于积分曲率的计算方法，可以看到等残留连通费马螺旋线路径的硬拐角数量也明显低于其他两种规划路径。

Patch	#sgZ	#sC	#sgF	%tnZ	%tnC	%tnF	t_Z	t_C	t_F
#1 (BUNNY)	9	4	**1**	7.1%	4.7%	**1.5%**	450	368	**342**
#2 (FERTILITY)	18	6	**1**	6.6%	4.0%	**3.8%**	1908	1054	**1034**
#3 (MAXPLANK)	5	**1**	**1**	7.6%	6.0%	**2.5%**	245	232	**205**
#4 (SQUIRREL)	6	**1**	**1**	6.0%	2.8%	**1.9%**	539	428	**416**
#5 (KITTEN)	11	2	**1**	7.4%	3.7%	**2.8%**	469	381	**370**

表 3-1 等残留连通费马螺旋线路径（F），平行扫描路径（Z）和轮廓平行路径（C）在路径段数(#sg)，硬拐角点比例(%tn)和实际加工时间的对比结果

3.5 本章小结

本章将前一章提出的满足全局连续性和平滑性连通费马螺旋线路径，应用在数控加工的路径规划中，并拓展其满足等残留高度的特征，提出了等残留连通费马螺旋线的生成算法。等残留连通费马螺旋线，对于自由曲面的加工能够同时满足连续性，平滑性以及等残留高度的特性，与传统的路径规划方法相比，显著提升的加工效率和质量。为了证明算法的有效性，对于不同复杂度的自由曲面生成等残留连通费马螺旋线路径，并在路径几何特征，实际的打印时间方面，与平行扫描路径和轮廓平行路径进行对比。

第4章 数控加工的装夹规划

4.1 引言

数控加工中的装夹规划步骤，对于完整工件的铣削加工往往是必不可少的，例如用五轴数控机床加工一个完整零部件，该零部件外表面上的大部分区域都需要进行加工，即使是刀具可达范围相对大的五轴机床，仍不可能在一次装夹后就完成零部件所有待加工区域的加工，需进行多次重新装夹定位。

数控加工的装夹规划是数控加工流程设计的核心内容之一，需要综合考虑目标工件的几何形状，尺寸和公差，可用加工资源等信息，确定工件装夹的次数，顺序以及每次装夹中的定位基准，加工特征和加工方法[89]。具体的，装夹规划需要确定装夹过程工件方向规划及对应加工范围划分，以及设计或选择的装夹工具对工件进行加紧定位。如图 4-1，在一台三轴数控铣床上加工经典的 Bunny 模型，需要用到三次装夹规划过程，图中展示了各次装夹方向下的粗加工过程二维示意图。

当前在数控加工领域大部分装夹规划方法，主要处理由基本几何元素组成的 CAD 模型，对于无明显特征线的自由曲面组成的全封闭工件研究较少。如绪论中所述，自由曲面的铣削加工通常在五轴数控铣床上采用五轴联动或定轴加工的工作模式进行。在实际生产中，装夹规划主要依赖于工程师的经验进行手动设计。本文针对三维封闭自由曲面模型，拟提出一种自动的装夹规划方法。

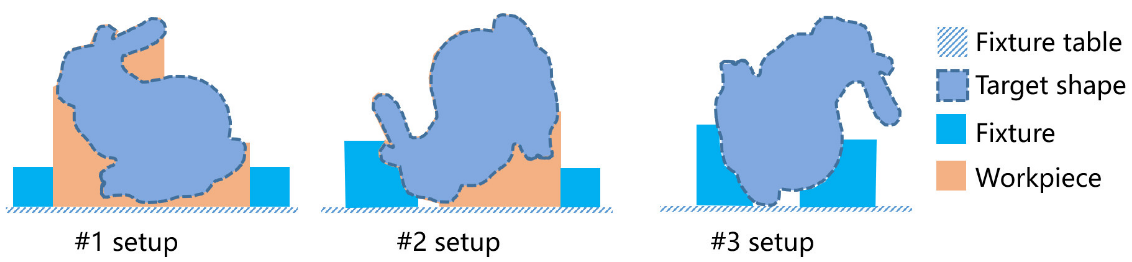

图 4-1 三轴数控机床装夹规划实例

4.2 相关工作

4.2.1 五轴联动和定轴加工

三轴数控铣床对“平面型腔”结构的加工过程与增材制造的打印过程类似，数控刀具主要在二维区域内进行铣削操作，不同之处在于数控铣床采用的是“减材”

的制造方式逐步从毛坯件上削减余料。由于具备加工范围大的优势，自由曲面工件常采用五轴数控铣床进行加工[13]。五轴数控铣床的运动轴由三个移动轴和两个转动轴组成，如图 4-2 所示。

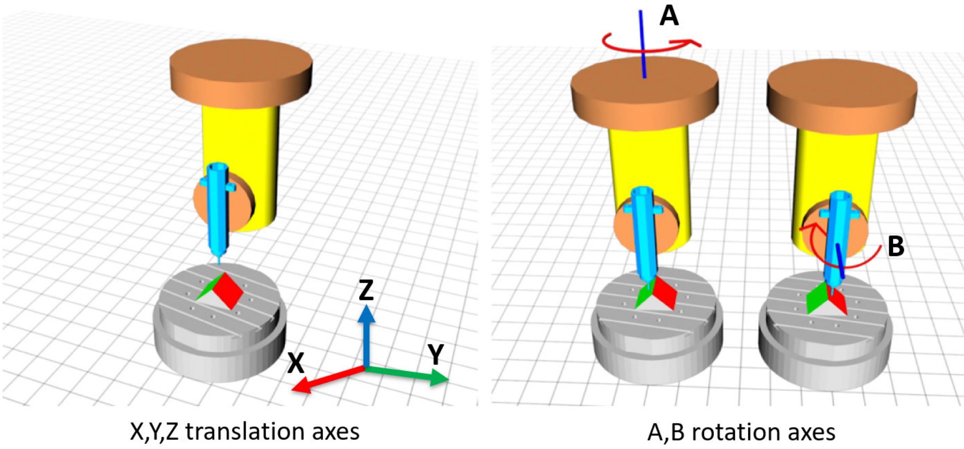

图 4-2 五轴数控铣床运动轴示意图，

左图：三个移动轴 XYZ；右图：两个转动轴 AB

五轴数控铣床加工，主要有两种不同的加工模式，五轴联动和定轴加工。两者不同之处在于，五轴联动加工模式在刀具铣削过程中五个运动轴同步运动；定轴加工在刀具切削过程中只有三个移动轴运动，只有在需要转换加工范围时，另外两转动轴才参与运动，如图 4-3。

两种加工模式相比，定轴加工在实际生产中应用更为广泛，定轴加工切削过程中同步运动的轴数少，路径生成更为容易，并且在加工过程中刀具切削力更为稳定支持高速切削。由于运行误差较少，工件的表面加工质量也会更好，传统的路径规划方法诸如平行扫描方法在定轴加工模式下也可以工作的更好。因此，本文在解决全封闭自由曲面模型加工的装夹规划问题时，选择定轴加工模式。

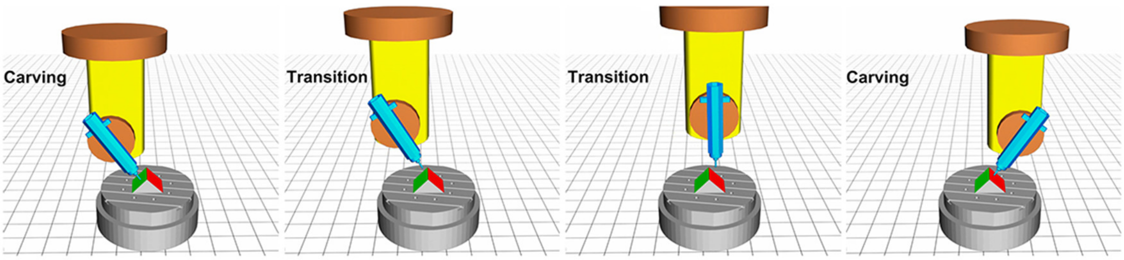

图 4-3 定轴加工示意图，加工绿色和红色区域时只有三个移动轴运动（carving process），在需要转换加工范围时（transition process），另外两转动轴参与运动

4.2.2 装夹规划

通常来说，装夹规划涉及到实际数控加工过程开始前工件夹紧部件的设计与规划[19-20]。装夹规划需要解决的核心问题在于以最优化加工质量和效率为目标规划工件朝向。能够最小化装夹次数是装夹规划的关键约束，因为每增加一次装夹过程，不可避免的需要增加夹具数目，且重定位过程中可能引入的定位误差也会对加工质量带来影响。当前在学术领域，大多学装夹规划方法主要处理由基本几何元素组成用于工业零件的 CAD 模型，比如旋转体模型或箱体模型[90]，如图 4-4。主要采用的方法有遗传算法、专家系统、决策树、训练学习等方法[91]。在工业生产中，装夹规划仍需要依赖工程师的经验进行手动设计。

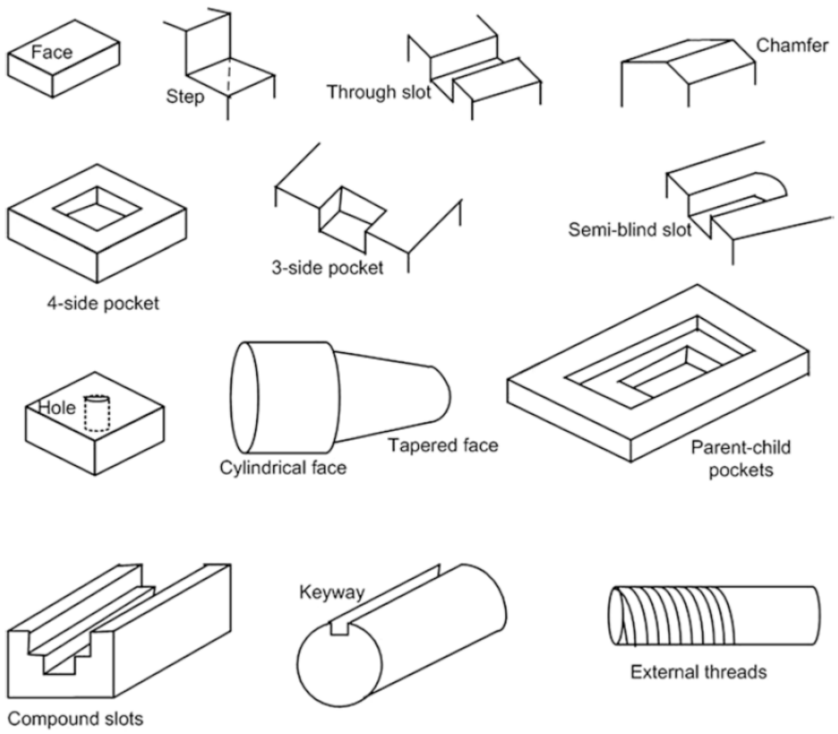

图 4-4 CAD 模型的基本几何元素

4.2.3 区域分割

如前文所述，装夹规划除了需要确定装夹过程的工件方向之外，还需要规划其对应的加工范围，在此对相关的区域分割方法进行介绍。图形学领域中出现了许多基于各种不同的约束进行形状分割或区域分解的方法[92]。装夹规划中的区域分割的核心约束在于对加工刀具可达范围进行分析。此外，分割区域边界的平滑性也是

很重要的因素，主要是因为装夹规划后的下一步就是需要进行路径规划，而区域边界平滑有利于进行路径规划[70-71]。在区域分割方面，数控加工领域已有许多对于平面区域的分割方法，主要目的是将复杂的二维区域分解为较为简单的区域进行加工[50][70][93]。本文需要解决的区域划分问题，主要是在可达性分析的基础上对待加工封闭自由曲面模型进行区域划分。

针对装夹规划涉及到的以最小化装夹次数为目的区域划分问题，前人已有工作证明该问题是一个 NP-hard 问题[94] [95]。Gupta 等人提出了一种贪婪算法进行装夹规划[94]。Frank 等人首先对组成 CAD 模型的基本几个单元进行刀具可达性的分析，之后将装夹规划问题转换为一个集合覆盖问题进行求解[95]。Herholz 等人将封闭自由曲面三维模型分割为近似高度场曲面[96]。

4.3 装夹规划

本文解决封闭自由曲面三维模型的装夹规划问题的基本思路为，算法输入二流型三角网格S，预处理阶段将网格S首先分解为最少数目的高度场曲面。高度场曲面的分解过程主要是考虑到定轴加工的约束，分解之后的各高度场曲面都可以采取定轴加工的方式固定刀轴方向只移动三个移动轴完成加工。之后根据装夹规划区域划分约束，将将网格S划分为在各装夹方向下可以加工的区域，并在此过程中整合预处理阶段的区域划分，图 4-5 给出了算法流程示意图。

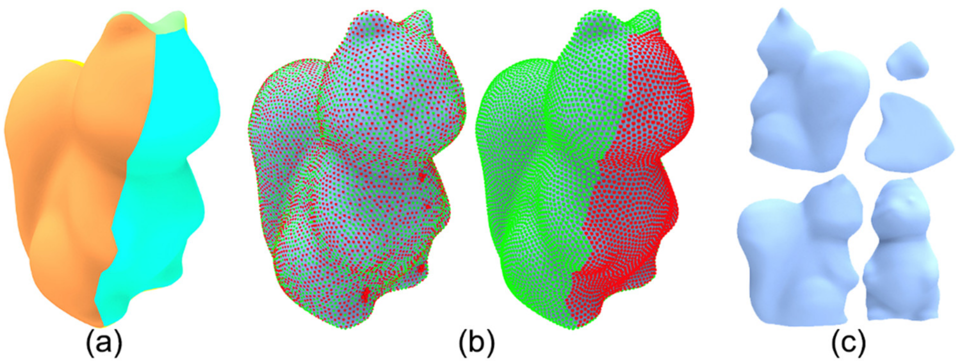

图 4-5 封闭自由曲面模型装夹规划算法流程，

(a)高度距离场 (b)可达性区域分割 (c) 定轴加工区域

无论是预处理阶段高度场曲面的分解，还是可加工区域的分解，都需要在可达性分析的基础上进行。可达性分析的目的是计算最少数目的装夹方向组合及其对应的加工范围。每个装夹方向对应着一个加工范围，在一次装夹完成后该加工范围

应用定轴加工的加工模式进行，因此需要对该加工范围进一步划分为定轴加工可加工的子区域。在定轴加工过程中，无需进行重新装夹，刀具相对于工件的朝向转换通过五轴数控机床的旋转轴和移动轴的配合完成。重新装夹是非常耗时耗力的操作过程，因此装夹规划的一个核心目标是最小化装夹次数。

对于给定的三维模型S，我们首先采样了一组可能的物体装夹方向并分析各装夹方向对应的可加工范围。以各采样装夹方向对应的加工范围为输入，将问题定义为一个最小覆盖问题的形式[97]。求得的最小覆盖集合中，装夹方向对应的加工范围的并集包含输入模型S的所有可加工区域。最小覆盖集合对应的并不是一个完整可用的可达区域划分结果，其中将会存在大量叠加区域。之后应用 Graph Cut 算法将这些叠加区域分解开，并在这个过程中将预处理中的高度场曲面分割结果进行整合。最后对划分区域边界进行平滑处理。图 4-6 给出了一个对封闭自由曲面三维模型进行装夹规划的结果实例，对图中的 Kitten 模型用需要用到两次装夹，并用不同的颜色对各装夹方向下对应的定轴加工范围进行了可视化。

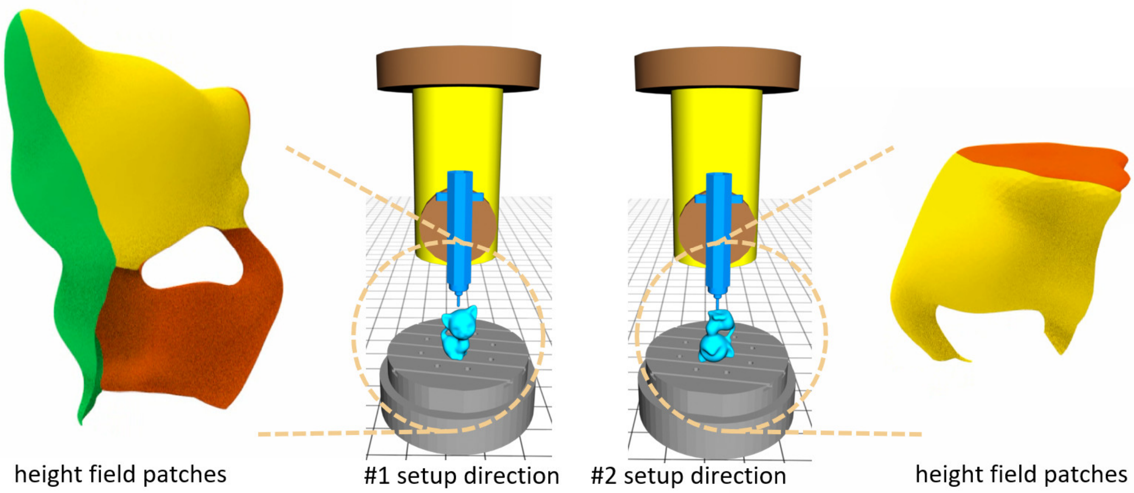

图 4-6 装夹规划实例

4.3.1 高度场区域分割

预处理阶段基于 Herholz 等人的方法[96]，我们将输入模型S分解为一组最少数量的高度场曲面。基本步骤为：首先在高斯球上均匀采样一组加工方向$\mathrm{d}_i, i = 1 \cdots n$；对于每个采样方向$\mathrm{d}_i$，在工件模型表面的采样点$\mathrm{p}_j$中可加工的采样点。具体计算方法为，若$\mathrm{d}_i$在采样点$\mathrm{p}_j$的可用加工方向集合中，则点$\mathrm{p}_j$可以在方向$\mathrm{d}_i$下加工。

将输入模型S的高度场曲面分解问题，定义为一个基于 Graph Cut 方法[99]求解的图中能量最小化问题。定义输入模型S采样点p_j为图的节点，采样点p_j邻接关系为边的图G_F。定义图G_F中每个节点p_j可取得 label 值为其可加工的采样方向d_i。使用经典的 Graph Cut 问题求解器[99]求得高度场曲面的分割区域。最终每个采样点p_j对应一个加工方向d_i。

上述步骤与 Herholz 等人文章中的方法大体一致，区别主要有两点：一是本文算法并未对输入模型S进行变形操作；二是在判断采样点p_j能否在方向d_i下加工时，用一个头部附有球体的圆柱体形状代替原文方法中的空间射线。如图 4-7 展示了一个预处理阶段高度场区域分割的实例。

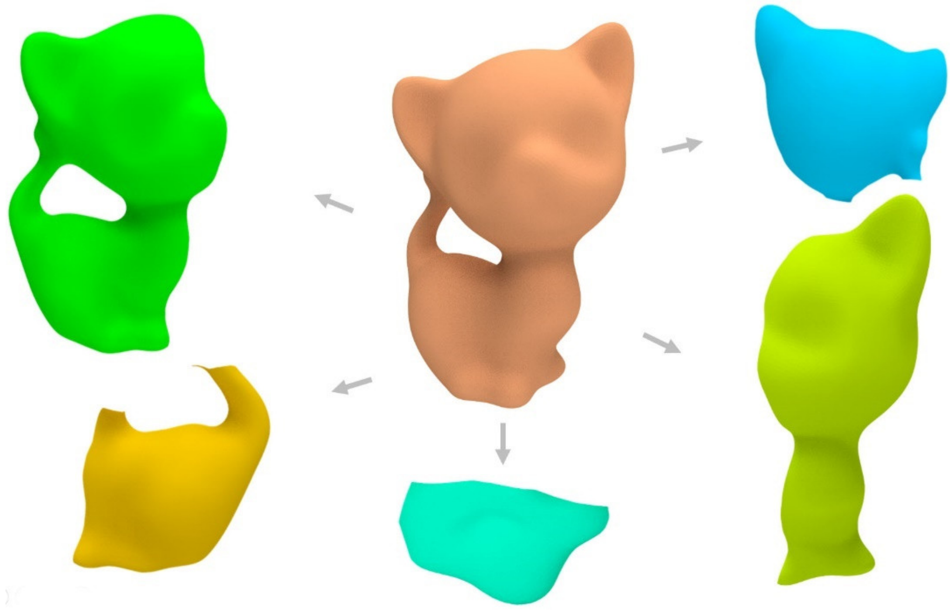

图 4-7 高度场区域分割实例

4.3.2 加工可达锥体

为了便于说明刀具朝向与输入模型S上的采样点p_j的相对关系，不妨定义角度φ为刀具朝向与点p_j表面法向的偏置角度。在偏置角度φ范围内的刀具方向集合组成了点p_j的加工可达椎体。在某装夹方向d_i下，若五轴数控机床的刀具可以转换到采样点p_j的加工可达椎体中，称之为点p_j在装夹方向d_i下是可达的。在本文的工作中，角度φ设置$\pi/2$。由于可能发生的刀具干涉，完整的偏置角度为$\pi/2$的加工可达椎体可能被分解为原椎体的一个子集，如图 4-8 中点p_1和p_2的可达椎体被分为了两部分。

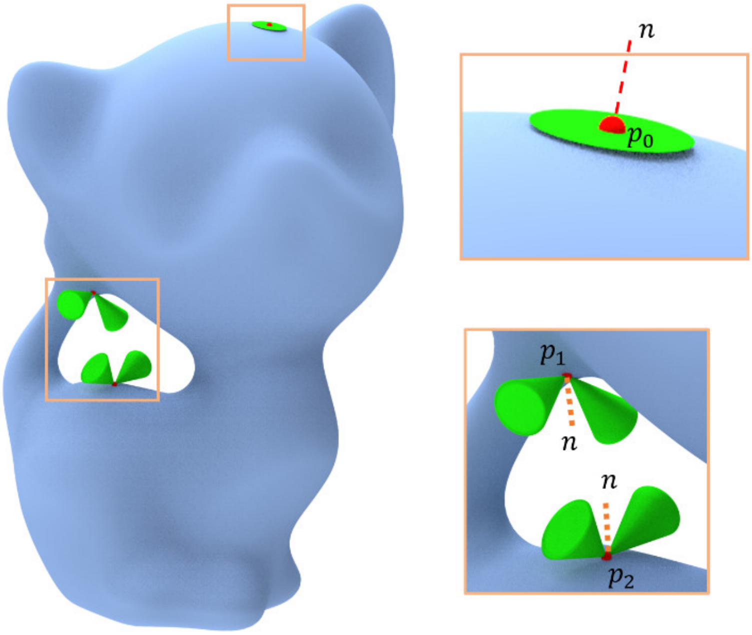

图 4-8 Kitten 模型上三个采样点的加工可达椎体实例

如图 4-2，大部分五轴数控机床的刀具方向受限于选择轴 A 的自由度为 $0^o \sim 360^o$，旋转轴 B 的自由度为$0^o \sim 90^o$，换言之相对于装夹平台来说，五轴数控机床的刀具朝向只能向下指。如图 4-8，在当前的装夹方向下，点p_0是完全可达的，点p_2的加工可达椎体部分可达，而点p_1则完全不可达。

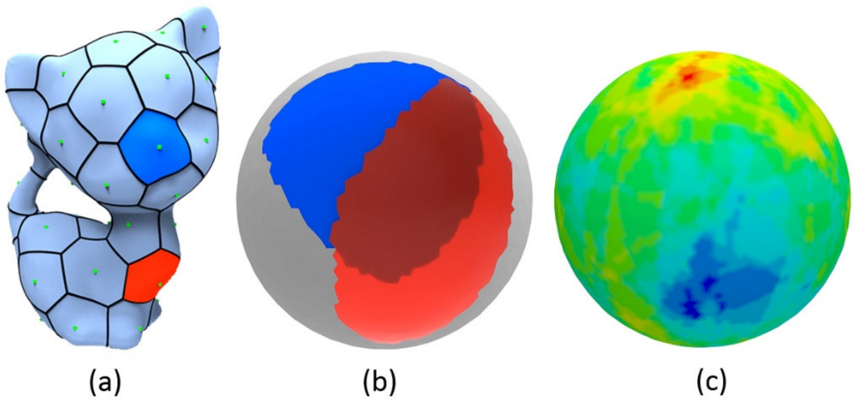

图 4-9 Voronoi 单元可达性，

(a)Voronoi 区域划分 (b)两 Voronoi 单元在高斯球对应可达方向 (c)高斯球可达方向

4.3.3 单元可达性

如图 4-9，首先在输入模型S上均匀采样以获得采样点$\{p_i\}_{i=1}^N$，并以采样点$\{p_i\}_{i=1}^N$为站点在曲面S上计算内蕴 Voronoi 划分。对于 Voronoi 单元$c_i, 1 \le i \le N$，需要计算一组模型方向R_i使得单元c_i区域中的所有点对于装夹方向R_i下都是可达

的。将 Voronoi 单元c_i对应的可达装夹方向R_i投影到高斯球上的对应区域$\Re_i$，如图 4-9 中红蓝两块 Voronoi 单元对应的可达装夹方向R_i投影到高斯球上对应的红蓝两块区域。

将所有 Voronoi 单元对应的可达装夹方向投影到高斯球上，得到图 4-9(c)所示的添加了颜色的高斯球，图中的颜色从红色到蓝色分别代表了高斯球上某一点对应的装夹方向可加工的 Voronoi 单元数量的多少。之后通过均匀或非均匀采样的方式在方向高斯球上选择备选方向$R_i, 1 \le i \le M$，对于每个备选方向R_i计算其对应的加工可达区域，如图 4-10 展示了三个备选方向性的加工可达区域。

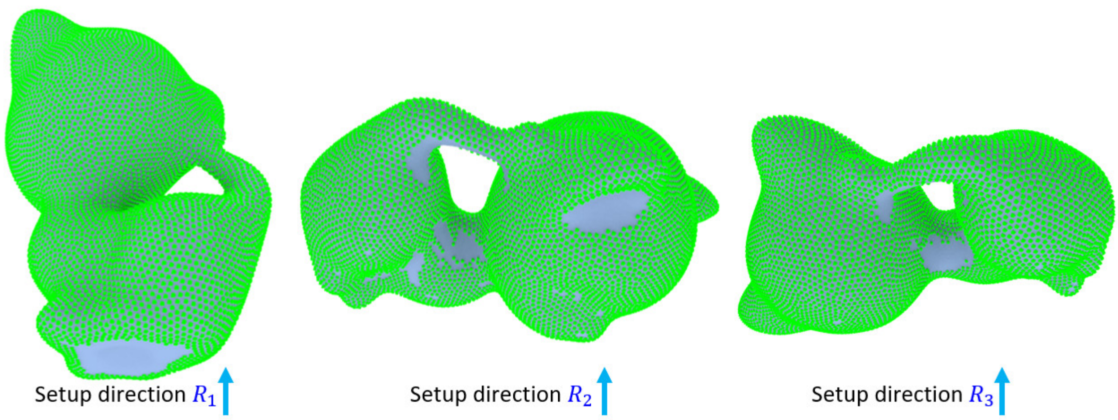

图 4-10 三个备选方向的加工可达区域

4.3.4 可达性覆盖

我们将可达区域划分的问题转化为一个集合覆盖问题进行求解，然后通过消除最小覆盖集合中的叠加区域得到可达区域的划分。给定全集$U = \{1,2,\cdots \mathrm{n}\}$，以及集合$U$的一系列子集组成的集合$S$，集合覆盖问题就是要找到$S$中最小的一个子集，使得他的并集等于全集$U$。形式化的定义为，给定全集$U$和他的一组子集组成的集合$S$，覆盖指的是一个集合$C, C \subseteq S$，且$C$的元素的并集为$U$。集合覆盖问题是典型的 NP 完全问题，最优化问题的集合覆盖问题是 NP 困难问题[97]。

在我们的问题中，我们将采样的 Voronoi 站点$c_i, 1 \le i \le N$视为集合U中的元素，将备选方向$R_i, 1 \le i \le M$对应的加工可达范围$S_i, 1 \le i \le M$视为集合的子集合组成的集合S。通过对集合覆盖问题的求解，可以得到一组最少数目的备选方向R_i的组合，使得该组备选方向的可达加工范围的并集为集合U，不妨称这样的集合为 MINORI（minimal number of orientations）。此处，应用 chvatal 等人提出的贪婪算

法求解 MINORI[98]。通常对于一个特定模型采样一组备选装夹方向，求解得出的满足最小数目方向的 MINORI 不只有一组，并且每组 MINORI 解中存在大量的叠加区域，如图 4-11 给出了对于 Kitten 模型求解最小覆盖问题得出的三个 MINORI 结果。如图 4-5(b)图所示，一组 MINORI 结果中存在大量的叠加区域，图中大红点和大绿点是只能被某一个备选方向加工可达的采样点，而其他的小红点和小绿点是可以同时被两个加工方向加工可达的采样点。

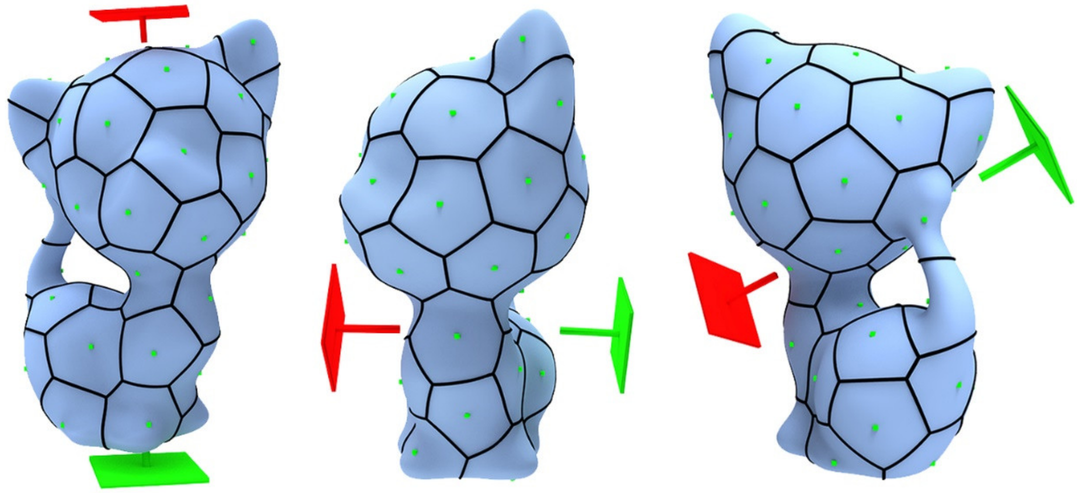

图 4-11 通过求解最小覆盖问题得出的三个 MINORI 结果

4.3.5 叠加区域消除

一组 MINORI 结果中存在大量的叠加区域，这些叠加区域对应的待加工区域可以同时在多个备选方向下加工可达。由于五轴数控机床刀具运动自由度较大，MINORI 中的叠加区域的范围可能很大，如图 4-5(b)图所示。MINORI 中的一个备选装夹方向对应着一组加工可达区域，即在该装夹方向下需要完成对该加工可达区域的加工。MINORI 存在的这些叠加区域必须消除，以避免可能的重复加工。另一方面，如前文所述我们采样定轴加工的方式对一个装夹方向下的可达区域进行加工，一个装夹方向下的加工可达区域必须依据定轴加工的约束进一步的划分为高度场区域。预处理中我们已经将输入模型分解为一组最少数量的高度场曲面，在此为了消除 MINORI 中的叠加区域以及考虑到定轴加工的区域划分，我们首先将预处理阶段得到的高度场区域划分整合到 MINORI 中，若整合后的 MINORI 中仍然存在叠加区域，则用一个 Graph Cut 算法[99]加以消除。

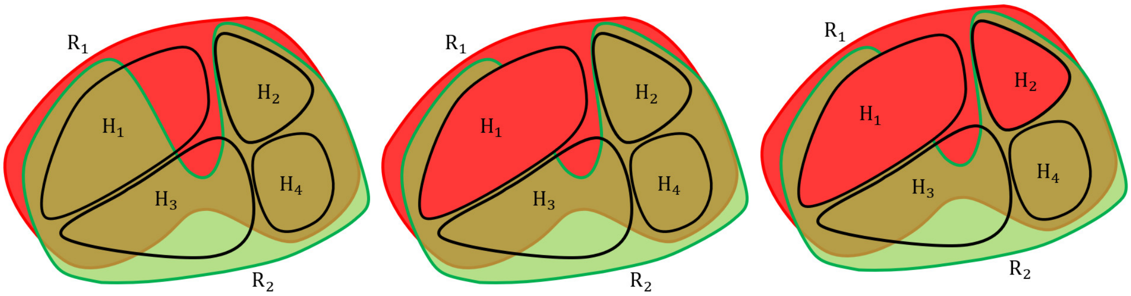

图 4-12 叠加区域消除，H_1直接被指定了R_1的可达方向标签；
区域H_1将其具备的可达方向标签R_1传播给了高度场区域H_2

4.3.6 区域整合

区域整合的目的，是将预处理阶段的高度场区域划分应用到 MINORI 覆盖区域消除的过程中。一个有效的 MINORI，可以看作给每个采样点p_i都附加了相应的加工可达方向标签，MINORI 中的叠加区域指的是附加了多个方向标签的采样点集合。根据预处理阶段的高度场区域的划分，每个采样点p_i可以说又附加了相应的所属的高度场区域标签。

我们提出了一种标签传播的方法，用已有的高度场区域标签消除 MINORI 中叠加区域中采样点多方向标签情况。具体的，首先遍历每个高度场区域H_i，如果高度场区域H_i的一部分采样点处于非重叠区域，其他部分处于重叠区域，则将非重叠区域的加工可达方向标签指定给重叠区域的方向标签，从而达到消除高度场区域H_i中重叠区域的目的，如图 4-12 中的H_1直接被指定了R_1的可达方向标签；如果高度场区域H_i中的全部采样点都处于非重叠区域，则将高度场区域H_i的加工可达方向标签传播的与高度场区域H_i临近的高度场区域H_j中，只要高度场区域H_j中的所有采样点都处于重叠区域，如图 4-12 中高度场区域H_1将其具备的可达方向标签R_1传播给了高度场区域H_2。

标签传播方法以尽量不破坏高度场区域的方式消除 MINORI 中的重叠区域。换言之，标签传播方法实际是将重复区域中涉及到的高度场区域，以最优化的方式分配到各装夹方向下的加工范围中。

4.3.7 Graph Cut 方法

应用标签传播的叠加区域消除方法后，可能仍然存在的重叠区域，如图 4-12 中高度场区域H_3和H_4，则用一个 Graph Cut 算法[99]消除。将重叠区域中的采样点p_i视为图G_F的节点，采样点p_i的邻接关系定义为图G_F中节点边。Graph Cut 在当前情况下定义的能量函数为：

$$E(\mathrm{r}) = \sum_{i=1}^{m} D(r(p_i)) + \alpha \sum_{(ij)} S(r(p_i), r(p_j)),$$

其中，D为 Graph Cut 的数据项，S 为平滑项，α为权重因子，本文的工作中设置为 100。数据项D用于描述重叠区域中采样点p_i被设置为装夹方向$r(p_i)$的概率。平滑项S用于表征邻接的两采样点p_i和p_j设置为不同装夹方向后的惩罚项，具体设置为点p_i和p_j的连接边的垂直方向的方向曲率。最后，应用几何 snake 优化方法对最终划分的区域的边界进行平滑化[100]，如图 4-13 给出了边界平滑之前和只有的结果。

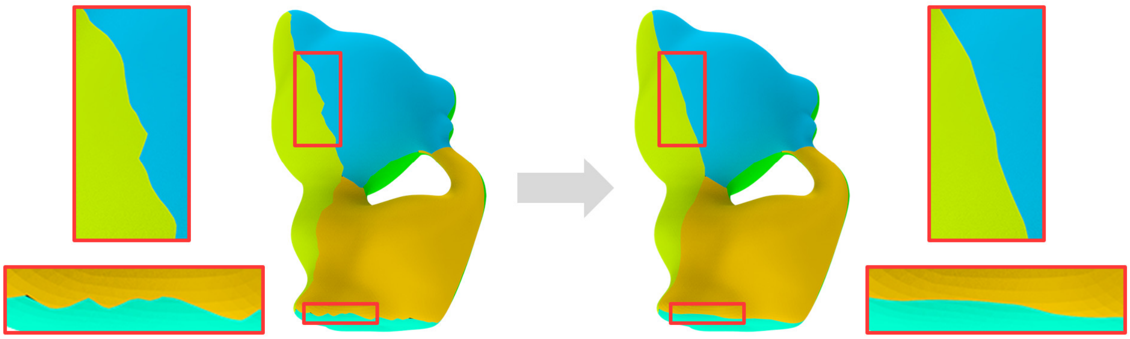

图 4-13 区域边界平滑，

左图：边界平滑操作前；右图：边界平滑操作后

4.3.8 最优 MINORI 选择

如上文所述，求解几何覆盖问题得出的满足最小数目方向的 MINORI 结果可能不是唯一的，对于每一组有效的 MINORI 结果都需要进行上述的叠加区域消除操作，从中选择定轴加工高度场区域数量最少的 MINORI 最为最终的装夹规划的结果。如果仍然存在多组满足要求的 MINORI，则可以参考区域边界平滑度选择最优的 MINORI。

4.4 实验结果与分析

为了充分验证算法的有效性，本章针对一系列具备不同复杂度的封闭自由曲面模型进行装夹规划，并在实际的五轴数控机床上进行加工实验。

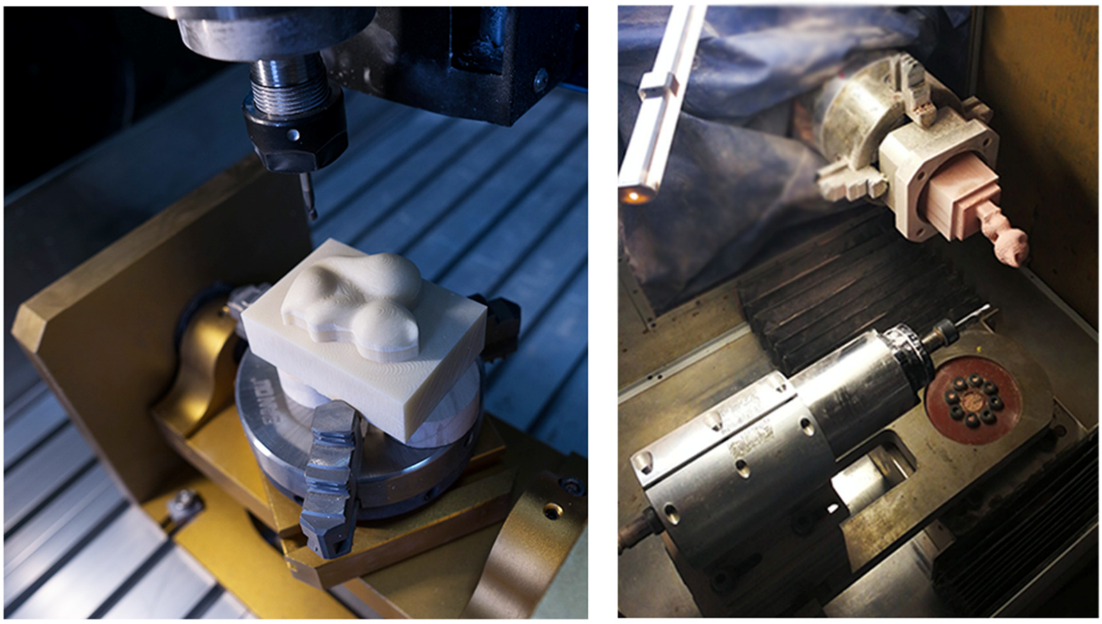

图 4-14 五轴数控机床实验环境

4.4.1 实验环境

如图 4-14，实际加工实验在五轴数控机床 CNC 6040 2200W 上进行，应用一种可加工的树脂材料（代木）作为实验材料。五轴数控机床的相关参数如下，刀具选取的是直径 4.0mm 的球头刀，最大进给速度为 500mm / min，路径弦差为 0.001mm，机床主轴速度为 15,000 r/min。G 代码用于输入机床进行实际的加工实验。图 3-12 展示了应用本文提出的装夹规划方法的实际加工工件。

4.4.2 装夹规划

如图 4-15 展示了应用本文提出的装夹规划方法生成的区域划分结果，图中每行展示了输入三维模型的装夹规划结果，图中前两列展示了装夹方向对应的加工可达区域的划分，后两列给出了定轴加工约束下的高度场曲面的区域划分。表格 4-1 展示了装夹规划实例的部分统计信息，包括装夹方向的数目，定轴加工高度场曲面数目，以及进行装夹规划各算法子步骤的运行时间。算法运行时间报告了可达

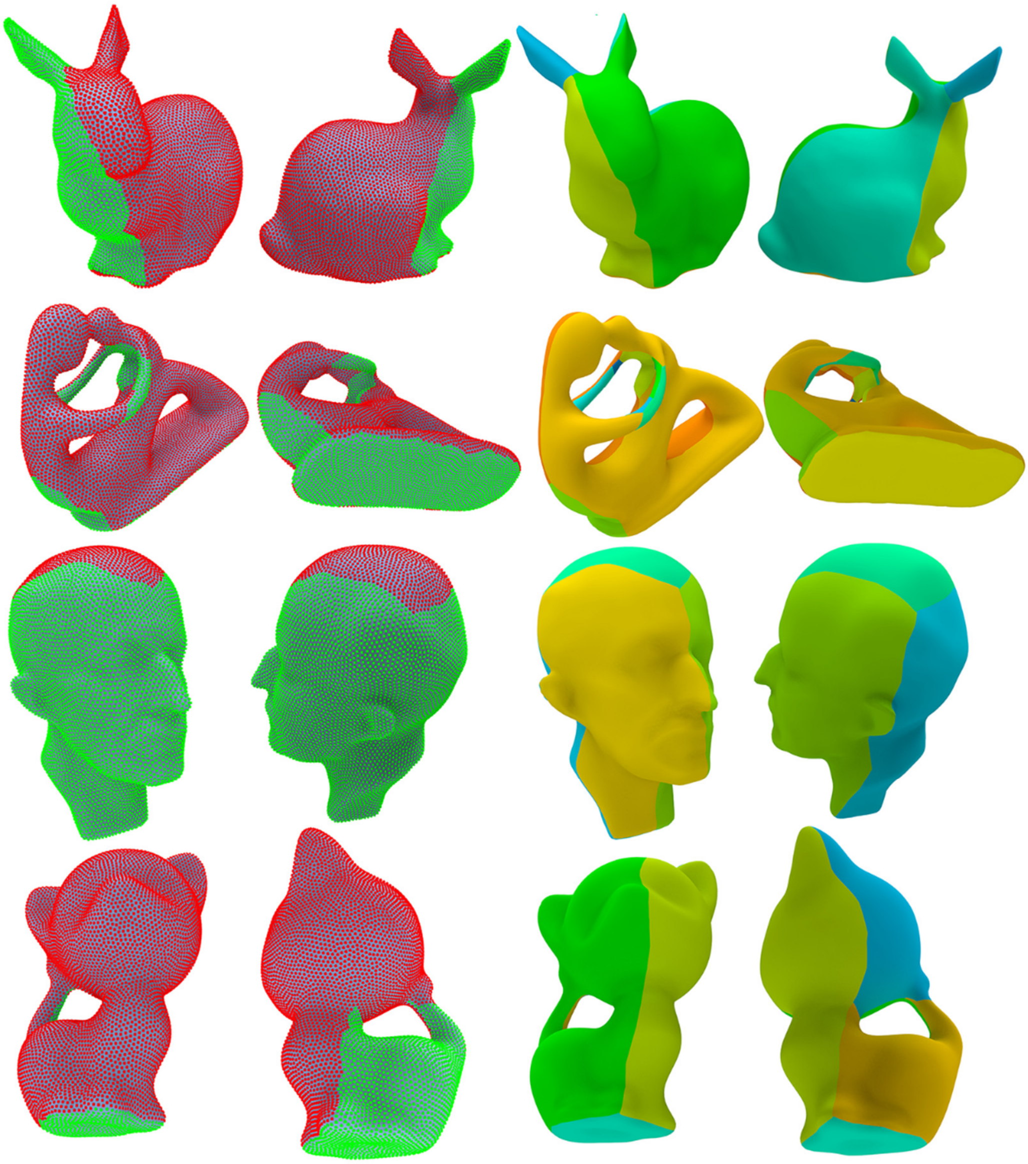

图 4-15 装夹规划区域划分的实例

3D Model	$\#A$	$\#P$	t_A(s)	t_P(s)
RABBIT	2	4	14.2	17.5
SQUIRREL	2	5	17.5	21.0
BUNNY	2	5	18.3	21.1
KITTEN	2	5	24.2	28.4
MAXPLANCK	2	4	27.1	30.5
FERTILITY	2	11	48.9	57.2

标 4-1 装夹规划实例统计信息，装夹方向的数目(#A)，定轴加工高度场曲面的数目(#P)，可达性分析的时间($t_A(s)$)，装夹规划区域划分的时间$t_P(s)$)

性分析的时间以及装夹规划区域划分的时间。程序运行时间数据是在一台 16GB 内存的 Intel® CoreTM i7-6700 CPU 4.0GHz 台式机上测试得到的。可以看到，本文提出的路径规划算法可以应用于不同复杂度的自由曲面模型，包括像 Fertility 这样高亏格的模型。如图 4-16 展示了应用本文提出的装夹规划方法进行实际加工的工件实例照片。定轴加工的高度场曲面采用上一章提出的等残留连通费马螺旋线路径生成刀具路径，图 4-16 特写图片展示了加工残留的细节情况。

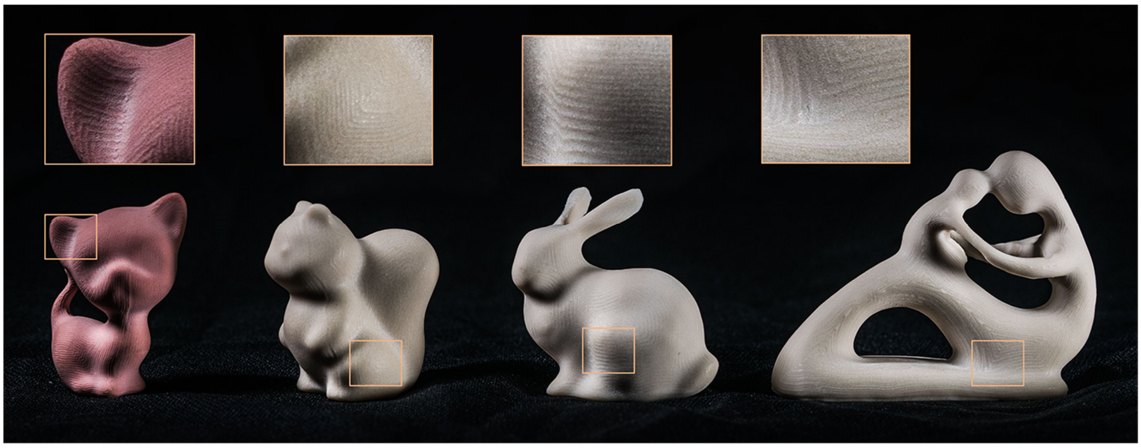

图 4-16 应用本文提出的装夹规划方法实际加工的工件实例

4.5 本章小结

本章针对封闭自由曲面模型，提出了一种自动的装夹规划方法。本章假设采用五轴数控机床的定轴加工模式加工封闭自由曲面模型。首先对自由曲面模型相对于五轴数控机床刀具的可达性进行了分析，对于自由曲面模型的每个采样点计算其加工可达椎体，在此加工可达性分析的基础上，首先考虑到定轴加工的约束在预处理阶段将自由曲面模型分割为高度场曲面，然后将装夹方向及其对应加工范围的求解问题转化为一个集合覆盖问题进行求解。对于集合覆盖结果中存在的大量重叠加工区域问题，先后采用标签传播和 Graph Cut 分割的方法进行处理，完成最终的装夹规划过程。

本章提出的装夹规划算法主要解决了装夹方向指定及其对应加工范围确定的问题，忽视了很多装夹规划中的其他约束，比如夹具设计问题，刀具切削力的问题，也忽视了夹具可能对工件可达范围的影响问题。然后本章提出的装夹规划算法具有很强的开放性，这些因素在未来的工作中有可能可以加入到算法框架中。

第5章 半色调投影与模型生成

5.1 引言

增材制造技术，可以直接以数字模型文件为输入制造任意复杂形状的三维实体，适用于可定制化的制造。近年来，在基于三维打印的创意设计与制造方面，以及出现了很多很有意思的工作，广泛应用于艺术设计，玩具设计，功能连接件等方面。本学位论文拟基于三维打印在图像个性化展示，考虑光线介质在可打印几何结构中的传播特性，提出了一种面向 3D 打印的半色调投影与模型生成方法。

半色调图像，通过网点的大小或稀疏表达图像的灰度，受到分辨率的限制半色调图像能够表现的色调则相对较少。半色调技术已经广泛应用于传统的纸面印刷和数字显示术等领域。其核心在于结构保持，色调再现，点密度和空间解析问题。以保持原始图像的相对色调为目的，国内国外的研究学者们提出了很多相应的半色调技术。然而，已有的半色调图像生成的技术，所面向的是数字半色调图像或者 2D 图像的点刻画表达。

我们将传统的半色调技术应用于光线上，将光线透射形成的光斑作为显示介质，根据用户给定的灰度图像和三维模型，通过在模型表面上设置微小孔洞调制投影图像。对于模型上的微孔优化其大小、位置和相对光源朝向角度，同时保证可打印性的结构约束，使光源透过这些孔洞在投影面上形成一幅与给定图像最相近的连续灰度图像，如图 5-1 所示。与传统的半色调技术不同之处在于我们表达半色调图像的基本单元是透过小孔成像的尺寸可以连续变化的光斑；投影光斑是通过控制灯罩上多孔结构的分布，尺寸和角度得到的；最终形成的半色调图像是投影生成的，在多孔结构灯罩生成过程中还需要考虑三维打印的相关约束。

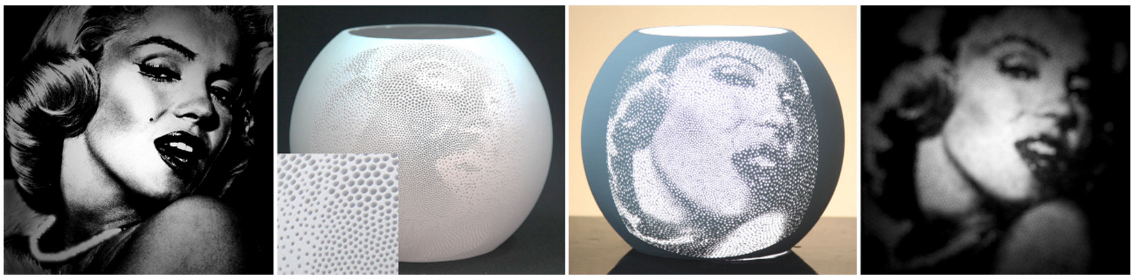

图 5-1 基于三维打印可投影任意连续灰度图像的多孔结构灯罩，从左到右依次为：目标灰度图像；三维打印的多孔结构灯罩；内部放置了光源的多孔结构灯罩；灯罩投影图像

5.2 相关工作

基于半色调技术的图像表达属于计算机图形学领域的经典问题，在传统的纸制印刷出版行业以及新兴的电子显示技术中应用非常的广泛[101]。本文将经典的半色调技术与先进的增材制造技术相结合，提出了一种基于投影的半色调图像表达方式。在相关工作部分，本章将分别对典型的半色调图像生成技术以及智能制造领域相关的创意图像表达的工作进行介绍。

5.2.1 半色调与点刻画

在计算机图形学领域，关于半色调图像生成方法的研究吸引了众多研究者的目光[102-103]。具体的研究工作有，考虑到输入图像结构特征的增强表达，Kim 等人提出了一种特殊的点分布方法使得半色调采样点沿着图像中的结构特征分布[104]。Pang 等人提出了一种基于优化技术的半色调技术，优化目标函数中同时考虑了图像结构特征的增强和灰度色调的保持[102]。Chang 等人应用了一种误差扩散的迭代策略以提升半色调图像生成算法的效率[105]。Li 等人提出了一种各项异性的蓝噪声采样方法并将其应用于图像点刻画表达中[106]。之后 Li 和 Mould 等人应用了一种非线性优先级调整的方法，生成的点刻画图像能够以最少数量的点提升半色调图像的对比度[107]。

在半色调图像生成技术中，存在一系列基于 CVT（Centroidal Voronoi tessellation）划分的方法。Balzer 等人将一种带容量约束的 Voronoi 划分（capacity-constrained Voronoi tessellation，CCVT）应用到点刻画的生成中，使得最终的点刻画分布中每个点区域具有相关的权重大小[108]。然后这种方法的缺点在于计算效率低下。在基于 CVT 的半色调图像生成技术中，一项经典工作是 de Goes 等人做出的，将等权重的 CCVT 划分问题转化为一个最有传输问题，生成的点刻画中能够保证严格满足权重一致的约束[109]。本文工作中应用了 de Goes 等人的方法，输入一个密度标量场得到相关的点刻画分布。

上述提到的半色调图像生成技术大部分都是针对二维图像提出的，本文提出的基于光学投影的半色调显示技术在在三维空间中生成的图像半色调表达。在三维空间中的半色调图像生成方面，Stucki 等人首次提出了三维数字半色调的概念，

探索了一种基于连续密度函数的三维半色调生成技术与“增材制造技术”的结合[110]。Lou 和 Stucki 等人将一种顺序抖动结合误差传播的算法应用到三维中[111]。Zhou 和 Chen 等人反过来将三维半色调技术应到三维打印中，用于介绍三维打印的制造时间[112]。与这些工作相比，我们的工作主要在考虑三维打印相关约束的条件下，提出一种可投影在半色调图像的三维多孔结构灯罩模型的生成方法。

5.2.2 制造相关的创意光影艺术

近年来，智能制造领域出现了很多富有创意的光影艺术方面的工作。Mitra 和 Pauly 等人提出了一种三维实体模型生成方法 shadow art，从多个不同的角度向该实体投影光线可以得到多幅二值投影图像[113]。基于 shadow art 的工作又出现了很多后续拓展工作，包括可以投影彩色图像的三维实体设计方法[114]，以及借助透明亚克力板形成三维全息光影艺术效果[115]。

本文的工作受到了 Alexa 和 Matusik 等人工作的启发[116], 通过在板型结构上生成不同深度的钻孔，不同深度的钻孔由于自遮挡效应会形成色调不同的灰度，从而形成半色调图像[116]，如图 5-2 所示。

图 5-2 基于自遮挡钻孔的半色调图像[116]

本领域的研究者还将光的反射和折射现象应用到半色调图像的生成中，形成焦散图像。这方面的代表性工作有，通过微面片[117]，微区域[118]，B 样条曲面[119]，连续曲面[120-121]，或者法向场[122]改变物体表面的几何结构，之后通过数控加工或激光雕刻完成实体的制造。

光影成像技术的应用也很广泛，比如信息伪装或产品外观设计等。Papas 等人设计了一种被动式的显示设备，隐藏图像只能被特定解码镜头破译[123]。Malzbender 等人提出了一种生成只能从特定方向观察的可打印 4D 反射比函数的曲面[124]。Levin 等人应用波动光学的原理生成高分辨率的定制反射曲面[125]。Lan

等人通过对局部着色框和反射率的空间变化来进行制造外观设计[126]。Willis 等人应用可打印的光导纤维，提出了一种可交互的定制化光线传导显示装置[127]。Pereira 等人引入了一种自动纤维寻路算法用于最小化光线传播的路径曲率[128]。

上文所述的制造相关的光影显示技术大部分都依赖于昂贵的专门设备或者特殊的制造原材料。相比较之下，本文提出的方法只需要普通的三维打印设备就可以制造完成。本文方法应用的物理原理是光线的直射传播原理，生成一种投影任意灰度图像的多孔结构灯罩。对灯罩制造材料只存在遮光性较好的约束，因此本方法的适用材料范围也很广泛，比如常用于桌面三维打印的塑性材料以和粉末材料。使用此种原材料形成的打印成品的透光率比较低，光线照射在该打印成品上大部分都会发生反射或漫反射。特别需要说明的是，本文采用了统一厚度的多孔结构灯罩，以避免因不同厚度产生的其他可打印性问题。

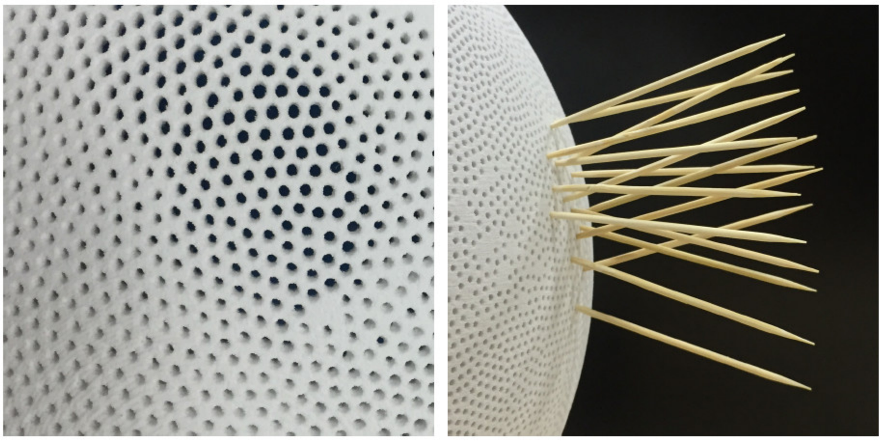

图 5-3 三维打印的多孔灯罩实例，插入牙签用于标明灯罩表面孔洞的朝向

5.3 多孔灯罩模型生成

本章的目标是提出一种可打印的多孔结构灯罩的模型生成方法，使得光源透过该多孔结构灯罩在附近墙面上投影出与用户设定的目标灰度图像非常接近的半色调投影图像。从光源发出的光线通过多孔结构灯罩时遮罩了部分光线，没有被遮罩的光线投影在附近墙面上形成最终的投影图像。特定投影图像的取得，需要对灯罩上的透光区域分布进行精心的设计。我们在给定三维灯罩曲面上生成了一组透光的锥形孔洞结构，这些孔洞结构的大小、位置和相对光源朝向角度可以根据特定输入图像的约束进行优化，如图 5-3。在孔洞的生成过程中还需要考虑满足可打印性的约束，以保证生成的多孔结构灯罩是可打印并且具备一定的强度。

不妨用符号I^t表征用户输入的灰度图像，灯罩灰度投影图像为I^P，本文提出的多孔灯罩模型生成方法主要目标和约束有：

a) 灰度投影图像I^P与目标灰度图像I^t的差异要尽量小。需要注意的是在评估两者差异时需要乘上一个相应的系数，因为灰度投影图像I^P的整体亮度受到相机曝光时间，感光度等因素的影响；

b) 灰度投影图像I^P要尽可能的保持目标图像的连续色调变化，并且尽可能的提高图像分辨率，换言之需要尽可能的提高孔洞的分布密度；

c) 多孔结构灯罩需要满足特定的可打印约束有，锥形孔洞的半径不能小于r_{min}，孔洞间距不能小于d_{min}。

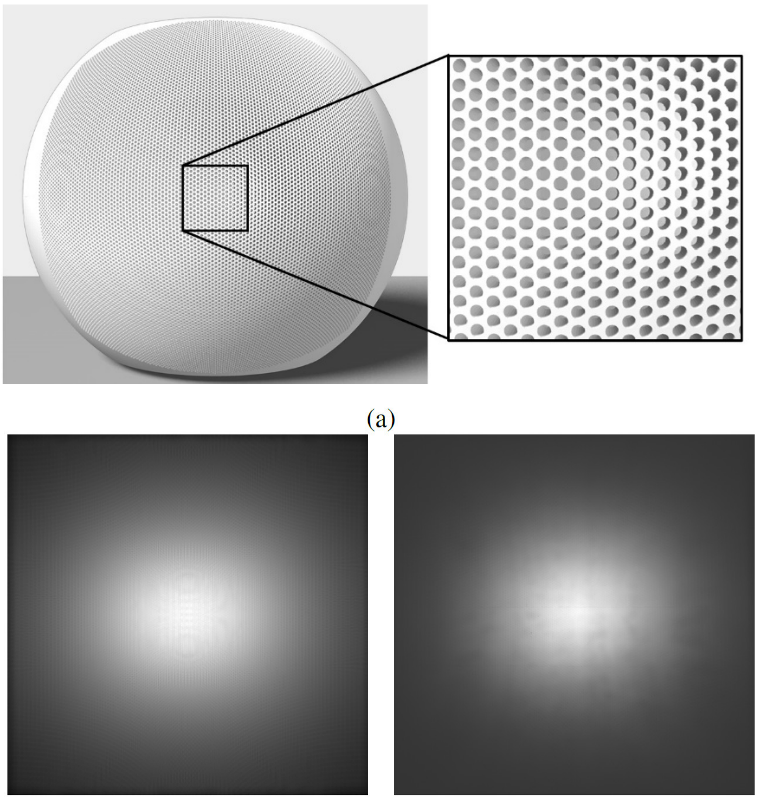

(a)　(b)　(c)

图 5-4 用最小孔洞按最紧密的排列方式生成的多孔灯罩(a)，
其对应的投影模拟图像(b)和实际投影图像(c)

如图 5-4 展示了满足可打印性约束的条件下的最密集排列的孔洞结构，并给出对应的投影模拟图像和实际投影图像。该排列以最小的孔洞间距d_{min}排列半径为r_{min}的最小尺寸孔洞，对应着一组半径为$r_{min}+0.5d_{min}$的紧密圆排列，如图 5-4(a)。为了使得投影图像I^P与目标灰度图像I^t的差异要尽量小，必须根据I^t的约束对孔洞

排列进行相应的调整。如图 5-4(b)给出了最紧密孔洞排列的投影模拟图像，与之相比，如果要在相应的投影位置获得亮度更高的灰度色调，可以增大相应位置的孔洞半径尺寸；然而如果要在相应的投影位置获得更暗的灰度色调，则不能通过减少相应位置的孔洞半径尺寸达到。

较容易想到的一个替代策略是，降低相应区域的孔洞数目，以一种更稀疏的排列方式生成暗部色调区域的孔洞结构。然而，这种方案会显著的降低半色调图像的连续性。对于用户输入的目标灰度图像 5-5(a)，应用目前最先进的点刻画生成算法生成的点刻画为图 5-5(b)。将该点刻画中的采样点分布位置直接作为多孔结构灯罩的孔洞位置生成多孔结构灯罩。为了满足可打印性的约束，点刻画中点数目被限制在 3000 左右，生成的模拟投影图像为图 5-5(c)。显然投影模拟图像暗部区域（如鼻子和左眼区域）出现了显著的离散光斑，极大的破坏了色调的连续性。

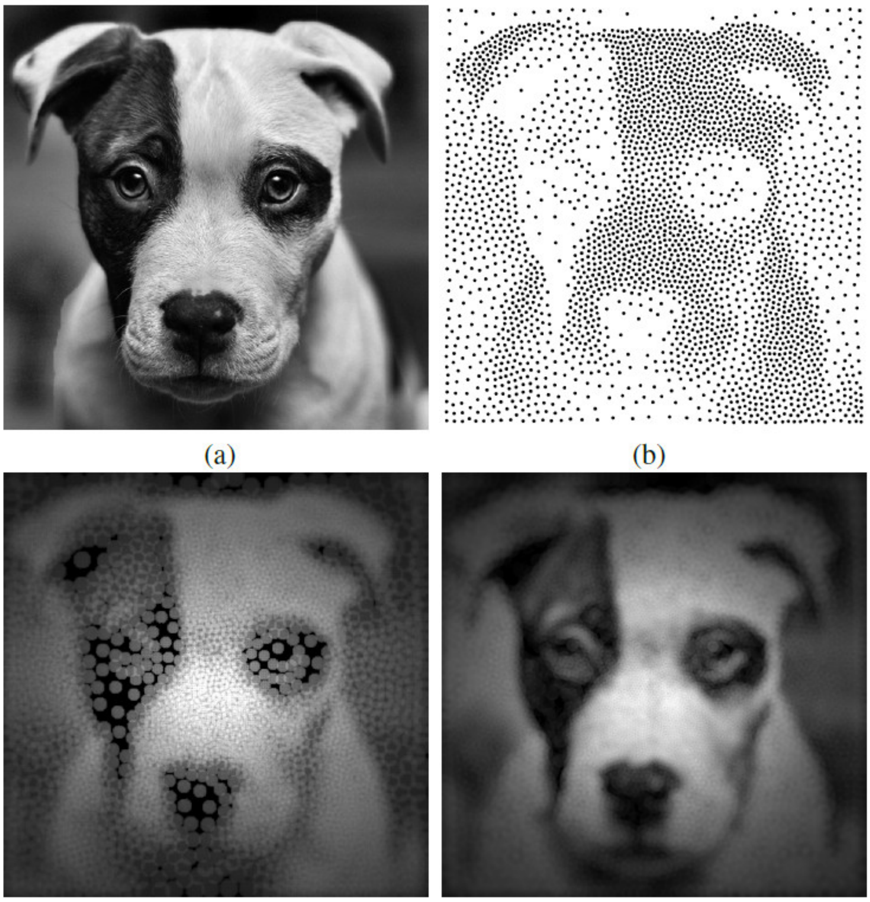

(a) (b)

(c) (d)

图 5-5 对于用户输入的目标图像(a), 直接按照点刻画的结果(b)的孔洞位置生成多孔结构灯罩产生的模拟投影图像(c)，本文方法生成的多孔结构灯罩的模拟投影图像(d)

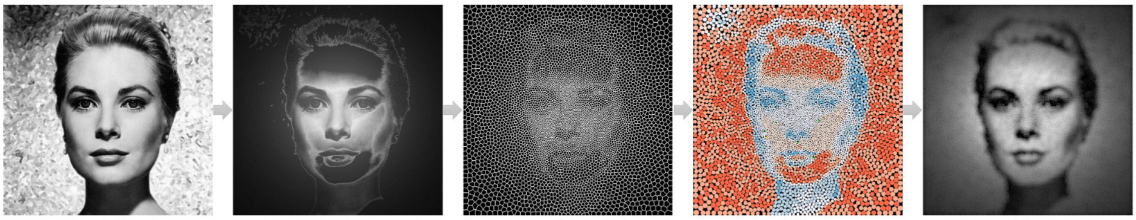

图 5-6 多孔灯罩模型生成算法流程，(a)目标灰度图像；(b)密度图；(c)带容量约束的 Voronoi 划分；(d)对应圆排列；(e)模拟投影图像

为了提升暗部色调区域图像的连续性，我们采取的策略是调整相应位置的孔洞相对于光源的朝向。这一策略使得孔洞仍然以紧密的方式排列，并不会影响图像的连续性。在图 5-5 给出的实例中，应用上述方法可以在多孔灯罩上分布 6000 个左右的孔洞，图 5-5(d)展示了相应的模拟投影图像，暗部区域的色调连续性得到了明显的改善。

任意灰度图像I^t对应的多孔结构灯罩上面的孔洞排列，都可以看作是一种紧闭的圆排列。该圆排列中任意两圆都不相交，相邻两圆满足相切关系。灯罩上面的孔洞处于圆排列中圆盘内部，为了满足可达性的约束，圆盘内部孔洞外沿到圆盘边界的距离不能小于$0.5d_{min}$。根据I^t生成特定圆排列的问题，实际上指的是I^t中某处的灰度值可以对应为相应位置圆盘的半径距离，这两个满足意义对应的关系。本文中将表示圆盘中各处圆盘半径大小组成一个密度标量场。求解该密度场，必须依赖于解决图像特定位置灰度与其对应圆盘半径大小的对应关系。

如图 5-6，基于该密度图，我们通过一个带容量约束的 Voronoi 划分计算出相应的圆排列。基本思路为要求生成的带容量约束的 Voronoi 划分之后的 Voronoi 单元的权重与密度标量场是相对应的，之后通过在每个 Voronoi 单元内部生成其最大内接圆，得到相对应的圆排列。根据圆排列结构在灯罩曲面上生成三维多孔结构，用于三维打印制造，最终取得投影图像。

5.3.1 密度标量场

对于用户给定的灯罩三维曲面模型，目标灰度图像I^t以及相应的投影接收面设置，首先生成满足可打印性约束的最密集排列的孔洞结构，将对应的投影模拟图像用符号B_0表示，如图 5-4(b)。具体的投影模拟方法将在下文中介绍。

模拟投影图像B_0表明了单独通过调节孔洞半径可以达到的最暗的色调值。更暗的色调只能通过调整孔洞相对于光源的朝向得到。在此根据孔洞是否调整过相对于光源的朝向，将孔洞分为扩大型孔洞和倾斜型孔洞。称模拟投影图像B_0为投影参考图像。与投影参考图像B_0相比，扩大型孔洞用于生成较B_0亮的色调；倾斜型孔洞用于生成较B_0暗的色调。

根据成像原理，人眼能够观察到投影接收面上的投影图像，是因为投影接收面对光源发出的光线进行了漫反射，摄入人的眼睛形成视觉可以感知的图像。人类视觉可以感知的灰度图像与实际摄入的光线能量值必须经过 gamma 校正的过程。基于此，对于给定的灰度图像I^t，通过逆 Gamma 校正得到照度图。对于灰度图像I^t上某一点$p(x,y)$的灰度$I^t(p(x,y))$，辐射照度为$E_v(p)=g^{-1}\left(I^t(p)\right)$，其中$g^{-1}(.)$为逆 Gamma 校正过程，gamma 参数取标准值 2.2。

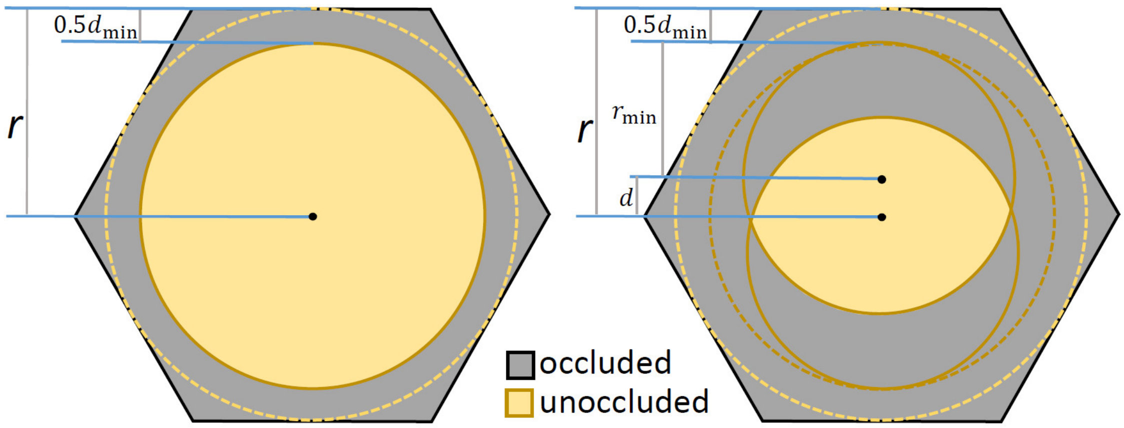

图 5-7 正六边形中遮光率的计算，左图：扩大型孔洞；右图：倾斜型孔洞

对于照度图的每一点$p(x,y)$，其对应辐射照度为$E_v(p)$。我们通过控制点$p(x,y)$处光线被多孔结构灯罩遮挡的程度，以达到特定的辐射照度$E_v(p)$：

$$E_v(p)=KE_v^0(p(x,y)) \qquad (5\text{-}1)$$

其中，$E_v^0(x,y)$为点$p(x,y)$在没有任何三维模型遮挡的情况下的总辐射照度$E_v^0(x,y)=\sum_i\frac{\Phi_i}{\pi r_i^2}\cos(\theta_i)\cos(\theta_p)$。$E_v^0(x,y)$的计算细节请参考下文的投影模拟的计算部分。$K$表示点$p(x,y)$处灯罩对光源发生光线形成遮罩的遮光率，可以被定义为：$K=Area(unoccluded)/Area(Cell)$。可将$K$表示为$r$的函数形式。如图 5-7，$r$为正六变形内最大内切圆的半径，$r_{min}$为可打印孔洞的最小半径，$d_{min}$为可打印两孔洞间的最小距离。

若$I^t(p(x,y)) \geq B_0(p(x,y))$，需要排列扩大型孔洞，有：

$$K(r) = \frac{\pi(r-0.5d_{min})^2}{2\sqrt{3}r^2} \quad (5\text{-}2)$$

若$I^t(p(x,y)) < B_0(p(x,y))$，需要排列倾斜型孔洞，有：

$$K(r) = \frac{r_{min}^2 cos^{-1}\left(\frac{d}{r_{min}}\right) - d\sqrt{r_{min}^2 - d^2}}{\sqrt{3}r^2} \quad (5\text{-}3)$$

其中$d = r - r_{min} - 0.5d_{min}$。由上述公式可得，对于照度图上点$p(x,y)$，为达到$E_v(p)$，期望最大内切圆的半径为$r$。$r$为三维模型表面上相应最大内切圆的半径，其在投影接收面对应圆的半径为r_w，使投影接收面上相应位置上半径为r_w的圆在点$p(x,y)$对应三维模型处的投影面积与半径为r的圆的面积相等；对于照度图上点$p(x,y)$，其相应的投影接收面上圆半径为r_w，定义点$p(x,y)$处密度$\rho_w(x,y) = 1/r_w^2$，经过归一化，得到密度图M。

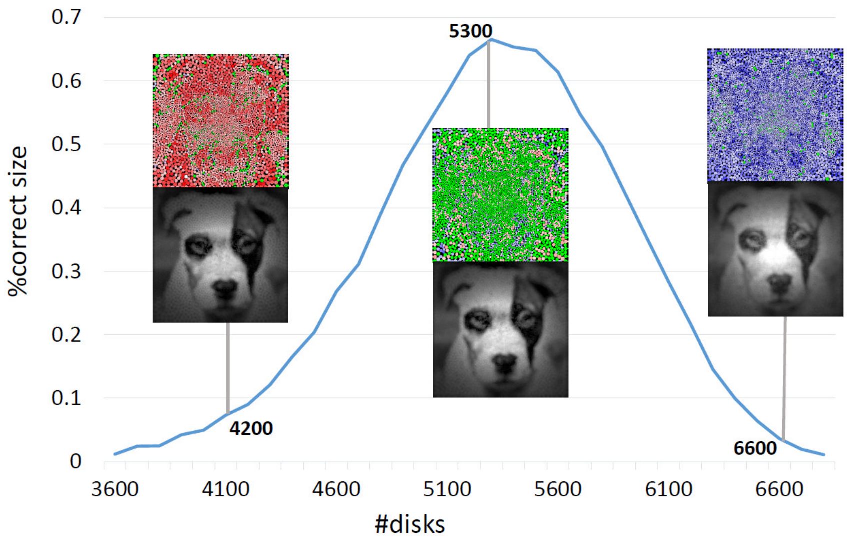

图 5-8 圆尺寸正确率与目标圆个数的变化关系

5.3.2 圆排列

给定上一步骤计算的密度图M，设定最优目标圆盘个数为N，调用 de Goes 等人提出以最有传输方法求解带容量约束的 Voronoi 划分[109]，之后在每个 Voronoi 单元中生成其最大内接圆，得到结果圆排列。

尽管 de Goes 等人的方法能够保证严格满足容量一致的约束，然而生成的 Voronoi 单元形状不可能都是正六变形的形状，因此生成的最大内接圆的大小有可能达不到密度图M中标明的理想大小。理想的最优目标圆盘个数为N的计算公

式为$N=\rho_m N_0/\rho_0$，其中ρ_m为密度图M的累加密度值，ρ_0为B_0的累加密度值，N_0为B_0的圆个数。给定密度图M和目标圆个数N，通过调用 de Goes 的方法计算 CCVT。在结果 CCVT 的每个 Voronoi 单元中计算其最大内切圆得到一组圆排列。对于某个 Voronoi 单元，其对应密度图M的某一块区域，区域中所有采样点对应的半径r_w的均值作为该区域的期望圆大小。由此判定该区域的最大内切圆是否达到其期望圆大小。以目标圆个数N为上界，通过二分搜索查找达到最优圆正确率的 CCVT。如图 5-8 对圆尺寸正确率与目标圆个数的变化关系进行了可视化。

如图 5-8，经过二分查找得到的最优圆正确率为70%左右，即表明仍有 30%左右的圆盘实际尺寸与期望的理想尺寸不符合。对于这些圆盘，我们采取一种后处理的方式提升最优圆正确率。后处理的基本思路为，对于实际尺寸偏大的圆盘，直接在相应 Voronoi 单元内部放置满足理想尺寸的圆盘；对于实际尺寸偏小的圆盘，局部的删除部分 Voronoi 站点，进行局部的多次 Lloyd 迭代[129]，以期扩大局部的 Voronoi 单元内接圆盘的尺寸。

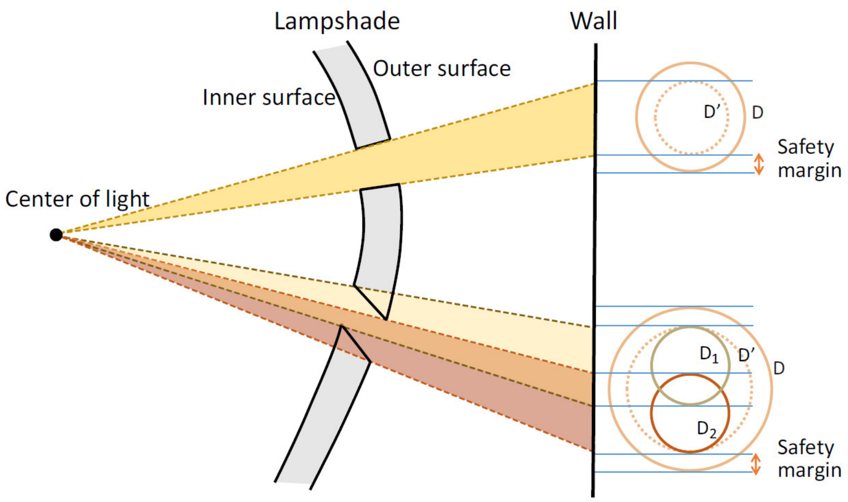

图 5-9 扩大型孔洞和倾斜型孔洞的生成

5.3.3 孔洞生成

根据上一步骤生成的圆排列，生成其对应的多孔结构灯罩上的孔洞。首先根据得到的最优正确率的 Voronoi 区域和其对应圆排列，将其对应的密度图的区域中多数点标明的孔洞类型作为该 Voronoi 区域期望的孔洞类型；之后根据任意 Voronoi 区域期望的孔洞类型，在其三维模型的对应位置生成相应的孔洞。

如图 5-9，若某 Voronoi 单元对应的孔洞类型为扩大型孔洞，生成方法为：在该 Voronoi 单元的最大内切圆嵌套一个缩小一个安全距离$0.5d_{min}$的内切圆，将该内切圆按照中心投影的方式投影在三维壳状模型的外表面和内表面，分别形成两个相交的椭圆，使用一个圆柱形结构连接内外表面的椭圆形成该扩大型孔洞。

如图 5-9，若某 Voronoi 单元对应的孔洞类型为倾斜型孔洞，生成方法为：在该 Voronoi 区域的最大内切圆嵌套一个缩小一个安全距离$0.5d_{min}$的内切圆，在该内切圆内选一个随机方向放置两个半径满足可打印条件的最小圆D_1和D_2，分别将D_1和D_2通过中心投影的方式投影在三维壳状模型的内表面和外表面，分别形成两个相交的椭圆，使用一个圆柱形结构连接内外表面的椭圆形成该倾斜型孔洞。

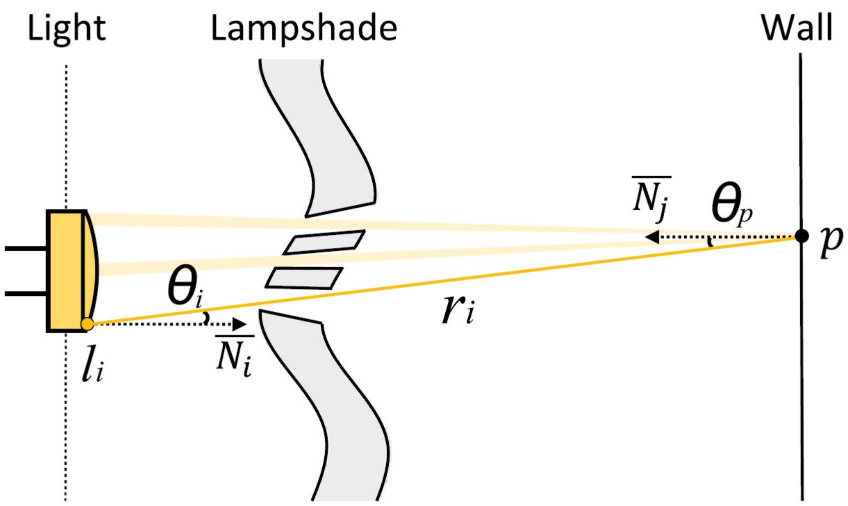

图 5-10 投影模拟

5.3.4 投影模拟

放置在灯罩内部的光源发出光线，通过多孔结构灯罩上面的孔洞结构照射在投影接收表面上，经过投影接收平面的漫反射作用将光线反射进入人眼或相机等图像采集设备，最终形成投影图像。投影接收平面上投影区域每一点的漫反射光照强度与光源本身的光源特性，二者的相对位置关系，多孔灯罩的遮罩等因素都有关系。

本工作中使用的光源假定为一个小而亮的 COB(Chips on Board) LED 面光源，该光源的光通量为Φ，可看作直径为 9mm 的状近似圆盘形状。将光通量为Φ的光源L离散化为数量为n的离散点光源$\{l_i\}_{i=1}^{n}$，每个点光源l_i的光通量为$\Phi_i =$

Φ/n。本文的实验中设置$n = 76$。在投影接收面的投影区域离散采样有限个数的投影接收点，如图 5-10 中的点p。COB 面光源可以看作是一种朗伯体光源[130]，根据朗伯体光源的光线传播特点，在多孔灯罩的遮挡作用下，投影接收点p的总辐射照度$E_v(p)$为所有点光源$\{l_i\}_{i=1}^n$发出的光到该点p的辐射照度累加和:

$$E_v(p) = \sum\nolimits_i \frac{\Phi_i}{\pi r_i^2} \cos(\theta_i) \cos(\theta_p) \mathrm{V}(\mathrm{p}, l_i)$$

其中，r_i为点p到光源l_i的欧式距离，θ_i和θ_p为连接点p和l_i的直线和点p和l_i处法线$\overline{N}_j$和$\overline{N}_i$的夹角，$\mathrm{V}(\mathrm{p}, l_i)$为点$p$和$l_i$的可见关系，取值为 0 代表不可见，取值为 1 代表可见；将投影接收点的总辐射照度$E_v(p)$，通过 Gamma 校正得到投影模拟图像灰度值$I^t(p) = g(E_v(p)) = (E_v(p))^{1/\gamma}$，其中$g(.)$表示 Gamma 校正过程，通常 Gamma 函数γ取值为 2.2。

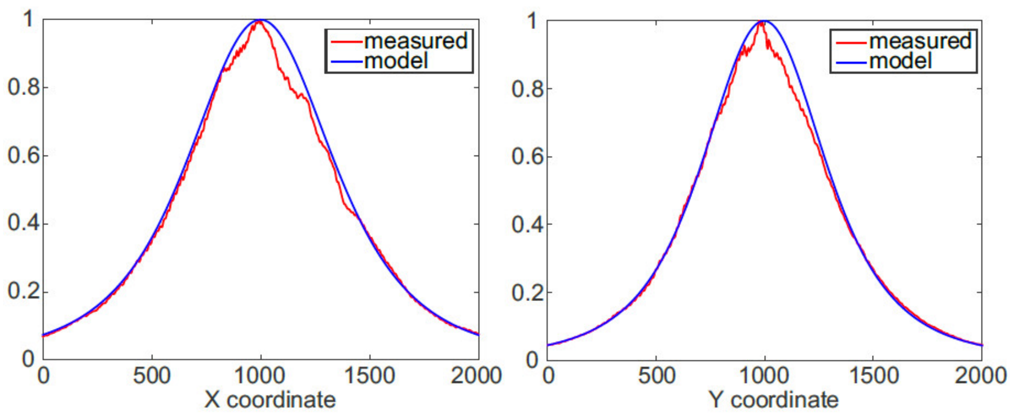

图 5-11 光源校正

在实际实验中，我们发现本文中应用的 COB 面光源并不完全满足朗伯体光源的发光特征，具体表现在随着角度θ_i的增大，光源发出的光照强度会随之衰减，另外该 COB 光源表现处一定的各项异性的特征，在投影接收面的的垂直方向上光照强度衰减的更快。为了校正光源的这种差异，我们对投影接收面上的点p的坐标增加了两个修正系数，对于水平和垂直方向的系数分别为 1.7 和 1.9。如图 5-11，应用修正系数后用照度计分别测量水平和垂直方向的照度，与模拟的数值进行比较。

为了验证投影模拟算法的有效性，我们针对一个具有不同倾斜角度的倾斜型孔洞进行了实际测试并生成其对应的模拟效果。如图 5-12 展示了实际测试的投影光斑照度值和模拟计算的照度值，可以看到模拟算法还是非常准确的。

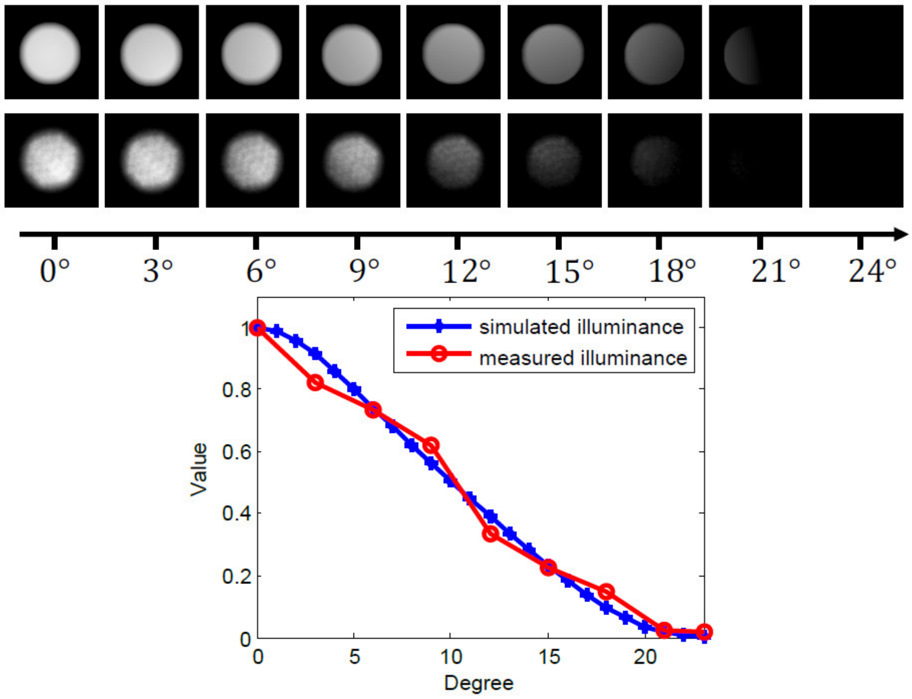

图 5-12 不同角度的倾斜型孔洞的实际投影和模拟计算的比较

5.4 实验结果与分析

图 5-13 多孔结构灯罩实验环境设置

5.4.1 实验环境

我们在不同的灰度图像上测试上文提出的多孔结构灯罩模型生成方法，并且搭建了相应的投影实验环境，以测试生成的多孔结构灯罩的真实投影效果。如图 5-1 和图 5-14 展示了打印的多孔结构灯罩模型及其投影图像，其中的灯罩模型的三

维形状是标准的球形，每个球灯罩前后两面制作了可以投影不同灰度图像的多孔结构灯罩。如图 5-13 展示了本文的投影实验环境，所用光源为色温3000K的 Cree® XLamp® CXA1507 LED，该光源大致成直径约为$9mm$的圆盘形。用一个漫反射效果良好的投影幕布作为投影接收面，投影接收区域范围设置为$100 \times 100cm^2$。文中所有的实际投影照片都是从幕布后面拍摄得到的，所用相机的型号为 Canon EOS 5D Mark II，曝光时间设置为1/80秒，焦距 f/4.0，感光度 ISO 设置为 400，拍照过程中保证室内其他光源都关闭。

图 5-14 多孔结构灯罩及其投影图像的结果展示

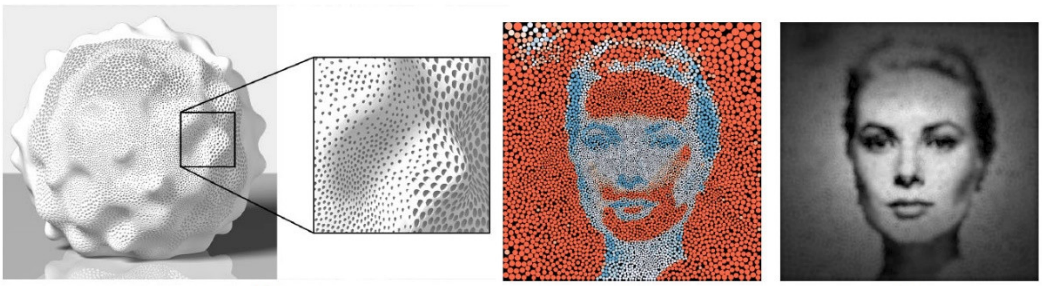

图 5-15 非球形多孔结构灯罩及其投影图像的结果展示

5.4.2 多孔结构灯罩

如果 5-14 中展示了针对不同的灰度图像生成的多孔结构灯罩及其对应的真实投影图像。这些测试用的多孔结构灯罩是在一台粉末打印机上打印完成的，所用三维打印机的型号 ProJet® 660Pro，球形灯罩壁厚设置为$3mm$。在所用粉末三维打印机上测试可得，孔洞的最小半径r_{min}设置为$0.6mm$，相邻孔洞的最小间距d_{min}设置为$0.5mm$。打印的球形灯罩的直径设置为$22cm$，制造一个完整的球形灯罩所需的打印时间约为16.5小时再加上 1 个小时干燥处理过程。本文提出的方法同样适用

于非球形的灯罩结构，如图 5-15 展示了一个表面起伏不妨的多孔结构灯罩及其对应的模拟投影图像。表 5-1 给出了多孔结构灯罩的部分统计信息，包括模型生成过程中计算的初始孔洞数目，最终的孔洞数目以及最终的圆尺寸正确率。算法运行时间方面，本文提出的多孔结构灯罩模型生成算法最耗费时间的步骤为，应用 de Goes 等人的方法生成带容量约束的 Voronoi 划分的步骤，和生成孔洞几何结构的步骤，生成一组孔洞数目为 6000 左右的多孔结构灯罩，前者通常花费 5 分钟，后者大约花费时间为 1 分钟。该程序运行时间数据是在一台 8GB 内存的 Intel® Core™ i5 CPU 3.3GHz 台式机上测试得到的。

Model	Initial #disks	Final #disks	% correct size
Marilyn	7323	5789	79.47
CircularRamp	7914	6321	87.73
Hepburn	7617	5945	82.50
Kelly	7563	5914	80.74
Marlon	7167	5607	81.34
Toucan	6926	5352	75.76
Lion	7243	5650	74.81
Dog	7891	6055	82.12
Kelly (bumpy)	8912	7120	65.17

表 5-1 多孔结构灯罩的统计信息

5.4.3 量化测试

我们还对本文生成的多孔结构灯罩进行了定量分析，如图 5-16 给出了两张输入灰度图像及其对应的模拟投影图像，真实投影图片，并给出了他们各自的灰度直方图。从同心圆图像的量化分析结果可以看出，本文算法生成的投影图像难以表现只有四个色调的灰度图像，生成的模拟投影图像和实际拍摄投影图像的直方图中也有四个类似的波峰，然后都分散在附近的灰度范围附近。从梦露图像的量化分析结果可以看出，输入图像的直方图分布比较均匀，然而本文方法生成的模拟图像和实际拍摄摄影图像的直方图中的暗部区域过多。

从如上量化分析的结果可以看出，本文方法生成投影模拟图像的劣势。本文方法生成的投影模拟图像中心区域不利于表达暗色调图像，因为需要极大的倾斜角度，而倾斜角度的增大又会降低图像的分辨率；而生成投影模拟图像的边界区域，不利于表达亮色调图像，因为随着偏离光源投射正方向距离的增大，能表现的最高

亮度会相应的缩减。

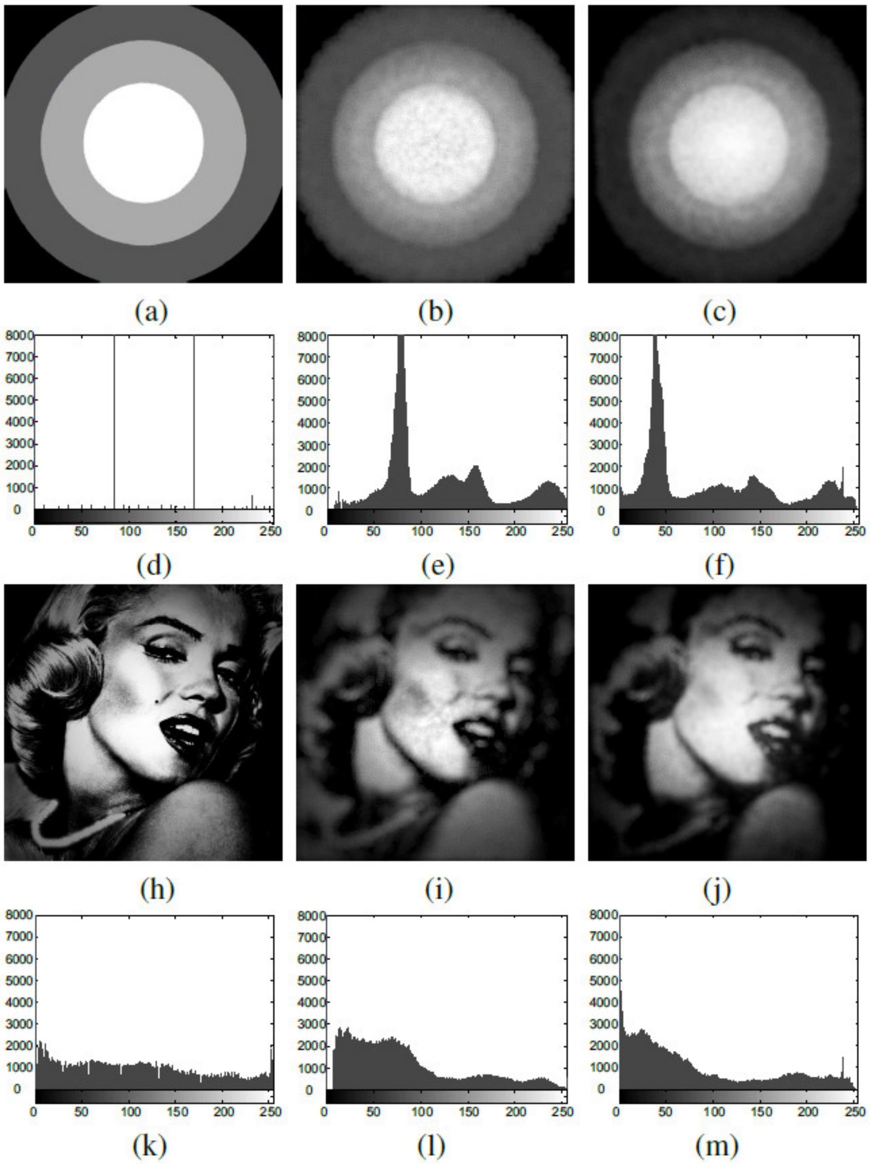

表 5-16 投影图像的量化分析

为了更准备的测试本方法对图像频率的复现能力，如图 5-17 给出了本文方法对于一系列从低频到高频的余弦图生成的模拟投影头像，从上到下分别是低频图像到高频图像，输入图像右侧给出了本文方法生成的模拟投影图像，右侧给出了输入输出图像的频率图，其中红线为输入图像，蓝线为本方法图像生成的曲线。可以看到，随着频率的提升，本方法能够表现的色调越来越差，而且最大振幅也会相应的变小。

此外，为了测试本方法生成多孔灯罩模型投影的鲁棒性，如图 5-18 给出了不同灯光位置以及偏移角度上生成的模拟投影图像。

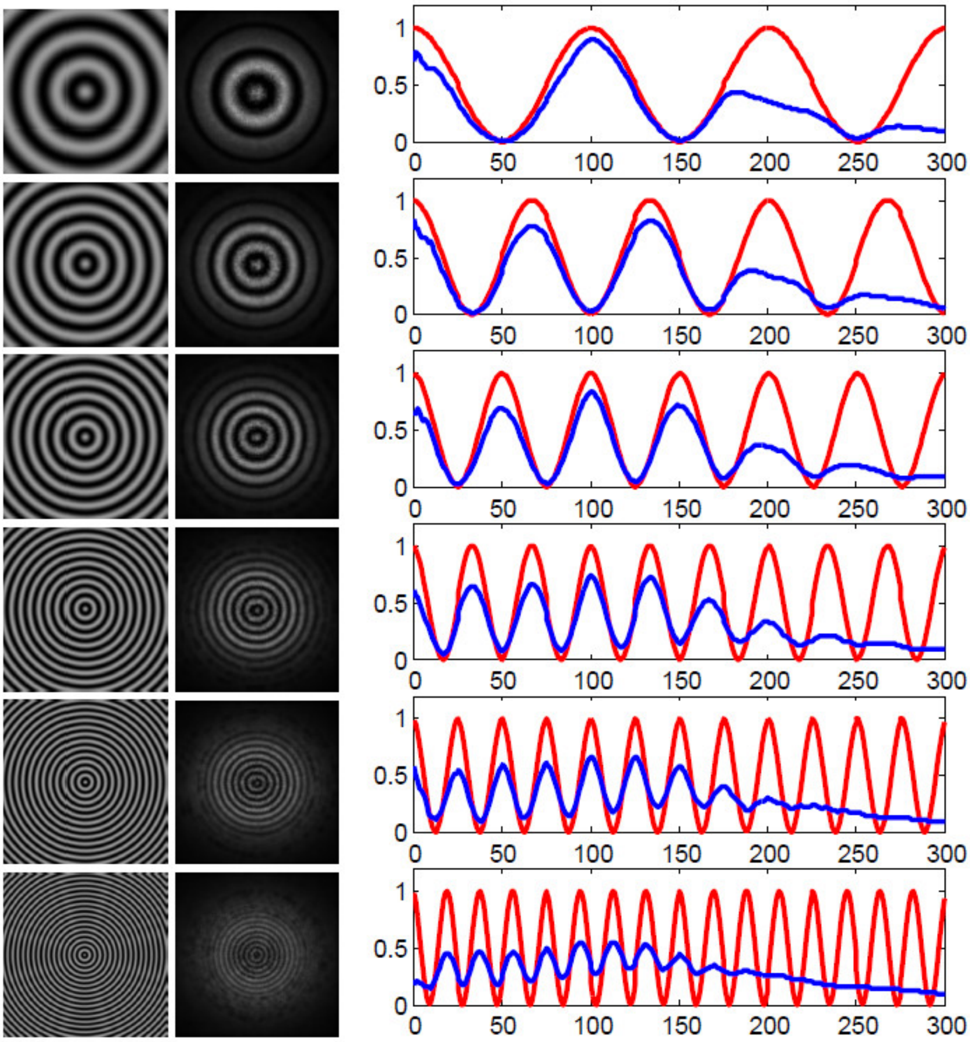

表 5-17 投影图像的量化分析

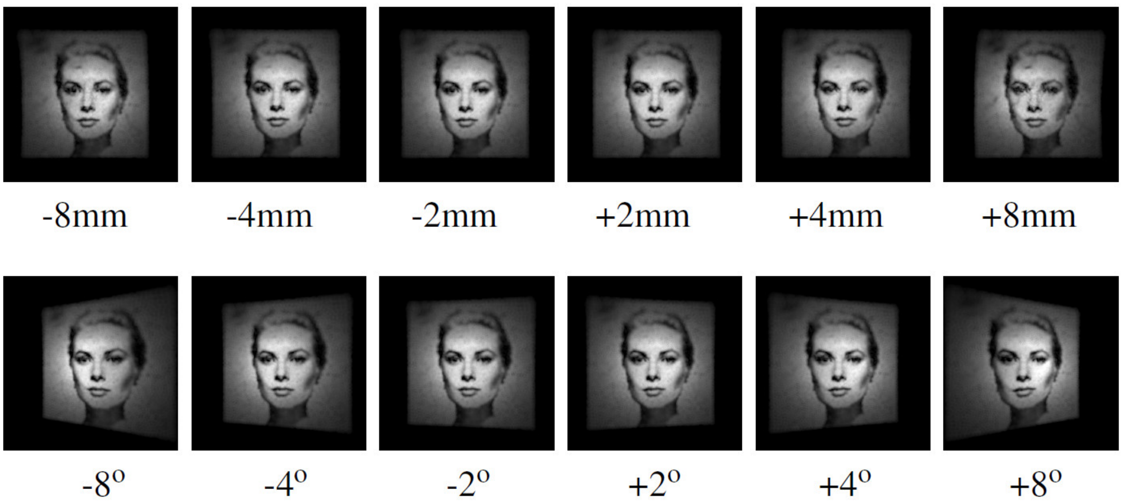

表 5-18 模型生成方法的鲁棒性分析

5.5 本章小结

本章提出了一种能够投影灰度图像的多孔结构灯罩。将传统的半色调技术应用于光线上，将光线透射形成的光斑作为显示介质，从而提出了一种新的半色调图像表达方式。提出了一种可投影该半色调图像的三维打印多孔结构灯罩的模型生成方法和一种特定的模拟方法。根据用户给定的灰度图像和三维模型，通过在模型表面上设置微小孔洞调制投影图像。对于模型上的微孔优化其大小、位置和相对光源朝向角度，同时保证可打印性的结构约束，使光源透过这些孔洞在投影面上形成一幅与给定图像最相近的连续灰度图像。实际实验表明，本文提出的模型生成方法构建的三维可打印灯罩的投影效果非常接近于原始灰度图像。

第6章 总结与展望

6.1 全文总结

本学位论文面向智能制造中的几何问题及其应用，在制造流程规划方面，具体研究了增减材制造路径规划相关的空间填充曲线生成问题，数控加工封闭自由曲面模型的装夹规划相关的区域分割问题；在增减材制造的应用方面，具体研究了基于三维打印可定制化制造的创意投影灯罩几何模型生成方法。针对这些问题，结合特定的增减材制造的约束背景，本学位论文提出了相应的解决方案。本学位论文的主要工作如下：

（1）提出一种基于费马螺旋线的三维打印路径规划方法

面向三维打印路径规划问题，提出了一种同时具有全局连续和平滑两种特性的截面填充曲线生成方法。本文将费马螺旋线引入到空间填充曲线的生成中，详细阐述了费马螺旋线作为一种新的空间填充曲线基础图案式样的优良特性。针对任意拓扑连通的区域，提出了一种连通费马螺旋线生成算法。采用分而治之的方法，将任意的拓扑连通区域分为多个相互独立的子区域分别填充费马螺旋线，之后将多条独立的费马螺旋线连接起来生成一条连续不断且平滑的空间填充曲线，并应用一种全局优化的方法在保持曲线路径间距一致的约束下对打印路径进行平滑。将连通费马螺旋线应用到三维打印的截面填充路径规划中，并与现有的三维打印路径进行比较，证明应用连通费马螺旋线路径规划算法，能够显著提升打印质量并降低打印时间。

（2）提出一种基于费马螺旋线的减材制造路径规划方法

本文探索了连通费马螺旋线的三维形式，将上文提出的截面填充曲线生成方法拓展到自由曲面精加工路径生成中，提出了一种同时满足全局连续，平滑和等残留三种特性的曲面填充曲线生成方法。等残留路径规划，要求在满足用户指定的最大残留高度的前提下，自由曲面上残留高度均匀分布。为了获得均匀分布的残留高度，自由曲面上的路径间距需要根据相邻路径对应点处的方向曲率去调节。针对用户指定的最大残留高度，自由曲面不同采样点处的方向曲率对应不同的路径间距约束。本文将自由曲面各采样点不同的路径间距约束，统一在一个约束相关的距离标量场的迭代求解中。从该约束相关的距离标量场中抽取出残留高度等值线，恰恰

满足均匀残留高度的路径分布约束，并将提取的等值线连接为连通费马螺旋线，最后对生成的连通费马尔螺旋线进行平滑处理。面向自由曲面精加工，本文提出的路径规划方法能够同时满足连续不断且平滑、区域边界相关、残留高度分布均匀的形状，通过实际的加工实验与已有的路径规划方法对比表明，本文方法可以在满足加工质量的前提下显著提升加工效率。

（3）提出一种针对封闭自由曲面数控加工的装夹规划方法

已有的装夹规划方法主要处理基本几何图元组成的 CAD 模型，本文针对三维封闭自由曲面模型，首次探索了一个自动的装夹规划方法。具体的本文设置的装夹规划的前提背景为，五轴数控机床采用定轴加工的方式（3+2 工作模式）对自由曲面模型进行加工。本文对五轴数控机床刀具相对于曲面模型的可达性进行了分析。将该装夹规划问题定义为一个可达性分析驱动的带方向标签的区域分割问题。考虑到定轴加工（3+2 工作模式）的约束，用 graph cut（图割）方法将输入模型预分割为高度场子区域。之后通过求解一个可达性分析相关的最小覆盖问题，生成装夹规划的工件方向及其对应的加工范围划分。本文提出的装夹规划技术方案具备很好的开放性，适合将装夹规划中的其他本文为考虑到的约束融合考虑。

（4）提出一种投影半色调光影图像的多孔结构灯罩几何模型生成方法

本文将传统的半色调技术应用于光线上，将光线透射形成的光斑作为显示介质，从而提出了一种新的半色调图像表达方式。提出了一种可投影该半色调图像的三维打印多孔结构灯罩的模型生成方法和一种特定的模拟方法。根据用户给定的灰度图像和三维模型，通过在模型表面上设置微小孔洞调制投影图像。对于模型上的微孔优化其大小、位置和相对光源朝向角度，同时保证可打印性的结构约束，使光源透过这些孔洞在投影面上形成一幅与给定图像最相近的连续灰度图像。实际实验表明，本文提出的模型生成方法构建的三维可打印灯罩的投影效果非常接近于原始灰度图像。

6.2 工作展望

本学位论文的研究成果将为增减材制造包括路径规划，装夹规划，以及基于三维打印的创意设计与制造提供新的思路和方法，为解决增减材制造中的其他几何问题和应用提供借鉴。论文成果有望直接应用于指导实际的增减材制造，减少人工

成本，提升增减材制造过程的加工效率和成品质量。在基于三维打印的创意设计与制造方面提出了一种新的投影图像展示技术，在室内家具，创意产品展示，艺术形象展示等领域有广泛的应用前景。但是仍有许多问题有待进一步深入研究解决，未来研究工作可沿下述方向展开：

（1）连通费马螺旋线生成算法的改进及应用推广

本文提出的连通费马螺旋线生成算法，基本思路为对距离标量场等值线进行重新连接操作，再借助一个后处理过程对路径的路径间距和平滑性进行优化。这种方法的缺点在于计算步骤比较繁复，并且无法保证绝对的空间填充特性。作为未来工作，很有必要研究一种更直接而简单的费马螺旋线生成方法。初步的解决方案为，基于阿基米德螺旋线生成原理，直接从二维截面或者三维自由曲面的距离标量场中提取连通费马螺旋线，即抛弃之前算法的提取等值线步骤。并且从距离标量场提取连通费马螺旋线的过程中同时考虑到空间填充（路径间距均匀）以及路径平滑性的约束，即无需再进行后处理优化过程。另外一方面考虑到本文当前的连通费马螺旋线生成前期并没有进行特定的区域分割操作，而针对三维打印或数控加工的路径规划的具体约束对费马螺旋线的生成区域应当有不同的考虑，因此研究不同应用背景下的自适应的区域分割方法同样是非常必要的。

此外连通费马螺旋线作为一种新的空间填充区域，探索在其他领域的应用和推广也很重要。本文已其应用于增减材制造的路径规划中。除此之外，Schüller 等人将费马螺旋线应用于三维物体的平面展开上[131]，Dai 等人将连通费马螺旋线应用于多轴打印的喷头轨迹规划上[132]。

（2）考虑超截面约束的三维打印路径规划方法

包括本文算法在内的当前大部分三维打印路径规划方法，只考虑在给定二维截面中进行填充路径的生成，对于截面生成之上的约束考虑较少。考虑超截面约束的三维打印路径规划是非常有意义的研究方向。该研究方向下可能的具体研究问题有：考虑相邻截面的路径的交错性约束生成三维打印路径规划，具体指的是为了提升打印成品模型侧向的力学特征，需要最大化相邻层路径的交错率；考虑三维打印模型方向对路径规划截面的影响，具体指的是不同的打印方向会生成不同的截面区域从而影响路径规划的质量；考虑非平面的截面生成过程并生成适于曲面截面的路径规划方法，采取非平面的截面生成主要目的是为了提升侧向的力学特征。

（3）支持夹具设计的封闭自由曲面装夹规划方法

如前文所述数控加工的装夹规划是一个典型的 NP 难问题，并且传统的装夹规划方法大多只考虑处理一般的 CAD 模型，据我们所知，本文首次针对封闭自由曲面模型提出一个实际可行的装夹规划方法。然而当前的装夹规划方法中忽视了很多实际的加工约束，比如粗加工的路径规划对装夹规划的影响，以及装夹规划过程中的夹具设计。自动的夹具规划本身就是挑战非常大的问题，需要考虑刀具切削力模拟，工件形变量计算等多种因素。当前针对于封闭自由曲面模型的自动夹具设计还研究的非常少，因此将夹具设计过程融合入本文提出的装夹规划算法中具备很好的科研价值以及应用前景。

（4）针对复杂模型的粗加工路径规划算法

本论文在第三章和第第四章分别对数控加工的路径规划和装夹规划问题提出了相应的解决方案，其中路径规划主要针对的是数控加工的精加工阶段，而装夹规划过程也没有对粗加工阶段进行进一步的探讨。针对复杂模型的粗加工路径规划算法是非常有意义的研究工作，当前学术界已有的路径生成算法大多只关注了精加工阶段的路径规划，在生成实践中粗加工阶段的路径规划仍然依赖于大量的手工操作。与精加工路径规划不同，粗加工阶段的路径规划是在三维实体空间中进行的区域分割和路径生成，其中可达性分析以及路径规划的难度可想而知

（5）投影多幅灰度图像或彩色投影图像的多孔灯罩模型生成方法

本文提出的多孔结构灯罩模型生成方法当前只考虑了一副灰度图像的投影，一项显而易见的未来工作是研究多幅灰度图像投影或者彩色图像投影。投影多幅灰度图像或者彩色投影图像的基本思路是在多孔结构灯罩中放置多个灯光源，通过设置不同的开关次序或者灯光颜色，在投影接收面上形成不同的多幅灰度投影图像或者彩色投影图像。

参考文献

[1] https://en.wikipedia.org/wiki/Manufacturing

[2] 吴鹏程. 基于曲面分片的球头刀 NC 加工刀具轨迹规划研究[D]. 南昌大学, 2012.

[3] Liu L, Shamir A, Wang CC, Whiting E. 3D printing oriented design: geometry and optimization. In SIGGRAPH ASIA Courses 2014 Nov 24 (pp. 1-1).

[4] 吴怀宇. 3D 打印：三维智能数字化创造. 北京: 电子工业出版社, 2014

[5] 刘利刚, 徐文鹏, 王伟明,等.3D 打印中的几何计算研究进展 [J][J].计算机学报, 2015, 38(6).

[6] A third industrial revolution [EB/OL], http://www.economist.com/node/21552901.2013,12,16

[7] http://www.miit.gov.cn/n1146290/n1146402/n1146435/c3328742/content.html

[8] 王伟明. 几何特征的稀疏与低秩表达及在三维打印中的应用[D]. 大连理工大学, 2016.

[9] https://en.wikipedia.org/wiki/Machining

[10] https://baike.baidu.com/item/数控加工/373170?fr=aladdin

[11] 李骏, 樊留群, 赵建华, 等. 基于区域划分的刀轨生成算法的研究[J]. 组合机床与自动化加工技术, 2014 (5): 123-126.

[12] 陈英俊，陈小童．MasterCAM 在复杂曲面数控铣削加工中的应用研究[J]．组合机床与自动化加工技术，2013(4)：96—98．

[13] Lasemi, Ali, Deyi Xue, and Peihua Gu. "Recent development in CNC machining of freeform surfaces: A state-of-the-art review." Computer-Aided Design 42, no. 7 (2010): 641-654.

[14] Hazarika M, Dixit U S. Setup planning for machining[M]. Heidelberg: Springer, 2015.

[15] Dwivedi R, Kovacevic R. Automated torch path planning using polygon subdivision for solid freeform fabrication based on welding[J]. Journal of Manufacturing Systems, 2004, 23(4): 278-291.

[16] Ding D, Pan Z S, Cuiuri D, et al. A tool-path generation strategy for wire and arc additive manufacturing[J].The international journal of advanced manufacturing technology, 2014, 73(1-4): 173-183.

[17] Jin Y, He Y, Fu J, et al. Optimization of tool-path generation for material extrusion-based additive manufacturing technology[J]. Additive Manufacturing, 2014, 1: 32-47.

[18] Gibson I, Rosen D, Stucker B. Additive manufacturing technologies: 3D printing, rapid prototyping, and direct digital manufacturing[M]. Springer, 2014.

[19] Hazarika M, Dixit U S. Setup planning for machining[M]. Heidelberg: Springer, 2015

[20] Xu N, Huang S H, Rong Y K. Automatic setup planning: current state-of-the-art and future perspective[J]. International journal of manufacturing technology and management, 2007, 11(2): 193-208

[21] https://hcie.csail.mit.edu/fabpub/

[22] Song, Peng, Xiaofei Wang, Xiao Tang, Chi-Wing Fu, Hongfei Xu, Ligang Liu, and Niloy J. Mitra. "Computational design of wind-up toys." ACM Transactions on Graphics (TOG) 36, no. 6 (2017): 238.

[23] Wang, L., & Whiting, E. (2016, May). Buoyancy optimization for computational fabrication. In Computer Graphics Forum(Vol. 35, No. 2, pp. 49-58).

[24] Li, D., Levin, D. I., Matusik, W., & Zheng, C. (2016). Acoustic voxels: computational optimization of modular acoustic filters. ACM Transactions on Graphics (TOG), 35(4), 88.

[25] Ulichney, Robert A. "Dithering with blue noise." Proceedings of the IEEE 76.1 (1988): 56-79.

[26] Lau, Daniel L., and Gonzalo R. Arce. Modern digital halftoning. CRC Press, 2008.

[27] Pang, Wai-Man, et al. "Structure-aware halftoning." ACM Transactions on Graphics (TOG) 27.3 (2008): 89.

[28] Schmaltz, Christian, et al. "Electrostatic halftoning." Computer Graphics Forum. Vol. 29. No. 8. Oxford, UK: Blackwell Publishing Ltd, 2010.

[29] Schwartzburg, Yuliy, et al. "High-contrast computational caustic design." ACM Transactions on Graphics (TOG) 33.4 (2014): 74.

[30] Prévost, Romain, et al. "Make it stand: balancing shapes for 3D fabrication." ACM Transactions on Graphics (TOG) 32.4 (2013): 81.

[31] Stava, Ondrej, et al. "Stress relief: improving structural strength of 3D printable objects." ACM Transactions on Graphics (TOG) 31.4 (2012): 48.

[32] Hildebrand, Kristian, Bernd Bickel, and Marc Alexa. "Orthogonal slicing for additive manufacturing." Computers & Graphics 37.6 (2013): 669-675.

[33] Lu, Lin, et al. "Build-to-last: strength to weight 3D printed objects." ACM Transactions on Graphics (TOG) 33.4 (2014): 97.

[34] Zhang, Xiaoting, et al. "Perceptual models of preference in 3d printing direction." ACM Transactions on Graphics (TOG) 34.6 (2015): 215.

[35] Vanek, Juraj, Jorge A. Garcia Galicia, and Bedrich Benes. "Clever support: Efficient support structure generation for digital fabrication." Computer graphics forum. Vol. 33. No. 5. 2014.

[36] Hu, Ruizhen, et al. "Approximate pyramidal shape decomposition." ACM Trans. Graph. 33.6 (2014): 213-1.

[37] Luo, Linjie, et al. "Chopper: partitioning models into 3D-printable parts." (2012).

[38] Vanek, Juraj, et al. "Packmerger: A 3d print volume optimizer." Computer Graphics Forum. Vol. 33. No. 6. 2014.

[39] Chen, Xuelin, et al. "Dapper: decompose-and-pack for 3D printing." ACM Trans. Graph. 34.6 (2015): 213-1.

[40] Yao, Miaojun, et al. "Level-set-based partitioning and packing optimization of a printable model." ACM Transactions on Graphics (TOG) 34.6 (20)

[41] Kulkarni, Prashant, Anne Marsan, and Debasish Dutta. "A review of process planning techniques in layered manufacturing." Rapid prototyping journal 6.1 (2000): 18-35.

[42] Ding, Donghong, et al. "A tool-path generation strategy for wire and arc additive manufacturing." The international journal of advanced manufacturing technology 73.1-4 (2014): 173-183.

[43] GIBSON, I., ROSEN, D., AND STUCKER, B. 2015. Additive Manufacturing Technologies, 2nd ed. Springer.

[44] Dinh, H. Quynh, et al. "Modeling and toolpath generation for consumer-level 3D printing." ACM SIGGRAPH 2015 Courses. ACM, 2015.

[45] Jin, Yu-an, et al. "Optimization of tool-path generation for material extrusion-based additive manufacturing technology." Additive manufacturing 1 (2014): 32-47.

[46] YANG, Y., LOH, H., FUH, J., AND WANG, Y. 2002. Equidistant path generation for improving scanning efficiency in layered manufacturing. Rapid Prototyping Journal 8, 1, 30–37.

[47] El-Midany, Tawfik T., Ahmed Elkeran, and Hamdy Tawfik. "Toolpath pattern comparison: Contour-parallel with direction-parallel." Geometric Modeling and Imaging--New Trends, 2006. IEEE, 1993.

[48] Jin, G. Q., W. D. Li, and L. Gao. "An adaptive process planning approach of rapid prototyping and manufacturing." Robotics and Computer-Integrated Manufacturing 29.1 (2013): 23-38. 8.

[49] Ren, Fei, Yuwen Sun, and Dongming Guo. "Combined reparameterization-based spiral toolpath generation for five-axis sculptured surface machining." The international journal of advanced manufacturing technology 40.7-8 (2009): 760-768.

[50] Held, Martin, and Christian Spielberger. "Improved spiral high-speed machining of multiply-connected pockets." Computer-Aided Design and Applications 11.3 (2014): 346-357.

[51] https://en.wikipedia.org/wiki/Space-filling_curve

[52] Dafner, Revital, Daniel Cohen‐Or, and Yossi Matias. "Context‐based space filling curves." Computer Graphics Forum. Vol. 19. No. 3. Oxford, UK and Boston, USA: Blackwell Publishers Ltd, 2000.

[53] Pedersen, Hans, and Karan Singh. "Organic labyrinths and mazes." Proceedings of the 4th international symposium on Non-photorealistic animation and rendering. ACM, 2006.

[54] Wasser, Tobias, Anshu Dhar Jayal, and Christoph Pistor. "Implementation and evaluation of novel buildstyles in fused deposition modeling (FDM)." Strain 5.6 (1999): 425-430.

[55] Arkin, Esther M., Sándor P. Fekete, and Joseph SB Mitchell. "Approximation algorithms for lawn mowing and milling☆." Computational Geometry 17.1-2 (2000): 25-50.

[56] WIKIPEDIA, 2015. Fermat’s spiral — wikipedia, the free encyclopedia. [Online; accessed 28-November-2015].

[57] JOHNSON, A., 2015. Clipper - an open source freeware library for clipping and offsetting lines and polygons. http://www.angusj.com/delphi/clipper.php.

[58] Gallager, Robert G., Pierre A. Humblet, and Philip M. Spira. "A distributed algorithm for minimum-weight spanning trees." ACM Transactions on Programming Languages and systems (TOPLAS) 5.1 (1983): 66-77.

[59] Lu, L., Sharf, A., Zhao, H., Wei, Y., Fan, Q., Chen, X., ... & Chen, B. (2014). Build-to-last: strength to weight 3D printed objects. ACM Transactions on Graphics (TOG), 33(4), 97.

[60] SLIC3R, 2016. Slic3r. http://slic3r.org/.

[61] Pottmann, Helmut, et al. "Integral invariants for robust geometry processing." Computer Aided Geometric Design26.1 (2009): 37-60.

[62] B. Choi and R. Jerrard. 1998. Sculptured Surface Machining: Theory and Applications. Kluwer Academic Publishers.

[63] Fei Ren, Yuwen Sun, and Dongming Guo. 2009. Combined reparameterization-based spiral toolpath generation for five-axis sculptured surface machining. Int. J. of Adv. Manufac. Tech. 40, 7 (2009), 760–768.

[64] Feng H Y, Teng Z. Iso-planar piecewise linear NC tool path generation from discrete measured data points[J]. Computer-Aided Design, 2005, 37(1): 55-64.

[65] Kristian Hildebrand, Bernd Bickel, and Marc Alexa. 2013. Orthogonal slicing for additive manufacturing. Computers & Graphics 37, 6 (2013), 669 – 675. Shape Model. Intl. (SMI) Conf.

[66] Debananda Misra, V Sundararajan, and Paul K Wright. 2005. Zig-zag tool path generation for sculptured surface finishing. In Geometric and algorithmic aspects of computer-aided design and manufacturing: DIMACS workshop computer aided design and manufacturing, Vol. 67. 265.

[67] Marshall S, Griffiths JG. A survey of cutter path construction techniques for milling machines. International Journal of Production Research 1994;32(12):2861–77.

[68] Cox J J, Takezaki Y, Ferguson H R P, et al. Space-filling curves in tool-path applications[J]. Computer-Aided Design, 1994, 26(3): 215-224.

[69] Griffiths J G. Toolpath based on Hilbert's curve[J]. Computer-Aided Design, 1994, 26(11): 839-844.

[70] Steffen Hauth and Lars Linsen. 2012. Double-spiral tool path in configuration space. The International Journal of Advanced Manufacturing Technology 54, 9 (2012), 1011–1022.

[71] Bo Zhou, Jibin Zhao, Lun Li, and Renbo Xia. 2016. A smooth double spiral tool path generation and linking method for high-speed machining of multiply-connected pockets. Precision Engineering (2016).

[72] Suresh K, Yang D C H. Constant scallop-height machining of free-form surfaces[J]. Journal of engineering for industry, 1994, 116(2): 253-259.

[73] Sang C Park, Chang Y C, and Byoung Kyu Choi. 2003. Contour-parallel offset machining without tool-retractions. Computer-Aided Design 35, 9 (2003), 841 – 849.

[74] Zhao, Haisen, et al. "DSCarver: decompose-and-spiral-carve for subtractive manufacturing." ACM Transactions on Graphics (TOG) 37.4 (2018): 137.

[75] Yu Wang, Kai-Min Yu, and Charlie CL Wang. 2015. Spiral and conformal cooling in plastic injection molding. Computer-Aided Design 63 (2015), 1–11.

[76] Rajneesh Kumar Agrawal, D. K. Pratihar, and Roy Choudhury. 2006. Optimization of CNC iso-scallop free form surface machining using a genetic algorithm. The International Journal of Advanced Manufacturing Technology 46, 7-8 (2006), 811–819.

[77] Ahmet Can and Ali Ünüvar. 2010. A novel iso-scallop tool-path generation for efficient five-axis machining of free-form surfaces. The International Journal of Advanced Manufacturing Technology 51, 9-12 (2010), 1083–1098.

[78] Qiang Zou, Juyong Zhang, Bailin Deng, and Jibin Zhao. 2014. Iso-level tool path planning for free-form surfaces. Computer-Aided Design 53 (2014), 217–225.

[79] Pi J, Red E, Jensen G. Grind-free tool path generation for five-axis surface machining. Computer Integrated Manufacturing Systems 1998; 11(4):337–50

[80] Marshall S, Griffiths JG. A new cutter-path topology for milling machines.Computer-Aided Design 1994;26(3):204–14.

[81] Feng, H. Y., & Li, H. (2002). Constant scallop-height tool path generation for three-axis sculptured surface machining. Computer-Aided Design, 34(9), 647-654.

[82] Makhanov, Stanislav S. "Adaptable geometric patterns for five-axis machining: a survey." The International Journal of Advanced Manufacturing Technology 47.9-12 (2010): 1167-1208.

[83] Sarma R. An assessment of geometric methods in trajectory synthesis for shape creating manufacturing operations[J]. Journal of Manufacturing Systems, 2000, 19(1): 59.

[84] Dragomatz D, Mann S. A Classified Bibliography of Literature on NC Tool Path Generation Preprint version of article that appeared in Computer-Aided Design, Vol 29, No 3, March 1997[J].

[85] Su Jin Kim, Dong Yoon Lee, Hyun Chul Kim, Sung Gun Lee, and Min Yang Yang. 2006. CL surface deformation approach for a 5-axis tool path generation. International Journal of Advanced Manufacturing Technology 28, 5-6 (2006), 509–517.

[86] Keenan Crane, Clarisse Weischedel, and Max Wardetzky. 2013b. Geodesics in heat: A new approach to computing distance based on heat flow. ACM Transactions on Graphics 32, 5 (2013), 13–15.

[87] Marcel Campen, Martin Heistermann, and Leif Kobbelt. 2013. Practical anisotropic geodesy. In Computer Graphics Forum, Vol. 32. Wiley Online Library, 63–71.

[88] Siemens. 2016. NX Software. http://www.plm.automation.siemens.com/en_us/products/nx/index.shtml. (2016).

[89] 许本胜，王灿, and 黄美发. "基于图论的计算机辅助装夹规划方法研究." 制造业自动化 36.8 (2014): 104-107.

[90] Amaitik, Saleh M., and S. Engin Kiliç. "An intelligent process planning system for prismatic parts using STEP features." The International Journal of Advanced Manufacturing Technology31.9-10 (2007): 978-993.

[91] Y-J Tseng and SB Joshi. 1998. Recognition of interacting rotational and prismatic machining features from 3D mill-turn parts. International Journal of Production Research 36, 11 (1998), 3147 – 3165.

[92] Keenan Crane, Clarisse Weischedel, and Max Wardetzky. 2013a. Geodesics in Heat: A New Approach to Computing Distance Based on Heat Flow. ACM Trans. on Graph 32, 5 (2013), 152:1 – 152:11.

[93] Haisen Zhao, Fanglin Gu, Qi-Xing Huang, Jorge Garcia, Hao Zhang, Daniel Cohen-Or, Yong Chen, Changhe Tu, and Baoquan Chen. 2016. Connected Fermat Spirals for Layered Fabrication. ACM Trans. on Graph 35, 4 (2016).

[94] Matthew C Frank, Richard A Wysk, and Sanjay B Joshi. 2006. Determining setup orientations from the visibility of slice geometry for rapid computer numerically controlled machining. Journal of manufacturing science and engineering 128, 1 (2006), 228–238.

[95] Prosenjit Gupta, Ravi Janardan, Jayanth Majhi, and TonyWoo. 1996. Efficient geometric algorithms for workpiece orientation in 4-and 5-axis NC machining. Computer-Aided Design 28, 8 (1996), 577–587.

[96] Philipp Herholz, Wojciech Matusik, and Marc Alexa. 2015. Approximating Free-form Geometry with Height Fields for Manufacturing. Computer Graphics Forum (Eurographics) 34, 2 (2015), 239–251.

[97] Thomas H. Cormen, Charles E. Leiserson, Ronald L. Rivest, and Clifford Stein. 2001. Introduction to Algorithms. MIT Press and McGraw-Hill.

[98] V. Chvatal. 1979. A Greedy Heuristic for the Set-Covering Problem. Mathematics of Operations Research 4, 3 (1979), pp. 233 – 235. http://www.jstor.org/stable/3689577

[99] Yuri Boykov, Olga Veksler, and Ramin Zabih. 2001. Fast Approximate Energy Minimization via Graph Cuts. IEEE Trans. Pat. Ana. & Mach. Int. 23, 11 (2001), 1222 – 1239.

[100] Yunjin Lee and Seungyong Lee. 2002. Geometric Snakes for Triangular Meshes. Computer Graphics Forum 21, 3 (2002), 229 – 238.

[101] KIPPHAN, H. 2001. Handbook of Print Media: Technologies and Production Methods. Springer-Verlag.

[102] Pang, Wai-Man, et al. "Structure-aware halftoning." ACM Transactions on Graphics (TOG) 27.3 (2008): 89.

[103] Schmaltz, Christian, et al. "Electrostatic halftoning." Computer Graphics Forum. Vol. 29. No. 8. Oxford, UK: Blackwell Publishing Ltd, 2010.

[104] Kim, Dongyeon, et al. "Feature - guided image stippling." Computer Graphics Forum. Vol. 27. No. 4. Oxford, UK: Blackwell Publishing Ltd, 2008.

[105] Chang, Jianghao, Benoît Alain, and Victor Ostromoukhov. "Structure-aware error diffusion." ACM Transactions on Graphics (TOG). Vol. 28. No. 5. ACM, 2009.

[106] Li, Hongwei, et al. "Anisotropic blue noise sampling." ACM Transactions on Graphics (TOG) 29.6 (2010): 167.

[107] Li, Hua, and David Mould. "Structure-preserving stippling by priority-based error diffusion." Proceedings of Graphics Interface 2011. Canadian Human-Computer Communications Society, 2011.

[108] Balzer, Michael, Thomas Schlömer, and Oliver Deussen. Capacity-constrained point distributions: a variant of Lloyd's method. Vol. 28. No. 3. ACM, 2009.

[109] De Goes, Fernando, et al. "Blue noise through optimal transport." ACM Transactions on Graphics (TOG) 31.6 (2012): 171.

[110] Bares, J., Bartlett, C. T., Delabastita, P. A., Encarnacao, J. L., Tabiryan, N. V., Trahanias, P., & Weeks, A. R. (1997, February). Imaging Sciences and Display Technologies. In Imaging Sciences and Display Technologies (Vol. 2949).

[111] Lou, Qun, and Peter Stucki. "Fundamentals of 3D halftoning." Electronic Publishing, Artistic Imaging, and Digital Typography. Springer, Berlin, Heidelberg, 1998. 224-239.

[112] Zhou, Chi, and Yong Chen. "Three-dimensional digital halftoning for layered manufacturing based on droplets." Transactions of the North American Manufacturing Research Institution of SME 37 (2009): 175-182.

[113] Mitra, Niloy J., and Mark Pauly. "Shadow art." ACM Transactions on Graphics. Vol. 28. No. EPFL-CONF-149329. 2009.

[114] Wetzstein, Gordon, et al. "Layered 3D: tomographic image synthesis for attenuation-based light field and high dynamic range displays." ACM Transactions on Graphics (ToG). Vol. 30. No. 4. ACM, 2011.

[115] Baran, Ilya, et al. "Manufacturing layered attenuators for multiple prescribed shadow images." Computer Graphics Forum. Vol. 31. No. 2pt3. Oxford, UK: Blackwell Publishing Ltd, 2012.

[116] Alexa, Marc, and Wojciech Matusik. "Irregular pit placement for dithering images by self-occlusion." Computers & Graphics36.6 (2012): 635-641.

[117] Weyrich, Tim, et al. "Fabricating microgeometry for custom surface reflectance." ACM Transactions on Graphics (TOG). Vol. 28. No. 3. ACM, 2009.

[118] Papas, Marios, et al. "Goal-based caustics." Computer Graphics Forum. Vol. 30. No. 2. Oxford, UK: Blackwell Publishing Ltd, 2011.

[119] Finckh, Manuel, Holger Dammertz, and Hendrik PA Lensch. "Geometry construction from caustic images." European Conference on Computer Vision. Springer, Berlin, Heidelberg, 2010.

[120] Zhou, C., & Chen, Y. (2009). Three-dimensional digital halftoning for layered manufacturing based on droplets. Transactions of the North American Manufacturing Research Institution of SME, 37, 175-182.

[121] Yue, Yonghao, et al. "Poisson-based continuous surface generation for goal-based caustics." ACM Transactions on Graphics (TOG) 33.3 (2014): 31.

[122] Schwartzburg, Y., Testuz, R., Tagliasacchi, A., & Pauly, M. (2014). High-contrast computational caustic design. ACM Transactions on Graphics (TOG), 33(4), 74.

[123] Papas, M., Houit, T., Nowrouzezahrai, D., Gross, M. H., & Jarosz, W. (2012). The magic lens: refractive steganography. ACM Trans. Graph., 31(6), 186-1.

[124] Malzbender, Tom, et al. "Printing reflectance functions." ACM Transactions on Graphics (TOG) 31.3 (2012): 20.

[125] Levin, Anat, et al. "Fabricating BRDFs at high spatial resolution using wave optics." ACM Transactions on Graphics (TOG) 32.4 (2013): 144.

[126] Lan, Y., Dong, Y., Pellacini, F., & Tong, X. (2013). Bi-scale appearance fabrication. ACM Trans. Graph., 32(4), 145-1.

[127] Willis, Karl, et al. "Printed optics: 3D printing of embedded optical elements for interactive devices." Proceedings of the 25th annual ACM symposium on User interface software and technology. ACM, 2012.

[128] Pereira, T., Rusinkiewicz, S., & Matusik, W. (2014). Computational light routing: 3d printed optical fibers for sensing and display. ACM Transactions on Graphics (TOG), 33(3), 24.

[129] Du, Qiang, Vance Faber, and Max Gunzburger. "Centroidal Voronoi tessellations: Applications and algorithms." SIAM review 41.4 (1999): 637-676.

[130] Basri, Ronen, and David Jacobs. "Lambertian reflectance and linear subspaces." Computer Vision, 2001. ICCV 2001. Proceedings. Eighth IEEE International Conference on. Vol. 2. IEEE, 2001.

[131] Schüller, C., Poranne, R., & Sorkine-Hornung, O. (2017). Shape Representation by Zippable Ribbons. arXiv preprint arXiv:1711.02450.

[132] Dai, C., Wang, C. C., Wu, C., Lefebvre, S., Fang, G., & Liu, Y. J. (2018). Support-free volume printing by multi-axis motion. ACM Transactions on Graphics (TOG), 37(4), 134.

致 谢

十一年前，爸爸和舅舅带着我从老家聊城来到省城济南上大学，记得那是我第一次离开聊城，在通往济南的长途汽车上第一次亲眼见到了那么高的山，到后来才知道济南的山顶多算是些小丘陵并不算那么高，不过在当时已经足够震撼到我了，我的老家身处华北平原东部，满眼望去都是一马平川。从济南的长途汽车总站下车，记得当时总站周边还是一片荒地，现在去看已经都是高楼大厦了。那会儿绝不会想到自己会在我的大学呆那么长时间，软件学院的四年本科，计算机学院的三年硕士和四年博士。我想今后不管走到那里，山大这个名字都将会伴随我走一生吧！最喜欢校友之歌里面的一句话，“我的山大我的家”，真心希望山大能越变越好，不负百年的历史，不负辉煌的过去！

我的博士阶段，非常非常幸运能够成为陈宝权教授的学生，并且是陈老师在山大的第一批学生。陈宝权教授是 2013 年加入山东大学的五名全球招聘院长之一，学院的其他老师都称呼陈院长，我们还是更习惯叫陈老师。陈老师是图形领域的大牛，视野非常开阔，非常重视与人交流，待人接物方方面面太多优点可以学习了。陈老师身上由一股很强的人格魅力，有陈老师在身边总是感觉很踏实，自觉不自觉的就能受到鼓舞。陈老师对我个人的影响是多方面的。科研方面对我最大的影响是将我引入到了图形学领域的“奥林匹克竞赛”——ACM SIGGRAPH 的世界中。SIGGRAPH 会议要求极致和完美的精神深深影响了我。读博这几年，粗略一算，已经赶了 7 次 SIGGRAPH 的 deadline，也参加了 5 次 SIGGRAPH 会议。从最开始的懵懵懂懂，到能够提出核心算法；从参加 SIG 会议在台下听各种大佬神采飞扬的报告，到自己也能在大会上作报告，都要感谢陈老师的悉心培养。科研之外，陈老师还为我提供了非常多参与公共服务或实验室管理的工作，组织实验室的第一次开放日活动，参与和中国青年报的合作项目，长期负责实验室讨论班的组织，每年参与许多新生的招聘面试工作，这些工作对自己的影响不亚于科研方面的培养。我原来的性格偏于沉默，在刚开始读博的时候当众说话都会紧张，这些服务型的工作锻炼了我，变了开朗乐观了很多。衷心感谢五年来陈老师对我的栽培！

2013 年，我开始了一段和交叉研究中心密不可分的奇妙旅程。在这五年时间

里，中心的老师和同学给了我非常多帮助。感谢实验室的屠长河老师、秦学英老师、吕琳老师、汪云海老师、辛士庆老师、钟凡老师、李扬彦老师及王雅芳老师等对我的帮助。其中屠长河老师经常给我鼓劲，也是我项目的固定合作者，给了我非常多有效的指导和建议；秦学英老师非常和蔼可亲，实验室的同学都称秦老师为“秦妈”，感谢秦老师带给我们的温暖；吕琳老师从我硕士阶段就是我的具体指导老师，能有机会加入交叉研究中心也要感谢吕琳老师的介绍，吕琳老师可以说是我能够开始博士阶段学习的“贵人”，非常感谢吕琳老师一直以来对我的科研工作和个人生活的关心和帮助；汪云海老师是所见过的最富有激情的科研人员，对科研工作的无比热情和积极的工作态度一直是我学习的榜样；辛士庆老师，乐观幽默的性格和扎实的学术功底让我在生活和学习中受益匪浅；钟凡老师，大隐隐于市的学者风范，不跟风不浮躁的治学态度非常值得我学习；李扬彦老师，是中心新加入的年轻老师，李老师富有创见的洞察力屡屡让我钦佩，李老师做的科研扎实实用我也是非常的欣赏；王雅芳老师和我年龄相仿，感觉王老师向知心大姐一样在我博士刚开始的阶段帮我解答了许多的疑惑。还要感谢中心的科研秘书段晓甜老师，段老师和我同届硕士毕业，平辈论交倍感亲切，非常感谢为实验室付出的辛勤汗水！

除此以外，我深深感谢的交叉研究中心的“同窗”好友们，每天与你们见面简单聊几句都让我身心愉悦。特别感谢实验室的王国峰师兄，曾琼师姐，姜新波师兄，蒋鹏师兄，徐敏峰师兄，万国伟老师，秦红星老师，魏源，陈学霖，樊庆楠，王斌，刘萌，刘健，周佳然，葛桐，王妍彦，包晓克，李茜楠，陈文拯，李昊，李化永，韩福波，王欢，李华东，徐未来，于悠扬，应建明，冯康，张梦琳，刘旸，何莎，吴伟，薄志涛，卜瑞，董思言，周强，刘珅岐，刘晓康，史明镒，邓园旻，顾方霖，曹金明，高增幅，刘霖，彭昊，李曼祎，李双，闫鑫，饶聪，孙铭超，魏卓，陶睿，徐凡，杨静如等等，是你们让我了解了该以怎样的态度做科研、该怎么与周围人更好的相处。当然，还有很多没有提到的同学；能与你们在最美好的年华相遇，是我一生的荣幸。

也特别感谢学校和学院的各位领导老师在我求学期间对我的帮助和关心，特别感谢我硕士和博士 7 年的辅导员贺平老师，张四化老师，周广鹏老师，张炜老师，何玉娟老师和于水老师等。

在读博的几年里，我有幸与以色列特拉维夫大学的 Daniel Cohen-Or 教授、加

拿大西蒙弗雷泽大学何 Richard Zhang 教授，以色列耶路撒冷希伯来大学的 Dani Lischinski 教授、以色列本古里安大学的 Andrei Sharf 教授，香港大学的王文平教授，普度大学的 Bedrich Benes 教授，南加州大学的 Yong Chen 教授，德克萨斯大学的 Qixing Huang 教授合作；他们考虑问题的方式、踏实认真的态度、善于提问的习惯都给我留下了深刻的印象，感谢！

感谢我的父母赵文臣和薛桂芝的养育之恩！和村里的同龄人相比，当年一块长大的小伙伴都是好几个孩子的爸爸妈妈了，早就开始能挣钱养家了，而我还是每天背个双肩包去实验室上学的样子，心中惭愧！漫长的求学生涯充满了二老的殷切付出，也感谢我的姐姐赵秀民，妹妹赵秀秀对我无尽的关怀！

感谢我的妻子郭倩倩，是她在博士期间给予了我无限的爱与包容。记不清有多少次因为实验课题忙的都回不了家，只能让她独自承受孤独！可以说，当科研遇到困难我束手无策的时候，文章屡投不中我心灰意冷的时候，如果没有她给我的支持，我不可能度过一个个这样的灰暗时刻。博士期间取得的所有成绩的，可以说都归功于她无怨无悔的支撑！2015 年的冬天我们领证结婚了，但是迟迟没有举办婚礼，过几天的 10 月 5 号是我们大婚的日子，在我们老家举行，愿我们长长久久，幸福美满，有一个美好的未来！

攻读学位期间发表的学术论文目录

[1] Variational circular treemaps for interactive visualization of hierarchical data. Visualization Symposium (PacificVis 2015), 81-85, 2015. (EI 收录，第一作者)

[2] 面向层次化数据的变分圆形树图,《软件学报》, 27(5):1103-1113, 2016. 第一作者(EI 收录，第一作者)

[3] Printed perforated lampshades for continuous projective images, ACM Transactions on Graphics (TOG), 35(5): 154, 2016. (CCF A 类，第一作者)

[4] Connected fermat spirals for layered fabrication, ACM Transactions on Graphics (SIGGRAPH 2016), 35(4):100, 2016. 第一作者，(CCF A 类，第一作者)

[5] DSCarver: decompose-and-spiral-carve for subtractive manufacturing, ACM Transactions on Graphics (SIGGRAPH 2018), 37(4):137, 2018. (CCF A 类，第一作者)

国家发明专利：

[1] 一种面向 3D 打印的半色调投影与模型生成方法，申请号：CN201410420912.4，授权日期：2015-11-05，第四位。

[2] 一种改进的面向 3D 打印的半色调投影与模型生成方法，申请号：CN201610150875.9，授权日期：2016-08-19，第二位。

[3] 一种自定义模型表面镂空的 3D 打印方法，申请号：CN201510656994.7，授权日期：2015-12-23，第三位。

[4] 一种面向 3D 打印的物体内部结构优化方法，申请号：CN201410230442.5，授权日期：2016.05.11，第五位。

[5] 一种基于费马尔螺旋线的 3D 打印路径规划方法，申请号：CN201610242579.1，授权日期：2016-06-29，第四位。

攻读学位期间参与科研项目及获奖情况

1、面向3D打印的物理建模与几何优化，国家自然科学基金面上项目(61272242)，参与人，2016－2019.

2、城市大数据的计算理论和方法， 国家 973 项目（No. 2015CB352500），参与人，2012－2014.

获奖情况：

[1] 山东大学 2018 年学术成果奖

[2] 山东大学 2016 年博士研究生国家奖学金

[3] 山东大学 2016 年校长奖学金

[4] 山东大学 2016 年学术成果奖

[5] 山东大学 2016 年度优秀研究生标兵

[6] 山东大学 2015 年博士生一等学业奖学金

外文论文

Printed Perforated Lampshades for Continuous Projective Images

Abstract: We present a technique for designing 3D-printed perforated lampshades that project continuous grayscale images onto the surrounding walls. Given the geometry of the lampshade and a target grayscale image, our method computes a distribution of tiny holes over the shell, such that the combined footprints of the light emanating through the holes form the target image on a nearby diffuse surface. Our objective is to approximate the continuous tones and the spatial detail of the target image, to the extent possible within the constraints of the fabrication process. To ensure structural integrity, there are lower bounds on the thickness of the shell, the radii of the holes, and the minimal distances between adjacent holes. Thus, the holes are realized as thin tubes distributed over the lampshade surface. The amount of light passing through a single tube may be controlled by the tube's radius and by its orientation (tilt angle). The core of our technique thus consists of determining a suitable configuration of the tubes: their distribution across the relevant portion of the lampshade, as well as the parameters (radius, tilt angle) of each tube. This is achieved by computing a capacity-constrained Voronoi tessellation over a suitably defined density function, and embedding a tube inside the maximal inscribed circle of each tessellation cell.

Keywords: Light projection, perforation

1. Introduction

The emergence of 3D printing technology opens new interesting opportunities for computerized halftoning. In this paper, we introduce the generation of 3D-printed perforated lampshades designed to project grayscale images onto surrounding surfaces. The spatial distribution of tone across the projection is generated by carefully controlling the amount of light shining through the printed surface. Similar to the dots used in halftoning, our basic idea is to perforate the physical 3D shell of the lampshade with small tubes, whose parameters are used to control the amount and the spatial distribution of light that emanates from the lamp and reaches a receiving surface. Figure 1 shows an example of such a lampshade and its projected image. Projecting continuous tone imagery via a perforated surface can thus be regarded as *halftoning with light* or *3D halftoning*.

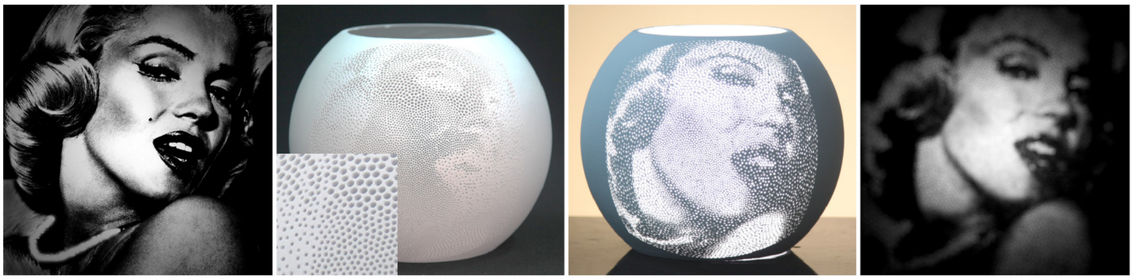

Fig. 1. A 3D-printed lampshade projecting a continuous grayscale image of Marilyn Monroe. From left to right: the target image, the 3D-printed perforated lampshade, the lampshade with a light source inside, and the resulting projection onto a nearby wall. The superposition of the individual light footprints on the wall forms a visually continuous image.

Halftoning is a technique used to represent continuous shades of gray through the use of discrete dots of the same color, varying either in size, in shape, or in spacing. The method relies on the natural low-pass spatial filtering of the human visual system that blends the discrete dot pattern into a continuous tone. Traditional halftoning uses simple-shaped dots, typically circular, of continuously varying size. However, when the dots all have the same size, spatial resolution can be traded for perceived tone resolution [Ulichney 1988; Lau and Arce 2008].

The 3D halftoning technique that we present differs from ordinary halftoning in a number of ways. First, unlike other common digital media, here one can generate dots of continuous sizes. In that sense, the technique is closer to analog halftoning, where the dot sizes are continuous. Second, dots are holes in a surface, realized as tiny 3D tubes, hence having both radius and orientation with respect to the light source. Third, the resulting image is not printed but projected, which requires to consider the geometry of both the projecting surface (the lampshade) and the receiving surface (the wall). Lastly, since the projected light footprint of each tube is slightly blurred, and multiple footprints add up in areas of overlap, there is already some low-pass filtering inherent in the image formation process. We explicitly account for the effect of overlapping footprints of adjacent tubes, which is inhibited in digital halftoning, and take advantage of it.

Moreover, it should be stressed that in our setting, the major challenge is to ensure the printability and structural integrity of the perforated lampshade. Specifically, there are strict lower bounds on the radii of the tubes, and on the inter-tube spacing. Violating the former constraint would result in clogged tubes, and the latter would render the shell fragile and prone to breakage. In particular, having a lower bound on the tube radius means that darker tones cannot be achieved by simply using smaller holes; instead, we reduce the amount of light passing through a tube by tilting it away from the light source center.

We present a 3D halftoning technique that, given the geometry of the lampshade surface, a target grayscale image, and a receiving surface, produces a spatial distribution of tubes, along with their radii and orientations, such that the resulting projected image faithfully reproduces the input image. The goal is to produce a continuous tone projected image, which strives to match the distribution of tones and the spatial detail of the original.

The target intensity at each projected location is matched by placing tubes with suitable radii and tilt angles around the corresponding location on the lampshade. Brighter areas are reproduced using tubes with a larger radius, while in darker areas we place minimal radius tubes, tilted away from the light source center. In order to maximize the spatial resolution, the tubes must be placed as densely as possible, but they must not violate the inter-tube distance constraint. To achieve this, we embed each tube inside a disk that incorporates a safety margin around the tube. Note that differently from ordinary halftoning or stippling, in our case both brighter and darker areas require larger disks, with the maximal density of disks corresponding to the middle of the grayscale range.

Having reduced the problem to one of finding a dense packing of disks with spatially varying radii, we solve it by computing a capacity-constrained Voronoi diagram over a suitably defined density function, whose value at each location is inversely proportional to the required disk area. The process is illustrated in Figure 2.

In summary, the contributions of this paper are as follows:

—We tackle the novel problem of generating projected imagery by shining light through a 3D-printed perforated surface.

—We introduce a novel 3D halftoning approach, where the halftoning dots are realized as a distribution of tubes passing through a solid surface, with varying radii and orientations.

—We present a method that determines the spatial distribution and the parameters of the individual tubes, while striving to match the target image, subject to fabrication constraints.

Our results demonstrate the effectiveness of the proposed technique using a variety of target images. The limitations of the process are also demonstrated and discussed.

2. Related works

2.1 Halftoning and Stippling

Halftoning is a classical technique which played a major role in traditional paper printing and in digital displays [Kipphan 2001; Ulichney 1987]. Our work leverages this classical technique in the new domain of digital fabrication and 3D printing.

Throughout the evolution of digital halftoning over the past decades, the dominating issues have persistently been ones point density and spatial resolution, reduction of noticeable regular patterns [Mitsa and Parker 1992], and preservation of structural details [Eschbach and Knox 1991; Pang et al. 2008; Chang et al. 2009; Li et al. 2010].

Similar to halftoning, stippling also uses spatially-varying dot patterns to convey shading. Balzer et al. [2009] propose using the capacity-constrained Voronoi tessellation (CCVT) for enforcing the constraint of equal weighted area for the region around each point in a stippled image. However, the method they propose suffers from high computational complexity. Consequently, considerable attention was given to developing faster alternatives. In particular, de Goes et al. [2012] formulate CCVT as a constrained optimal transport problem. This results in a fast-continuous constrained minimization method, which is able to enforce the capacity constraints exactly. In this work, we show how to encode the objectives and the requirements of our 3D halftoning method as a density function, which enables solving the problem by constructing a CCVT, and use the method of de Goes et al. for this purpose.

The works mentioned earlier are concerned with generating halftoning and stippling patterns in 2D, while our work focuses on creating a perforation pattern on a 3D surface with finite thickness, in the context of 3D printing. In this context, Stucki [1997] first introduced the idea of 3D digital halftoning for transforming continuous-density objects into binary representations for rendition with additive fabrication technologies. Lou and Stucki [1998] further adapt the ordered-dither and error diffusion algorithms to the 3D case, focusing on stereolithography (SLA) printing techniques. Zhou and Chen [2009] utilize 3D digital halftoning by replacing a dot with a droplet, to achieve satisfied approximation accuracy with larger layer thickness, thus reducing the fabrication time for layered based inkjet printing processes. In contrast to these works, our 3D halftoning method is designed for the purpose of forming projected imagery that reproduces the tones of a target image, subject to fabrication constraints.

2.2 Optics-related Fabrication

Recently, design or generation of illumination effects via geometric modulation has been drawing increasing attention. Mitra and Pauly [2009] introduce shadow art, an algorithm for computing a 3D volume, whose shadows best approximate multiple binary images. Subsequent approaches generalize this to colored shadows using volumetric objects manufactured by transparent acrylic [Wetzstein et al. 2011; Baran et al. 2012]. In general, they build transmittance functions to simulate light attenuation through multi-layered attenuators.

Our work is inspired by the technique of Alexa and Matusik [2012], who drill holes with varying depths on a surface to induce the given image based on the occlusion of small holes.

Research in this area has also addressed controlling light reflections and refractions using surface modeling methods. These works cast a desired caustic image by modulating the geometry using microfacets [Weyrich et al. 2009], micro-patches [Papas et al. 2011], B-spline surfaces [Finckh et al. 2010], continuous surfaces [Kiser et al. 2013; Yue et al. 2014] or normal fields [Schwartzburg et al. 2014], and then milling or engraving the surfaces. Researchers have also shown light effects in a wide range of applications, such as steganography [Papas et al. 2012], image display [Malzbender et al. 2012; Levin et al. 2013] and appearance design [Lan et al. 2013].

Printing optical fibers that control light propagation through total internal reflection between two surfaces has drawn some research attention thanks to the cutting-edge multi-material 3D printers. Willis et al. [2012] design optical fibers for customizing interactive devices in display and illumination. Pereira et al. [2014] introduce automatic fiber routing algorithm that minimizes curvature and compression for optimal light transmission.

All of the above are high-end techniques, which rely on expensive manufacturing equipment and specific materials. In contrast, our method is designed for standard 3D printing technologies and common, widely used fabrication materials, such as plastic and powder. For such materials, the light transmittance is very low, as light mostly scatters due to the surface roughness. Therefore, shape modulation for light or shadow effects based on surface reflection and refraction cannot be easily adapted. In particular, using varying material thickness to control the projected image intensity is infeasible, and our approach is designed for lampshade shells of uniform thickness.

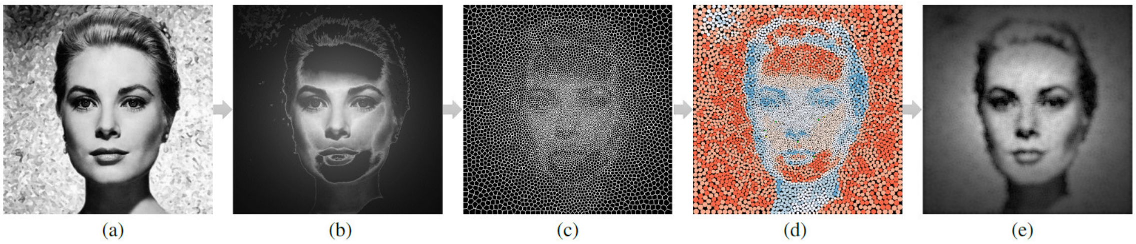

Fig. 2. Process overview: given a target image (a) we compute a density map (b) whose value at each location is inversely proportional to the required disk area (as explained in Section 3.1). Next, we compute a capacity-constrained Voronoi tessellation (c), and inscribe a maximal disk inside each cell (d). Red shades indicate disks where the radius of the embedded tube is larger than the minimal size (increasing the brightness), while blue shades indicate disks where the embedded tube is tilted (decreasing the brightness). The simulated projected image is shown in (e).

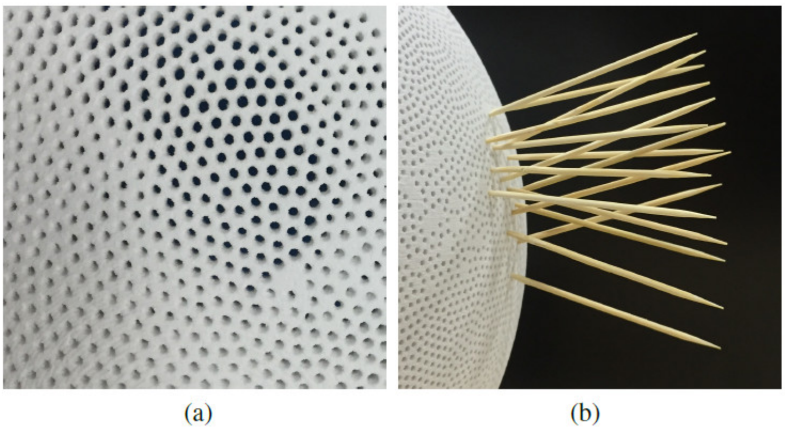

Fig. 3. The physical 3D-printed lampshade shell perforated with tubes of varying sizes and density (a), and different tilt angles (b), as may be seen from the directions of the toothpicks.

3. Perforated lampshade design

Recall that our goal is to design a 3D-printable perforated lampshade, such that the light emanating from the lamp forms a continuous tone image, which is as close as possible to a target grayscale input. Light emanates from the lamp through holes in the lamp's surface. Due to the finite thickness of the lamp's shell, the holes may be thought of as tiny tubes, whose density, radii, and orientations vary across the surface, as may be seen in Figure 3. Since the total distribution of light across the projected image is determined by the combined effect of light passing through the tubes, our challenge is to determine the tubes' parameters, while respecting fabrication constraints imposed by the need to obtain a printable and structurally sound surface.

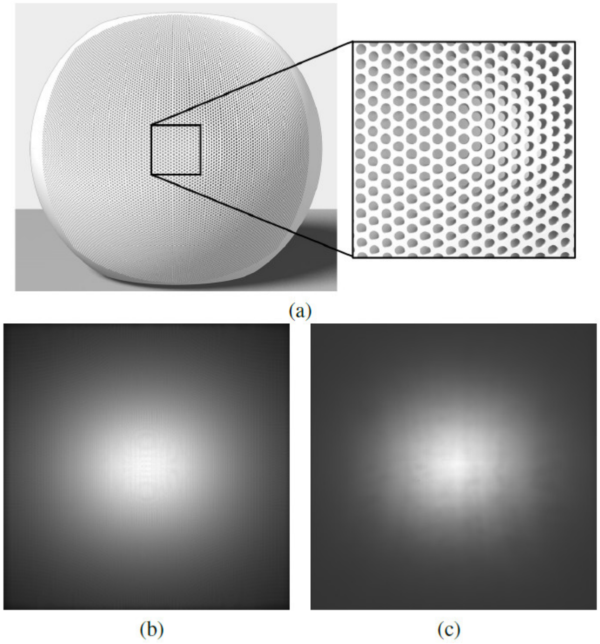

Fig. 4. (a) Maximally dense packing of the smallest printable tubes, oriented towards the center of the light source. (b) The corresponding simulation results. (c) A photograph of the actual projected image corresponding to this pattern.

Specifically, given a target grayscale image I^t our task is to configure a set of tubes perforating the lampshade shell, such that the following objectives and requirements are satisfied:

a) The projected image I^p on a given diffuse surface, henceforth referred to as the wall, closely approximates the target grayscale values across the projection. Note that the approximation is up to some scaling factor, since we have control over the total amount of luminous flux emitted by the light source, as well as over the exposure time, when capturing the projection with a camera.

b) The projected image should exhibit continuous tones, while resolving fine spatial detail, as much as possible. In order to achieve this objective, the density of the tubes should be maximized, while their radii should be minimized.

c) Fabrication constraints: (a) the radius of a tube is bounded below by r_{min} to prevent clogging during the manufacturing process; and (b) any two adjacent tubes must have a gap of width greater than d_{min} of solid material between them. When the latter constraint is violated, the shell becomes too fragile.

The densest arrangement of tubes that satisfies the fabrication constraints above is shown in Figure 4(a). This arrangement corresponds to a hexagonal packing of disks of radius $r_{min} + 0.5d_{min}$, with a tube of radius r_{min} embedded at the center of each disk. The resulting projected pattern is shown in Figure 4(c). Our setup uses a disk-shaped approximately Lambertian light source that faces a planar projection surface. Thus, the intensity falls off away from the center due to the increase in distance and in the angles between the outgoing and incident light to the surface normal of the source and the receiving surface, respectively. In order to match a target image I^t, the tube arrangement must be adjusted in a spatially varying fashion. In order to achieve brighter tones, we must increase the tube radii, but darker tones cannot be achieved by decreasing the radii, since this would violate the first fabrication constraint above.

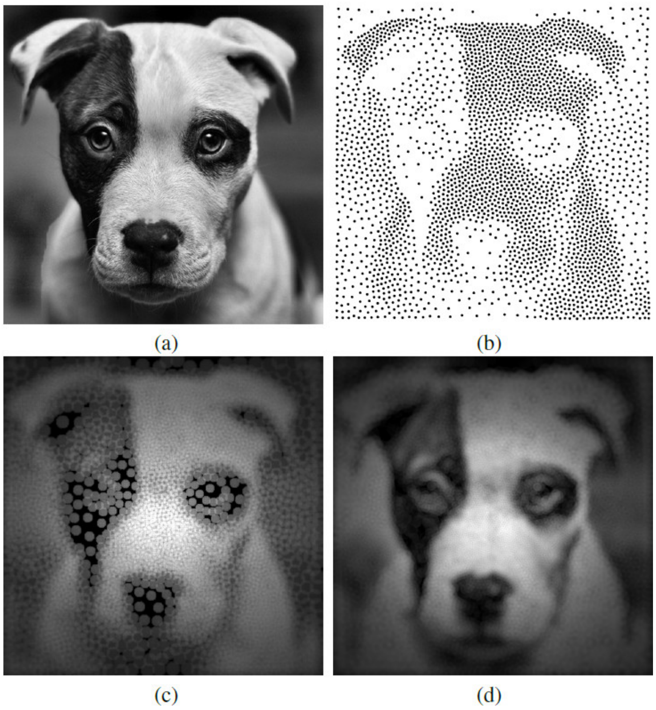

Fig. 5. For an input image (a), if we directly apply the stippling result (b) while ensuring the printability constraints, continuity and target grayscale tones cannot be achieved simultaneously in the projected imagery (c). Our method achieves a continuous result (d) by employing tube tilting to darken the tone. Here, (c) and (d) are both simulated images.

One alternative is to employ a stippling approach to generate a variable density set of tube positions that would satisfy the fabrication constraints above. However, such an approach necessitates spacing tubes much farther apart from each other in the darker areas of the image, resulting in projection of isolated light dots inside such areas. Thus, continuity and spatial detail resolution has to be severely compromised. Instead, we propose decreasing the amount of light passing through tubes in darker areas by tilting their directions away from the light source center. This solution avoids unnecessarily isolating tubes, and plays an essential role in achieving continuous gray tones in the projected imagery. It is worth mentioning that the tilting angle is not restricted by fabrication capabilities, which offers enough variable tuning range.

The inadequacy of a stippling-based approach is demonstrated in Figure 5. Here, starting from an input image (a), we use a state-of-the-art stippling method [de Goes et al. 2012] to generate the pattern in (b). In order to satisfy the fabrication constraints, the number of dots in this pattern is limited to roughly 3K. This results in a (simulated) projected image with poor continuity and isolated light spots, especially inside the darker tone areas around the dog's eyes and nose. Using our proposed solution, we are able to distribute roughly 6K tubes across the lampshade, thereby achieving the same apparent grayscale range, but in a much more continuous fashion.

Note that in order to ensure a minimal inter-tube distance, both widened tubes and tilted tubes must be placed inside larger disks on the lampshade surface, as illustrated in Figure 8. The radius of each disk is chosen so as to accommodate the widened or tilted tube, in addition to a safety margin of width $0.5d_{min}$. In summary, each target intensity at a particular location corresponds to a certain disk radius, and our goal is to distribute a set of tightly packed nonoverlapping disks with the desired radii across the relevant portion of the lampshade surface.

We attempt to achieve the required disk arrangement by computing a capacity-constrained Voronoi tessellation over a suitably defined density function, and inscribing a maximal circle inside each tessellation cell. The density function for a particular target image is determined from the differences between the target image intensity and the simulated projected image corresponding to the maximum uniform density pattern, shown in Figure 4(b).

3.1 Computing the target density function

Given the lamp setup (lampshade and wall geometry), we compute the densest arrangement of tubes that satisfies the fabrication constraints. Thus, the surface is tessellated by uniform hexagonal cells, and for each cell the maximal inscribed circle is with radius $r_{min} + 0.5d_{min}$, such that the smallest tube (radius r_{min}) can be perforated. We take the projected image as the reference B_0. The arrangement, the result of the simulation, and a photograph of the actual projected image are shown in Figure 4. The simulation process is described in detail in Section 3.4.

Image B0 indicates the darkest continuous tones that can be achieved via varying radii; hence, darker tones are achieved by tilting tubes. Given a target image I^t, the reference B0 enables us to determine the tube mode, radius enlarging or tilting. For both modes, an embedding disk with radius larger than $r_{min} + 0.5d_{min}$ is needed for shape modulation. Then we will define a density function on the wall based on the desired radii, which is used to compute a capacity-constrained Voronoi tessellation.

Since the projected image is formed on the wall by a linear combination of light transmitted through the tubes, we first linearize the given target image I^t by applying an inverse gamma correction. We assume that the target image is gamma corrected with a standard gamma value of 2.2.

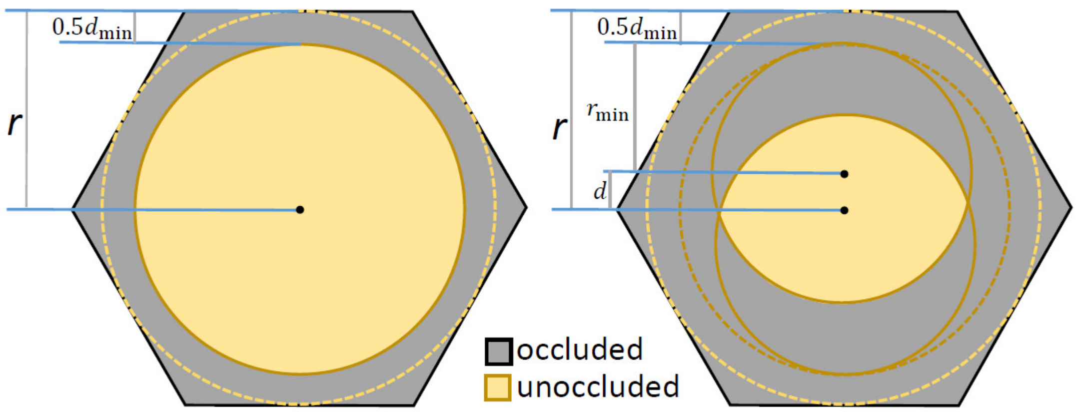

Fig. 6. The un-occluded area inside one hexagonal cell on the lampshade.

Left: un-tilted tube case; Right: tilted tube case.

For each projected image pixel $p(x, y)$, whose target grayscale value is given by $I^t(p(x, y))$, we match the target intensity by controlling the degree of occlusion of the light source by the perforated lampshade:

$$E_v(p) = KE_v^0(p(x, y)); \quad (1)$$

where $E_v^0(x, y)$ is the unoccluded illuminance of (x; y) on the wall (eq. 4), and K indicates the proportion of light un-occluded by the lampshade. For a uniform hexagonal tessellation on the lampshade, inside each cell we have $K = Area(unoccluded)/$

$Area(Cell)$. Approximating the area of each cell by that of a planar hexagon, we can express K as a function of r.

Specifically, for the un-tilted case (Figure 6 left), let r be the radius of the maximal inscribed circle inside the hexagon, then the un-occluded area is a disk of radius $r_{min} + 0.5d_{min}$ and we have:

$$K(r) = \frac{\pi(r-0.5d_{min})^2}{2\sqrt{3}r^2} \quad (2)$$

For the tilted case, the tilted tube has the radius r_{min}, and it is tilted by the maximal angle afforded by a disk of radius $0.5d_{min}$. The un-occluded area is the intersection of two disks (see Figure 6 right and Figure 8), and we have:

$$K(r) = \frac{r_{min}^2 cos^{-1}\left(\frac{d}{r_{min}}\right) - d\sqrt{r_{min}^2 - d^2}}{\sqrt{3}r^2} \quad (3)$$

where $d = r - r_{min} - 0.5d_{min}$.

Thus, starting with the densest manufacturable arrangement of tubes, by comparing the corresponding projected image B0 to the target image It we determine the locations where the tubes must be enlarged or tilted. Specifically, if $I^t(p(x,y)) \geq B_0(p(x,y))$ the relevant tubes must be enlarged with the desired cell radius determined by equation (2). On the other hand, if $I^t(p(x,y)) < B_0(p(x,y))$, the relevant tubes must be tilted and the desired cell radius is determined by equation (3).

In our current implementation, we compute the capacity-constrained Voronoi tessellation on the planar wall domain. Thus, we need to convert the desired radii on the lampshade to ones on the wall. Specifically, given a radius r of a disk on the lampshade, we compute the radius r_w of a disk on the wall, such that its projection back onto the lampshade (ellipse in the spherical case) has the same area as the original disk of radius r.

Given the target disk radii r_w across the projection area, we set the density to be proportional to the inverse of the disk area, $\rho_w(x,y) = 1/r_w^2$. The density values are normalized, such that max $\rho_w = 1$. In practice, we impose an upper bound of 1.3mm on the tube radius. Thus, the density function is bounded from below, with the actual bound varying across the projection surface.

3.2 Computing the disk distribution

Given the density function ρ_w, and a desired number of disks N, we use the method of de Goes et al. [2012] to compute the optimal Voronoi tessellation satisfying the equal capacity constraint, and fit a maximal inscribed disk inside each of the resulting tessellation cells.

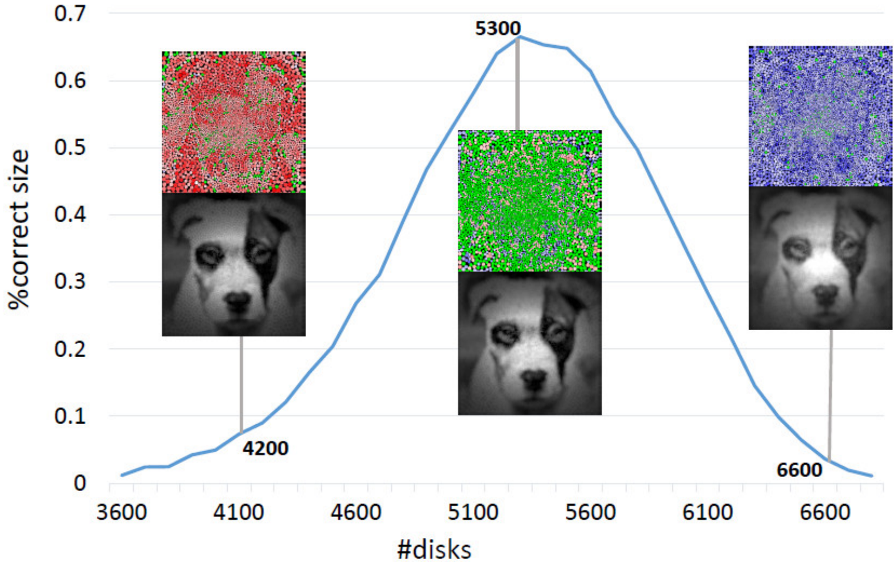

Fig. 7. The percentage of correctly sized disks is plotted as a function of the total number of disks. The disks and corresponding simulated images are shown for three locations on this curve. Disks that achieve their intended radius are indicated by green shades. Red and blue disks indicate that they are larger or smaller than the desired radius, respectively.

Although the above method is able to enforce the capacity constraints exactly, the resulting Voronoi cells are not necessarily hexagonal, and thus some of the maximal inscribed disks may deviate from their intended size. We estimate an initial value for N by computing ρ_d, the amount of density per disk in the dense reference pattern B_0, and dividing the integral of the target density function by ρ_d. We found that this estimate typically results in a large percentage of disks being too small. We thus employ a binary search to find the number of disks N for which the percentage of disks which achieve their intended radius (within 0.05mm) is greatest. Figure 7 shows demonstrates how the percentage of correctly sized disks varies with the total number of disks for the dog example.

While most disks are acceptably close to their desired radius, there are still disks which are too large or too small. Consequently, the amount of light transmitted through the embedded tubes could be smaller or larger than the desired intensity. Larger disks are handled by reducing the embedded tube radius or tilt angle, as needed to match the originally intended ones. Smaller disks are resolved by locally reducing the density in such areas. For each group of such disks, whose Voronoi cells are connected, we remove disks randomly one by one. After each disk removal, we enlarge the group of cells along the one-ring neighborhood to include their immediately neighboring cells, and locally relax the remaining disks in this area via centroidal Voronoi tessellation using Lloyd's method.

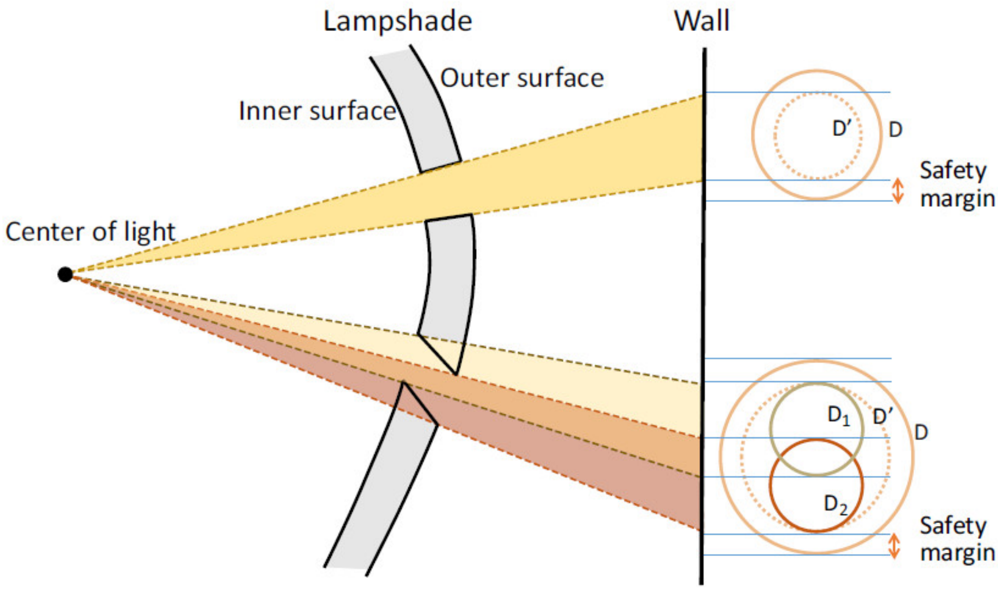

Fig. 8. Illustration of the tube generation.

3.3 Tube generation

For each disk D centered at $p(x,y)$ with radius r_w onS_w, we first subtract the safety margin to obtain a smaller concentric disk D_0.

In the case where $I^t(p(x,y)) \geq B_0(p(x,y))$, we generate a tube directed at the center of the light source by intersecting the oblique circular cone defined by D_0 and the light source center with the lampshade shell, as shown in Figure 8.

If $I^t(p(x,y)) < B_0(p(x,y))$, a minimal radius tilted tube is generated inside the inner disk D0. In order to avoid structured artifacts, the orientation of the tilted tube inside D0 is chosen at random by placing two minimal radius disks D_1 and D_2 near the circumference of D_0. D_1 and D_2 are then projected onto the outer and the inner surfaces of the lampshade shell, respectively (see Figure 8). The tilted tube is formed by connecting the two resulting contours. Note that the tilt angle grows with the radius of D_0.

At this point, a printable 3D model of the perforated lampshade may be generated and printed by a 3D printer.

3.4 Projected image simulation

The projected image is formed by the light emanating from the light source inside the lamp, passing through the tubes in the lampshade and reaching a receiving surface (wall). Thus, the amount of reflected light at each point on the wall depends on the emission characteristics of the light source, the geometric relationship between the light source and the receiving point, the visibility between them, and the reflectance characteristics of the wall.

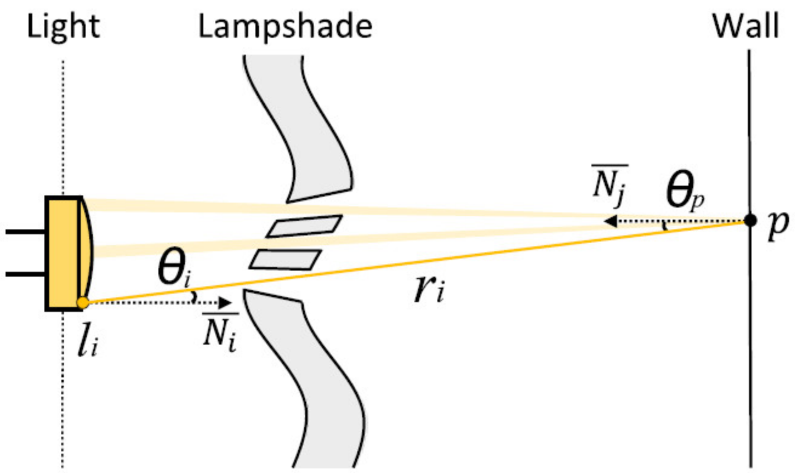

Fig. 9. Illustration of the illuminance computation.

The light source that we use in this work is a small and powerful COB (Chips on Board) LED, which is roughly disk-shaped with a diameter of 9mm. In our simulations, we represent this area light source as a collection of n point light sources $\{l_i\}_{i=1}^{n}$, each emitting a luminous flux of $\Phi_i = \Phi/n$, where Φ_i is the luminous flux for the entire light source, measured in lumens. We use $n = 76$ in our results.

For a Lambertian light source and a Lambertian reflector, the total illuminance $E_v(p)$ (in lux) reaching a point p on the receiving surface is given by

$$E_v(p) = \sum_i \frac{\Phi_i}{\pi r_i^2} \cos(\theta_i) \cos(\theta_p) \mathrm{V}(\mathrm{p}, l_i) \quad (4)$$

where r is the distance from p to l_i, and θ_i and θ_p are the angles between the line connecting the two points and the two normals, as shown in Figure 9. $\mathrm{V}(\mathrm{p}, l_i)$ is the visibility between p and l_i.

In practice, we found that our light source is not Lambertian, and its emitted luminance diminishes as the angle θ_i increases. Furthermore, we found that this behavior is slightly anisotropic, and the luminance diminishes more quickly in the vertical direction. Empirically, we found that the non-Lambertian behavior and the anisotropy are still well modeled by Equation (4), provided that the horizontal and vertical coordinates of the point p (with respect to the center of the image) are each scaled by an appropriate factor. Specifically, the scaling factors that we use are 1.7 and 1.9 for the horizontal and the vertical coordinate, respectively.

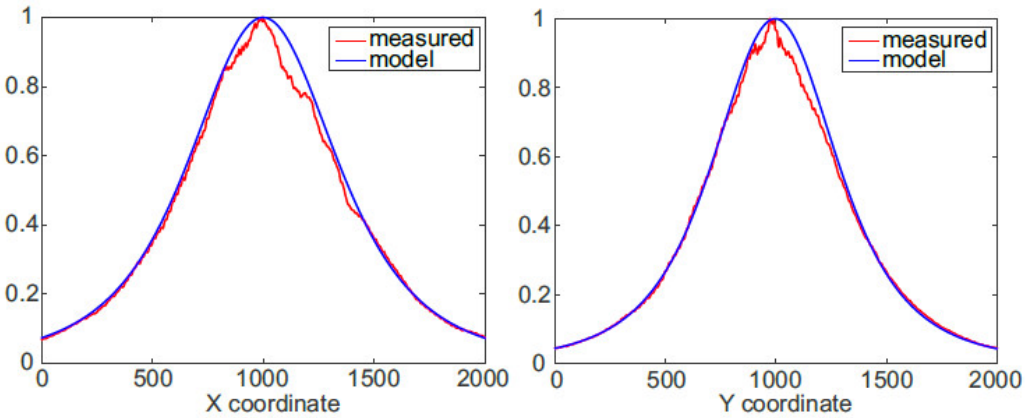

Fig. 10. The measured intensity of the projected image (red) is well predicted by our model (blue). Left: a horizontal slice through the center, right: a vertical one. Note that the horizontal and vertical falloff rates is different.

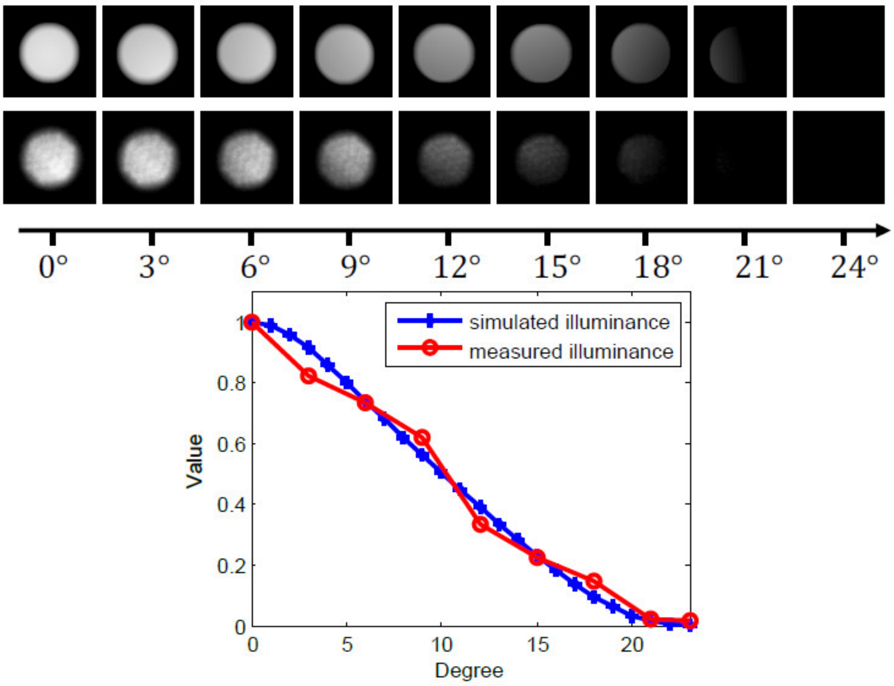

Fig. 11. One tube (diameter 1.2mm) with varying tilting angles. Top row: simulated footprints; Second row: the physical footprints; Bottom: plot of the normalized sum of simulated illuminance values in the footprint and the sum of grayscales across an actual footprint photo.

The accuracy of our empirical model is demonstrated in Figure 10. The red curves show a horizontal (left) and a vertical (right) cross section through the projected image shown in Figure 4(c), and the blue curves are the values predicted by our model.

We evaluate the visibility of points on the light source using ray casting (see Figure 9). Note that it is not necessary to intersect rays with the complete geometric model of the perforated lampshade shell. Instead, we quickly determine a small set of tubes that are relevant for a given ray, and check whether the ray passes through one of these tubes, without intersecting the tube's surface. Note that the above approach accounts only for direct illumination, without considering reflections, subsurface scattering, etc. In order to assess the magnitude of these effects, we have sprayed the interior of lamps with black paint, and found the differences in the measured intensity very small. The main difference is that this reduces the amount of ambient light in the room, leading to projected images with slightly better contrast.

Accurate light source visibility estimation is particularly important for correctly simulating tilted tubes. Figure 11 shows the simulated and the actual light footprints of a single tube, for a variety of different tilt angles. The sum of the intensity across the area of the footprint is plotted below (normalized such that the maximal sum is 1.0). We can observe that the simulation predicts the illuminance reasonably well, with some deviations between the two curves due to imprecisions in the manufacturing process.

Finally, in order to visualize the simulated results, we convert them into grayscale values by scaling the result into a [0-1] range, and applying a gamma correction (we use gamma 2.2 in all our results). Fig. 11. One tube (diameter 1.2mm) with varying tilting angles. Top row: simulated footprints; Second row: the physical footprints; Bottom: plot of the normalized sum of simulated illuminance values in the footprint and the sum of grayscales across an actual footprint photo.

4. Results

We have implemented the method described in the previous section, and have used the resulting system to design a number of lampshades for projecting a variety of target images. The results may be seen in Figures 1 and 16. The lampshades in all of these results have spherical geometry, with a diameter of 22cm. To save material we typically perforate each spherical lamp with two images on two opposing sides. The light source we use in our results is a Cree® XLamp® CXA1507 LED with 3000K color temperature, which is roughly disk-shaped with a radius of 9mm. The perforated lamp projects its image onto a planar rear projection screen that offers high light transmission, located at a distance of 40cm from the light source. The physical size of the projected image is $100 \times 100cm^2$. Figure 12 shows a photograph of our setup. The photographs of the projected images shown in this paper are shot from the opposite side of the screen for eliminating distortion, using a Canon EOS 5D Mark II camera, with exposure 1/80 sec, f/4.0, and ISO 400 settings, in a room without any additional light sources.

Fig. 12. A photograph of our setup.

The resulting lampshade designs have been 3D-printed to allow a qualitative evaluation of the projected imagery. The lampshades were printed on a powder-based binder-jet printer (ProJet® 660Pro). The thickness of the lampshade shells was set to 3mm, which, in our experience, is the lower bound to ensure the structural integrity. We found that it is hard to blow the powder away from the tubes when r_{min} is smaller than 0.6mm, and that adjacent tubes are prone to collapse when d_{min} is smaller than 0.5mm. Therefore, we set r_{min} = 0:6mm and d_{min} = 0:5mm. The manufacturing time for such a spherical lampshade includes 16.5 hours of printing and 1 hour of drying. The inside surfaces of the lamps were sprayed with black paint, which somewhat improves the contrast of the projected images.

Our method is also applicable to non-spherical lampshades, as demonstrated in Figure 17, where the lampshade is a bumpy surface (bounded by a sphere of diameter 22cm). This is made possible by the fact that the capacity-constrained Voronoi tessellation takes place on the planar receiving surface, rather than on the more general lampshade surface. The tubes are generated by back-projecting disks from the receiving surface through the lampshade shell, which can thus be of a general, non-spherical shape. It should be noted, however, that our current implementation assumes that the lampshade shape is free from self-occlusions.

Model	Initial #disks	Final #disks	% correct size
Marilyn	7323	5789	79.47
CircularRamp	7914	6321	87.73
Hepburn	7617	5945	82.50
Kelly	7563	5914	80.74
Marlon	7167	5607	81.34
Toucan	6926	5352	75.76
Lion	7243	5650	74.81
Dog	7891	6055	82.12
Kelly (bumpy)	8912	7120	65.17

Table I. Statistics for our results Initial disks is our initial estimate of the required number of disks, which serves as a starting point for a binary search, after which we achieve the final number of disks. The percentage of correctly sized disks among these are reported in the right column.

Table I reports several statistics for each of these results. The computation time of our method consists of two main parts: computing the disk distribution and generating the 3D model of the lampshade perforated with tubes. For the lamps shown in the paper it takes less than 5 minutes to run the method of de Goes et al. [2012] up to 10 times, while searching for the optimal number of disks. The resulting lamps have around 6000 tubes, and the 3D model generation takes roughly 1 minute. For verification, we typically compute a simulated result before sending a lamp to be printed, which takes roughly 1 minute. All of the above times are measured on an Intel® Core™ i5 CPU 3.3GHz with 8GB RAM.

Figure 13 shows two qualitative comparisons between the target image, the simulated result, and the physical projected image. This is done on two examples: a concentric circles pattern featuring four regions of a constant grayscale value, and a more complex natural image. Below each image, we show the corresponding histogram, in order to better examine the differences between the corresponding tone distributions.

In the concentric ramp case (13a), it obviously infeasible to reproduce the ideal four-way distribution of grayscale values with our process. Our design process approximates this distribution with four wider peaks (the black peak coincides with the left edge of the histogram). A photograph of the actual projection features four similar peaks, although there are slight differences in their positions and spread. The target image of Marilyn

Monroe (13h) has a nearly uniform histogram. This histogram is reproduced reasonably well by our process, however, both the simulated and the actual projected image have more mass in the lower part of the grayscale range.

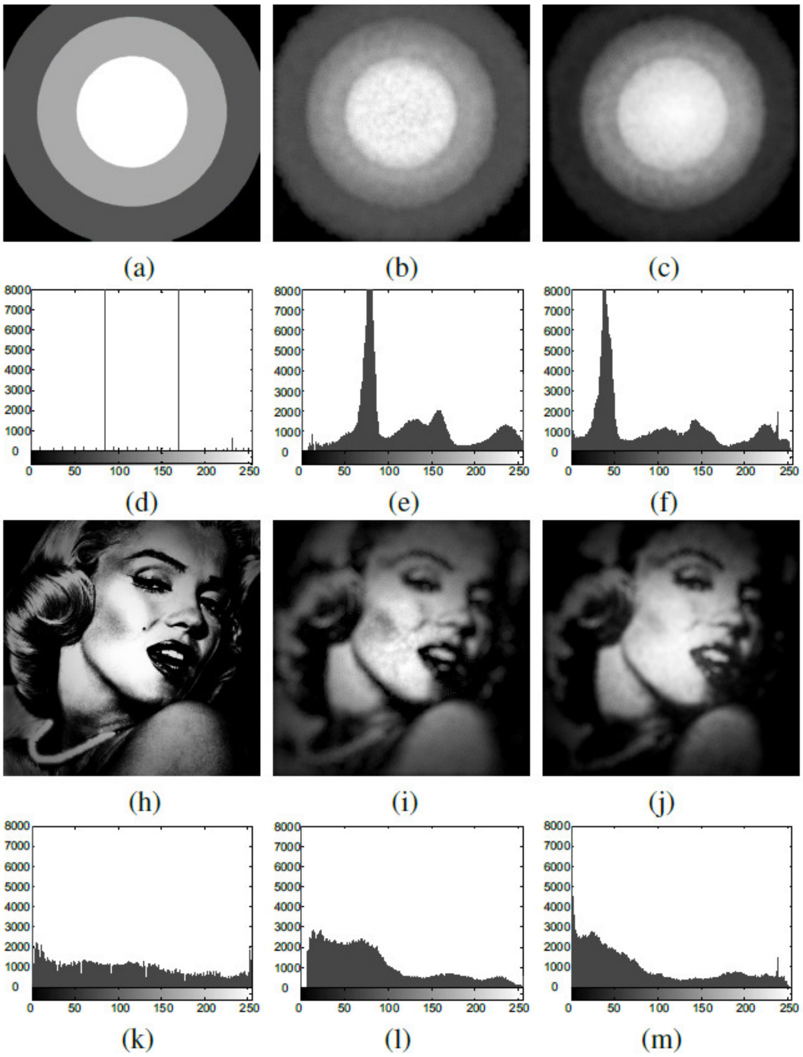

Fig. 13. Two comparisons of the target image (a, h), our simulation result (b, i), and a real photo of the projected image (c, j). The corresponding histogram is below each image. The circular ramp (a) consists of three gray values: 85, 170, 255.

These two examples illustrate well some of limitations of this new medium. Achieving bright tones in the middle of the image is relatively easy (since the distance between the receiver and the light source is minimal there, and both cosines in Eq. (4) are near 1.0). However, reproducing dark tones in the central region is challenging because of the necessity to use large tilt angles. As explained earlier, extensive use of tilting requires reducing the tube density, thereby reducing spatial resolution. Conversely, achieving light tones at the periphery of the image is difficult, because of the falloff in the illuminance, and increasingly wider tubes are needed to produce a light tone in the periphery. Thus, there’s a tradeoff between our ability to reproduce the full tonal range, and our desire for better spatial resolution. In particular, by imposing an upper bound (1.3mm) on the embedding disk radii across the lamp surface, we are not able to match the lighter tones of the target image beyond a certain radius.

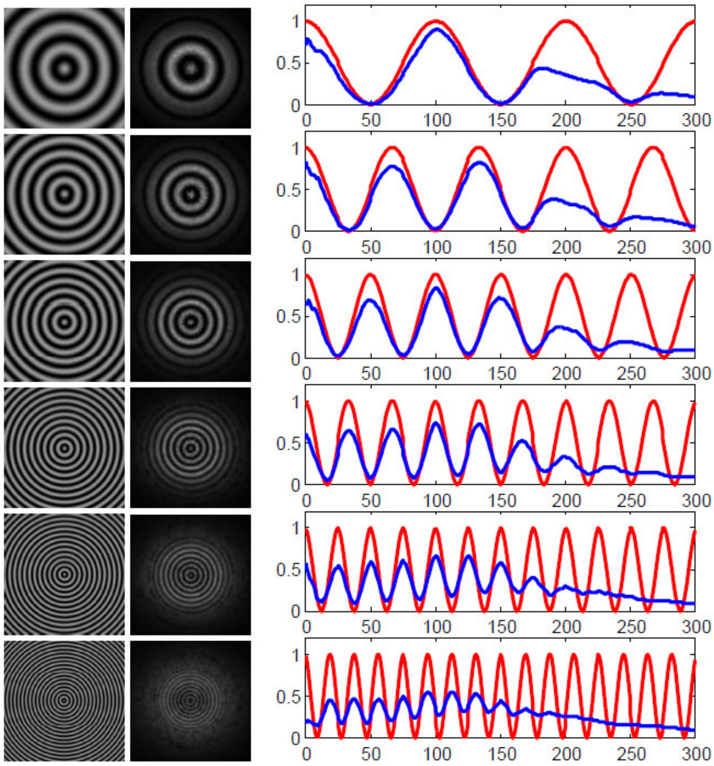

Fig. 14. Frequency and contrast response. Given the radial cosine waves as the input patterns (left), the results of our method (middle) are influenced by both frequency and radial distance from the center, as shown in the amplitude plot (right).

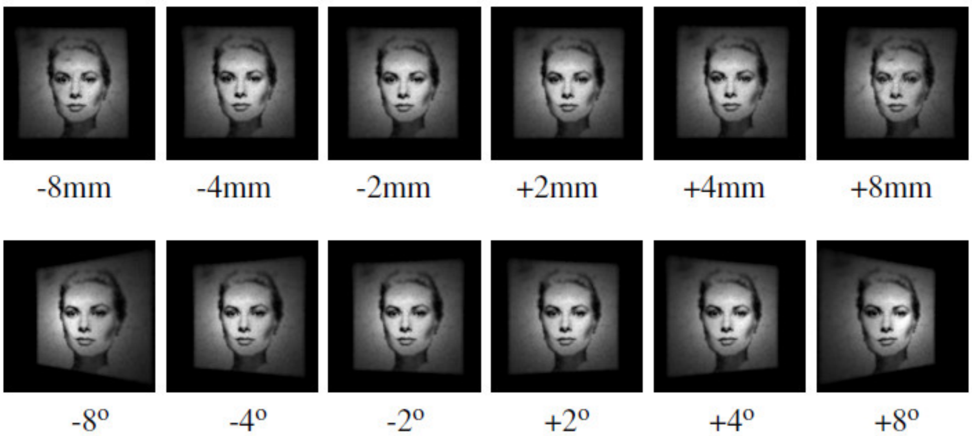

Fig. 15. Simulated projected images with the position of the lampshade shifted horizontally (top row) and lampshade rotated (bottom row) for the Kelly model shown in Figure 17.

Fig. 16. Additional results on spherical lampshades. Left: our 3D-printed lampshade, with light projecting through the surface. Right: the photo of projected image. The lamps are 22cm in diameter.

The above can be observed in a more quantitative manner in Figure 14, which shows the response of our method to several radial cosine waves with the frequency increasing from top to bottom row. Next to each input pattern we show the simulated result produced by our method and plot the amplitudes of the input wave (in red) and the result (blue), as a function of the radial distance. It may be observed that for all frequencies our method fails to reproduce the waveform beyond a certain radial distance, with the distance slightly decreasing as the frequency increases. It may also be seen that in the areas where the waveform is reproduced, the contrast response also decreases with frequency: while in the top row the ratio between the reproduced amplitude to the input one is roughly 0.89, this ratio drops to 0.40 in the bottom row.

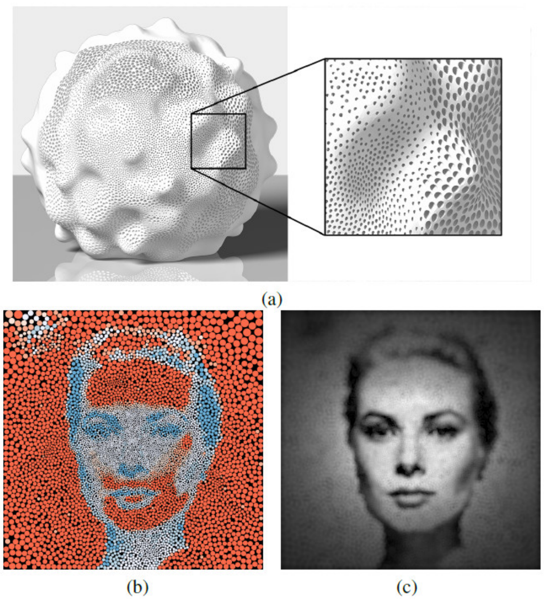

Fig. 17. A non-spherical lampshade(a), the maximal inscribed disks inside each cell of the CCVT (b), shown using the same color coding as in Figure 2, and the resulting simulated image (c).

In practical usage, the position of the lampshade or the inside light source, or the relative orientation between the two may differ slightly from the ideal conditions assumed in the design process. Figure 15 demonstrates that the projected image is still acceptable, so long as these deviations are not too large.

Fig. 18. One of our manufactured lamps in a natural setting.

5. CONCLUDING REMARKS

We have presented a technique to design printable perforated lampshades. The main challenge was to control the light emanating through the lampshade under the unique printability constraints and engineering setting. The technique that we developed extends classical halftoning to a novel domain, where the “dots” are not printed, or physically tangible, but projected, effectively *halftoning with light*.

Our current implementation assumes that the receiving surface is planar, and that there are no self-occlusions due to the shape of the lampshade. Thus, the distribution and the geometry of the perforating tubes can be determined by intersecting cones formed by disks on the receiving surface and the center of the light source with the lampshade shell. However, our framework is able to support more general lampshade shapes and receiving surfaces. Specifically, the generation of tubes needs to be adjusted to ensure that light reaches the receiving surface even in areas where self-occlusions exist, and the transformation between areas on the receiving surface and tube cross sections must be computed in a more general fashion.

The 3D printing technology is emerging and growing quickly, and many new intriguing applications are introduced. We believe that the combination of light and 3D printing has much more to offer. One direction which we now consider is not to use the light directly, but indirectly, by using the printed surface as reflector. The printed surface can be customized to the given environment, to its geometry and photometric properties, so as to optimize the distribution of light by a custom-made reflector.

Another direction for future work is to go beyond the printability constraints, by assembling a large-scale lampshade from surface pieces printed separately. This will allow using bigger and stronger light sources, and possibly compound arrays of light sources. A larger surface area will allow increasing the relative resolution of printed holes, and project an image on larger and more distant receiving surfaces. We are also considering focusing on the design of aesthetic imagery on the lampshade itself. Halftoned and stippled images have their own aesthetic virtue. In Figure 18, we show our lamp in a bedroom. Light effects combined with halftoning can lead to creative artistic media.

Acknowledgments

This work is partially supported by China National 973 Program (2015CB352501), Natural Science Foundation of China (61232011, 61572291, 61332015), NSFC-ISF (61561146397), and the Israel Science Foundation (ISF).

References

ALEXA, M. AND MATUSIK, W. 2012. Irregular pit placement for dithering images by self-occlusion. Computers & Graphics 36, 6, 635 – 641. 2011 Joint Symposium on Computational Aesthetics (CAe), Non-Photorealistic Animation and Rendering (NPAR), and Sketch-Based Interfaces and Modeling (SBIM).

BALZER, M., SCHL¨OMER, T., AND DEUSSEN, O. 2009. Capacity constrained point distributions: A variant of Lloyd’s method. ACM Trans. Graph. 28, 3 (July), 86:1–86:8.

BARAN, I., KELLER, P., BRADLEY, D., COROS, S., JAROSZ, W., NOWROUZEZAHRAI, D., AND GROSS, M. 2012. Manufacturing layered attenuators for multiple prescribed shadow images. Comp. Graph. Forum 31, 2 (May), 603–610.

CHANG, J., ALAIN, B., AND OSTROMOUKHOV, V. 2009. Structure-aware error diffusion. ACM Trans. Graph. 28, 5 (Dec.), 162:1–162:8.

DE GOES, F., BREEDEN, K., OSTROMOUKHOV, V., AND DESBRUN, M. 2012. Blue noise through optimal transport. ACM Trans. Graph. 31, 6 (Nov.), 171:1–171:11.

ESCHBACH, R. AND KNOX, K. T. 1991. Error-diffusion algorithm with edge enhancement. J. Opt. Soc. Am. A 8, 12 (Dec), 1844–1850.

FINCKH, M., DAMMERTZ, H., AND LENSCH, H. 2010. Geometry construction from caustic images. In Computer Vision - ECCV 2010, K. Daniilidis, P. Maragos, and N. Paragios, Eds. Lecture Notes in Computer Science, vol. 6315. Springer Berlin Heidelberg, 464–477.

KIPPHAN, H. 2001. Handbook of Print Media: Technologies and Production Methods. Springer-Verlag.

KISER, T., EIGENSATZ, M., NGUYEN, M., BOMPAS, P., AND PAULY, M. 2013. Architectural caustics – controlling light with geometry. In Advances in Architectural Geometry 2012, L. Hesselgren, S. Sharma, J. Wallner, N. Baldassini, P. Bompas, and J. Raynaud, Eds. Springer Vienna, 91–106.

LAN, Y., DONG, Y., PELLACINI, F., AND TONG, X. 2013. Bi-scale appearance fabrication. ACM Trans. Graph. 32, 4 (July), 145:1–145:12.

LAU, D. L. AND ARCE, G. R. 2008. Modern Digital Halftoning, Second Edition (Signal Processing and Communications), 2 ed. CRC Press.

LEVIN, A., GLASNER, D., XIONG, Y., DURAND, F., FREEMAN, W., MATUSIK, W., AND ZICKLER, T. 2013. Fabricating BRDFs at high spatial resolution using wave optics. ACM Trans. Graph. 32, 4 (July), 144:1– 144:14.

LI, H., WEI, L.-Y., SANDER, P. V., AND FU, C.-W. 2010. Anisotropic blue noise sampling. ACM Trans. Graph. 29, 6 (Dec.), 167:1–167:12.

LOU, Q. AND STUCKI, P. 1998. Fundamentals of 3D halftoning. In Electronic Publishing, Artistic Imaging, and Digital Typography, 7th International Conference on Electronic Publishing, EP ’98, Held Jointly with the 4th International Conference on Raster Imaging and Digital Typography, RIDT ’98, St. Malo, France, March 30 - April 3, 1998, Proceedings. 224–239.

MALZBENDER, T., SAMADANI, R., SCHER, S., CRUME, A., DUNN, D., AND DAVIS, J. 2012. Printing reflectance functions. ACM Trans. Graph. 31, 3 (June), 20:1–20:11.

MITRA, N. J. AND PAULY, M. 2009. Shadow art. ACM Trans. Graph. 28, 5 (Dec.), 156:1–156:7.

MITSA, T. AND PARKER, K. J. 1992. Digital halftoning technique using a blue-noise mask. J. Opt. Soc. Am. A 9, 11 (Nov), 1920–1929.

PANG, W.-M., QU, Y., WONG, T.-T., COHEN-OR, D., AND HENG, P.- A. 2008. Structure-aware halftoning. ACM Trans. Graph. 27, 3 (Aug.), 89:1–89:8.

PAPAS, M., HOUIT, T., NOWROUZEZAHRAI, D., GROSS, M., AND JAROSZ, W. 2012. The magic lens: Refractive steganography. ACM Trans. Graph. 31, 6 (Nov.), 186:1–186:10.

PAPAS, M., JAROSZ, W., JAKOB, W., RUSINKIEWICZ, S., MATUSIK, W., AND WEYRICH, T. 2011. Goal-based caustics. Comp. Graph. Forum 30, 2 (June), 503–511.

PEREIRA, T., RUSINKIEWICZ, S., AND MATUSIK, W. 2014. Computational light routing: 3D printed optical fibers for sensing and display. ACM Trans. Graph. 33, 3 (June), 24:1–24:13.

SCHWARTZBURG, Y., TESTUZ, R., TAGLIASACCHI, A., AND PAULY, M. 2014. High-contrast computational caustic design. ACM Trans. Graph. 33, 4 (July), 74:1–74:11.

STUCKI, P. 1997. 3D halftoning. In Proc. SPIE 2949, Imaging Sciences and Display Technologies. Proc. SPIE 2949, 314–317.

ULICHNEY, R. 1987. Digital Halftoning. MIT Press, Cambridge, MA, USA.

ULICHNEY, R. 1988. Dithering with blue noise. Proceedings of the IEEE 76, 1 (Jan), 56–79.

WETZSTEIN, G., LANMAN, D., HEIDRICH, W., AND RASKAR, R. 2011. Layered 3D: Tomographic image synthesis for attenuation-based light field and high dynamic range displays. ACM Trans. Graph. 30, 4 (July), 95:1–95:12.

WEYRICH, T., PEERS, P., MATUSIK, W., AND RUSINKIEWICZ, S. 2009. Fabricating microgeometry for custom surface reflectance. ACM Trans. Graph. 28, 3 (July), 32:1–32:6.

WILLIS, K., BROCKMEYER, E., HUDSON, S., AND POUPYREV, I. 2012. Printed optics: 3D printing of embedded optical elements for interactive devices. In Proceedings of the 25th Annual ACM Symposium on User Interface Software and Technology. UIST ’12. ACM, New York, NY, USA, 589–598.

YUE, Y., IWASAKI, K., CHEN, B.-Y., DOBASHI, Y., AND NISHITA, T. 2014. Poisson-based continuous surface generation for goal-based caustics. ACM Trans. Graph. 33, 3 (June), 31:1–31:7.

ZHOU, C. AND CHEN, Y. 2009. Three-dimensional digital halftoning for layered manufacturing based on droplets. Transactions of North American Manufacturing Research Institute of SME 37, 175–182.

Connected Fermat Spirals for Layered Fabrication

Abstract: We develop a new kind of "space-filling" curves, connected Fermat spirals, and show their compelling properties as a tool path fill pattern for layered fabrication. Unlike classical space-filling curves such as the Peano or Hilbert curves, which constantly wind and bind to preserve locality, connected Fermat spirals are formed mostly by long, low-curvature paths. This geometric property, along with continuity, influences the quality and efficiency of layered fabrication. Given a connected 2D region, we first decompose it into a set of sub-regions, each of which can be filled with a single continuous Fermat spiral. We show that it is always possible to start and end a Fermat spiral fill at approximately the same location on the outer boundary of the filled region. This special property allows the Fermat spiral fills to be joined systematically along a graph traversal of the decomposed sub-regions. The result is a globally continuous curve. We demonstrate that printing 2D layers following tool paths as connected Fermat spirals leads to efficient and quality fabrication, compared to conventional fill patterns.

Keywords: connected Fermat spirals, space-filling curve, layered fabrication, tool path, continuous fill pattern

1. Introduction

The emergence of additive manufacturing technologies [Gibson et al. 2015] has led to growing interests from the computer graphics community in geometric optimization for 3D fabrication. The focus of many recent attempts has been on shape optimization: how to best configure a 3D shape, e.g., via hollowing or strengthening, to achieve quality and cost-effective fabrication. In this work, we look at the problem from a different angle. Instead of addressing the higher-level question of what to print, we examine lower-level yet fundamental issues related to how to print a given object.

At the most elementary level, additive or layered fabrication operates by moving a print head which extrudes or fuses print material layer by layer. When printing each layer, the print head follows a prescribed tool path to fill the 2D region defined by the shape of the printed object. Topologically, continuity of a tool path is critical to fabrication. A tool path discontinuity or contour plurality forces an on-off switching of the print nozzle, negatively impacting build quality and precision [Dwivedi and Kovacevic 2004; Ding et al. 2014]. Geometrically, sharp turns and corners are undesirable since they lead to discretization artifacts at layer boundaries and cause de-acceleration of the print head, both reducing print speed and degrading fill quality [Jin et al. 2014].

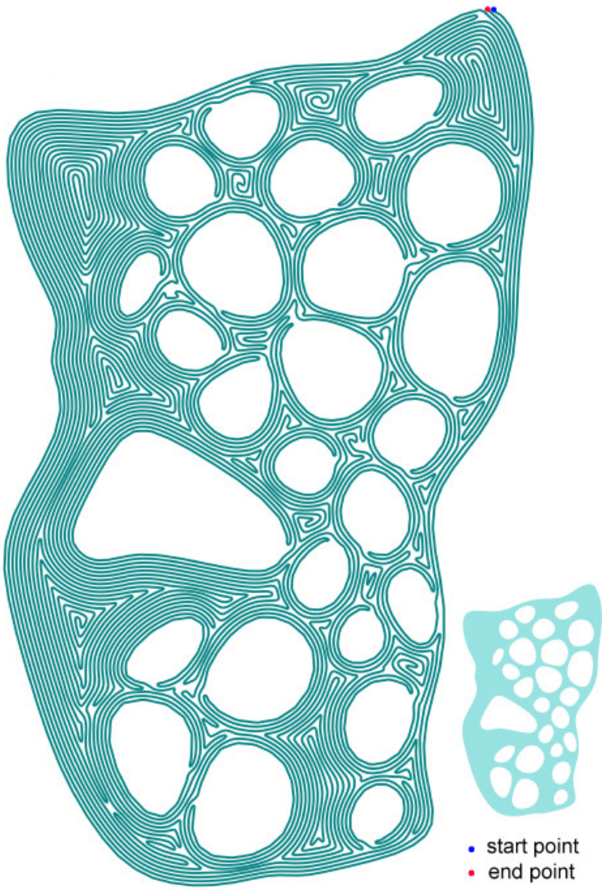

Figure 1: A new kind of “space-filling” curves called connected Fermat spirals. Unlike classical space-filling curves which wind and bend, the new curve is composed mostly of long, low curvature paths, making it desirable as a tool path fill pattern for layered fabrication. The tool path shown is continuous with start and end points marked; the input 2D layer shape is displayed on the side.

Zigzag has been the most widely adopted fill pattern by today’s 3D printers due to its simplicity [Gibson et al. 2015]; see Figure 2 for various fill patterns. However, a zigzag fill consists of many sharp turns, a problem that is amplified when printing shapes with complex boundaries or hollow structures. A contour-parallel tool path, formed by iso-contours of the Euclidean distance transform, provides a remedy, but it leads to high contour plurality since the iso-contours are disconnected from each other. A spiral fill pattern, for simple shapes such as a square, is continuous. However, for more complex shapes, both contour-parallel fills and spiral fills tend to leave isolated “pockets” corresponding to singularities of the distance transform, as shown in Figure 3(a). These pockets are disconnected and result in path plurality. An intriguing geometry question is whether a connected 2D region can always be filled by a *continuous* pattern formed by one or more spirals.

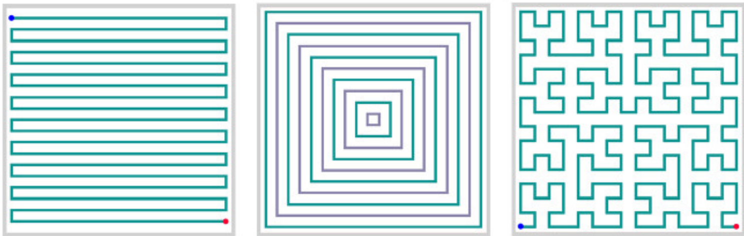

(a) Zigzag. (b) Contour-parallel. (c) Hilbert.

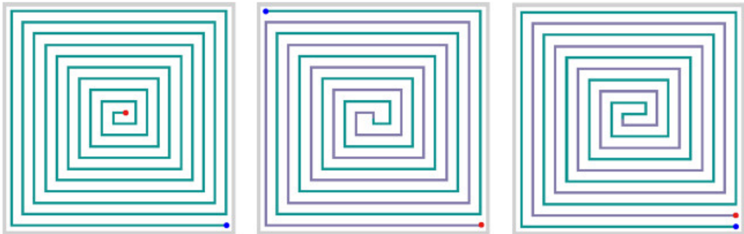

(d) Spiral. (e) Fermat spiral 1. (f) Fermat spiral 2.

Figure 2: Various space-filling patterns. For a Fermat spiral, the start and exit points on the boundary can be chosen freely (e-f).

In this paper, we introduce the use of Fermat spirals [Wikipedia 2015] as a fundamental 2D fill pattern and develop a tool path planning algorithm based on connected Fermat spirals or CFS to continuously fill a connected 2D region. A Fermat spiral is an interesting space-filling pattern with two interleaving sub-spirals, one inward and one outward; see Figure 2(e). Fermat spirals had not been exploited for tool path planning before and they possess three key properties to make them attractive as a fill pattern:

1. Like contour-parallel paths, a Fermat spiral conforms to the region boundary, with one sharp turn in the center.

2. Several Fermat spirals covering a 2D region can be continuously connected. While a conventional spiral travel either inward or outward, a Fermat spiral goes in and then out, allowing several of them to be joined at their boundaries.

3. The start and exit points of a Fermat spiral can be chosen arbitrarily over its boundary; see Figures 2(e-f). This special property facilitates connections between

Fermat spirals.

We develop an algorithm to construct a CFS curve to fill a singly connected 2D region. First, the algorithm decomposes the input region into a set of sub-regions each of which admits a continuous fill by a single Fermat spiral; we call these sub-regions spirallable. The start and exit points for each Fermat spiral are placed next to each other along the spiral boundary. We then obtain a continuous traversal of the spirallable sub-regions and connect their respective Fermat spirals through the start/exit points to form a globally continuous curve. Further optimization can be applied to improve fairness and spacing. The resulting curve has fewer sharp turns than a zigzag fill and composed mostly of long, low-curvature paths.

We show CFS curves constructed for input shapes with varying exterior and interior complexity. We fabricate 2D layers and 3D prints using CFS patterns and compare the results visually and numerically to those provided by conventional fills via zigzag and contour parallel tool paths. The new fill pattern appears to excel at handling shapes with much concavity and many interior holes.

In retrospect, the desirable properties we seek from connected Fermat spirals are almost completely opposite to those possessed by classic space-filling curves such as Hilbert curves; see Figure 2(c). Hilbert or Peano curves are designed to wind and bend to preserve locality of the space traversal. CFS curves are meant to avoid bending as much as possible to attain a higher degree of fairness. In general, CFS curves are not guaranteed to completely cover an arbitrary 2D region even at infinitely high resolution. As well, our new curves do not possess recursive properties as the classical space-filling curves. For layered fabrication however, the new curve is clearly more attractive than fractal-like fill patterns.

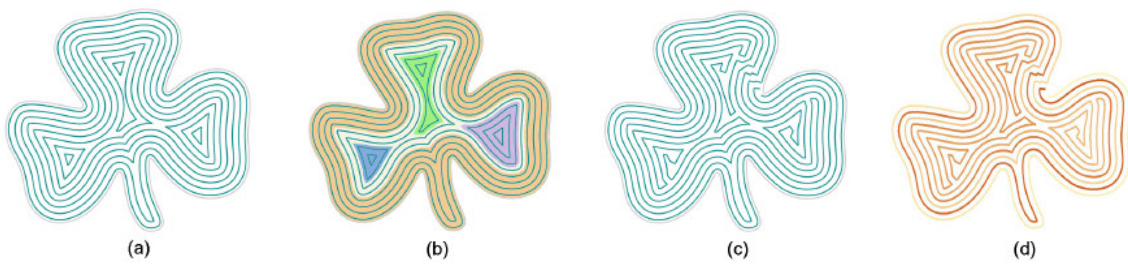

Figure 3: Overview of connected Fermat spiral algorithm. (a) Iso-contours via distance transform lead to four “pockets”. (b) Decomposition into four sub-regions, each to be filled using a single Fermat spiral. (c) Connecting single spirals into a globally continuous curve. (d) Visualization (lower resolution for ease of visualization) of the continuous curve through smooth color transition.

2 Background and Related Work

Recently, there has been a flourishing of works in computer graphics on optimizing 3D shapes or their configurations for efficient and effective fabrication, e.g., to ensure or improve physical stability [Pr´evost et al. 2013], structural strength [Stava et al. 2012; Hildebrand et al. 2013; Lu et al. 2014], or appearance [Zhang et al. 2015] of the print, to save material [Vanek et al. 2014b; Hu et al. 2014], and to adapt to the limited print volume [Luo et al. 2012; Vanek et al. 2014a; Chen et al. 2015; Yao et al. 2015].

In this section, we focus on the tool path planning problem in the context of additive manufacturing (AM). First, to explain the importance of continuity and fairness for the tool paths, we present some background material on nozzle mechanisms that control the viscoelastic material that is extruded along the path, as well as the mechanics of the motors that control the tool paths. Then we discuss related geometric and engineering approaches for optimizing tool paths. Our coverage is not meant to be exhaustive. Interested readers should refer to the book by Gibson et al. [2015], short surveys from [Kulkarni et al. 2000; Ding et al. 2014], as well as the recent SIGGRAPH course by Dinh et al. [2015].

Tool path continuity. Fused Deposition Modeling or FDM is the most widely applied AM technology. During the FDM process, filament is melted into viscoelastic material and extruded from a small opening of the print nozzle. Due to liquid compressibility, it is generally hard to predict the amount of viscoelastic material to emit in order to create a continuous extrusion control. Consequently, the first portion of the filament from the nozzle usually under- or over-fills. Such uneven fills cause visual artifacts when they occur near the surfaces of the printed object. When they occur between fill paths, attachment between filaments can be weakened, lowering the strength of the print. When turning off the extrusion, the temporal gap between the stopping of the feed motor and that of the filament extrusion is difficult to control, which again leads uneven fills. Similar situations also arise when the print material is fused by the print head, e.g., for powder-based printing. As well, any discontinuity along a tool path necessitates a nozzle movement which does not contribute to the print. Thus, the primary objective in designing tool paths is to minimize the on/off switching along the path, or in other words, to maximize its *continuity*.

Tool path geometry. The geometry of tool paths, in particular their curvature, influences fabrication time and quality. As a tool path rounds itself about a sharp turn, more de-acceleration and acceleration times are required, causing more of a slow-down of the extrusion head, as compared to the case of a soft turn. As well, acute turn angles also lead to more over-fill or under-fill of the filament [Jin et al. 2014]. Hence, a long and continuous tool path without sharp turns may enable the extrusion head to move along the whole tool path at a speed that is close to the highest allowed with small changes, leading to efficient and quality fabrication.

Direction-parallel vs. contour-parallel fills. The most popular fill method in commercial AM systems follows the zigzagging pattern [Ding et al. 2014]. Along with raster scans, zigzagging belongs to the class of direction-parallel fills. In contrast, contour-parallel paths are comprised of a set of closed contours parallel to the outline of a given slice [Yang et al. 2002]. Over simple 2D regions, such paths lead to smoother turns and object boundaries compared zigzagging [El-Midany et al. 1993], but they always have a high contour plurality. Hybrid fills have also been proposed [Jin et al. 2013]; they generate a few contours inward before filling the remaining interior area with a zigzag, but attachment between the two fill patterns can become suspect. When the 2D slice to be filled has a complex shape with many concavities, standard implementations of both fill patterns are prone to discontinuity issues.

Spiral tool paths. Spiral tool paths have been widely applied for pocket machining [Ren et al. 2009]. Held and Spielberger [2014] decompose a 2D layer into spirallable pockets and machine each pocket following a separate, classical spiral pattern; no globally continuous path was constructed. Spiral tool paths are less common for AM and one major reason (also applicable to contour-parallel fills) is that due to a lack of direction bias, spiral patterns for adjacent slices replicate each other and cannot be “cross-weaved” at an angle; this could compromise fabrication strength for FDM printers [Gibson et al. 2015]. This problem may be fixed by hybrid fills, e.g., alternating between spiral and zigzagging layers. Our work focuses on how to optimize the continuity of spiral fills.

Space-fill curves. A continuous tool path that fills a 2D region is a space-filling curve (SFC). SFCs have been adopted for various applications, e.g., image encoding [Dafner et al. 2000] and maze design [Pedersen and Singh 2006]. Fractal-like SFCs have been suggested as fill patterns for AM [Wasser et al. 1999]. However, they are complex to realize and full of sharp turns. The tool path fill problem has some resemblance to lawn mowing [Arkina et al. 2000], which is formulated under a rather different setting: it seeks the shortest path for a "cutter" with a prescribed shape to cover all points (possibly multiple times) in a 2D region.

Labyrinths. Mazes and many famous labyrinth patterns are also space-filling [Wikipedia 2016]. A unicursal labyrinth curve is continuous and starts and ends at the same point, just like our connected Fermat spirals. Pedersen and Singh [2006] developed a stochastic curve evolution algorithm to produce expressive, space-filling labyrinths where the Brownian motion of the curve particles are subject to attraction-repulsion forces, as well as local fairness and field alignment constraints. In contrast, our algorithm is top-down and with more global structural control in the construction. The resulting curves have smoother boundaries and less turns.

Domain decomposition. One interesting way to obtain a continuous tool path is to decompose a 2D region into several subregions each of which admits a continuous fill. Then these regional fills are connected to achieve global continuity. Along these lines, [Dwivedi and Kovacevic 2004] decompose a polygon into monotone sub-polygons and fill each sub-polygon using a closed zigzagging curve, along which the start/entry point can be chosen arbitrarily. Ding et al. [2014] execute convex decomposition and for each convex polygon, an optimal zigzagging direction is found to facilitate continuous connection between the polygon fills. However, both methods were designed to deal with polygon inputs and cannot properly handle shapes with smooth concave boundaries.

Our work also relies on a region decomposition while it can deal with arbitrary 2D shapes as input. Instead of using zigzags, we employ Fermat spiral fills to achieve both continuity and a higher degree of fairness. The decomposition scheme is designed to accommodate contour-parallel and spiral tool paths.

Continuously fillable shapes. Polygon convexity [Ding et al. 2014] and monotonicity [Dwivedi and Kovacevic 2004] were chosen in the domain decomposition approaches to achieve tool path continuity since both shape properties ensure a continuous fill by the zigzagging pattern. For monotone polygons, a limited set of scan directions guarantee this, while for a convex polygon, any scan direction leads to a continuous zigzagging fill. Spirallability is their counterpart for spiral or contour-parallel fills and to the best of our knowledge, such a shape property has not been studied before.

3 Spirals, Fermat Spirals, and Spirallability

Before introducing spirals, we first study contour-parallel tool paths and relate them to the Euclidean distance transform of a 2D region. Then, we describe how to convert the parallel contours into a regularly spaced spiral pattern and define spirallability. Finally, a spiral fill is converted into a Fermat spiral fill, where we can choose the start and end points on the boundary arbitrarily.

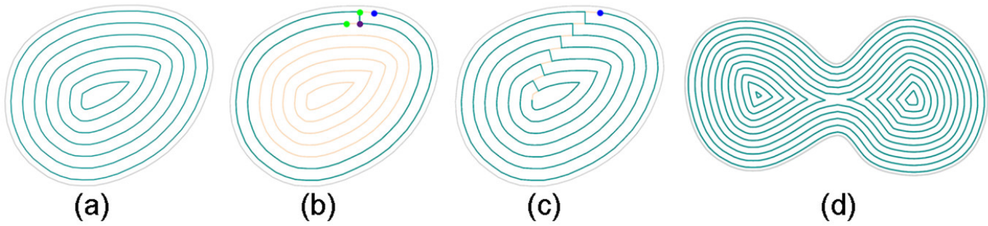

Figure 4: From contour-parallel paths (a) to a spiral (c), by breaking and rerouting adjacent iso-contours (b). In general, the distance transform has multiple local maxima (d). If the maximum is unique, the region is spirallable (a-c).

Contour-parallel path as iso-contour. Let R be a connected 2D region whose boundary is denoted by ∂R. A Euclidean distance transform for ∂R defines a scalar distance field ϑ_R over R where for each point $p \in R$, $\vartheta_R(p)$ is the shortest distance from p to ∂R. An iso-contour associated with distance d is composed of all points in R whose scalar value is d; the boundary ∂R is the isocontour associated with the iso-value 0. Subject to the width of the fill material for the fabrication process, the set of contour-parallel tool paths correspond to a set of equidistant iso-contours, which are all disconnected from each other, as shown in Figure 4(a).

Spiral and spirallability. Two adjacent iso-contours can be connected to form a single continuous path by breaking and rerouting the contours, as shown in Figure 4(b). Rerouting adjacent contours in such an offsetting fashion would lead to a spiral pattern. If the distance field within R has a single local maximum or plateau, to which all the iso-contours would ascend, then these contours can be rerouted into a single continuous spiral path that fills the 2D region R, as shown in Figure 4(c). We call such a region R spirallable. Non-spirallable regions have multiple pockets corresponding to separate local maxima and cannot be converted into a single continuous spiral with a simple rerouting as described.

Fermat spiral. A spiral fill path π for a spirallable region R can be converted into a Fermat spiral. As we show below, we can also choose the start and end/exit points of the Fermat spiral traversal arbitrarily, with both points lying on the region boundary.

Starting from a point $p \in \pi$, trace the upward gradient line over the distance field ϑ_R to intersect π at $\mathcal{L}(p)$, if it exists. If p is close to the maximum of ϑ_R or center of the region R, where the path π is thinning out, then the gradient line may not intersect π. We call $\mathcal{L}(p)$ the inward link for p with respect to π; see Figure 5(a). Similarly, we define the outward link $\mathcal{O}(p)$ for p by tracing the downward gradient and intersect. If p lies on ∂R, then such an intersection would not exist. The outward and inward links will serve as rerouting points for the conversion to a Fermat spiral.

To help describe the rerouting procedure, we impose a partial order < along path π based on inward traversal. Thus, the first point is the end point of π on the region boundary and the last point is at the region center. Two points $p < q$ if the inward traversal along π reaches p before q. Next, we impose a discretization spacing and denote the point preceding (respectively, succeeding) p along π at a distance by $\mathcal{B}(p)$ (respectively, $\mathcal{N}(p)$); see Figure 5(a).

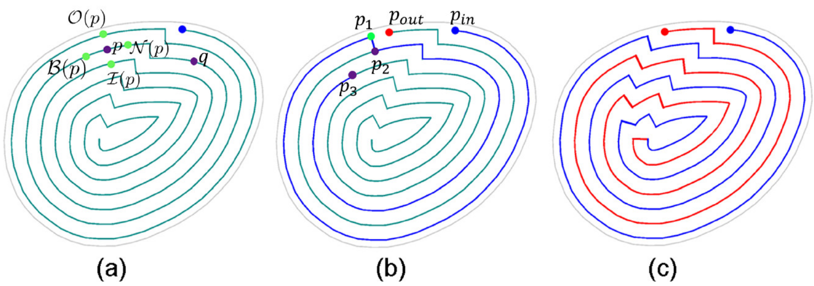

Figure 5: Rerouting a spiral (a) into a Fermat spiral (c). (a) A point p and its corresponding inward $\mathcal{L}(p)$ and outward link $\mathcal{O}(p)$, as well as points $\mathcal{B}(p)$ and $\mathcal{N}(p)$ which are before and after p along the path. (b) Starting at p_{in}, reroute at $p_1 = \mathcal{B}(p_{out})$ and go inward to $p_2 = \mathcal{L}(\mathcal{B}(p_{out}))$, and continue. (c) Resulting Fermat spiral.

Let p_{in} be the starting point of π and suppose that we would like the Fermat spiral to exist at pout along the outermost portion of π. As shown in Figure 5(b), we start at pin and travel along π until reaching $p_1 = \mathcal{B}(p_{out})$. Then we reroute the path inward from $p_1 = \mathcal{B}(p_{out})$ to its inward link $p_2 = \mathcal{L}(p_1)$, continue traveling along π until reaching $p_3 = \mathcal{B}(\mathcal{L}(\mathcal{B}(p_1)))$, and reroute from this point to its inward link. This form of inward rerouting is executed iteratively until reaching the center of the region, at which point, the traversal is reversed into an outward one with a turn. The outward rerouting is through the outward links, starting at the region center, passing through portions of π that were not traversed during the inward spiral, until the outward spiral exits at pout; see Figure 5(c).

The way the rerouting points are placed in the above conversion procedure leads to jaggies or staircasing at every turn along the Fermat spiral. These artifacts are removed by a post-optimization.

4 Continuous Fermat Spiral Fill

In this section, we describe our algorithm for constructing a continuous path fill, as connected Fermat spirals, for an arbitrary, singly connected 2D region R. The key is to properly reroute level set curves or iso-contours derived from the Euclidean distance transform of the region boundary ∂R. Within a pocket, the rerouting produces a Fermat spiral. Between pockets and near branching regions, rerouting serves to connect the spirals.

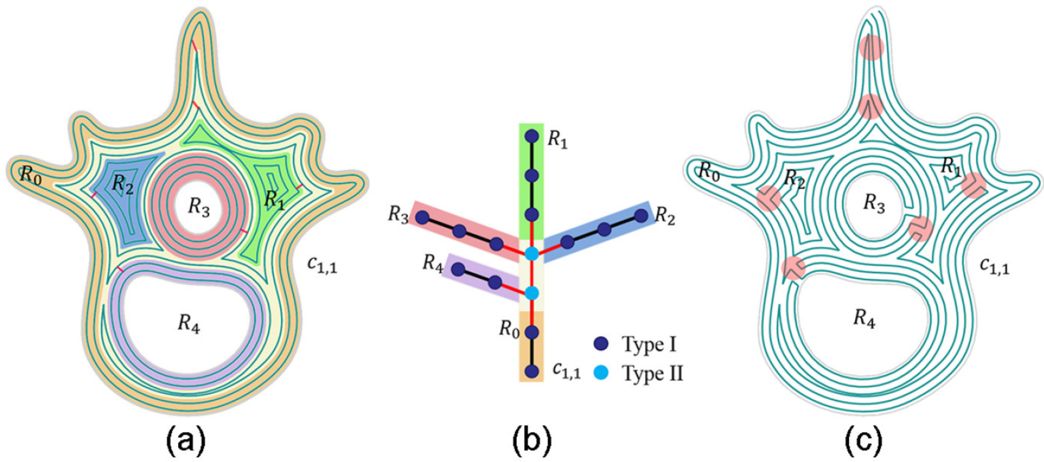

Figure 6: An example of a spiral-contour tree with five spirallable regions. (a) Interior decomposed sub-regions shown in distinctive colors. The short red lines indicate connection locations. (b) The minimum spanning tree of the spiral-contour tree. (c) Connecting adjacent Fermat spirals to form a single continuous path.

Given a prescribed path fill width w specifying spacing between iso-contours, we construct the set L of iso-contours using the Clipper algorithm [Johnson 2015] over R. We index an iso-contour by $C_{i,j}$, where i indicates its distance from the region boundary ∂R, $d(\partial R, C_{i,j}) = (i-0.5)w$, and j is an index among all iso-contours with the same distance index i. For example, $C_{i,j}$ and $C_{i,j'}$ with $j \neq j'$, would belong to two separate pockets. Without loss of generality, we assume that $C_{1,1}$ is always the outer region boundary ∂R.

We build a tree, called the spiral-contour tree, whose nodes are the iso-contours and whose edges denote their connectivity with edge weights encoding how preferable it is to connect the iso-contours. The tree is used to recursively reroute the contours in a bottom-up fashion, producing a single continuous path.

Tree construction. We first connect iso-contours with consecutive iso-values, e.g., $C_{i,j}$ with $C_{i+1,j'}$, into an initial graph. To this end, we define a connecting segment on c$C_{i,j}$ towards $C_{i+1,j'}$ as:

$$\mathcal{O}_{i,j,j'} = \{p \in C_{i,j} \mid d(p, C_{i+1,j'}) < d(p, C_{i+1,k}), k \neq j'\},$$

where $d(p,C)$ denotes the distance from a point p to points along a contour C. The segment $\mathcal{O}_{i,j,j'}$ is formed by possible rerouting points between the two iso-contours. We add an edge between $C_{i,j}$ and $C_{i+1,j'}$ to the graph if $\mathcal{O}_{i,j,j'} \neq \theta$. The weight assigned to the edge is length $(\mathcal{O}_{i,j,j'})$. The preference is to not reroute over a long connecting segment since such a segment is preferred to remain intact to form long, low-curvature paths.

After building the initial graph on iso-contours, we compute a minimum-weight spanning tree, the spiral-contour tree, with $C_{1,1}$ as the root; see Figure 6(b). The tree nodes fall into two types. Type I nodes have degrees less than or equal to two and they correspond to iso-contours that form spirallable regions. Specifically, each such region, e.g., $R_0, R_1 \cdots R_4$ in Figure 6(a), is formed by a path of Type I nodes. Type II nodes have degrees greater than two, e.g., those colored in light blue in Figure 6(b), and they correspond to branching iso-contours. Such an iso-contour provides an interface between spirallable regions and possibly other Type II nodes.

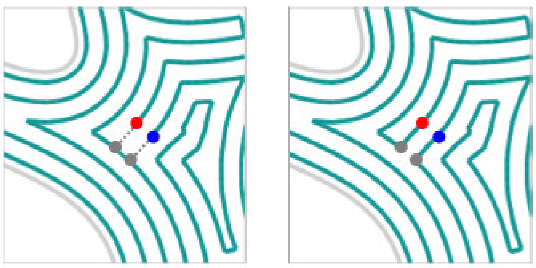

Rerouting. To obtain a globally continuous path, we reroute the iso-contours in a bottom-up fashion, starting from leaf nodes and ending at the root. There are two types of rerouting operations. The first connects iso-contours in a spirallable region, e.g., R_0

in Figure 6, into a single Fermat spiral with start and exit points next to each other. This operation follows the procedure described in Section 3 and illustrated in Figure 5. The second operation connects the start and exit points of a Fermat spiral to a Type II iso-contour, at the closest points (gray points), as shown in the inset figure. Wherever possible, rerouting points are reused to avoid creating new points representing sharp turns.

Curve optimization. The tool path obtained so far is globally continuous and covers the input region R, but it is only C^0 continuous and possibly suffers from highly nonuniform spacing. In postprocessing, we locally optimize the curve to improve its fairness and spacing. The current curve is first adaptively sampled based on curvature so that more samples are placed near sharp turns. The objective function is a weighted sum of three terms: the first term penalizes large perturbations; the smoothing term is defined by a chord-length weighted 1D discrete Laplacian; and the spacing term keeps shortest distances between adjacent curve segments close to a fixed, pre-defined patch spacing. We solve the optimization via iterative Gauss-Newton until curve updates become negligible; a result showing the paths before and after optimization is shown in Figure 7. Implementation details of the optimization step, including precise problem formulation, optimization procedure, and parameter setting, can be found in the appendix.

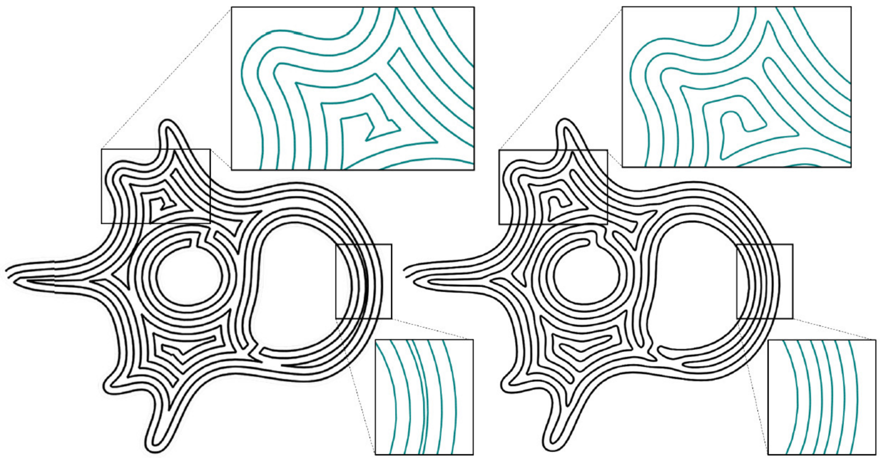

Figure 7: Connected Fermat spirals before (left) and after (right) local optimization. Observe improved curve spacing and reduction of staircasing artifacts in the optimized spirals.

5 Results

We show tool path generation results on shapes with varying degrees of concavity and hollowness. Comparisons are made to conventional zigzag and contour-parallel fill patterns in terms of path continuity, amount of sharp turns, print time, as well as visual quality of the interior fill and fabricated surface exterior.

3D printer and setting. Our experiments have been conducted on a RepRap Prusa i3 FDM 3D printer with firmware Marlin 1.1.0- RC. Printing results and analyses are based on the default printer setting, with tool path width set at 0.4mm, layer thickness at 0.2mm, and maximal nozzle speed at 80 mm per second. G-code is used to transfer the tool paths to the 3D printer.

Input	#segZ	#segC	%stZ	%stC	%stF
dancer 1	22	14	5.87%	1.40%	**1.38%**
dancer 2	19	10	6.58%	1.55%	**1.08%**
dancer 3	21	13	4.11%	1.19%	**0.81%**
crane	8	17	4.86%	**0.46%**	0.93%
butterfly	16	24	1.81%	0.83%	**0.52%**
hand	9	11	4.84%	1.07%	**0.56%**
gear	51	105	1.18%	2.11%	**0.23%**
paw	20	55	1.25%	0.51%	**0.31%**
h-slice1	53	58	4.35%	1.08%	**0.81%**
h-slice2	47	56	5.12%	0.88%	**0.70%**

Table 1: Number of tool path segments (#seg) and percentage of sharp turn points (%st), which we explain in the text, for conventional zigzag (Z), contour-parallel (C), and our CFS fills (F). The 10 shapes are from the last two rows of Figure 8.

Input	#P	#R	CFSt (s)	OPt (s)	Total (s)
dancer 1	4	31	0.25	1.676	1.926
dancer 2	6	27	0.297	1.59	1.887
dancer 3	4	33	0.203	7.085	7.288
crane	2	42	0.125	1.917	2.042
butterfly	4	51	0.359	4.479	4.838
hand	1	30	0.125	7.277	7.402
gear	19	143	0.766	8.978	9.744
paw	8	147	0.813	9.429	10.242
h-slice 1	22	148	0.834	7.092	7.926
h-slice 2	22	145	0.95	7.412	8.362

Table 2: Some statistics and running times for our CFS tool path generation algorithm. We report the number of pockets (#P) and the number of rerouting points (#R) of the tool paths. For running times, we report time needed for rerouting to generate the initial connected Fermat spirals (CFSt) and time for curve optimization (OPt), as well as the total. All running times are in seconds.

Tool path generation. Figure 8 shows tool paths generated by our algorithm for a variety of shapes with varying exterior and interior structures. Note that the two honeycomb input shapes in Figure 8 and the one from Figure 1 are all 2D slices of the

3D porous structures constructed by the work of Lu et al. [2014]. Each tool path is continuous and composed of connected Fermat spirals. All results are produced with the default parameter setting. There are no tunable parameters for initial CFS construction. For curve optimization, the parameters are fixed as discussed in the Appendix.

Table 1 shows the percentage of sharp turns and the number of disconnected tool path segments for three fill patterns: conventional zigzag, contour-parallel fills, and ours. We do not report the latter number for CFS since it always produces a single path. All the zigzag and contour-parallel paths shown and fabricated in our experiments were generated with the Slic3r software [2016].

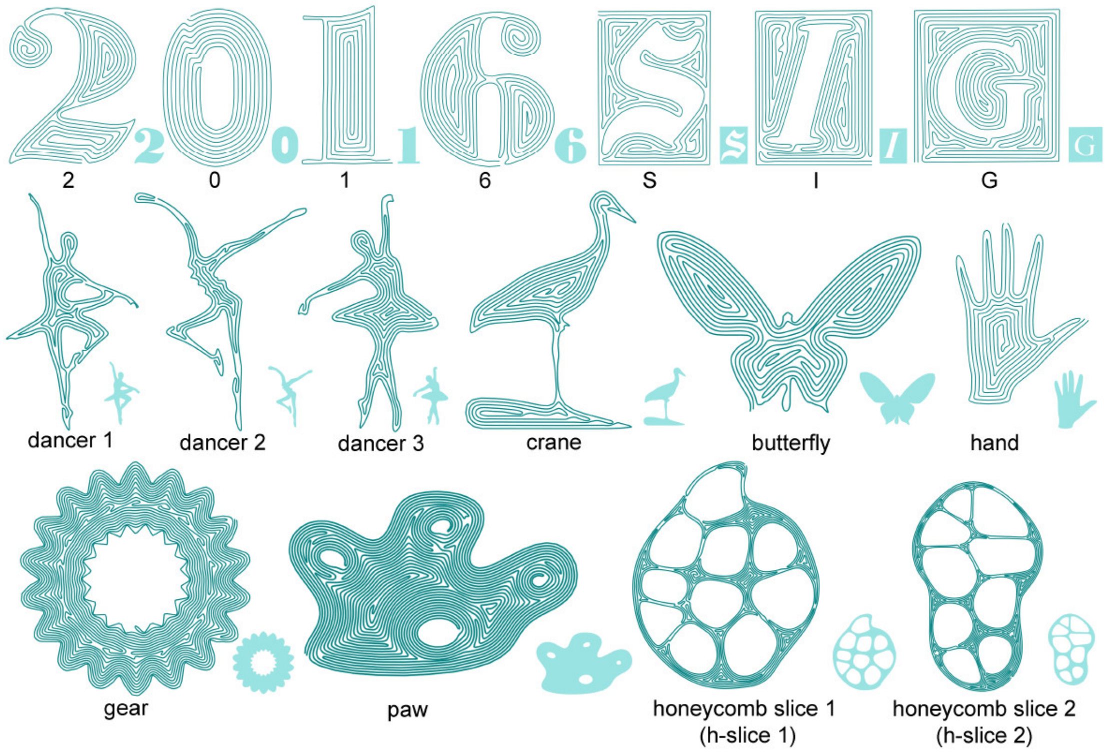

Figure 8: A gallery of continuous CFS tool paths generated by our algorithm. Shown as insets, the input shapes, both synthetic and from slices of fabricated 3D objects (see the honeycomb slices in last row as well as in Figure 1), exhibit varying degrees of complexity in terms of convexity/concavity of boundaries and hollowness. The top two rows show lower-resolution results for ease of visualization. The bottom row shows higher-resolution results, which are closer to that of real fabrication and also demonstrate robustness of our method.

To count the number of sharp turns along a tool path , we uniformly sample 50000 points along π and at each point, we estimate its integral curvature [Pottmann et al. 2009] with a circle of radius 0:2mm, which is appropriate for the size of fabricated layers and the default fill with in our experiments. A point is deemed to represent a sharp turn if the smaller of its associated area coverage for curvature estimation is less than 30% of the circle area. In Table 1, we report the percentages of points deemed as sharp turns. It is quite evident that the number of sharp turns produced by CFS is much lower than that of zigzags and it is more comparable to, but generally still lower than, that of contour-parallel fills. On the other hand, the latter exhibits high contour plurality.

We report running times of our algorithm in Table 2 for a partial list of shapes in Figure 8; other relevant statistics are provided as well. Currently, the spiral construction and connection algorithm is implemented in C++ while the curve optimization phase is implemented in MATLAB. All of the above times are measured on an Intel® Core™ i7-6700 CPU 4.0GHz with 16GB RAM.

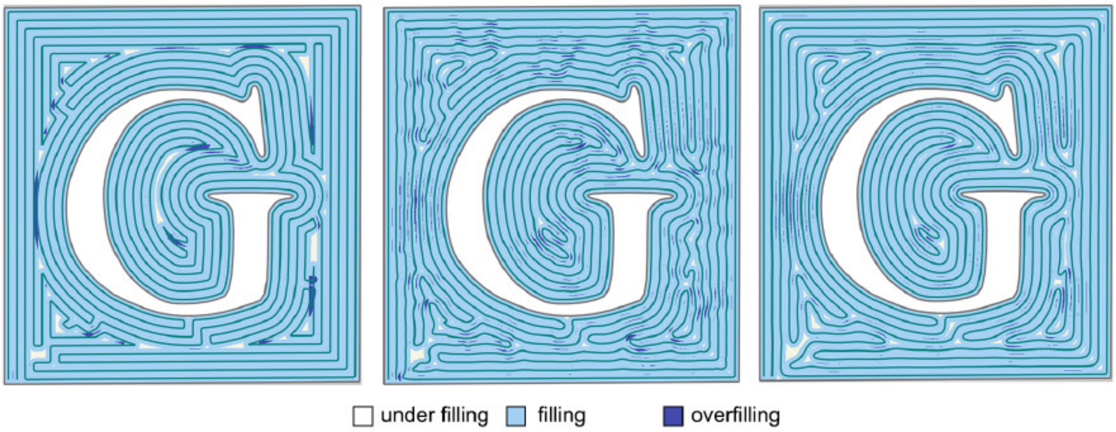

Figure 9: Estimated under- and over-fills visualized for a CFS tool path. Left: before path optimization. Middle: path optimized with even spacing only. Right: optimization with smoothing and even spacing, our default post-processing scheme, attenuates severe over-fills (dark blue spots in left), reduces total over-fills in most cases, but may introduce more gaps, especially near sharp corners (the four corners of the plate) due to curve smoothing.

Under- and over-fill. Under- and over-fills occur as a result of non-uniform spacing between curve segments along a tool path. Since it is difficult to measure the extent of these fill artifacts for real prints, we provide an estimate by thickening a computed tool path at its expected fill width and measure the intersection and gap after the process. Figure 9 visualizes the over- and under-fills for one CFS path before and after path optimization. Figure 10 (top) compares the amount of under- and over-fills over several shapes.

As one would expect, smoothing tends to increase gaps and underfills, especially near sharp corners (e.g., four corners of the rectangular ‘G’ and many corners of the gear model). Overall, our curve optimization (smoothing plus spacing) tends to increase under-fills and reduce over-fills; see Figure 10. As shown in Figure 9, the spacing term is seen to effectively remove or at least, more evenly distribute, severe over-fills of an un-optimized path.

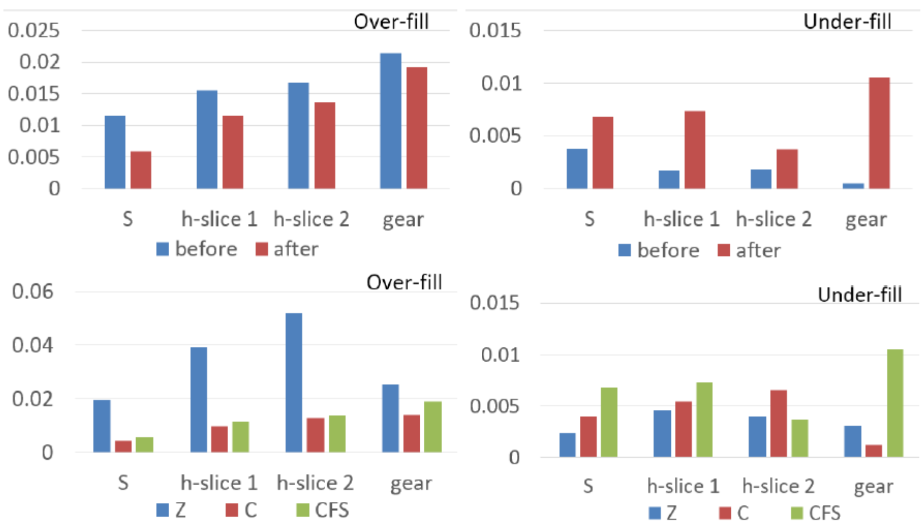

Figure 10: Estimated over- and under-fill rate comparisons on the four shapes from Figure 11. Top: Before and after curve optimization. Bottom: comparison between the three fill methods zigzag (Z), contour-parallel (C), and CFS.

The inability of our current curve optimization scheme to fill all the gaps can be attributed to limited curve movements. For example, curves cannot be elongated to alleviate under-fills. Near sharp corners and turns, there is a trade-off between curve fairness and gap size. Since the gaps are typically few and far in between, sacrificing fairness at few places to fill the gaps, e.g., by elongating the curve locally, is possible; we leave this for future work.

Visual quality. Figure 11 shows photos taken of four 2D layer shapes (the ’S’, gear, and the two honeycomb slices from Figure 8) fabricated using the three fill patterns. Figure 10 (bottom) plots the estimated under- and over-fills over the four shapes.

Visually, we observe that zigzag incurs little under-fill and can generally maintain even material distribution along straight tool paths. However, fill quality degrades near region boundaries, showing both roughness and “aliasing” artifacts. The latter shows up near boundaries which are close to being parallel to, but are not parallel to, the scan direction (see the ‘S’ example). Since the zigzag fill is not globally continuous, fill artifacts also occur over areas where separate zigzag-filled segments join. In terms of estimated overfills, as shown in Figure 10 (bottom left), zigzag incurs a larger amount than its counterparts since paths generated by Slic3r next to region boundaries have a distance smaller than 1 2w to the boundaries, leading to excessive over-fills along these paths.

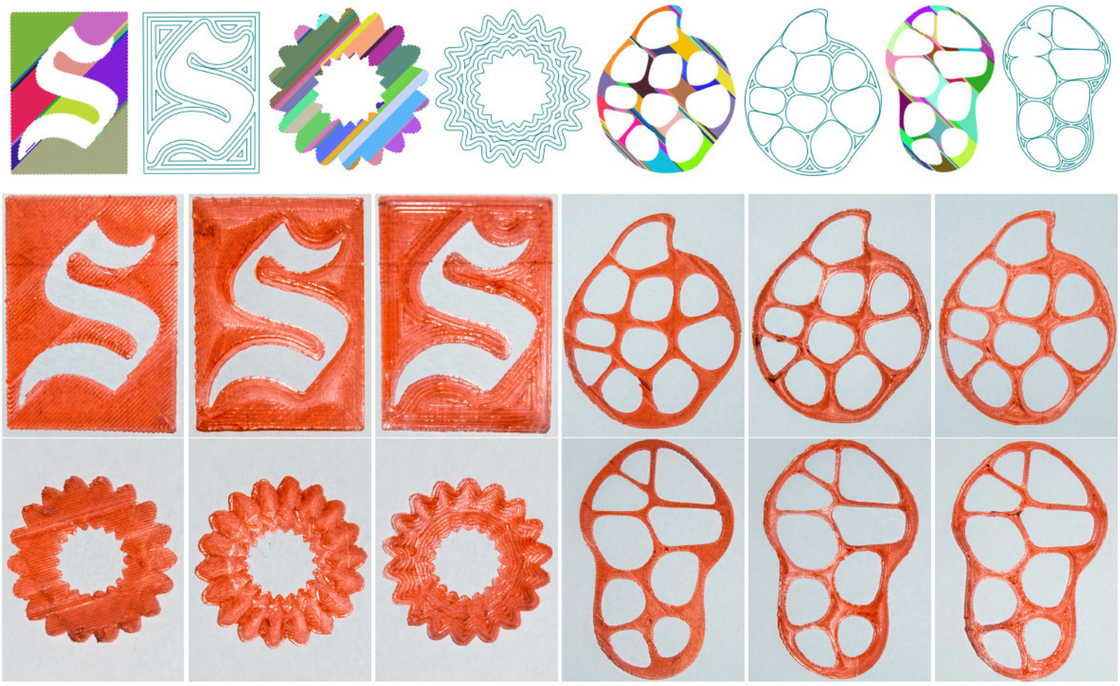

Figure 11: Photographs of fabricated layers using three fill methods (bottom two rows). In each of the four groups, the left result is from zigzag, the middle from contour-parallel, and the last from CFS. Top row shows schematic displays of the zigzag and contour-parallel fill patterns; for zigzag, we color the disconnected fill segments. The CFS fill patterns for the four shapes can be found in Figure 8.

For contour-parallel fills, visible artifacts (under- or over-fills) occur near the center of pockets and between adjacent, but separately contoured regions. In contrast, fabrication resulting from CFS appear to exhibit better overall quality with less visible artifacts. However, CFS appears to lead to relatively large number of under-fills due to curve smoothing; see Figure 10 (bottom right). Of course, one should bear in mind that since 3D printing is a physical process, random device imprecisions which may cause visible artifacts in the filled layers are possible.

Figure 12 examines the surface qualify of a 3D object fabricated using our FDM printer, contrasting CFS fills to zigzag fills. The object is formed by a 50-fold vertical extrusion of the gear layer from Figure 8; the final cylinder is 1cm tall. There are visible gaps from a top view of the CFS fills, due to path smoothing as we discussed. On the other hand, our tool path optimization effectively distributes the (relatively large) total amount of under-fills over a large number of spots so that most individual gaps are small and can be filled by melting of the filament material. From the side views, CFS fills lead to smoother boundaries, while surface roughness arising from zigzag fills is evident. However, the latter is typically corrected by external contouring, but at the expense of under-fills between the contoured exterior and boundaries of the interior zigzag fills.

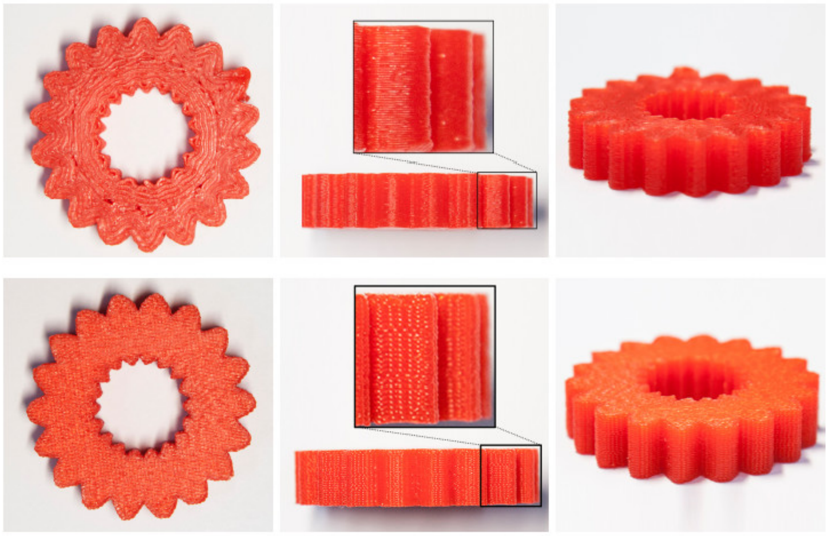

Figure 12: Photographs of 3D fabrications using FDM. The object is an extruded cylinder from the gear layer of Figure 8). A few views and closeups are shown to reveal surface quality. Top: using CFS fills. Bottom: the same gear cylinder fabricated with zigzag.

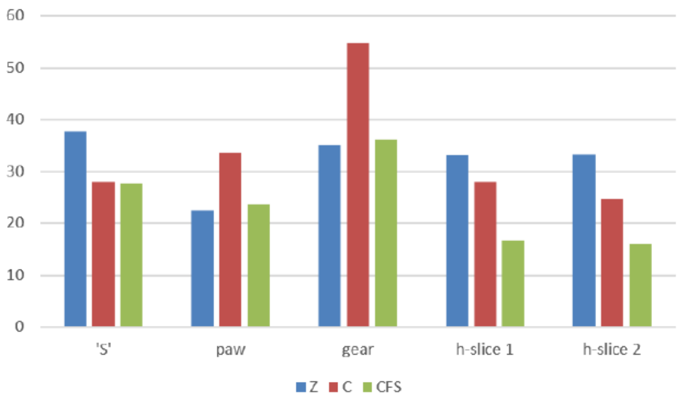

Figure 13: Real 3D printing times (in seconds) for fabricating several layer shapes, from the relatively simple ‘S’ to the more complex honeycomb slices from Figure 8, using CFS (orange), contour parallel (C: cyan), and zigzag (Z: purple) tool path fills.

Fabrication time. Figure 13 compares fabrication times recorded on the RepRap Prusa 3D printer for the three fill methods. We observe that while the fabrication speed for CFS tool paths is generally more favorable than their counterparts on an FDM printer, the speed gains vary. For more complex layers, e.g., the honeycomb slices, the speed gains tend to be more significant.

Comparison to evolved labyrinths. In Figure 14, we compare our connected Fermat spirals to a result from stochastic curve evolution by Pederson and Singh [2006]. The results become more visually comparable if the evolution is rewarded by better alignment of the curves with the boundary of the input shape, as shown. However, the curve evolution performs inward erosions and as such, it is unlikely to maintain a fair and outline-conforming exterior path as our spiral approach. Moreover, the local stochastic movements are likely to result in more sharp turns throughout.

Figure 14: Our CFS fill (left) vs. a result from stochastic curve evolution [Pedersen and Singh 2006], which is copied from Figure 16 of the paper. It is important to note that the outer boundary (right) is the input contour and not part of output of the curve evolution. The evolution results in the interior curve structure.

6 Conclusion, limitation, and future work

We present a region fill algorithm using connected Fermat spirals, achieving global continuity. Our algorithm extends the use of spirals as space-filling curves from regular convex shapes to nonconvex shapes, even shapes with many interior holes. Our contributions are two-fold. At a conceptual level, we introduce the use of Fermat spirals to the construction of a new kind of space-filling patterns. The construction reflects compelling properties of Fermat spirals. The use of Fermat spirals prevents the curve from being locked in pockets. Furthermore, the freedom allowed in choosing start and end points along the boundary of a Fermat spiral facilitates a scheme which systematically joins a set of Fermat spirals. Practically, the new curves possess appealing properties for tool path planning in the context of layered fabrication.

In retrospect, connected Fermat spirals are not necessarily suitable for all layer shapes. Compared to their counterparts, it appears that they excel at filling layers with complex geometry, especially those with many holes, to achieve higher build quality both inside and on the exterior. If one were to print a 3D object with honeycomb interiors [Lu et al. 2014], a sensible plan would be to print the middle slices using our CFS fills while topping off the print, where the layer shapes are likely to be convex or spirallable, with zigzag or hybrid fills, possibly alternating between them.

As discussed previously, the connected Fermat spirals are not guaranteed to be truly space-filling. They also lack the regularities and mathematical rigors possessed by Peano or Hilbert curves; the definition of connected Fermat spirals is constructive and not conceptual. Our current algorithm generally results in a smaller number of sharp turns compared to zigzag. However, it makes no attempt to minimize them. The local curve optimization scheme also leaves room for improvements. In particular, current curve displacements cannot "slide" adjacent segments against each other or elongate the curve to fill gaps. These operations are possible by adding attraction-repulsion forces as in the curve evolution scheme of Pedersen and Singh [2006]; we leave this for future work.

The amount of gains afforded by our new tool paths for layered fabrication is dictated by the mechanics of the motor controllers of the 3D printers. Contemporary, low-end printers rely on simple motor controls, approximating a smooth curve by piecewise linear segments. One may regard such a mechanism as catering to zigzagging tool paths. This may also be accounted for as a limitation of our approach, as we seek low-curvature but non-straight tool paths and do not take advantage of the control mechanisms of these lowed printers. On the other hand, it is possible to incorporate more sophisticated look-ahead and adaptive speed control algorithms to achieve higher motor speed for low-curvature but non-straight tool paths [Wang and Cao 2012]. As well, higher-end printers with more sophisticated controllers, like those of current Computer Numerical Control (CNC) machines, can also achieve a higher motor speed for tool path with smaller curvatures [Wang et al. 2010]. With such controllers, Fermat spirals would incur a significant speed-up.

In the future, we would like to investigate the interplay between fill patterns of consecutive layers. For better strength of FDM prints, consecutive layers should not be fabricated with close-to-identical fill patterns. Our construction scheme may be slightly perturbed so that the Fermat spiral fills of consecutive layers may interweave. Another inter-layer optimization to consider is with respect to the start and end points of each layer, in term of increasing the coherence and avoiding redundant moves of the nozzle from one layer to the next. Finally, it would be interesting to re-examine optimization problems involving object orientation or decomposition while taking into account how the resulting 2D slices are filled.

Acknowledgments

We would first like to thank all the reviewers for their valuable comments and suggestions. The development of our problem formulation was critically influenced by discussions with Dan Halperin, to whom we are grateful. Thanks also go to Yang (Sherry) Liu (illustration), Shenqi Liu (3D printing), Sha (Ada) He (video), and the rest of the SDU lab-mates for their tremendous help on production. This work is supported in part by grants from National 973 Program (2015CB352501), NSFC (61232011, 61202147, 61332015, 61572291), NSERC Canada (No. 611370), Israeli Science Foundation (No. 1790/12), U.S.-Israel Bi-National Science Foundation (No. 2012376), and gift awards from Adobe and Intel.

References

ARKINA, E. M., FEKETEB, S. P., AND MITCHELL, J. S. 2000. Approximation algorithms for lawn mowing and milling. Computational Geometry 17, 1-2, 25–50.

CHEN, X., ZHANG, H., LIN, J., HU, R., LU, L., HUANG, Q., BENES, B., COHEN-OR, D., AND CHEN, B. 2015. Dapper: Decompose-and-pack for 3D Printing. ACM Trans. on Graph 34, 6, 213:1–213:12.

DAFNER, R., COHEN-OR, D., AND MATIAS, Y. 2000. Contextbased Space Filling Curves. Computer Graphics Forum 19, 3, 209–218.

DING, D., PAN, Z. S., CUIURI, D., AND LI, H. 2014. A tool-path generation strategy for wire and arc additive manufacturing. Int. J. of Adv. Manufact. Tech. 73, 1-4, 173–183.

DINH, H. Q., GELMAN, F., LEFEBVRE, S., AND CLAUX, F. 2015. Modeling and Toolpath Generation for Consumer-level 3D Printing. In ACM SIGGRAPH Courses, 17:1–17:273.

DWIVEDI, R., AND KOVACEVIC, R. 2004. Automated torch path planning using polygon subdivision for solid freeform fabrication based on welding. J. of Manufact. Sys. 23, 4, 278–291.

EL-MIDANY, T. T., ELKERAN, A., AND TAWFIK, H. 1993. Tool path pattern comparison: contour-parallel with direction parallel. In Geom. model. and imaging — new trends, 77–82.

GIBSON, I., ROSEN, D., AND STUCKER, B. 2015. Additive Manufacturing Technologies, 2nd ed. Springer.

HELD, M., AND SPIELBERGER, C. 2014. Improved spiral highspeed machining of multiply-connected pockets. Computer- Aided Design and Applications 11, 3, 346–357.

HILDEBRAND, K., BICKEL, B., AND ALEXA, M. 2013. Orthogonal slicing for additive manufacturing. Computers & Graphics 37, 6, 669 – 675. Shape Model. Intl. (SMI) Conf.

HU, R., LI, H., ZHANG, H., AND COHEN-OR, D. 2014. Approximate pyramidal shape decomposition. ACM Trans. on Graph 33, 6, 213:1–213:12.

JIN, G., LI, W., AND GAO, L. 2013. An adaptive process planning approach of rapid prototyping and manufacturing. Robotics and Computer-Integrated Manufacturing 29, 1, 23–38. J

IN, Y. A., HE, Y., FU, J. Z., GAN, W. F., AND LIN, Z. W. 2014. Optimization of tool-path generation for material extrusion based additive manufacturing technology. Additive Manufacturing 1, 4, 32–47.

JOHNSON, A., 2015. Clipper - an open source freeware library for clipping and offsetting lines and polygons. http://www.angusj. com/delphi/clipper.php.

KULKARNI, P., MARSAN, A., AND DUTTA, D. 2000. A review of process planning techniques in layered manufacturing. Rapid Prototyping Journal 6, 18–35.

LU, L., SHARF, A., ZHAO, H., WEI, Y., FAN, Q., CHEN, X., SAVOYE, Y., TU, C., COHEN-OR, D., AND CHEN, B. 2014. Build-to-last: Strength to weight 3D printed objects. ACM Trans. on Graph 33, 4, 97:1–97:10.

LUO, L., BARAN, I., RUSINKIEWICZ, S., AND MATUSIK, W. 2012. Chopper: Partitioning models into 3D-printable parts. ACM Trans. on Graph 31, 6, 129:1–129:9.

PEDERSEN, H., AND SINGH, K. 2006. Organic labyrinths and mazes. In Proc. of Non-photorealistic Animation and Rendering (NPAR), 79–86.

POTTMANN, H., WALLNER, J., HUANG, Q.-X., AND YANG, Y.- L. 2009. Integral invariants for robust geometry processing. Comp. Aided Geom. Design 26, 1, 37–60.

PR´E VOST, R., WHITING, E., LEFEBVRE, S., AND SORKINEHORNUNG, O. 2013. Make It Stand: Balancing shapes for 3D fabrication. ACM Trans. on Graph 32, 4, 81:1–81:10.

REN, F., SUN, Y., AND GUO, D. 2009. Combined reparameterization-based spiral toolpath generation for five-axis sculptured surface machining. Int. J. of Adv. Manufac. Tech. 40, 7, 760–768.

SLIC3R, 2016. Slic3r. http://slic3r.org/.

STAVA, O., VANEK, J., BENES, B., CARR, N., AND MˇE CH, R. 2012. Stress relief: improving structural strength of 3D printable objects. ACM Trans. on Graph 31, 4, 48:1–48:11.

VANEK, J., GARCIA, J., BENES, B., MECH, R., CARR, N., STAVA, O., AND MILLER, G. 2014. PackMerger: A 3D print volume optimizer. Computer Graphics Forum 33, 6, 322–332.

VANEK, J., GALICIA, J. A. G., AND BENES, B. 2014. Clever support: Efficient support structure generation for digital fabrication. Computer Graphics Forum 33, 5, 117–125.

WANG, L., AND CAO, J. 2012. A look-ahead and adaptive speed control algorithm for high-speed CNC equipment. Int. J. of Adv. Manufact. Techn. 63, 705–717.

WANG, L., CAO, J. F., AND LI, Y. Q. 2010. Speed optimization control method of smooth motion for high-speed CNC machine tools. Int. J. of Adv. Manufact. Tech. 49, 313–325.

WASSER, T., JAYAL, A. D., AND PISTOR, C. 1999. Implementation and evaluation of novel buildstyles in fused deposition modeling. Strain 5, 6, 95–102.

WIKIPEDIA, 2015. Fermat's spiral — wikipedia, the free encyclopedia. [Online; accessed 28-November-2015].

WIKIPEDIA, 2016. Labyrinth — wikipedia, the free encyclopedia. [Online; accessed 10-April-2016].

YANG, Y., LOH, H., FUH, J., AND WANG, Y. 2002. Equidistant path generation for improving scanning efficiency in layered manufacturing. Rapid Prototyping Journal 8, 1, 30–37.

YAO, M., CHEN, Z., LUO, L., WANG, R., AND WANG, H. 2015. Level-set-based partitioning and packing optimization of a printable model. ACM Trans. on Graph 34, 6, 214:1–214:11.

ZHANG, X., LE, X., PANOTOPOULOU, A., WHITING, E., AND WANG, C. C. L. 2015. Perceptual Models of Preference in 3D Printing Direction. ACM Trans. Graph. 34, 6, 215:1–215:12.

DSCarver: Decompose-and-Spiral-Carve for Subtractive Manufacturing

Abstract: We present an automatic algorithm for subtractive manufacturing of freeform 3D objects using high-speed machining (HSM) via CNC. A CNC machine operates a cylindrical cutter to carve off material from a 3D shape stock, following a tool path, to “expose” the target object. Our method decomposes the input object’s surface into a small number of patches each of which is fully accessible and machinable by the CNC machine, in continuous fashion, under a fixed cutter-object setup configuration. This is achieved by covering the input surface with a minimum number of accessible regions and then extracting a set of machinable patches from each accessible region. For each patch obtained, we compute a continuous, space-filling, and iso-scallop tool path which conforms to the patch boundary, enabling efficient carving with high-quality surface finishing. The tool path is generated in the form of connected Fermat spirals, which have been generalized from a 2D fill pattern for layered manufacturing to work for curved surfaces. Furthermore, we develop a novel method to control the spacing of Fermat spirals based on directional surface curvature and adapt the heat method to obtain iso-scallop carving. We demonstrate automatic generation of accessible and machinable surface decompositions and iso-scallop Fermat spiral carving paths for freeform 3D objects. Comparisons are made to tool paths generated by commercial software in terms of real machining time and surface quality.

Keywords: Subtractive manufacturing, tool path planning, CNC, surface decomposition, set cover, Fermat spirals

1. Introduction

With the increasing popularity of additive manufacturing and 3D printing in computer graphics, one should not overlook the fact that subtractive processes remain the core and dominant technology in manufacturing today1. Compared to additive manufacturing in most cases, subtractive manufacturing is faster and more cost-effective for the same level of product precision, accommodates a vastly wider range of materials, and is capable of superior surface finishes. Moreover, while a 3D printer builds a 3D shape one 2D layer at a time, subtractive manufacturing of 3D objects is intrinsically a three-dimensional problem, involving direct manipulation of 3D objects and operation over curved surfaces. The ensuing geometry processing appears to possess more compelling twists and technical challenges than those arising from additive fabrication.

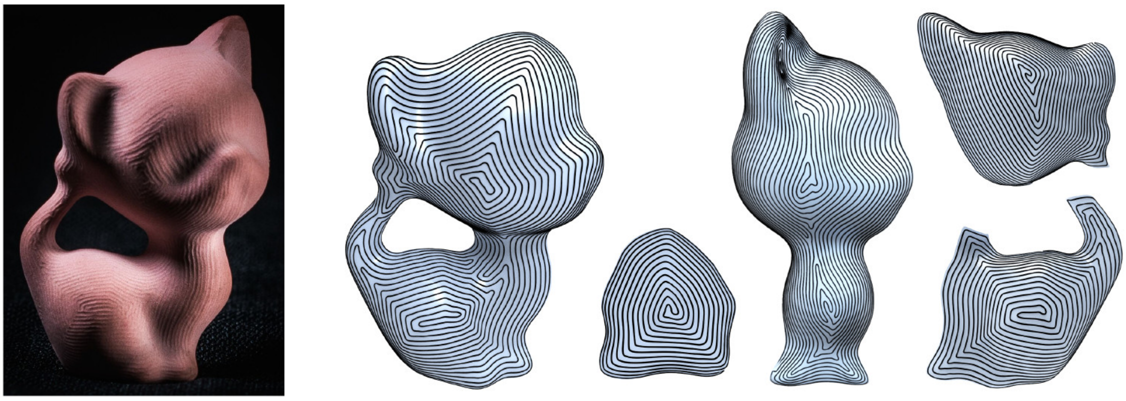

Fig. 1. A freeform 3D object, the kitten, automatically decomposed into five machinable patches, each carved using a CNC machine following a continuous iso-scallop Fermat spiral path. The fully machined object is shown on the left. We deliberately lowered the path resolution to ease path visualization.

Subtractive manufacturing is primarily realized by computer numerical control (CNC) machining tools. A CNC machine operates a cylindrical cutter to carve off material from a shape stock in 3D space to “expose” the target 3D object; see Figure 3. The cutter head traces out a space curve, called a tool path, which must completely fill the object surface. Desirable properties of tool paths for efficient CNC machining, in particular high-speed machining (HSM), include fairness (i.e., low-curvature) and continuity (i.e., less on/off switching or tool retractions), similar to additive manufacturing, but all considerations must be shifted from 2D regions to curved surfaces. One added twist for subtractive manufacturing is accessibility: in general, the CNC cutter may not be able to access all regions of the object no matter how it is oriented. Another new issue is controlling the amount of residual material, called scallop, after carving to ensure a quality surface finishing; see Figure 3. The typical goal for scallop optimization is to maximize uniformity of the scallops while minimizing their height without over-carving the surface.

Existing methods for CNC tool path planning from the computer aided design (CAD) and manufacturing (CAM) domains are primarily designed to machine relatively simple geometric primitives, e.g., planar and quadric surfaces, swept volumes, and CAD models composed of planes and other parameterizable patches. Conventional tool path patterns such as zigzags work quite effectively for such surfaces with simple boundaries and interior geometries. In terms of setup planning, where a machinist decides how to orient and stabilize the shape stock with fixtures for carving, it is highly critical to minimize the number of setups, i.e., to avoid re-fixturing and re-orientation of the object or the CNC machine cutters. In practice, setup planning is predominantly a manual process, where machinists rely heavily on their domain knowledge and experience.

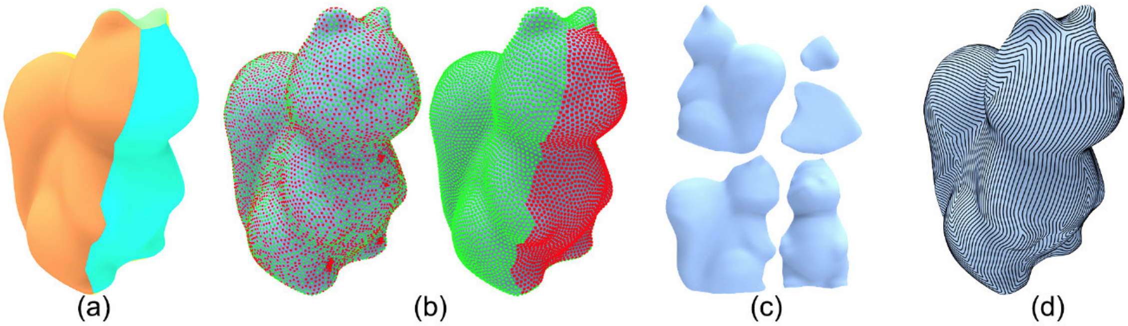

Fig. 2. Overview of DSCarver, our decompose-and-carve algorithm for 3+2-axis CNC machining of freeform 3D objects. (a) Input 3D shape with pre-segmentation into few height fields. (b) Decomposition into accessible regions (left: with overlaps; right: after boundary extraction). (c) Integration of accessibility decomposition (b) and height fields (a) into machinable patches. (d) Connected iso-scallop Fermat spiral paths computed for a few patches.

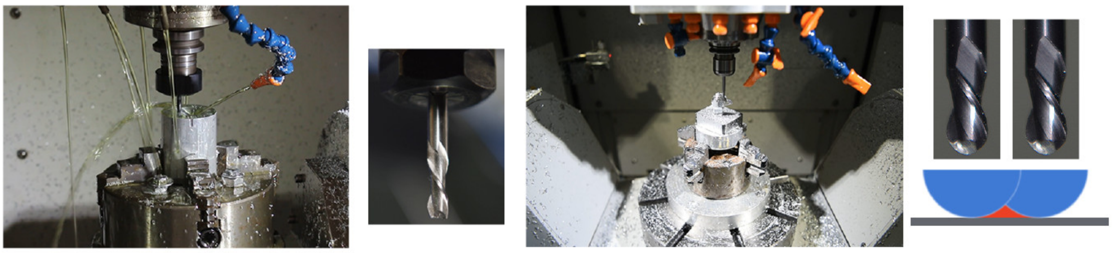

Fig. 3. 3-axis pocket milling (left) with a square cutter vs. 3+2-axis machining (cutter on top) with a ball cutter. Scallop (red) is the material residual left between adjacent ball cutter (green) paths.

In this paper, we are interested in efficient subtractive manufacturing of 3D objects formed by freeform or sculpted surfaces [Lasemi et al. 2010], such as the example shown in Figure 1. In general, a 3D object cannot be fully machined under a single setup. Thus during the setup planning phase, there is an inherent surface decomposition problem which seeks to segment the object's surface into a minimum number of patches each of which can be fully machined under one setup. For a freeform object with moderate complexity, regardless of how it is decomposed, the machinable patches are likely to exhibit irregular interior undulations and wavy boundaries, which would pose various challenges to tool path planning, especially when taking scallop optimization into account.

Our goal is automatic optimization of setup and tool path planning for finish-stage machining of free-form 3D objects using 3+2 machines, where at this finishing stage of the carving process, the current object is already geometrically close to the final product. In the CAD/CAM industries, freeform surfaces are typically carved by 5-axis machining and 3+2 machining represents a special but dominant configuration for 5-axis CNC machines. Specifically, the cutter of a 3+2 machine has a fixed orientation during carving, but can move with three degrees of freedom. The cutter orientation can be adjusted with two degrees of freedom for the next carving2.

Given an input 3D object represented by a closed two-manifold surface, we develop an algorithm to tackle two key technical problems in setup and tool path planning:

(1) Surface decomposition. During setup, the core problem is to minimize the number of object or cutter setups (i.e., re-fixturing or re-orientation of the CNC cutter) to ensure accessibility of the entire input surface by the CNC cutter. To this end, we cover the input surface with a minimum number of accessible regions by posing and solving a set-cover problem; see Figure 2(b). Then from each accessible region, we extract a set of patches each of which can be fully machined by 3+2 machining, in a single fixed cutter-object setup. We obtain these patches by integrating the accessible regions with a pre-segmentation of the input surface into a small set of height fields; see Figure 2(a). Together, these patches, which we refer to as machinable patches, form a decomposition of the input surface; see Figure 2(c).

(2) Tool path planning. In the carving phase, for each machinable patch obtained from the decomposition step, we compute a continuous, space-filling, and iso-scallop tool path which conforms to the patch boundary, where iso-scallop paths seek to maximize uniformity of the scallop height over the patch. To this end, we advocate the use of connected Fermat spirals [Zhao et al. 2016] as the preferred tool path pattern. This is justified by the observation that Fermat spirals tend to outperform zigzag, the dominant tool path patterns for CNC machining, as the patch boundary

and interior geometry become more complex.

To compute iso-scallop Fermat spirals, we first generalize the original Fermat spirals designed for layered manufacturing to work for curved surfaces. Then we develop a novel method to control the spacing of Fermat spirals based on directional surface curvature and adapt the heat method [Crane et al. 2013a] to obtain iso-scallop carving; see Figure 2(d).

We call our setup and tool path planning algorithm decompose-and-spiral-carve, or DSCarver, for short. We demonstrate automatic generation of accessible and machinable surface decompositions and iso-scallop Fermat spiral carving paths for 3+2 machining of freeform 3D objects. Comparisons are made to conventional tool paths generated by high-end CAD/CAM systems, both over real CNC machining time and surface quality.

2 BACKGROUND AND RELATED WORK

The core geometry problems for both additive and subtractive manufacturing can be classified into setup and tool path planning. In the setup stage for 3D printing, a 3D object may be hollowed [Lu et al. 2014], decomposed [Hu et al. 2014; Luo et al. 2012], or reconfigured in other ways [Bermano et al. 2017; Chen et al. 2015; Prévost et al. 2013; Stava et al. 2012] to improve print quality and/or save material consumption. Frequently adopted and commercially available tool path patterns for 3D printing include zigzag [Ding et al. 2014] and contour parallel paths [Yang et al. 2002]. Zhao et al. [2016] introduce connected Fermat spirals as an alternative and demonstrate their advantages over conventional tool paths for layered manufacturing.

CNC machining basics. CNC machining operates a cylindrical cutter with a prescribed length and size (measured on the cutter's horizontal profile) and goes around in 3D space with its head spinning at high speed to carve off material from a shape stock. During rough-stage machining, larger chunks of material are carved off along the path by a thicker cutter often with a flat end. In the surface finishing stage, a rounded or ball end cutter is often employed. The fine lines of residuals left between adjacent tool paths after surface finishing are referred to as scallop; see Figure 3. The height and width of the scallop should be properly controlled and they depend on path spacing, cutter orientation, and surface curvature. For example, over convex regions (compared to concave regions and assuming that the angle between the cutter orientations stay fixed), path spacing needs to be denser to reduce scallop height.

Full 5-axis vs. 3+2 machining. 3-axis machining or pocket milling is similar to layered manufacturing as it also traverses a 2D domain, but removes instead of injects material. Curved freeform or sculpted surfaces [Lasemi et al. 2010] are typically carved by full 5-axis or 3+2 machining. The cutter of a full 5-axis machine can move with five degrees of freedom. In contrast, the cutter of a 3+2 machine has a fixed orientation and moves in x,y, z directions only. In both cases, the cutters typically only point downward at an oblique angle, not upward. As well, it is desirable that the cutter orientation does not deviate from the surface normal too much to bound the scallop height [Farouki 2016; Farouki and Li 2013; Zhao et al. 2013].

In our current work, we choose 3+2 machining over full 5-axis CNCs due to several factors. 3+2 machining represents the dominant 5-axis CNC technology in the industry and 3+2 machines are a lot more accessible and easier to work with compared to full 5-axis machines. Conventional tool paths such as zigzag work much more naturally with 3+2 machining. Given the same surface patch to carve, 3+2 machining almost always beats full 5-axis CNC in speed and accuracy. Overall, improving the state of the art in 3+2 machining offers more value to the domain of subtractive manufacturing.

Fig. 4. Frequently applied CNC tool path patterns.

Setup planning for CNC machining. Generally, setup planning involves the preparation of instructions for setting up parts for CNC machining [Hazarika et al. 2015; Xu et al. 2007]. The key issue is how to orient the parts, perhaps in multiple configurations, to attain a high level of efficiency and surface quality. Setup planning methods from the CAD and manufacturing literature have mainly focused on CAD models, where it is widely assumed that the input consists of feature-based designs or outputs from a feature recognition system [Xu et al. 2007]. Typically, the machined parts are assumed to be composed of prismatic or rotational primitives [Amaitik and

Kiliç 2007], or geometric features that possess certain manufacturing or functional significance [Tseng and Joshi 1998], e.g., k-sided pockets, through semi-blind, or compound slots, etc.

Tool paths for CNC machining. Existing methods for carving curved surfaces can be roughly classified into parameterization based and drive surface methods [Choi and Jerrard 1998]. By parameterizing a curved patch onto the plane, a tool path can be planned on the plane and then mapped back to the surface patch, e.g., [Ren et al. 2009]. Methods based on drive surfaces intersect the input surface patch with a set of planes to obtain the tool paths. The most frequently adopted drive surfaces are equidistant parallel planes, resulting in iso-planar tool paths. The orientations of the drive planes can be optimized, resembling the slicing problem for additive manufacturing [Hildebrand et al. 2013]. Iso-planar curves resulting from plane-surface interactions can be turned into zigzag [Misra et al. 2005], contour-parallel offset, or spiral patterns [Hauth and Linsen 2012; Held and Spielberger 2014; Zhou et al. 2016]; see Figure 4.

Desirable properties of CNC tool paths include fairness, continuity, and good spacing for quality scallop and surface finishing. Improper spacing between adjacent, parallel tool paths can lead to over- or under-fill for layered manufacturing. For CNC machining, under-fill translates to uncut strips over the surface, which is caused by widely spaced tool paths. Such artifacts on machined surfaces are more problematic than inefficiencies caused by paths spaced too closely. The latter, an “over-fill” in the context of CNC machining, leads to overlapping between cutter trajectories over the surface and thus inefficiency; it may also over-cut the desired parts.

For high-speed machining, path continuity and fairness are even more critical than in the case of layered manufacturing since for CNC cutters operating at high speed, cutter lifting, retraction, and deacceleration, as the results of path discontinuities and sharp turns, are especially counter-productive [Park et al. 2003; Zhou et al. 2016]. Therefore, continuous tool paths based on Fermat or double spirals are preferred [Hauth and Linsen 2012; Wang et al. 2015; Zhao et al. 2016; Zhou et al. 2016]. In the CAD and manufacturing domains, many methods have been presented for iso-scallop tool path planning, e.g., [Agrawal et al. 2006; Can and Ünüvar 2010; Zoua et al. 2014]. However, most of these methods were designed to work with zigzag tool paths and our work is the first attempt at generating iso-scallop Fermat spiral paths for curved surfaces.

Surface decomposition. There have been many works in computer graphics on shape decomposition [Shamir 2008]. The central criterion for our decomposition analysis is accessibility. The fairness criterion for region boundaries is sought since conventional tool paths typically conform to the boundaries [Hauth and Linsen 2012; Lasemi et al. 2010; Zhou et al. 2016]. Existing works from the subtractive manufacturing domain, e.g., [Hauth and Linsen 2012; Held and Spielberger 2014; Zhao et al. 2016], mainly considered the problem of decomposing a planar region into simple geometric segments for efficient pocket machining. Such simple segments often admit continuous and fairer tool paths, e.g., using Fermat spirals, and the per-segment tool paths can be linked to attain global continuity [Zhou et al. 2016]. Our work follows a similar approach but must deal with free-form surfaces and accessible regions with complex boundaries and interior undulation.

With its connection to the set cover problem, it is known that generally, finding the minimum number of orientations to ensure full accessibility, i.e., the accessibility-based decomposition problem, is NP-hard [Frank et al. 2006; Gupta et al. 1996]. Early work by Gupta et al. [1996] takes a greedy approach which iteratively identifies accessible regions of maximal surface areas. Frank et al. [2006] analyze accessibility in one planar slice and solve a set cover problem. Various solution mechanisms including decision trees [Keeney and Raiffa 1993], swarm intelligence [Guo et al. 2009], and genetic algorithms [Bo et al. 2006] have been proposed to solve the difficult optimization problem. Also related is the problem of decomposing a surface into a set of approximate height fields [Herholz et al. 2015], which we adopt for pre-segmentation of the input surface.

3 OVERVIEW

The input to our algorithm is a freeform 3D object represented as a 2-manifold triangle mesh. During preprocessing, the input mesh surface is first segmented into a small number of height fields. We compute height fields since each such surface region can be fully machined by a 3+2 machine with a fixed cutter orientation and fixed cutter-object setup. Then we cover the input surface by a minimum number of accessible regions and integrate the resulting regions with the pre-segmentation to obtain a small number of machinable surface patches, which form a decomposition of the input surface. Tool path planning is carried out for each patch to obtain a continuous space-filling curve attaining maximal scallop uniformity. Figure 2 illustrates the algorithm pipeline.

Surface decomposition. Our accessibility analysis involves finding a minimum number of object setups to ensure accessibility of the entire input surface by the CNC cutter. Each object orientation induces an accessible region, which is the set of all points on the input surface that are accessible by the cutter in some valid orientation. When machining the same accessible region, the fixture setup for the CNC machine remains unchanged. Switching from one accessible region to another, the fixtures need to be adjusted to re-stabilize the shape stock, which is a delicate and time-consuming endeavor.

We proceed by sampling a set of object orientations, so that the union of their induced accessible regions completely covers the input surface. With this cover as input, we find the minimum number of orientations by solving a set-cover problem [Cormen et al. 2001]. Typically, the optimal solution incurs significant overlaps between the accessible regions. We resolve these overlaps and arrive at a surface decomposition by integrating the accessible regions with the pre-segmented height fields. This is followed by boundary optimization to obtain the set of machinable patches.

Tool path planning. Given a machinable patch, we produce a single continuous space-filling curve for that patch using connected Fermat spirals [Zhao et al. 2016]. The main innovation is to ensure that the patch finishing using the spiral carving path is optimized for scallop quality, i.e., to compute an iso-scallop Fermat spiral. To this end, we adjust the path spacing based on directional curvature over the input surface path, to optimize uniformity of the resulting scallops. We show that an nonhomogeneous version of the heat method [Crane et al. 2013a] for geodesic computations can be adapted to compute iso-scallop level-set contours over the surface patch, from which we can extract the connected Fermat spiral paths. Each machinable patch is machined separately following the iso-scallop Fermat spiral paths under a fixed 3+2 machining setup.

4 SURFACE DECOMPOSITION

In this section, we detail the surface decomposition step. It produces a small set of connected and machinable surface patches, each of which is fully accessible by the CNC cutter with respect to one of few machining setups. The patches possess fair or low-curvature boundaries to facilitate efficient tool path planning therein.

Height field decomposition. During preprocessing, we decompose the input object's surface into a small number of height fields by implementing a scheme that is very similar to [Herholz et al. 2015]. Our height field decomposition problem is almost exactly the same as the one addressed by the said approach except for two minor differences. First, we do not deform the input surface to lower the number of height fields produced. Second, the height fields in their work were defined using ideal lines/rays with infinitesimal thickness. In our implementation, we replace the rays with cylinders with nonnegligible radius which reflect the physical girth of the CNC cutter, assuming that the cutter is sufficient long during carving.

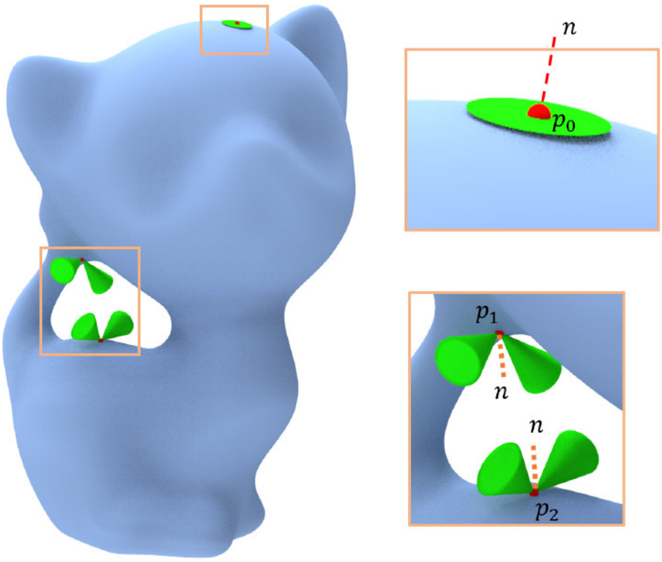

Fig. 5. Accessibility cones on the kitten model. For the object orientation shown, p_0 has a full accessibility cone; p_2 cone is split into two sub-cones due to cutter collision with the kitten's tail. p_1 is inaccessible.

Accessibility cones. In CNC machining, there is typically a bound on the angle φ between cutter orientation and surface normal at a point on the object surface. This bound defines an accessibility cone around each surface normal. If the surface is oriented in such a way that the cutter can orient itself to fall inside the accessibility cone at a point $p \in S$, then p is accessible with respect to that surface orientation. In our work, we liberally set the angle at $\varphi = \pi/2$ but account for the cutter's physical girth and possible global collision with parts of the 3D object. Such a collision leads to a splitting of the full cone into sub-cones conservatively to ensure full accessibility of the sub-cones; see point p_2 in Figure 5.

Point accessibility. Most 5-axis CNC machines can only point the cutter downward inside an oblique angle between 0^o and 90^o [Apro 2008]. For the orientation of the kitten model shown in Figure 5, point p_0 is accessible from any direction in its accessibility cone, p_1 is inaccessible since its cone is entirely pointing downward, and p_2 is partially accessible due to potential cutter collision.

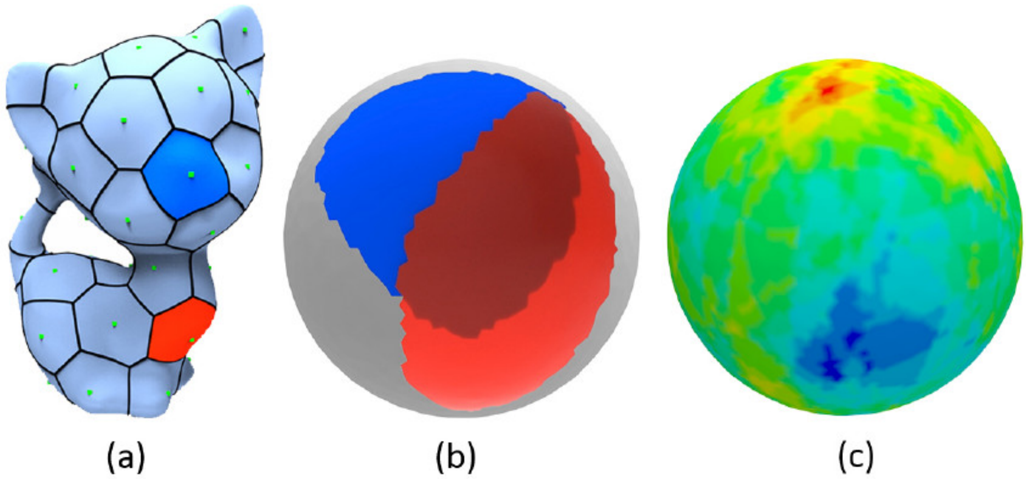

Fig. 6. Cell accessibility and illustrations on the Gaussian sphere. (a) Intrinsic Voronoi cells over object surface. (b) Corresponding regions on the Gaussian sphere representing object orientations which would allow the blue and red cells (a) to be accessible. (c) Color coding of the number of accessible Voronoi cells for each object orientation (red = higher count).

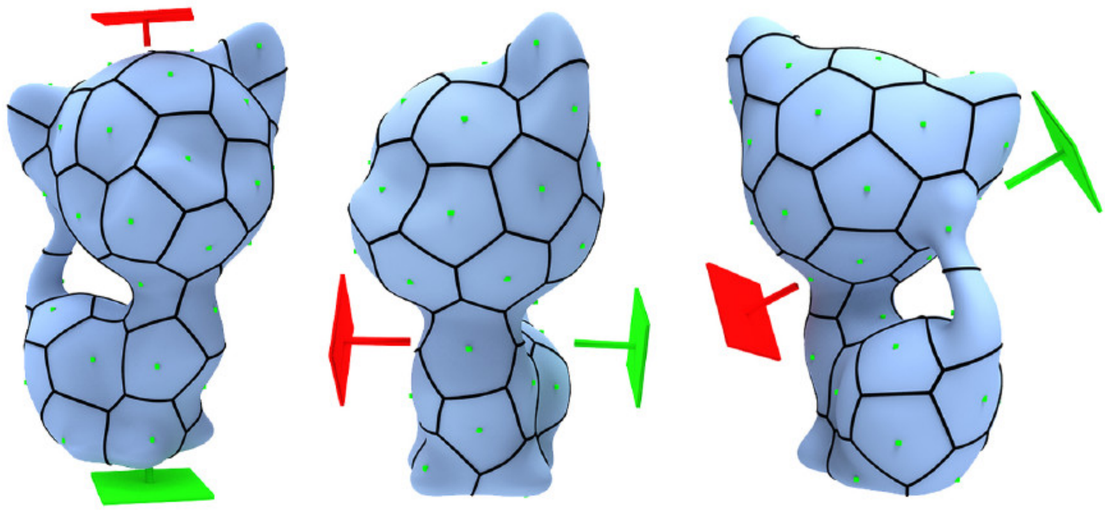

Fig. 7. Three different MINORI solutions computed by SCP, with the same object orientations count (three).

Cell accessibility. We start by uniformly sampling N points over the input surface mesh and computing an intrinsic Voronoi tessellation with the sample points as sites. For each Voronoi cell $c_i, 1 \leq i \leq N$, based on point accessibility and accessibility cones, we estimate a set Ri of object orientations each of which would allow all points in ci to be accessible by the CNC cutter. Mapping R_i onto the Gaussian sphere defines a region R_i on the sphere; see Figure 6. The color coding indicates the number of accessible Voronoi cells for a number of orientation candidates. Red colors are associated with orientations for which many cells are accessible. The set of candidate object orientations can be sampled uniformly or randomly.

Accessibility cover. We compute the accessible regions by formulating the problem as an instance of the set-cover problem (SCP). Then we resolve overlapping between the obtained covers to arrive at a surface decomposition. Given a set $U = \{1,2,\cdots \mathrm{n}\}$, called the universe, and a collection S of subsets of the universe whose union equals the universe, the set cover problem is to identify the smallest sub-collection (one with the fewest subsets) of S whose union equals to U. SCP is one of most classic NP-hard problems in combinatorics and computer science [Cormen et al. 2001].

For our accessibility region problem, we consider all the Voronoi cells $c_i, 1 \leq i \leq N$ as the elements of the universe U, and for each sampled orientation P, all of its accessible cells consist of a subset S of universe U. Then given all sampled orientation Pi and their corresponding subsets $S_i, 1 \leq i \leq M$, using SCP we could get a minimal number of orientations $P_i, 1 \leq i \leq k$, the union of their corresponding subsets $S_i, 1 \leq i \leq k$ k equals to U. We call such a set of minimal number of orientations MINORI.

To solve the MINORI problem, which is an instance of the overlapping SCP, we resort to the greedy scheme from Chvatal [1979]. For a typical freeform 3D object with the prescribed set of sampled orientations, our MINORI solution often include only a handful of orientations. Moreover, solutions with the same orientation count are often not unique. Figure 7 shows three possible MINORI solutions for the kitten model. After overlap resolution, the MINIORI solution that leads to the smallest number of machinable patches is selected for tool path planning, after boundary refinement.

Overlap resolution. A MINORI solution typically contains many cells that are accessible from more than one object orientation. Thus, the accessible regions in a MINORI are expected to overlap significantly; see Figure 7. On the other hand, the number of accessible regions in a MINORI gives us the minimum number of object orientations, or fixture setups, for CNC machining. By definition, an accessible region thus obtained can be fully accessed by the CNC, assuming that the CNC cutter can be oriented differently. However, when machining a surface piece, the cutter orientation is fixed in a 3+2-axis setup. For the piece to be fully machinable with that fixed orientation, the piece must be a height field. Hence, to resolve the overlap and obtain a surface decomposition into 3+2-axis machinable patches, we must integrate the accessible regions from a MINORI with the height fields computed from pre-segmentation.

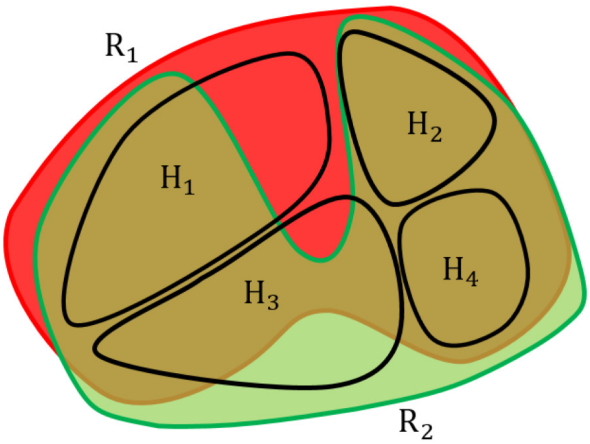

Fig. 8. Orientation label assignment and propagation. (a) Height field H1 is assigned region R1's label since it covers some non-overlapping parts (red) of R1 and of R1 only. H3 is not assigned any label since it covers non-overlapping parts from both R1 and R2. (b) H1 propagates its label to H2 since H2 is entirely covered by an overlap (yellow) involving R1. (c) Unassigned height fields H3 and H4 may be split by graph cut.

Integrating accessible regions and height fields. The integration step produces a surface decomposition for a given MINORI solution by assigning object orientation labels associated with the MINORI to height fields from the pre-segmentation. The label assignment starts away from the overlaps between active regions and progresses towards the overlaps via label propagation. Specifically, we first identify any height field that contains surface points which belong to some non-overlapping part of one and only one accessible region; we assign the orientation label associated with this accessible region to the height field; see Figure 8(a). Then we propagate, recursively, orientation labels from assigned height fields to adjacent unassigned ones only when they are entirely covered by an overlap between appropriate accessible regions. For example, height field H1, with label from accessible regionR1, propagates its label to H2 only when H2 is entirely covered by an overlap involving R1; see Figure 8(b). After the propagation, any remaining unassigned height field may be split by the boundary extraction process we outline next.

The integration step keeps the number of accessible regions or fixture setups fixed, but can split a height field. The above assignment procedure aims to keep such splits to a minimum since the final number of height field pieces (i.e., the machinable patches for tool path planning) corresponds to how many times the 3+2-axis CNC machine needs to be re-oriented.

Boundary extraction and refinement. The orientation label assignments to the height fields already provide a partial set of patch boundaries. To "close the loop" and complete the remaining boundaries, we apply graph cut [Boykov et al. 2001] to split regions corresponding to unassigned height fields along low curvature paths. The graph cut is formulated as an energy minimization defined over the cells $c_i, 1 \leq i \leq m$ in the region of interests. Specifically, we seek a cell assignment r that minimizes the following energy function:

$$E(\mathrm{r}) = \sum_{i=1}^{m} D\big(r(p_i)\big) + \alpha \sum_{(ij)} S\left(r(p_i), r(p_j)\right)$$

where D is the unary data term, S is the pairwise smoothness term, and α provides a trade-off (we set $\alpha = 100$ in our experiments). The data term D estimates the likelihood of c_i to belong an orientation $r(c_i)$ by measuring its distance to a cell with a definite orientation. The smoothness term S measures the curvature of the object surface along the border between c_i and c_j and penalizes high-curvature edges. Finally, the combined patch boundaries are smoothed by geometric snakes [Lee and Lee 2002].

Final selection of surface decomposition. As described above, each MINORI solution would lead to a surface decomposition into machinable patches. We select one result which contains the least number of patches, and if there are ties, boundary quality is the tie breaker. Tool paths are computed for the final set of machinable patches.

5 TOOL PATH PLANNING

Once the surface is decomposed into a collection of surface patches, a tool path plan is designed for each patch. This tool path planning is not as simple as generating an equally-spaced filling curve, and commonly it is designed by skillful professionals in an ad hoc manner. For carving the surface, one needs to plan the path of a ball-end cutter, which has some physical prescribed radius, and hence implies two key requirements:

• Consideration of scallop. The problem is that equally-spaced curves may not necessarily lead to a uniform scallop distribution. To obtain uniform scallop on a surface, the gap between two neighboring paths needs to be adaptive to the directional curvatures of the points along two nearby paths. This requirement is the most distinct feature of this tool path planning problem.

• Smoothness. Generally speaking, a smooth tool path is preferred in practice due to the upper limit of velocity and the acceleration of the cutter. A zigzag path not only slows down the cutter, but also tends to cause damage to the cutter.

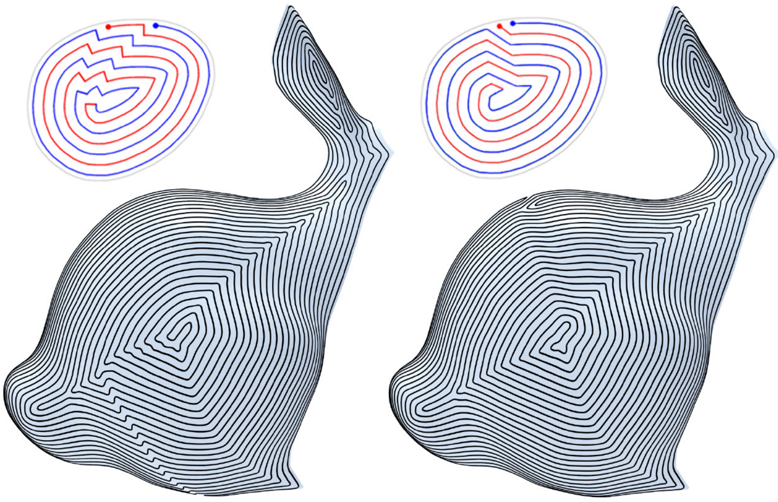

Fig. 9. Replacing zigzag re-routing connections (see top-left inset, which is taken from Figure 5(c) of [Zhao et al. 2016]) with “oblique” lines that conform better to tangential directions of the iso-contours, as shown in the top-right inset. This can effectively reduce the number of sharp turns in the final tool paths (after tool path optimization); see the before (left) and after (right) pictures of the bunny patch and focus on the lower left region.

Based on these two requirements, we design a three-step algorithm for generating the final tool path: (1) compute a shape aware scalar field whose isolines meet the gap requirement, (2) connect the isolines into a continuous tool path using the Fermat spiral generation technique, and (3) smooth the tool path while keeping the gap varying as small as possible. In the following, we shall elaborate the details of Step 1 and Step 3. For details on Step 2, we refer the reader to the recent work by Zhao et al. [2016], in particular, Figures 4 and 5 in that paper. In this work, we apply a simple trick to alter the way the iso-contours are re-routed to obtain the Fermat spirals, effectively reducing the number of sharp turns in the tool paths (as shown in Figure 9) and improving machining speed. Specifically, instead of making zigzag connections which would result in many right-angle turns, we replace them with short “oblique” curves which conform better to the tangential directions of the iso-contour at the re-routing points; see insets in Figure 9 for an illustration.

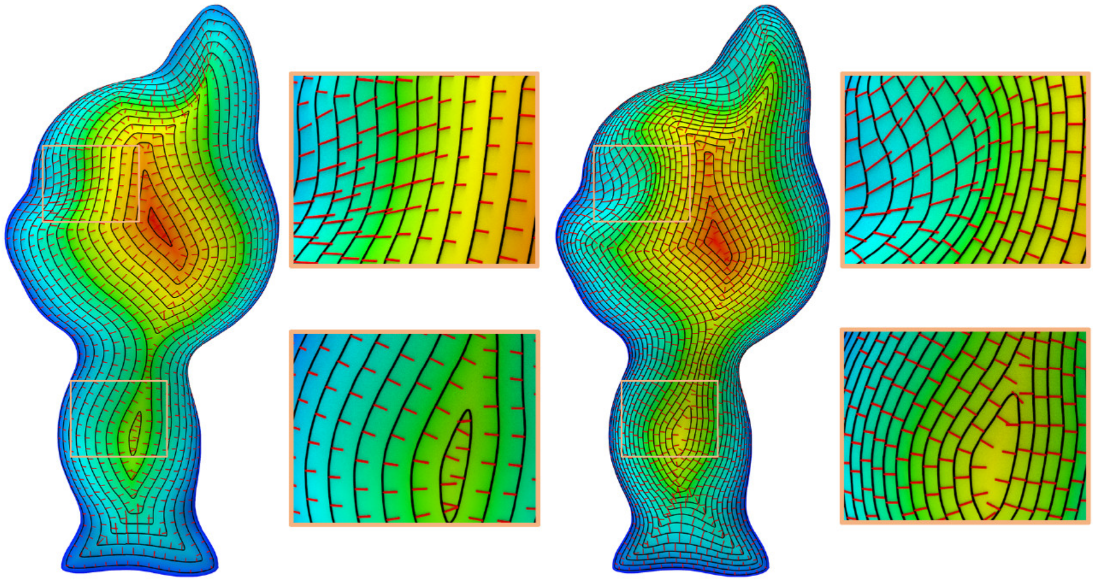

Fig. 10. The iterations of tool paths optimization: the black curves are the tool paths generated from the isolines of the surface geodesic distance field. The short red lines represent the desired gaps computed at the points sampled along the tool paths according to Eq. 1. From left to right, two time steps are depicted, showing that the gaps between two adjacent tool paths are quickly optimized to be consistent with the desired gaps and stable.

5.1 Shape-aware tool path generation

As mentioned above, the tool path design is constrained by geometry variations of the points along the path. More precisely, the scallop h is deemed to have close relationship with the directional curvature [Kim et al. 2006]. Let p be a point on a surface S and path Π that goes through p. Following [Kim et al. 2006], the dependency between the scallop h and the gap $g(p,\Pi)$ between adjacent sections of the path is empirically formulated as

$$g(p,\Pi)=\sqrt{\frac{8hR_{cutter}}{1+R_{cutter}G(p,\Pi)}}, R_{cutter}\gg h, (1)$$

where $G(p,\Pi)$ is the curvature of p at the direction perpendicular to the forward direction of tool path Π at point p. It is difficult to generate the tool path directly from this formula because one cannot determine the gaps before the continuation of the generated path is defined.

Our key idea when computing the tool path is to obtain a shape aware metric tensor field g on the surface from the directional curvature tensor field G, and use its isolines as the tool paths with the required uniform scallop. Once the metric field is defined, the boundary ∂S is set to be the zero-level isoline, and then the other isolines are iteratively defined, with respect to g, by increasing the geodesic distance to the boundary ∂G by Π during each step. We recall that a fast-marching method can be used for this purpose. After the isoline L_i has been extracted, it can be used to generate L_{i+1} by considering the projected metric tensor $g|L_i$ at L_i. Note that $g|L_i$ should be orthogonal to L_i. However, directly setting it is not easy since L_{i+1} has to be used to estimate $g|L_i$ but L_{i+1} is still undetermined before $g|L_i$ is known. Alternatively, we solve this problem by the following iterative optimization approach.

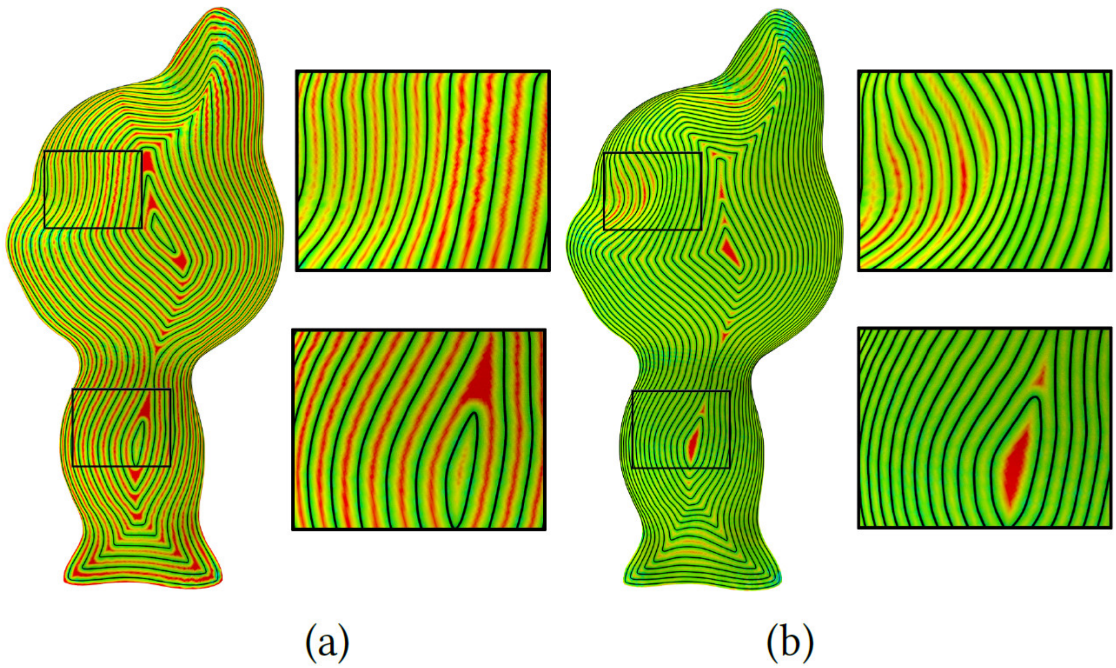

Fig. 11. Scallop (shown in red color on the machined surface) with uniform gap of tool paths (a) and with adaptive gap of tool paths (b).

As the output of the above PDE, the isolines of the resulting geodesic distance field is helpful in setting the desired tool paths. Moreover, we use the gap д defined in Eq. 1 at each point of the surface as a modifier to adjust the distance value in the field. This makes the gap between two adjacent paths vary from the directional curvature of the path points. The gradient direction at each point of the distance field is used to compute directional curvature. Recall that the heat method [Crane et al. 2013b] uses a PDE to solve the geodesic problem on a mesh surface S, and the heat, after diffusion for a short period t , provides a good approximation to the gradients of the real geodesic distance field. Inspired by the approximation power of the heat-based method, we apply a similar approach to the PDE:

$$(\mathrm{A} - \mathrm{t}L_c \otimes H)\mu = \delta_\gamma,$$

where A is the diagonal matrix given by the triangle areas, $A^{-1}L_c$ defines the Laplacian matrix, the Dirac function δ_γ provides an initial heat distribution rooted at the boundary, and the symmetric matrix H associates each mesh edge with the average of the gaps at the two end points of the edge. Note that H is absorbed into this PDE by an element-wise product.

To make the gap between isolines of the geodesic distances more consistent with the metric tensor g, we iteratively update the direction-related gap matrix H based on the values obtained in the previous iteration. As shown in Figure 10, our experiments confirm that the iteration converges extremely fast and in practice, only 2~3 iterations are sufficient to obtain a scalar field whose isolines meet the direction-related gap requirements. Figure 11 shows the resulting scallop reduction by adaptive gaps between two adjacent tool paths.

Note that while our tool path generation problem is directly related to geodesic distances, it is a bit different from a general distance field problem. We have to iteratively solve the problem, i.e., to update the existing distance field by considering the gap requirements of its iso-contours. However, during each iteration, we can use either the heat equation or other, possible better alternatives, such as Short-Term Vector Dijkstra (STVD) of Campen et al. [2013].

5.2 Tool path refinement

The initial tool path must be refined by considering two important spacing constraints: (i) the widest space at p, between adjacent sections of the path Π, cannot exceed the gap constraint $\mathrm{g}(p,\Pi)$ (written as g for simplicity), or equivalently, the largest empty circle has a radius not larger than $\mathrm{g}/2$, and (ii) the narrowest space at p is as close as possible to Π. Let $\{x_i\}_{i=1}^{k}$ be the point sequence that represents the tool path. The idea is to evolve the initial tool path by optimizing the following objective function:

$$\frac{dx_i}{dt} = \lambda_1 \times T_{Smooth} + \lambda_2 \times T_{Attraction} + \lambda_3 \times T_{Repulsion},$$

where T_{Smooth}, $T_{Attraction}$, $T_{Repulsion}$ characterize the smoothness requirement, the attraction of x_i to the centers of nearby large empty circles, and the repulsion between x_i and its nearby points on the path, respectively. Figure 12 shows a sequence of intermediate results (note that the time t can be understood as the number of iterations). On the right, plot shows the widest/narrowest spaces as function of time. We use a conventional Laplacian smoothing technique to express the smoothness requirement.

For the attraction term, we first find a collection of empty circles such that (i) each circle has a radius larger than $g/2$ and (ii) any two circle centers have a distance of at least Π. We call such points $\{q_j\}_{i=1}^{k_1}$ anchors; See the red points in Figure 12. The term $T_{Attraction}$ attracts the path to the nearby anchors, where each anchor has an influence geodesic disk with a radius of $3g/2$. The repulsion term is applied to xi if there are other points $\{x_j\}_{ij=1}^{k_2}$ along the path for which the geodesic in between, i.e. $||d_{i,j}||_g$, is less than g.

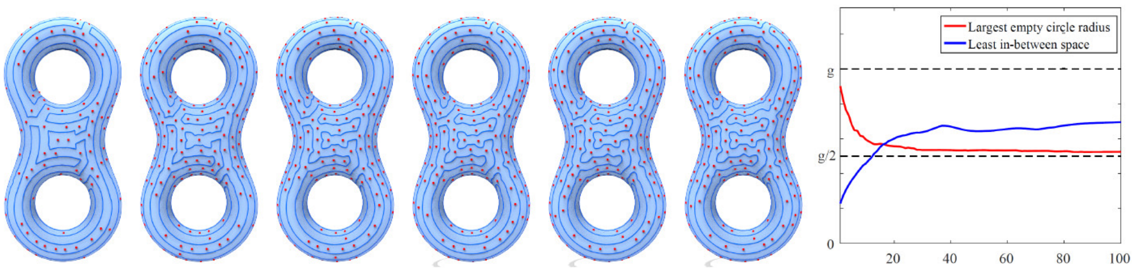

(a) Initial (b) #20 (c) #40 (d) #60 (e) #80 (f) #100 (g) Spacing plot

Fig. 12. Tool path optimization. Guided by the smoothness/spacing constraints, the initial tool path is evolved into a smooth pseudo-geodesic spiral with at most ($g/2 + \epsilon$) wide space on both sides after 100 iterations, where $g/2$ is the sweeping radius of the cutter. That is to say, when the program terminates, the largest empty circle has a radius that is very close to $g/2$ (the red points are the centers of the typical empty circles). The plot (g) shows the change of the largest empty circle radius and the least in-between space of the tool path. In other words, the cutter is able to cover the entire surface if following the optimized tool path. (Note that g varies on the surface in practice due to shape variation. We normalize g for the visualization purpose in the plot (g).

The above optimization is applied on a finite set of points sampled over the surface. In our current experiments for CNC machining, the size of the real models is about $50 \times 60 \times 70\text{mm}^3$. For such models, we found that a sampling of 80K points is sufficient. Hence, we precompute 80K blue noise points on the surface to serve as the anchor point candidates. For larger models, we can adaptively adjust the number of sample points according to the model size, treating it as a scaling issue.

During each iteration, for each candidate point q_j, we compute the largest empty circle centered at q_j and keep its radius r_j, for q_j,. The candidate points are then selected to form an anchor set in a decreasing order of the radius to define a largest empty circle. Two criteria for candidate selection include (i) the radius r_j is larger than $g/2$, and (ii) the newly added anchor point have a distance, of at least g, to the selected anchor points.

6 RESULTS AND EVALUATION

In this section, we show surface decomposition and tool path generation results for freeform 3D shapes with varying degrees of geometric complexity. Comparisons to conventional tool paths, i.e., zigzag and contour-parallel, for CNC machining are provided to evaluate our iso-scallop space filling curves using Fermat spirals. We also report real machining times and show fully machined 3D objects using a 3+2 machine with machining setups and tool paths planned by our fully automatic method.

Fig. 13. A gallery of surface decomposition results for 3+2-axis machining. For each model in each row, the first two images show the accessible regions obtained after overlap resolution in two different views; the next two images show the final machinable patches obtained in two views.

Implementation and parameters. Our surface decomposition and tool path generation methods have both been implemented in C++. We set the cutter diameter at 4.0mm during height field decomposition and for defining the accessibility cones. We produce physical machining of full 3D objects with high-quality surface finishing, setting the scallop height at 0.02mm. To make the carving paths more visible for visualization purposes only, we relax the scallop height to 0.045mm when machining some surface patches. All the results shown in this section were obtained with the same parameter setting: four iterations of the heat method and 40 iterations of tool path generation optimization.

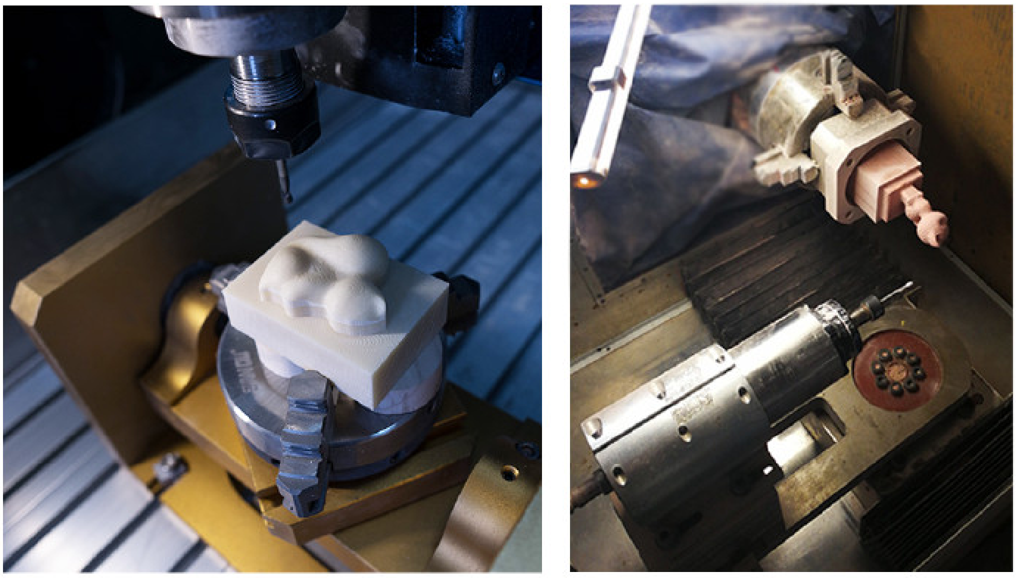

Fig. 14. Photographs capturing a couple of fixture configurations applied to stabilize the 3D objects during CNC machining.

Decomposition. Figure 13 shows results of our accessible surface decompositions as well as the final machinable patches obtained after integrating the accessible regions with the pre-segmentation into height fields suitable for 3+2 machining. Table 1 shows some statistics related to the surface decomposition step, including running times of the sub-steps. Running times were measured on an Intel® CoreTM i7-7700 CPU 4.2GHz with 16GB RAM. For geometrically complex models such as the fertility which also has a non-zero genus, our algorithm is able to obtain a small number of accessible regions and for each region, a small number of patches that can be machined by a 3+2 machine without changing the fixture. Figure 14 provides two photographs demonstrating the fixtures applied to stabilize the shape blocks for real machining.

Tool path generation. Figures 1 and 15 show continuous iso-scallop Fermat spiral paths generated by our algorithm for several curved surface patches obtained from the decomposition step. The patches exhibit varying geometric characteristics in their boundaries and interiors to demonstrate the generality of our tool path planning method. To make the carving paths more visible, we deliberately chose a low-resolution setting. Scallop heights for some of the patches in Figure 15 can be visualized in Figure 16, left column, and compared to zigzag (middle) and contour-parallel (right). Real machining results can be found in Figure 17. Average running times for computing the spiral tool paths for each patch are reported in the last column of Table 1. As we can see, our tool path planning scheme is quite efficient.

3D Model	$\#A$	$\#P$	t_A(s)	t_P(s)	$\bar{t}_P$(s)
RABBIT	2	4	14.2	17.5	5.6
SQUIRREL	2	5	17.5	21.0	5.7
BUNNY	2	5	18.3	21.1	4.3
KITTEN	2	5	24.2	28.4	6.2
MAXPLANCK	2	4	27.1	30.5	6.0
FERTILITY	2	11	48.9	57.2	4.8

Table 1. Some statistics and running times for our surface decomposition and tool path generation. We report the number of accessible regions (#A) and the number of machinable patches (#P) after integrating the height fields and accessible regions and boundary optimization. For running times (all in seconds), we report time needed for computing accessibility covers (t_A), the total time for the surface decomposition phase (t_P), and average time for computing tool paths for each machinable patch ($\bar{t_P}$).

Real machining. Our real machining experiments have been conducted on a CNC 6040 2200W 5-axis machine, with machinable resin board as the testing material to form solid 3D objects. CNC cutting results and analyses are based on the default machine setting: cutter diameter at 4.0mm, maximal feed rate at 500mm/min, chord error at 0.001mm, and spindle speed at 15,000r/min. G-code is used to transfer the tool paths.

Figure 17 shows several photographs taken of the real machining results obtained for several freeform 3D objects of varying geometric complexity. Close-ups are provided to show the carving paths and scallops from our iso-scallop Fermat spirals. Please also check out the supplementary video to see the Fermat spirals in action.

Comparison to conventional tool paths. The two most frequently adopted tool path patterns for CNC machining are zigzag and contour parallel (also referred to as iso-contour) paths. In Figure 16, we compare visually the scallop height distributions for zigzag paths, contour-parallel paths, and Fermat spiral paths generated by our method. All the zigzag and contour-parallel paths were generated with the NX package from Siemens PLM Software [2016]. Siemens NX, formerly known as NX Unigraphics, is a high-end CAD/CAM/CAE software package. Overall, our results exhibit a higher degree of height uniformity with the same path spacing.

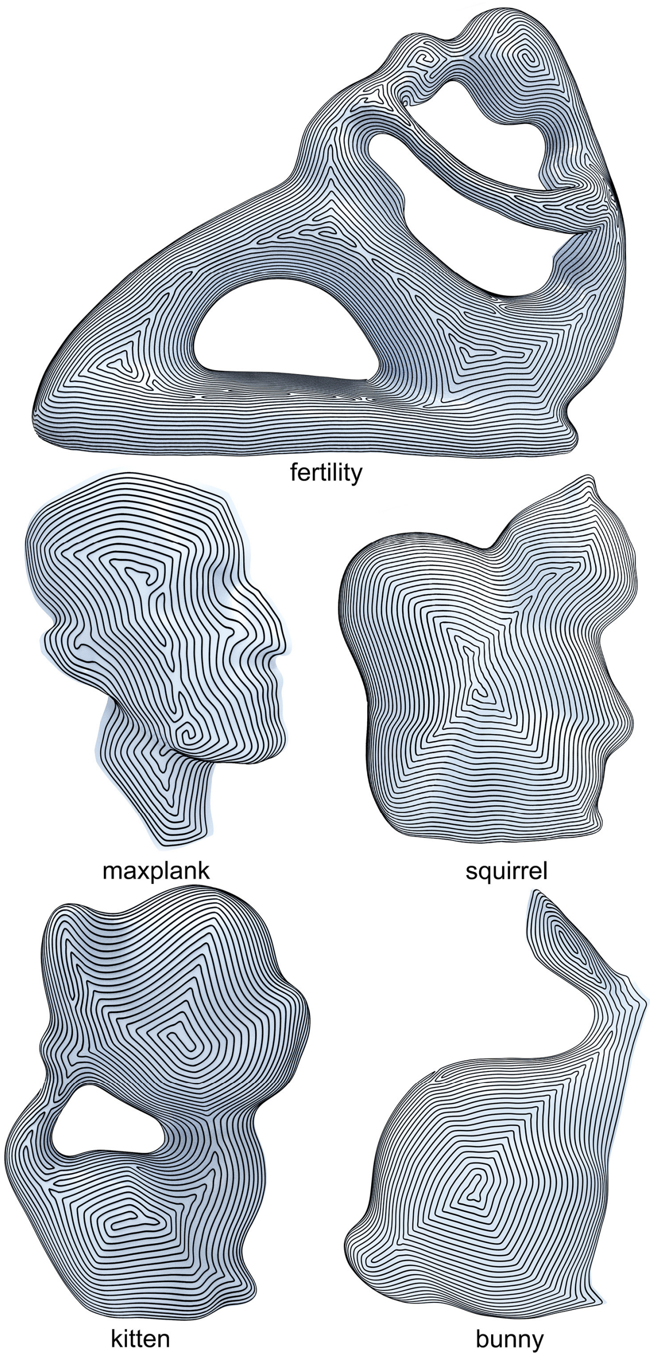

Fig. 15. Continuous iso-scallop Fermat spirals generated by our method, over patches with diverse geometric characteristics. To ease visualization, we show carving paths obtained at a low resolution.

Table 2 shows statistics collected for the three kinds of tool paths, including real machining time using the CNC 6040 2200W 5-axis machine. The tested patches are shown in Figure 15 and Figure 2. Unlike the Fermat spiral paths we produce, zigzag and contour-parallel paths are not always able to cover an entire patch using a single traversal, resulting more than one tool path segments. The segment counts are expected to increase when the patch boundary is wavier or contain more thin structures or multiple components, as in the case of the Fertility and Kitten patches with holes. In terms of real machining time, our iso-scallop Fermat spirals generally outperform zigzag and contour-parallel paths, while the improvement over contour-parallel paths is more marginal.

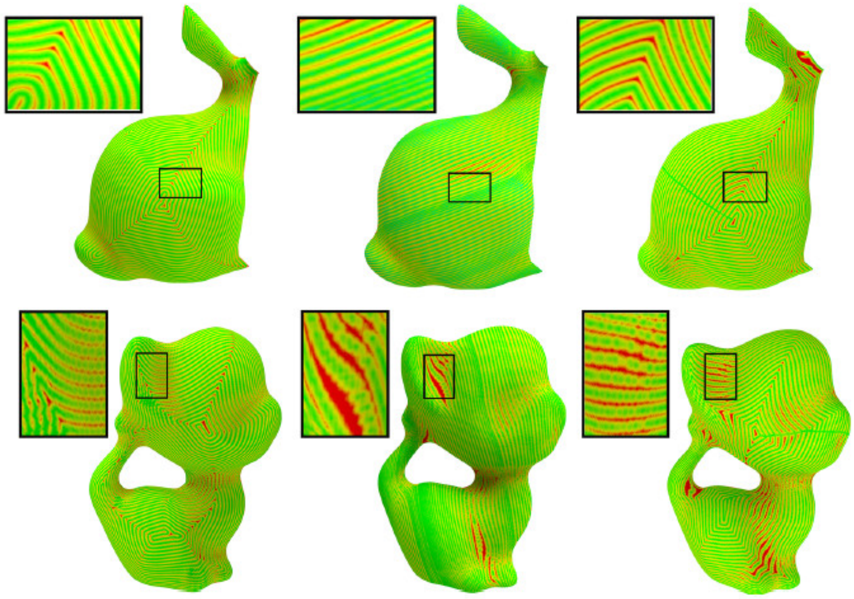

Fig. 16. Visualizing scallop heights over several machined patches using our Fermat spiral paths (left), conventional zigzag paths (middle), and contour parallel paths (right). Red regions indicate higher residual marks.

Patch	#sgZ	#sC	#sgF	%tnZ	%tnC	%tnF	t_Z	t_C	t_F
#1 (BUNNY)	9	4	**1**	7.1%	4.7%	**1.5%**	450	368	**342**
#2 (FERTILITY)	18	6	**1**	6.6%	4.0%	**3.8%**	1908	1054	**1034**
#3 (MAXPLANK)	5	**1**	**1**	7.6%	6.0%	**2.5%**	245	232	**205**
#4 (SQUIRREL)	6	**1**	**1**	6.0%	2.8%	**1.9%**	539	428	**416**
#5 (KITTEN)	11	2	**1**	7.4%	3.7%	**2.8%**	469	381	**370**

Table 2. Comparing zigzag (Z) and contour-parallel (C) tool paths generated by commercial software packages to iso-scallop Fermat spirals (F) generated by our method. We report results on patches shown in Figure 15 using the following statistics: number of tool path segments (#sgZ, #sgC, and #sgF); percentage of sharp turn points (%tnZ, %tnC, and %tnF), and real machining time in seconds (t_Z , t_C, and t_F), using the CNC 6040 2200W machine.

To count the number of sharp turns along a tool path π, we uniformly sample 50, 000 points along π and at each point, we estimate its integral curvature [Pottmann et al. 2009] with a circle of radius 0.2mm, which is appropriate for the size of fabricated layers and the default fill with in our experiments. A point is deemed to represent a sharp turn if the smaller of its associated area coverage for curvature estimation is less than 30% of the circle area. In Table 2, we report the percentages of points deemed as sharp turns. It is quite evident that the number of sharp turns produced by connected Fermat spirals is much lower than that of zigzags.

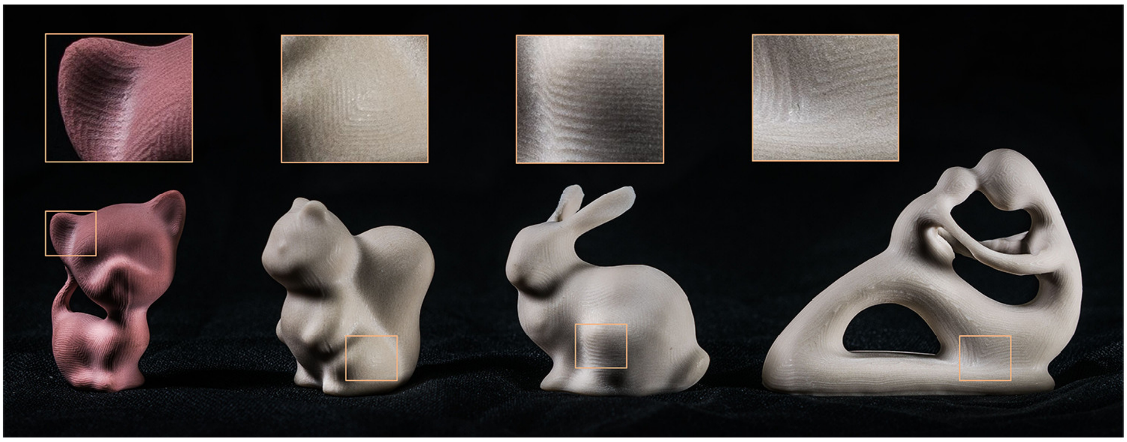

Fig. 17. Photographs and close-ups of real machining results for full 3D objects, following our fully automatic method for surface decomposition and tool path planning. The results were obtained using a CNC 6040 2200W 5-axis machine, with machinable resin board as the testing material.

7 DISCUSSION, LIMITATION, AND FUTURE WORK

Subtractive processes via CNC machining still dominate the manufacturing industry today. The CNC setup and tool path planning problem is rather complex in practice due to the multitude of factors that are at play. Most, if not all, of the factors involve geometry optimization spanning a diversity of forms and search spaces. The method we present focuses on two particular aspects of the problem: accessibility decomposition and efficient iso-scallop tool path generation, aiming for a fully automatic optimization. Results and comparisons to conventional tool paths demonstrate the effectiveness of our decompose-and-spiral-carve (DSCarver) approach.

The original Fermat spirals of Zhao et al. [2016] were developed for layered manufacturing. Our extension to curved surfaces shares all the desirable properties offered by this class of space-filling curves. In fact, Fermat spirals appear to be even more suited to CNC machining than to 3D printing via fused deposition modeling. The particular characteristics of Fermat spirals imply that gaps between tool paths may take relative long to fill. As a result, FDM using these tool paths may suffer from reduced material cohesion between adjacent and parallel tool paths since the long delay can cause material to cool down. Such issues are not encountered during CNC machining. In our work, we show that Fermat spirals can be adapted to produce iso-scallop carving paths for CNC.

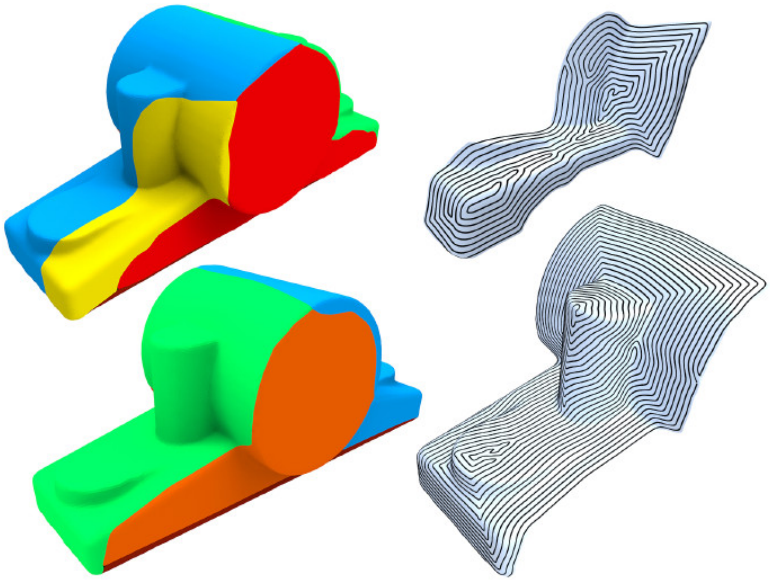

Fig. 18. Surface decomposition (two views are shown) and tool path planning results on an engineering/CAD part obtained by our method.

Engineering/CAD parts. We reiterate that the goal of our current work is to automate CNC machining of free-form 3D objects, not typical CAD/engineering parts. Also, Fermat spirals excel as tool paths for surface patches with wavy boundaries and irregular interior undulations, which are not characteristic of CAD models. Decompositions of CAD models with sharp features should respect these features, but neither the height field decomposition nor our accessibility analysis is feature-sensitive. In Figure 18, we show surface decompositions and tool paths obtained by our method on a CAD part. Clearly, the sharp features of the part would have been better accentuated if the tool paths were to conform to these features; this would require a feature-sensitive decomposition. One possibility would be to replace the height field decomposition with a feature-sensitive one, and we leave this for future work.

Practical CNC machining issues. DSCarver overlooks several such issues pertinent to CNC machining, including fixture design, cutter switching, and rough- vs. finish-stage machining. We also do not address situations of inaccessibility, e.g., tunnels or hollow parts, that are due to the physical (e.g., size) limitation of the cutter. In our work, we focus on finish-stage machining with a fixed cutter width and without factoring in constraints arising from fixture design. How a 3D object is clamped on object orientation. In other words, fixture placement is a factor that should be incorporated into tht MINORI problem. At the same time, fixtures affect cutter accessibility, namely, any surface regions that are attached to or covered by the fixture would be inaccessible. In general, fixture design is a highly non-trivial geometry optimization problem [Hazarika et al. 2015] and deserves separate investigation; it does seem to share some commonality with connector designs [Koyama et al. 2015]. Last but not the least, we only consider 3+2 machining where the CNC cutter holds a fixed orientation. Tool planning for full 5-axis CNC would involve a full five-dimensional search.

Rough surfaces. We experimented our machining algorithm mostly on locally smooth surfaces. For a 3D object whose surfaces are filled with many small concavities, small areas of the surface may not be reachable by the cutter. In such situations, CNC can benefit from approximating the surface with few height fields to reduce the number of 3+2-axis setups for machining. This is a strong merit of the work by Herholz et al. [2015] and is applicable here.

Global continuity of carving path. Our current method does not produce a globally continuous carving path over the whole accessibility region; the cutter needs to retracted to adjust to a different 3+2- axis setup when switching between different machinable patches. Global continuity may be possible using a full 5-axis CNC machine as its cutter head can move in five degrees of freedom, but this is a new tool planning problem. Another possibility is to only apply the 5-axis pass during the transitioning phase between machinable patches. Both problems are worth investigating in future work.

Future work. An obvious next step is to investigate the applicability of DSCarver for rough-stage machining, where the distinction, as well as challenge, is that the shape to be carved changes after each cutter pass over the surface. Along the same lines, it would be interesting to integrate our algorithm to existing practices from state-of-the-art CAD/CAM systems. Finally, automatic fixture design which combines accessibility and machinability analyses and globally continuous iso-scallop Fermat spirals under full 5-axis CNC machining are both intriguing problems to explore.

ACKNOWLEDGMENTS

We first thank all the reviewers for their valuable comments and suggestions. We are also grateful to Jibin Zhao, Libin Sun, Haoyuan Yu, among others, for sharing their expertise and advise on CNC machining. Wewould like to acknowledge Jinjie Lin for his contribution to the algorithm development in the very early stage of the project. Thanks for the bunny model from the Stanford Computer Graphics Laboratory and other models provided by the AIM@SHAPE Shape Repository. This work is supported in part by grants from National 973 Program (2015CB352501), NSFC (61232011, 61202147, 61332015, 61572291, 61772016), NSERC Canada (No. 611370), the Joint NSFCISF Research Program 61561146397 funded by the National Natural Science Foundation of China and the Israel Science Foundation, Israeli Science Foundation (No. 1790/12), U.S.-Israel Bi-National Science Foundation (No. 2012376), the Israel Science Foundation (2366/16), the ISF-NSFC Joint Research Program (2217/15, 2472/17), and gift funds from Adobe and Intel.

REFERENCES

Rajneesh Kumar Agrawal, D. K. Pratihar, and Roy Choudhury. 2006. Optimization of CNC isoscallop free form surface machining using a genetic algorithm. The International Journal of Advanced Manufacturing Technology 46, 7-8 (2006), 811–819.

Saleh M Amaitik and S Engin Kiliç. 2007. An intelligent process planning system for prismatic parts using STEP features. The International Journal of Advanced Manufacturing Technology 31, 9-10 (2007), 978–993.

Karlo Apro. 2008. Secrets of 5-axis machining. Industrial Press Inc.

Amit H Bermano, Thomas Funkhouser, and Szymon Rusinkiewicz. 2017. State of the Art in Methods and Representations for FabricationâĂŘAware Design. Computer Graphics Forum 36, 2 (2017), 509–535.

Zhang Wei Bo, Lu Zhen Hua, and Zhu Guang Yu. 2006. Optimization of process route by genetic algorithms. Robotics and Computer-Integrated Manufacturing 22, 2 (2006), 180–188.

John Bowers, Rui Wang, Li Yi Wei, and David Maletz. 2010. Parallel Poisson disk sampling with spectrum analysis on surfaces. ACM Transactions on Graphics 29, 6 (2010), 166.

Yuri Boykov, Olga Veksler, and Ramin Zabih. 2001. Fast Approximate Energy Minimization via Graph Cuts. IEEE Trans. Pat. Ana. & Mach. Int. 23, 11 (2001), 1222–1239.

Marcel Campen, Martin Heistermann, and Leif Kobbelt. 2013. Practical anisotropic geodesy. In Computer Graphics Forum, Vol. 32. Wiley Online Library, 63–71.

Ahmet Can and Ali Ünüvar. 2010. A novel iso-scallop tool-path generation for efficient five-axis machining of free-form surfaces. The International Journal of Advanced Manufacturing Technology 51, 9-12 (2010), 1083–1098.

Xuelin Chen, Hao Zhang, Jinjie Lin, Ruizhen Hu, Lin Lu, Qixing Huang, Bedrich Benes, Daniel Cohen-Or, and Baoquan Chen. 2015. Dapper: Decompose-and-pack for 3D Printing. ACM Trans. on Graph 34, 6 (2015), 213:1–213:12.

B. Choi and R. Jerrard. 1998. Sculptured Surface Machining: Theory and Applications. Kluwer Academic

Publishers.

V. Chvatal. 1979. A Greedy Heuristic for the Set-Covering Problem. Mathematics of Operations Research 4, 3 (1979), pp. 233–235.

http://www.jstor.org/stable/3689577

Thomas H. Cormen, Charles E. Leiserson, Ronald L. Rivest, and Clifford Stein. 2001. Introduction to Algorithms. MIT Press and McGraw-Hill.

Keenan Crane, Clarisse Weischedel, and Max Wardetzky. 2013a. Geodesics in Heat: A New Approach to Computing Distance Based on Heat Flow. ACM Trans. on Graph 32, 5 (2013), 152:1–152:11.

Keenan Crane, Clarisse Weischedel, and Max Wardetzky. 2013b. Geodesics in heat: A new approach to computing distance based on heat flow. ACM Transactions on Graphics 32, 5 (2013), 13–15.

Donghong Ding, Zengxi Stephen Pan, Dominic Cuiuri, and Huijun Li. 2014. A tool-path generation strategy for wire and arc additive manufacturing. Int. J. of Adv. Manufact. Tech. 73, 1-4 (2014), 173–183.

R. T. Farouki. 2016. Rational rotation-minimizing frames — Recent advances and open problems. Appl. Math. Comput. 272 (2016), 80–91.

R. T. Farouki and S. Li. 2013. Optimal tool orientation control for 5-axis CNC milling with ball-end cutters. Computer Aided Geometric Design 30, 2 (2013), 226–239.

Matthew C Frank, Richard A Wysk, and Sanjay B Joshi. 2006. Determining setup orientations from the visibility of slice geometry for rapid computer numerically controlled machining. Journal of manufacturing science and engineering 128, 1 (2006), 228–238.

Stefan Gottschalk, Ming Lin, Dinesh Manocha, and Eric Larsen. 1999. PQP–the proximity query package. Accessed October 4 (1999), 2011.

YW Guo, Antony R Mileham, Geraint W Owen, Paul G Maropoulos, and WD Li. 2009. Operation sequencing optimization for five-axis prismatic parts using a particle swarm optimization approach. Proceedings of the Institution of Mechanical Engineers, Part B: Journal of Engineering Manufacture 223, 5 (2009), 485–497.

Prosenjit Gupta, Ravi Janardan, Jayanth Majhi, and TonyWoo. 1996. Efficient geometric algorithms for workpiece orientation in 4-and 5-axis NC machining. Computer-Aided Design 28, 8 (1996), 577–587.

Steffen Hauth and Lars Linsen. 2012. Double-spiral tool path in configuration space. The International Journal of Advanced Manufacturing Technology 54, 9 (2012), 1011–1022.

Manjuri Hazarika, Uday Shanker Dixit, et al. 2015. Setup planning for machining. Springer. Martin Held and Christian Spielberger. 2014.

Improved Spiral High-Speed Machining of Multiply-Connected Pockets. Computer-Aided Design and Applications 11, 3 (2014), 346–357.

Philipp Herholz, Wojciech Matusik, and Marc Alexa. 2015. Approximating Free-form Geometry with Height Fields for Manufacturing. Computer Graphics Forum (Eurographics) 34, 2 (2015), 239–251.

Kristian Hildebrand, Bernd Bickel, and Marc Alexa. 2013. Orthogonal slicing for additive manufacturing. Computers & Graphics 37, 6 (2013), 669 – 675. Shape Model. Intl. (SMI) Conf.

Ruizhen Hu, Honghua Li, Hao Zhang, and Daniel Cohen-Or. 2014. Approximate Pyramidal Shape Decomposition. ACM Trans. on Graph 33, 6 (2014), 213:1–213:12.

Ralph L Keeney and Howard Raiffa. 1993. Decisions with multiple objectives: preferences and value trade-offs. Cambridge university press.

Su Jin Kim, Dong Yoon Lee, Hyun Chul Kim, Sung Gun Lee, and Min Yang Yang. 2006. CL surface deformation approach for a 5-axis tool path generation. International Journal of Advanced Manufacturing Technology 28, 5-6 (2006), 509–517.

Yuki Koyama, Shinjiro Sueda, Emma Steinhardt, Takeo Igarashi, Ariel Shamir, and Wojciech Matusik. 2015. AutoConnect: Computational Design of 3D-printable Connectors. ACM Trans. on Graph 34, 6, Article 231 (2015), 231:1–231:11 pages.

Ali Lasemi, Deyi Xue, and Peihua Gu. 2010. Recent development in CNC machining of freeform surfaces: A state-of-the-art review. Computer-Aided Design 42, 7 (2010), 641–654.

Yunjin Lee and Seungyong Lee. 2002. Geometric Snakes for Triangular Meshes. Computer Graphics Forum 21, 3 (2002), 229–238.

Lin Lu, Andrei Sharf, Haisen Zhao, Yuan Wei, Qingnan Fan, Xuelin Chen, Yann Savoye, Changhe Tu, Daniel Cohen-Or, and Baoquan Chen. 2014. Build-to-Last: Strength to Weight 3D Printed Objects. ACM Trans. on Graph 33, 4 (2014), 97:1–97:10.

Linjie Luo, Ilya Baran, Szymon Rusinkiewicz, and Wojciech Matusik. 2012. Chopper: Partitioning Models into 3D-Printable Parts. ACM Trans. on Graph 31, 6 (2012), 129:1–129:9.

Debananda Misra, V Sundararajan, and Paul K Wright. 2005. Zig-zag tool path generation for sculptured surface finishing. In Geometric and algorithmic aspects of computer-aided design and manufacturing: DIMACS workshop computer aided design and manufacturing, Vol. 67. 265.

Sang C Park, Chang Y C, and Byoung Kyu Choi. 2003. Contour-parallel offset machining without tool-retractions. Computer-Aided Design 35, 9 (2003), 841–849.

Helmut Pottmann, Johannes Wallner, Qi-Xing Huang, and Yong-Liang Yang. 2009. Integral invariants for robust geometry processing. Comp. Aided Geom. Design 26, 1 (2009), 37–60.

Romain Prévost, Emily Whiting, Sylvain Lefebvre, and Olga Sorkine-Hornung. 2013. Make It Stand: Balancing Shapes for 3D Fabrication. ACM Trans. on Graph 32, 4 (2013), 81:1–81:10.

Fei Ren, Yuwen Sun, and Dongming Guo. 2009. Combined reparameterization-based spiral toolpath generation for five-axis sculptured surface machining. Int. J. of Adv. Manufac. Tech. 40, 7 (2009), 760–768.

Ariel Shamir. 2008.A survey on Mesh Segmentation Techniques. CGF 27, 6 (2008),1539–1556.

Siemens. 2016. NX Software. http://www.plm.automation.siemens.com/en_us/products/ nx/index.shtml. (2016).

Ondrej Stava, Juraj Vanek, Bedrich Benes, Nathan Carr, and Radomír Měch. 2012. Stress relief: improving structural strength of 3D printable objects. ACM Trans. on Graph 31, 4 (2012), 48:1–48:11.

Y-J Tseng and SB Joshi. 1998. Recognition of interacting rotational and prismatic machining features from 3D mill-turn parts. International Journal of Production Research 36, 11 (1998), 3147–3165.

Yu Wang, Kai-Min Yu, and Charlie CL Wang. 2015. Spiral and conformal cooling in plastic injection molding. Computer-Aided Design 63 (2015), 1–11.

Nuo Xu, Samuel H Huang, and Y Kevin Rong. 2007. Automatic setup planning: current state-of-the-art and future perspective. International journal of manufacturing technology and management 11, 2 (2007), 193–208.

Y Yang, HT Loh, JYH Fuh, and YG Wang. 2002. Equidistant path generation for improving scanning efficiency in layered manufacturing. Rapid Prototyping Journal 8, 1 (2002), 30–37.

Haisen Zhao, Fanglin Gu, Qi-Xing Huang, Jorge Garcia, Hao Zhang, Daniel Cohen-Or, Yong Chen, Changhe Tu, and Baoquan Chen. 2016. Connected Fermat Spirals for Layered Fabrication. ACM Trans. on Graph 35, 4 (2016).

J. Zhao, B. Zhong, and Q. Zou. 2013. Tool orientation planning for five-axis CNC machining of open free-form surfaces. Journal of Systems Science and Complexity 26, 5 (2013), 667–675.

Bo Zhou, Jibin Zhao, Lun Li, and Renbo Xia. 2016. A smooth double spiral tool path generation and linking method for high-speed machining of multiply-connected pockets. Precision Engineering (2016).

Qiang Zoua, Juyong Zhanga, Bailin Deng, and Jibin Zhao. 2014. Iso-level tool path planning for free-form surfaces. Computer-Aided Design 53 (2014), 217–225.

学位论文评阅及答辩情况表

<table>
<tr><td rowspan="6">论文评阅人</td><td colspan="2">姓　名</td><td>专业技术职　务</td><td>是否博导（硕导）</td><td>所 在 单 位</td><td>总体评价※</td></tr>
<tr><td colspan="2">匿名评阅人1</td><td>–</td><td>–</td><td>–</td><td>优秀</td></tr>
<tr><td colspan="2">匿名评阅人2</td><td>–</td><td>–</td><td>–</td><td>优秀</td></tr>
<tr><td colspan="2">匿名评阅人3</td><td>–</td><td>–</td><td>–</td><td>优秀</td></tr>
<tr><td colspan="2"></td><td></td><td></td><td></td><td></td></tr>
<tr><td colspan="2"></td><td></td><td></td><td></td><td></td></tr>
<tr><td rowspan="11">答辩委员会成员</td><td colspan="2">姓　名</td><td>专业技术职　务</td><td>是否博导（硕导）</td><td colspan="2">所 在 单 位</td></tr>
<tr><td>主席</td><td>汪国平</td><td>教授</td><td>博导</td><td colspan="2">北京大学</td></tr>
<tr><td rowspan="9">委员</td><td>毋立芳</td><td>教授</td><td>博导</td><td colspan="2">北京工业大学</td></tr>
<tr><td>聂礼强</td><td>教授</td><td>博导</td><td colspan="2">山东大学</td></tr>
<tr><td>汪云海</td><td>教授</td><td>博导</td><td colspan="2">山东大学</td></tr>
<tr><td>吕琳</td><td>副教授</td><td>博导</td><td colspan="2">山东大学</td></tr>
<tr><td></td><td></td><td></td><td colspan="2"></td></tr>
<tr><td></td><td></td><td></td><td colspan="2"></td></tr>
<tr><td></td><td></td><td></td><td colspan="2"></td></tr>
<tr><td></td><td></td><td></td><td colspan="2"></td></tr>
<tr><td></td><td></td><td></td><td colspan="2"></td></tr>
<tr><td colspan="3">答辩委员会对论文的总体评价※</td><td>A</td><td>答辩秘书</td><td>钟凡</td><td>答辩日期　2018.11.16</td></tr>
<tr><td colspan="2">备注</td><td colspan="5"></td></tr>
</table>

※优秀为“A”；良好为“B”；合格为“C”；不合格为“D”。